Towards synthetic fuels via electrocatalysis

Electrochemical CO2 Reduction

Jovanov, Zarko; Chorkendorff, Ib; Stephens, Ifan

Publication date:
2014

Document Version
Peer reviewed version

DTU Technical University of Denmark
Department of Physics

Towards synthetic fuels via electrocatalysis

Electrochemical CO_2 Reduction

Zarko Jovanov

Center for Individual Nanoparticle Functionality

CASE
Catalysis for Sustainable Energy

Kongens Lyngby, Denmark, 2014

Cover page: Photograph of the electrochemical H-cell used in the project.

Photographer: Lisbeth Holten.

Technical University of Denmark

Department of Physics

Center for Individual Nanoparticle Functionality

Towards synthetic fuels via electrocatalysis

Electrochemical CO_2 Reduction

Thesis submitted for the Degree of Doctor of Philosophy

Zarko P. Jovanov

Supervisors:

Prof. Ib Chorkendorff

Assistant Prof. Ifan E. L. Stephens

Kongens Lyngby, Denmark

January 2014

Preface

This thesis is submitted in partial fulfilment for the degree of Doctor of Philosophy in Physics at the Technical University of Denmark. The work presented in the thesis has been carried out in Center for Individual Nanoparticle Functionality (CINF), from 1st November 2010 until 31st January 2014, under the supervision of Professor Ib Chorkendorff, Professor Søren Dahl and Assistant Professor Ifan Stephens.

A significant part of the thesis is inspired by and conducted in collaboration with the theoretical electrochemistry group of Jens Nørskov at SUNCAT Center for Interface Science and Catalysis, Department of Chemical Engineering, Stanford University, Stanford, CA, USA.

CINF is funded by The Danish Research Foundation. My Ph.D. project was a part of the Catalysis for Sustainable Energy (CASE) research initiative, founded through the Danish Ministry of Science, Technology and Innovation.

Zarko P. Jovanov

Kongens Lyngby, 31st January 2014.

Acknowledgements

I would like to thank Professor Ib Chorkendorff and Professor Søren Dahl for the opportunity to carry out my PhD project at the Department of Physics. I am very grateful to Ib for his guidance and suggestions on how to improve my research. Especially, I would like to thank Assistant Professor Ifan Stephens, for his commitment to guide me and advise me through the challenging periods of the project. I am pleased I was given the chance to learn a lot from our discussions about electrochemistry. I thank to Professor Jens Nørskov for his ever so encouraging attitude during our meetings.

I enjoyed myself very much a highly professional and friendly environment at CINF, CAMD and CEN. It was a great experience to work with everyone in the electrochemistry lab. In particular, I have to thank Dr. Ana Sofia Varela, who equally well understood the challenges with experimentation in CO_2 reduction project. In addition, I thank Dr. Heine Hansen and Dr. Andrew Peterson for all insightful comments and our discussions, which helped me to understand the theoretical modeling better. Furthermore, I thank Paolo Malacrida for being very helpful and carrying out the XPS measurements, Arnau Verdaguer-Casadevall for help with preparing the oxide derived gold electrodes and Dr. Björn Wickman for clarifying my doubts while establishing the experimental setup. Especially, I would like to acknowledge Jacqueline McAnulty for her care and her readiness to help me in the lab whenever needed. I admire the work of our highly skilled glassblower, Jan Patrick Scholer who always made efforts to understand our new ideas and produce unique glassware.

I want to thank Ifan, Heine and Ana Sofia for proofreading this thesis, Tobias for translating the thesis abstract into Danish and Juan Maria for making a Au_3Cd surface image.

Special thanks I owe to all my close friends for being always there for me – Vladimir and Tijana, Patricia and Tobias, Rosa, Phillip, Irie, Sofia, Maria, Aleksandar, Irantzu, Juan Maria and Billie. Thank you for making my days in Copenhagen unforgettable.

In spite of distance, my parents Petar and Stojana, as well as my brothers Ivan and Nenad, have always found a way to express their love and understanding. You have been a great support through the effortful times and I devote this thesis to you.

Zarko Jovanov

January 2014

Abstract

The storage of electricity in chemical bonds in form of fuels is a promising route for leveling the intermittent production of renewable energy. The present PhD thesis is concerned with the electrocatalysis of CO_2 reduction in aqueous media at ambient conditions, as an alternative process to Fischer-Tropsch fuel synthesis.

The thesis encompasses electrochemical CO_2 and CO reduction on pure metals consisting of polycrystalline copper and gold, as well as the bimetallic catalysts consisting of copper overlayers on platinum single crystals and bulk and surface alloys of gold-cadmium.

By roughening the surface of polycrystalline copper in a low buffer capacity electrolyte, we favoured the selectivity towards ethylene rather than methane production. We show trends between the selectivity towards CO, CH_4 and C_2H_4.

By depositing monolayers of copper onto platinum single crystals, we tuned the reactivity of copper by modifying the tensile strain. However, the overlayers appeared to be unstable under reaction conditions, due to the strong interaction of CO with platinum.

We investigate the reduction of CO_2 to CO on polycrystalline Au in neutral media. On the basis of our observations, we propose that the coverage of the adsorbed *CO under reaction conditions is significant. This suggests the existence of two types of adsorbed *CO, whereby the weakly bound *CO could be the reactive intermediate for CO evolution. We also carried out the reduction of CO on roughened Au in alkaline media, which yielded trace amounts of formaldehyde and methanol. The observation that adsorbed, strongly bound *CO is not reduced further, suggests the existence of additional kinetic barriers.

Guided by the theoretical models, we followed a strategy of alloying to break the existing scaling relations between the key CO_2 reduction intermediates. Density functional theory calculations suggested Au_3Cd should possess respectable stability, and higher catalytic activity than Au for CO evolution and CH_3OH. However, extensive CO_2 electrolysis measurements on gold-cadmium bulk and surface alloy exhibited lower activities for CO evolution, relative to Au. Despite the promising predictions about low overpotentials based on DFT calculations, CO electrolysis in alkaline media on cadmium alloyed gold surfaces revealed negligible activity for CO reduction. We hypothesise that adsorbate induced rearrangements of the surface take place, possibly involving segregation of elements and thus loss of active sites, analogous the copper-platinum system. The most likely candidates for these adsorbates are *CO and *H under reaction conditions and possibly *OH and *OCHO* at more positive potentials. Similar to Au, trace amounts of methanol and formaldehyde

were observed as products of CO reduction. Our results point towards the need to design a catalyst surface that is stable under reaction conditions, where reactive intermediates cannot restructure the active sites.

Resume

Lagring af elektricitet i kemiske bindinger i form af brændstof er en lovende vej til at udjævne den uregelmæssige produktion af vedvarende energi. Denne PhD afhandling handler om elektrokatalyse af CO_2 reduktion i vandig opløsning ved standardbetingelser, som et alternativ til Fischer-Tropsch processen.

Afhandlingen omfatter elektrokemisk CO_2 og CO reduktion på rene metaller, der består af polykrystallinsk kobber og guld, bimetalliske katalysatorer bestående af kobber overlag på platin enkeltkrystaller samt legeringer og overflade legeringer af guld-cadmium.

Ved at gøre overfladen af polykrystallinsk kobber ru i en elektrolyt med lav bufferkapacitet, fordelagtiggjordes selektiviteten for ethylen frem for produktionen af metan. Vi viser tendenser i selektivitet over for CO, CH_4 og C_2H_4.

Ved at deponere kobber monolag på platin enkeltkrystaller, ændrede vi reaktiviteten af kobber ved at ændre hvor meget kobber overlaget er strukket. Overlagene viste sig imidlertid at være ustabile under reaktionsbetingelserne, på grund af den stærke vekselvirkning mellem CO og platin.

Vi undersøger reduktion af CO_2 til CO på polykrystallinsk Au i neutrale medier. På baggrund af vores observationer forventer vi, at dækningsgraden af det adsorberede CO under reaktionsbetingelser er betydelig. Det tyder på, at der findes to typer af adsorberet CO, hvorved den svagt bundne CO kunne være det reaktive mellemprodukt for CO udvikling. Vi foretog også reduktion af CO på den ru guld i alkaliske medier, hvilket gav spormængder af formaldehyd og metanol. Observationen, at adsorberet, stærkt bundet CO ikke reduceres yderligere, indikerer at der eksisterer yderligere kinetiske barrierer.

Under vejledning af de teoretiske modeller, fulgte vi en strategi om at legere for at bryde de eksisterende skaleringer mellem de centrale CO_2-reduktions mellemprodukter. Tæthedsfunktionalteori (DFT) beregninger foreslog Au_3Cd som værende tilstrækkelig stabil og forventlig højere katalytisk aktiv end Au for CO og CH_3OH udvikling. Men omfattende CO_2 elektrolyse målinger på guld-cadmium legering og overflade legering udviste lavere aktiviteter for CO udvikling, i forhold til Au. På trods af de lovende forudsigelser om lave overspændinger baseret på DFT beregninger, viste CO elektrolyse i alkaliske medier på cadmium legeret guld overflader ubetydelig aktivitet for CO reduktion. Vi spekulerer at adsorbat-inducerede omrokeringer af overfladen finder sted, muligvis med segregering af atomer og dermed tab af aktive sites, analog til kobber-platin systemet. De mest sandsynlige kandidater til disse adsorbater er *CO og *H under reaktionsbetingelserne og eventuelt *OH og *OCHO* ved mere positive potentialer. Ligesom for Au blev spormængder af methanol og

formaldehyd observeret som produkter af CO-reduktion. Vores resultater peger i retning af behovet for at designe en katalytisk overflade, der er stabil under reaktionsbetingelserne og hvor reaktive mellemprodukter ikke kan omstrukturere de aktive steder.

Contents

"The scientific man does not aim at an immediate result. He does not expect that his advanced ideas will be readily taken up. His work is like that of the planter — for the future. His duty is to lay the foundation for those who are to come, and point the way. He lives and labors and hopes."

Nikola Tesla

CHAPTER 1

1. Introduction and motivation

1.1 Energy challenge and fossil fuels

In the 21st century, the most difficult challenge for mankind is to secure the supply of sufficient food, water and energy for the entire human race.[1-3] The world is facing a continuous growth in population, which apart from increase in demand for food and clean water, reflects in a higher energy demand.[1-4] Energy is needed for heating and powering the buildings in which we live and work, as well as for industry, which produces food, medications and all other products essential for humanity. In addition, transportation belongs to one of the largest energy consuming commodities.[4,5] Apart from growth of world's population, economic growth in the developing societies leads to a larger energy demand and consumption.[4]

Figure 1.1 shows comparative values of energy demand by regions (divided into two groups: countries members of the Organisation for Economic Co-operation and Development – OECD and the rest of the world), the primary use of energy and the resources exploited to meet these demands.[4] The plots indicate a projection of a rapid increase in primary energy demand by 2030, due to an increase in population and income growth, mostly in the developing economies.[4] The total world energy consumption in 2010 is marked with a vertical line on plots in Figure 1.1 and corresponds to roughly 12 billion tonnes of oil equivalent (*toe*) or 16 TWyear. The major growth in energy demand arises from the needs for the generation of power, industry and transportation. Nowadays, these demands are almost entirely met by fuels derived from the fossil resources: oil, natural gas and coal.[4] Modern technologies are mostly based on technological approach, consisting in conversion of crude oil, natural gas or coal to value-added chemicals and transportation fuels.[6,7] These technologies rely on processes, which can dissociate hydrogen and carbon, from different sources, and reorganise them into the feedstock units for either fine chemicals or high energy density fuels such as gasoline or diesel.[5,6] All these large scale processes – production of hydrogen, syngas, methane, methanol, higher hydrocarbons, liquid fuels – proceed at elevated pressures and temperatures using heterogeneous catalysis.[8]

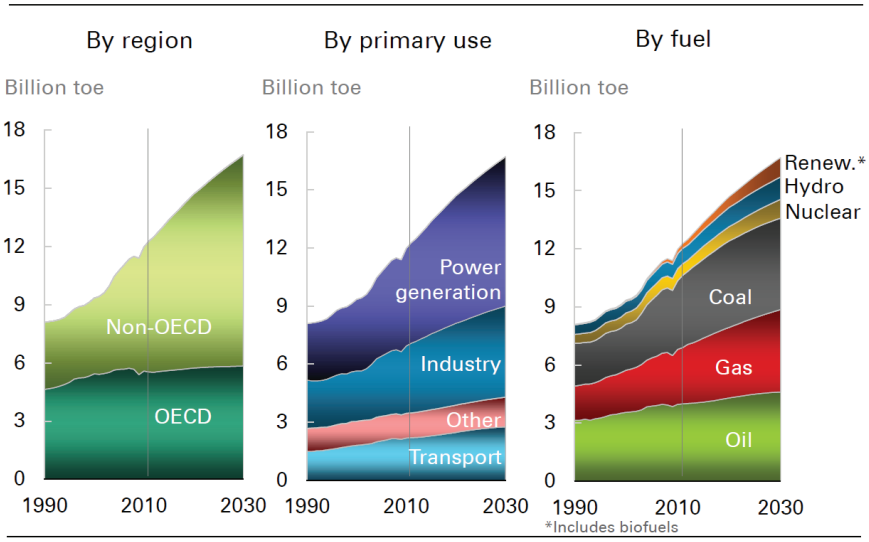

Figure 1.1: World energy consumption by region, by primary use and by resources used for meeting these demands. OECD refers to member countries of the Organisation for Economic Co-operation and Development. *toe* refers to energy unit – tonne of oil equivalent (equals to ~42 GJ). Reprinted from[4]

On the other hand, fossil resources are not infinite and are unequally distributed by the world's regions.[4] Hence, the technological solutions that are widely applied today are not sustainable in the long term. In addition, the emissions from burning fossil fuels extensively are related to pollution that affects the environment and may have an effect on the climate.[4,6] In this sense, novel technologies are necessary to ensure a sustainable production of chemicals and energy carriers in economically viable fashion and with minimal effects on the environment.[6]

The major existing alternative (non-fossil fuels) technologies involve power (electricity) generation employing hydro resources or nuclear fission.[3,7,9] However, the issues with the long term use of nuclear fission are related to the scarce fissile fuel materials and safe radioactive waste disposal.[7] Nuclear fusion is a promising technology yet to come and requires intense scientific efforts.[7]

Even though these technologies are an alternative to the fossil fuels, they are still not effectively applicable on large scale in the long term, and are thus unsustainable.

1.2 Sustainability: renewable energy sources and storage

There is no doubt that the renewable resources available on Earth have the capacity to fulfill the world's energy demand.[10] The energy irradiated from the sun is converted into the other forms, such as biochemical (biomass), thermal (heat, geothermal) and mechanical (wind and tidal) energy. In principle, the energy from all these phenomena could more or less efficiently be converted into electricity or heat, readily available for consumption.[3] However, the peak consumption does not usually match with the period when renewable energy is available. The fluctuations in renewable energy generation and energy demand could be managed by developing the advanced electric grids.[5] Nevertheless, the intermittent nature of solar and wind power implies the necessity for development of efficient processes for energy storage with high energy density.

There exists a variety of options for energy storage depending on the ultimate application. A comparative representation of the power density versus energy density is given in form of the Ragone plot on Figure 1.2. The plot focuses especially on the technologies available for the transportation sector: combustion engines using gasoline and hydrogen as fuels, fuel cell and battery technologies as well as supercapacitors and flywheels. The energy carriers possessing the highest energy density are liquid fuels – gasoline, diesel, methanol, etc.[3] A development of efficient technologies for synthesis of liquid fuels using alternative and renewable energy sources would contribute to a smoother transition from fossil fuel based economies to sustainable economies.[6,9]

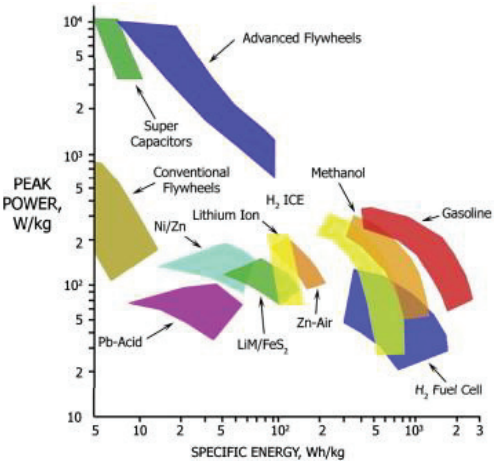

Figure 1.2: The Ragone plot – a comparison of the energy densities versus power densities of various options for energy storage, especially related to the transportation systems involving batteries, supercapacitors, flywheels and various gaseous and liquid fuels. Reprinted from[3].

The possibility to use the existing infrastructure would facilitate a cost-effective large scale implementation of the renewable technologies. On Figure 1.3, Graves et al propose a map of possibilities, including the technologies for energy collection, sources of carbon and hydrogen and processes that allow their conversion into high energy density synthetic fuels or feedstock chemicals.[9]

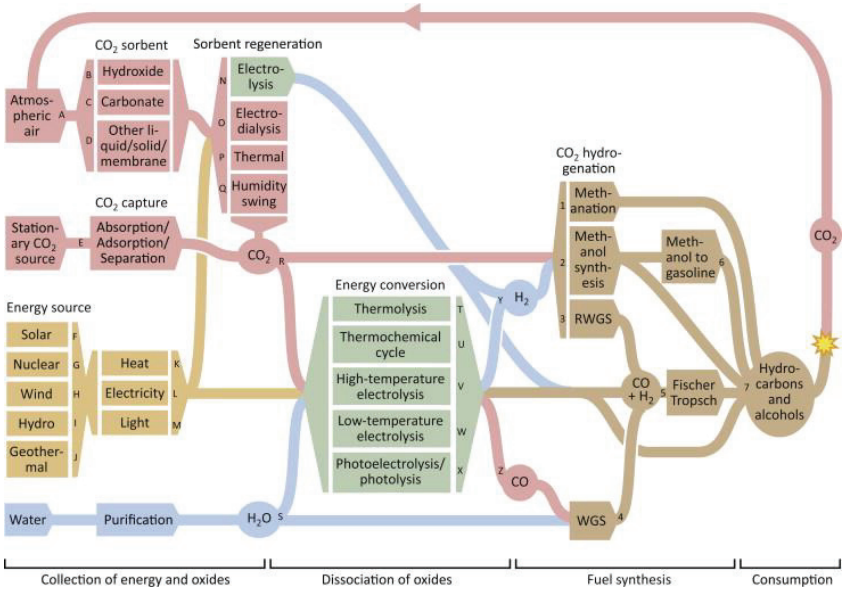

Figure 1.3: The map of possible routes for fuels synthesis using alternative technologies. H_2O is considered as a source of hydrogen and CO_2 as carbon source. Reprinted from[9]

The authors split the overall scheme into four stages: the collection of energy and oxides (carbon and hydrogen sources), dissociation of the oxides (water and carbon dioxide), fuel synthesis and finally consumption. They review possibilities of use of H_2O and CO_2 as sustainable sources of hydrogen and carbon, respectively. Water can be supplied sustainably from the oceans employing the desalination process.[9] Recycling of CO_2 from large industrial plants, or captured from the air, could open a possibility to manage carbon emissions. The heat, electricity or light from various renewable energy sources could be stored in high energy density chemical bonds, in form of hydrocarbons or alcohols. The authors identify several existing approaches to convert CO_2 to carbon based fuels, such as methanol synthesis based on the conventional CO_2 hydrogenation at high temperatures and pressures, using Cu and ZnO as catalyst. Another possibility involves use of syngas, a mixture of CO and H_2, which can be further converted to higher hydrocarbons in Fischer-Tropsch process (equation 1.1).[9]

$$(2n+1)H_2 + nCO = C_nH_{(2n+2)} + nH_2O \qquad \textbf{(1.1)}$$

The stage with the largest energy conversion is related to oxide (H_2O and CO_2) dissociation, to provide hydrogen and carbon.[9] These processes may involve direct use of solar heat (thermolysis) or electricity driven water and CO_2 splitting at elevated or ambient temperatures. Nonetheless, there is an economic and a scientific interest to develop an alternative process to Fischer-Tropsch, in order to avoid the dissociation stage and enable fuel synthesis directly from water and carbon dioxide.

The understanding and mimicking the natural process of photosynthesis may open a possibility for efficient conversion of direct solar energy into liquid fuels – solar fuels.[11] Such an *artificial photosynthesis* process may be rather complex, since it consists of both absorption of sunlight to produce electricity and electrolytic process to synthesise the fuels.[2,5,6,9]

In any case, regardless whether the photoelectrolysis or low temperature electrolysis is considered, fuel synthesis is relying on understanding and developing the catalytic process and finding suitable catalytic materials for an efficient implementation of the novel technology on large scale.[6]

1.3 Low temperature electrolysis

Low temperature electrolysis assumes an electrically driven splitting of H_2O and reduction of CO_2 at ambient conditions.[12] It is achieved by applying a potential difference between the two electrodes in a device known as electrolyser (see Figure 1.4). An electrolyser is a device consisting in two cell compartments – anode, where water oxidation reaction occurs, as shown in equation 1.2, and – cathode, where the electrochemical reduction of CO_2 occurs (equations 1.3 through 1.6). A proton (or anion) conducting membrane separates the two cells, avoiding the mixture of fuels and O_2 and allowing only passage of protons.[6,9]

$$2H_2O = O_2 + 4H^+ + 4e^- \qquad U_{eq} = 1.23 \text{ V vs. RHE} \qquad \textbf{(1.2)}$$

There is a variety of reactions that might occur at the cathode, depending on the reaction conditions and the catalyst. Some of the possible reactions are shown in equations 1.3 to 1.6.[12,13]

$$CO_2 + 8H^+ + 8e^- = CH_4 + 2H_2O \qquad U_{eq} = 0.17 \text{ V vs. RHE} \qquad \textbf{(1.3)}$$

$$CO_2 + 6H^+ + 6e^- = CH_3OH + 2H_2O \qquad U_{eq} = 0.02 \text{ V vs. RHE} \qquad \textbf{(1.4)}$$

$$CO_2 + 2H^+ + 2e^- = CO + H_2O \qquad U_{eq} = -0.10 \text{ V vs. RHE} \qquad \textbf{(1.5)}$$

$$2H^+ + 2e^- = H_2 \qquad U_{eq} = 0.00 \text{ V vs. RHE} \qquad \textbf{(1.6)}$$

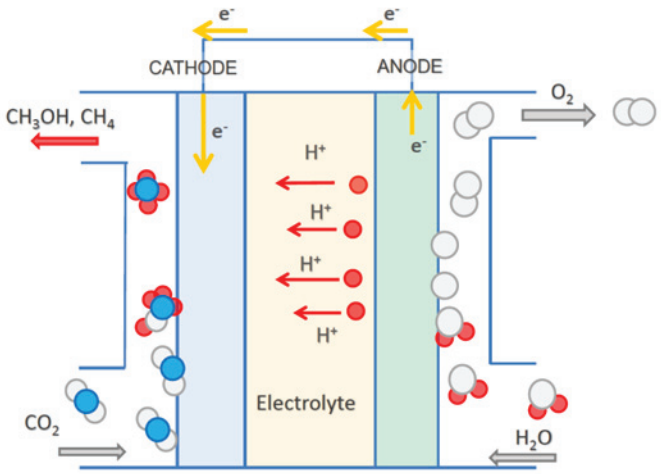

Figure 1.4: Schematic representation of an electrolyser for bulk CO_2 electrolysis. Adapted from the PhD thesis of Maria Escudero Escribano.[14]

Transition metal surfaces may serve as catalysts for electrochemical reduction of CO_2. Depending on the electrode surface, its morphology, applied potential, working electrolyte, its pH and many other factors, CO_2 can be reduced to high energy value compounds such as hydrocarbons – methane, ethylene, ethane, propane – as well as alcohols – methanol, ethanol.[6,9,15-20]

Apart from the capital and maintenance costs, the most relevant costs of an electrolyser device are related to the cost of the electricity and the efficiency for its conversion to chemical energy.[9] As shown in equation 1.7, the overall electricity-to-chemical energy efficiency ($\varepsilon_{\text{electrolysis}}$) for a specific half reaction depends on the overpotential, necessary for the reaction to achieve a certain current density (η) and the current (Faradaic) efficiency for a given product ($\varepsilon_{\text{Faradaic}}$). U_{eq} is an equilibrium redox potential, at which, theoretically, the reaction should be thermoneutral.[6,9]

$$\varepsilon_{electrolysis} = \frac{U_{\text{eq}}}{U_{eq}+\eta}\,\varepsilon_{Faradaic} \qquad \textbf{(1.7)}$$

In general, Faradaic efficiency describes the current selectivity for production of a given compound and it is related mainly to the nature of the catalyst, but may also depend on the reaction conditions. On the other hand, the overpotential depends exclusively on the thermodynamic properties of the catalyst material. To improve the efficiency of this process, the requirements for a catalyst material are that it has a high activity (high current density at low overpotential), and a high selectivity for a single valuable compound. Additionally, the stability and supply of the catalyst material are inevitably relevant when addressing the scalability of the novel renewable energy processes.[21]

1.4 Outline of the thesis

The present thesis aims to contribute to the fundamental understanding of the electrocatalytic processes occurring during the reduction of CO_2 and CO to synthetic fuels. As briefly discussed in section 1.3, the major barrier for designing an efficient device to perform bulk CO_2 electrolysis is related to finding a stable and available catalyst material; the catalyst should possess high selectivity and activity for CO_2 reduction towards an energy rich compound such as methane or methanol.

Chapter 1 provides a broader context of the research area. It points out the advantages of storing the energy coming from renewables in form of chemical bonds, i.e. high energy density synthetic or solar fuels. In Chapter 2, a thermodynamic background for electrochemical reduction of CO_2 and CO is discussed. We present the general concepts in catalysis and introduce a brief overview of the literature related to CO_2 reduction electrocatalysis on various transition metals, with emphasis on experimental works using copper and gold electrodes. Additionally, we provide a state-of-art theoretical understanding of CO_2 reduction catalysis obtained through density functional theory calculations. Chapter 3 lists all experimental methods, tools and equipment employed for the experimental work in this thesis for catalyst preparation, characterisation and conduction of the bulk electrolysis measurements, along with the qualitative and quantitative product analysis methods. Chapter 4 explores the surface morphology effects on the catalytic activity and selectivity of polycrystalline copper electrodes for CO_2 electro-reduction. The purpose of Chapter 5 is to give a brief insight into the possibilities of performing the CO_2 reduction on copper overlayers on platinum single crystals. This study reveals how adsorbate induced structural changes may affect the overall catalytic activity. Hence, the use of less reactive metal surfaces is suggested. Chapter 6 deals with polycrystalline gold electrodes. We present CO_2 reduction in neutral media, as well as CO reduction in alkaline media using a variety of product analysis methods with very low detection limits. In order to interpret the catalytic measurements, we combine theoretical and experimental methods. Finally, in Chapter 7, as a collaborative study, we explore the possibility of improving the catalyst performance, guided by density functional theory (DFT) calculations. The theoretical model predicts Au_3Cd alloy as the most promising catalyst for reducing the high overpotentials for CO_2 reduction. We investigate bulk and surface bimetallic structures containing gold and cadmium experimentally and interpret our observations using DFT. Finally, the conclusions from this study are summarised in Chapter 8, and the direction for future studies in Chapter 9.

CHAPTER 2

2. Theoretical background and literature overview

2.1 Catalytic activity of metals

2.1.1 Sabatier principle

Catalysis accelerates chemical reactions by enabling a lower energy pathway for reactants conversion to products. The lower energy pathway is provided through an interaction of the reactants with a catalyst, whereby the adsorbate's internal chemical bonds are weakened and thus, the formation of the new chemical bonds is facilitated.[8] Heterogeneous catalysis assumes the adsorption of the gas or liquid phase reactants on a solid surface of a catalyst material, followed by the reaction and subsequent product desorption. Various materials possess different affinities towards binding of different reactants and reaction intermediates, which determines their overall efficiency as a catalyst. The key reaction intermediates have to bind to the catalyst surface strong enough for the reaction to occur. However, the catalyst binding towards the final product should be weak enough to allow its facile desorption. Therefore, the most active catalyst materials possess a moderate binding towards the key reaction intermediate – the principle also known as a *Sabatier principle*.[22] A typical way of comparing catalyst activity involves plotting a measured parameter of activity (turn over frequency, current density, limiting potential, etc.) versus an activity descriptor – the binding energy of a key reaction intermediate.[23-29] Such representation orders the best performing catalysts around the optimal binding energy for a given intermediate – resulting in a plot shaped as a volcano.
The simpliest example of an electrocatalytic reaction is hydrogen evolution reaction (HER), as shown in equation 2.1:

$$2H^{+}_{(aq)} + 2e^{-} = H_{2(g)} \qquad U_{eq} = 0 \text{ V vs. RHE} \qquad \textbf{(2.1)}$$

Plot (a) in Figure 2.1 represents a free energy diagram for the hydrogen evolution reaction, proceeding through a single reaction intermediate, the adsorbed hydrogen. Nørskov and co-workers[29] employ the

density functional theory calculations to calculate the hydrogen chemisorption energy per atom (ΔE_H). The free energy of *H is shown for various transition metal surfaces. Bandarenka and co-workers use these calculated values as the activity descriptor to construct a volcano plot for the HER.[23]

The optimal activity, i.e. the highest values of the experimentally measured exchange current densities are obtained for the metal surfaces with intermediate binding of hydrogen (*H).[23] On the left hand side of the volcano on the plot (b) are the metals which bind *H strongly, in turn, causing it to slowly react further to molecular hydrogen. The right hand side of the volcano shows the metals that bind *H weakly, the reason for reaction kinetics to be limited by the reactant adsorption. Improving a catalyst activity hinges upon finding the material with optimal binding, whether by changing its composition or its structure.

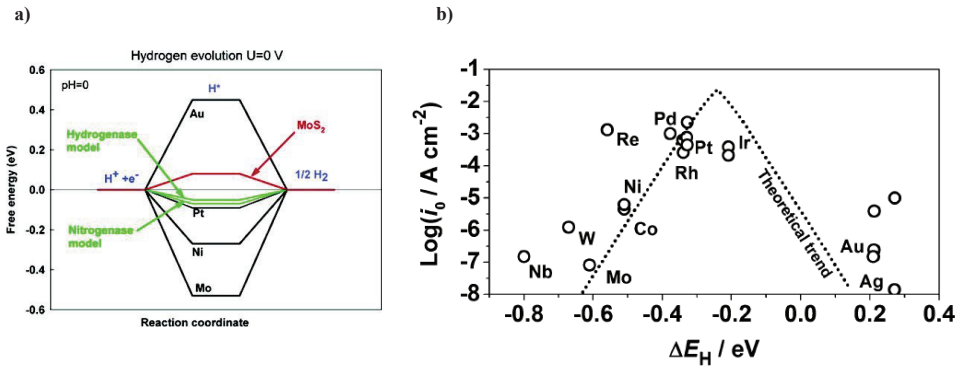

Figure 2.1: (a) A free energy diagram of *H for Au, Pt, Ni, Mo, MoS_2 as well as hydrogenase and nitrogenase enzymes models, calculated using density functional theory calculations; Reprinted from[29] (b) Volcano plot showing experimentally obtained exchange current densities plotted against the calculated hydrogen chemisorption energies per atom. Reprinted from[23].

The concept of volcano plot clearly distinguishes the reactivity of a catalyst from its activity. The reactivity is related to the binding energies as a measure of adsorbate-catalyst interaction. The activity depends on the surface reactivity and it represents an experimentally measurable parameter, in electrocatalytic reactions commonly expressed as current density.

2.1.2 The effect of surface structure on catalyst reactivity

A detailed insight into the nature of surface-adsorbate interaction offers an explanation which parameters are in control of surface reactivity. Figure 2.2 depicts a rearrangement of the electronic configuration of a molecule adsorbing onto a metal surface.[30] Initially, the interaction between the molecule and the surface is due to electrostatic van der Waals forces, followed by the chemisorption on the surface.

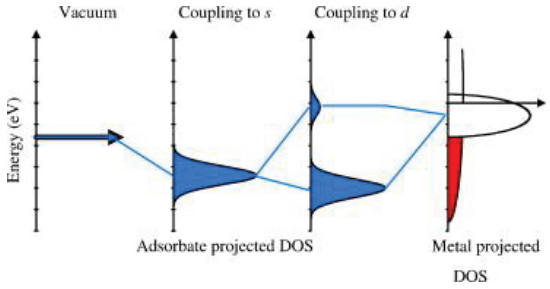

Figure 2.2: Schematic illustration of the bond formation between an adsorbate and a transition metal. (Figure reprinted from[30])

Due to interaction with the sp-band of a metal, the adsorbate level broadens and shifts downwards in energy, which stabilises the binding between the adsorbate and the surface. Additionally, the d-band of a transition metal causes the splitting of adsorbate's valance level in *bonding* and *anti-bonding*. Adsorbate-levels below the Fermi-level are occupied and contribute to the binding between the adsorbate and the metal. The adsorption energy is given by the adsorbate's valence states coupling to the d-band of the metal as proposed in the d-band model.[31] The strength of the adsorbate-metal interaction can be correlated to the d-band center of a metal.

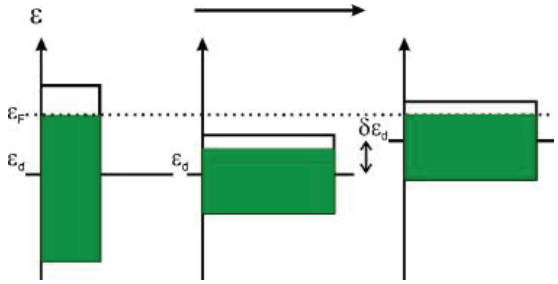

Figure 2.3: Schematic representation of the d-band center shift upon surface structure changes. (Figure reprinted from[30])

The surface structure of a metal affects its electronic properties and thus its reactivity. For instance, surfaces with atoms possessing low coordination numbers, such as steps and kinks, are more reactive than close packed surfaces. The overlap between the electronic orbitals depends on the coordination number of the surface atoms – atoms with low coordination number have smaller orbital overlap, which results in a narrower d-band. Since the d-band filling, i.e. the Fermi level need to remain

constant, the d-band shifts upwards, as illustrated in Figure 2.3. Higher d-band center means a stronger binding between the adsorbate and the metallic surface.

The overlap between the electronic orbitals may be tuned by changing the interatomic distance at the surface. The concept is known as the *strain effect*.[32] An expanded surface has a narrower d-band, consequently the d-band center is shifted upwards and surface is more reactive. On the other hand, a compressed surface possesses a broader d-band, whose center is shifted downwards making the surface less reactive.

2.1.3 The ligand effect on catalyst reactivity

The ligand effect is related to the change in the electronic structure of the metal, which can be achieved by introducing solute metal species into the host metal substrate. That can influence the changes in reactivity, depending on the nature of both solute and host metal.

In practice, this may be achieved either by alloying or by forming the overlayer structures. However, neither of these assures only the ligand effect on reactivity, but also involves the strain effect. Alloying not only affects the electronic structure, but also changes the lattice parameters of a new alloy phase.

On the other hand, if a monolayer of one metal is deposited on top of another metal as substrate, a pseudomorphic overlayer may form. Pseudomorphic metal overlayers adopt the same lattice constant as the host metal beneath. Therefore, the reactivity of such overlayer structure may be influenced not only via ligand effect from the host metal beneath, but as well via the tensile or compressive strain, produced due to the changes in interatomic distances.

Density function theory (DFT) calculations were employed to calculate the shifts of the d-band center for transition metals overlayer structures. Figure 2.4 shows that the d-band center varies the position significantly depending on the nature of the overlayer-host metal interaction.[30] For instance, a copper pseudomorphic overlayer on a platinum substrate produces a shift in copper d-band center of more than 0.7 eV in upward direction, hence enhancing the reactivity of the copper overlayer.

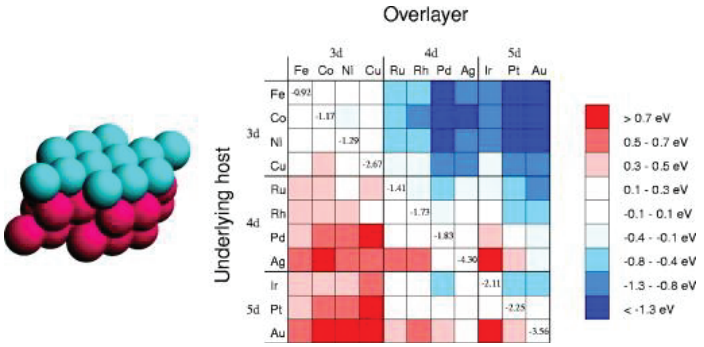

Figure 2.4: Changes in d-band center position of the overlayer metal deposited onto a host transition metal (Figure reprinted from[30])

2.1.4 Underpotential Deposition – Concept behind the preparation of Overlayers and Surface Alloys

This section introduces underpotential deposition, a concept behind the preparation routes employed both for preparing the copper overlayer structures on platinum (Chapter 5) as well as the surface alloy in case of gold-cadmium system (Chapter 6).[33]

There are two possibilities to consider regarding the adsorption of metal ions from a solution onto a foreign metal surface as a substrate. Both are related to the relationship between the Gibbs free energies of adsorbate-substrate interaction on one side and adsorbate-adsorbate interaction on the other side. If the adsorbate-substrate interaction is weaker compared to the adsorbate-adsorbate interaction, one may expect the deposition at the potentials more negative relative to the reversible equilibrium potential of bulk deposition and dissolution of the system. Such type of deposition usually forms small clusters or islands on the surface of a substrate. However, in a case of stronger adsorbate-substrate interactions, one can expect adsorbate deposition onto the substrate at potentials more positive relative to the equilibrium deposition/dissolution potential and is called *underpotential deposition* (*upd*). This method usually allows deposition of up to a monolayer of solute metal onto the host metal. The exact position of the upd can be calculated using the Nernst equation, given the solute metal ion concentration.

$$U_{eq} = U^{\circ} + \frac{RT}{2F} ln \frac{a_{Cd^{2+}}}{a_{Cd}} \qquad \textbf{(2.2)}$$

An underpotential deposition experiment usually consists of performing cyclic voltammetry in the range of potentials of interest using rather slow scan rates, of few millivolts per second. One may start

at a high enough potential where no adsorption takes place. Lowering the potential, one can observe cathodic currents giving sharp features on very ordered surfaces. The cathodic (negative) currents originate from the electron transfer related to the adsorption process of a positively charged species. Different peaks correspond to either different adsorption sites or changes in the structure of the adsorbate layer. After lowering the potential below the equilibrium potential for that system, a huge increase in cathodic current may be observed, corresponding to the bulk deposition. Upon changing the sweep direction, one can observe the anodic currents corresponding to bulk dissolution, followed by the dissolution of the overlayer. All these processes are represented for cases of Cu *upd* on Pt (Chapter 5, Figure 5.1) and Au (Chapter 6, Figure 6.2) and for Cd *upd* on Au (Chapter 3, Figure 3.7). At low concentrations of solute metals the deposition becomes slower, because the deposition rate starts to be limited by the mass transfer, which may imply the necessity for longer times of holding of potential in order to deposit a full monolayer. For this reason, in this work we used rather low solute metal concentrations, giving us the opportunity to use the time as parameter for submonolayer depositions.

Some of the metals form pseudomorphic overlayers on foreign substrate metals. This phenomenon can be used for formation of monolayers of metals with compressive or tensile strain, which may be used for investigations of metals reactivity in catalysis, as described more in Chapter 5.[23,33] Chapter 7 deals in more detail with the application of electrodeposition for preparation of submonolayer gold-cadmium surface alloys. On the other hand, *upd* can be used for electrochemical estimation of the active surface area of the catalyst, as described in Chapter 6.

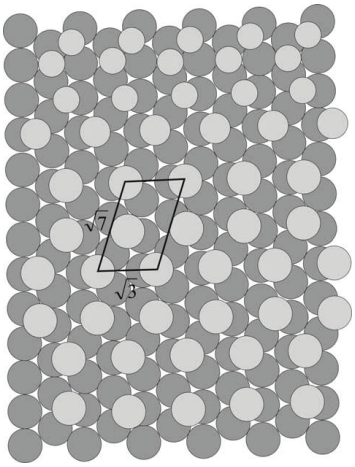

Figure 2.5: An STM model of the ($\sqrt{7} \times \sqrt{3}$) overlayer at 2/5th coverage, based on an image at -0.4 V vs. 3 M KCl Ag/AgCl (-0.19 V vs. NHE) in 0.2 mM $CdSO_4$ and 1 mM H_2SO_4.The Au lattice is represented by the darker circles. Figure reprinted from[34].

A pertinent example of use of upd is alloy formation during Cd deposition on Au.[35,36] In their reports, Horanyi and co-workers[35,36] examine a potential dependent specific adsorption of sulphate and perchlorate anions during Cd *upd*, as well as the alloy formation that follows. They propose various potential ranges. Initially, Cd deposition in form of adatoms, begins at +0.11 V vs. NHE. According to their study, Au-Cd alloy exists predominantly below -0.36 V vs. NHE, whereby below -0.5 V bulk Cd deposition begins. The standard thermodynamic potential of cadmium deposition/dissolution is -0.4885 V vs. NHE.[34,35] After deposition, at open circuit potential, they observe a fast Cd corrosion from the surface followed by the evolution of hydrogen and surface roughening. In addition, Stickney and co-workers have studied Cd *upd* on Au(111) using electrochemical scanning tunnelling microscopy (EC-STM).[34] Similarly, they observed formation of $CdSO_4$ bilayer, and formation of smallalloy nanoclusters near -0.29 V vs. NHE (reported originally as -0.5 V vs. 3M KCl/Ag/AgCl). In the fcc regions of Au(111) reconstruction (at potential range from -0.09 V to -0.19 V vs. NHE), they observe formation of $(\sqrt{7} \times \sqrt{3})$ overlayer at coverage of 2/5 of ML.

2.2. Electrocatalytic CO_2 reduction

2.2.1 Pourbaix-diagram of CO_2 – Potential-pH dependence

The Pourbaix diagram is essentially an electrochemical phase diagram that represents which species (oxidation states) of a given element (metal) are thermodynamically stable at a given pH value of the surrounding electrolyte and at a given potential relative to normal hydrogen electrode (NHE) scale. The Pourbaix diagrams show regions of stability of pure metals, corrosion regions where they dissolve in form of ions into the solution or passivity regions where metal oxides are thermodynamically stable.

As for metals, the thermodynamic stability of CO_2 can be represented as Pourbaix diagram[37], showing the thermodynamically existing species depending on solututions pH and potential. Equations below (2.2, 2.3 and 2.4) illustrate the possible equilibria between CO_2, water, carboxylic acid and its deprotonated species at potentials positive of 0 V vs. RHE. At most acidic environment, up to pH of ~6, formation of weak carboxylic acid is possible (Eq. 2.3). At pH range from 6 to ~10.3, bicarbonate anions are stable in solution, while at higher pH than 10.3 bicarbonate deprotonates further to carbonate anion.

$$CO_{2(g)} + H_2O_{(l)} \leftrightarrow H_2CO_{3(l)} \quad \textbf{(2.3)}$$

$$H_2CO_{3(l)} \leftrightarrow H^+ + HCO_3^-{}_{(aq)} \quad \textbf{(2.4)}$$

$$HCO_3^-{}_{(aq)} \leftrightarrow H^+ + CO_3^{2-}{}_{(aq)} \quad \textbf{(2.5)}$$

Table 2.1: Some of the possible CO_2 electro-reduction reactions, including corresponding thermodynamic reversible potentials given against the reversible hydrogen electrode (RHE), calculated using data from[13].

$$CO_{2(g)} + 2H^+ + 2e^- = HCOOH_{(l)} \qquad U_{eq} = -0.171 \text{ V} \quad \textbf{(2.6)}$$

$$CO_{2(g)} + 4H^+ + 4e^- = HCHO_{(l)} \qquad U_{eq} = -0.142 \text{ V} \quad \textbf{(2.7)}$$

$$CO_{2(g)} + 2H^+ + 2e^- = CO_{(g)} + H_2O_{(l)} \qquad U_{eq} = -0.103 \text{ V} \quad \textbf{(2.8)}$$

$$CO_{2(g)} + 6H^+ + 6e^- = CH_3OH_{(l)} + H_2O_{(l)} \qquad U_{eq} = +0.016 \text{ V} \quad \textbf{(2.9)}$$

$$CO_{2(g)} + 8H^+ + 8e^- = CH_{4(g)} + 2H_2O_{(l)} \qquad U_{eq} = +0.169 \text{ V} \quad \textbf{(2.10)}$$

$$2CO_{2(g)} + 12H^+ + 12e^- = C_2H_{4(g)} + 4H_2O_{(l)} \qquad U_{eq} = +0.079 \text{ V} \quad \textbf{(2.11)}$$

At potentials negative of ~0 V vs. RHE, various reduced carbon species are stable. Depending on many factors, electrochemical reduction of CO_2 may result in a variety of products such as formic acid, carbon monoxide, methane, ethylene, etc. The most interesting compounds with their corresponding standard potentials and the number of protons and electrons involved in the reaction are represented in Table 2.1.

On Figure 2.6 *Latimer-Frost* plot is shown, providing the Gibbs free energies of formation for various products relative to CO_2 plotted versus the number of proton-electron transfers required in the each reaction. The plot focuses only on one carbon atom products such as CO, formic acid, formaldehyde, methanol and methane. As the small red triangle in the corner of the plot suggests, the thermodynamic reversible potentials can be obtained from the ratio of the Gibbs free energy and number of electrons transferred (equation 2.12). Therefore, the slopes of the lines connecting CO_2 and a given product provide an indication of the reversible potentials.

$$U_{eq} = -\frac{\Delta G_{form}}{z} \qquad \textbf{(2.12)}$$

For obtaining higher energy value compounds, such as methane, ethylene or methanol, larger number of protons and electrons needs to be transferred.

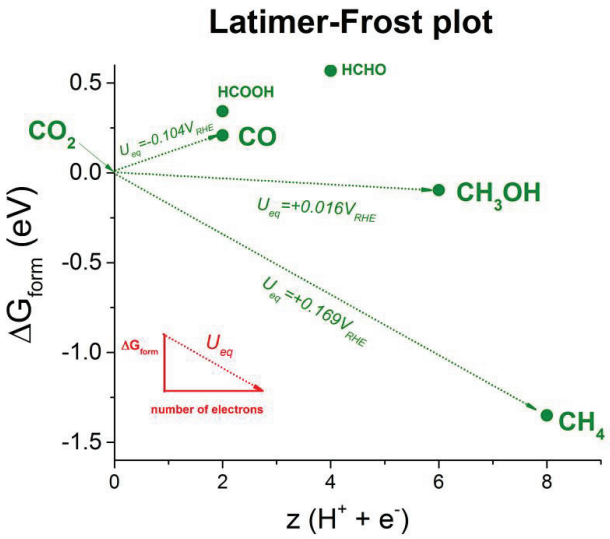

Figure 2.6: Adapted *Latimer-Frost* plot, showing the Gibbs free energy of formation for various C1 products of CO_2 electro-reduction as a function of number of transferred electrons (and protons). The thermodynamic reversible potentials are confined in the slope of the lines connecting CO_2 with the products. Enthalpies of formation from[13].

On Figure 2.7, shifts in theoretical reversible potentials are represented as an effect of switching to CO as a reactant gas instead of CO_2. Plot (a) represents Latimer-Frost plot with the slopes indicating the reversible potentials.

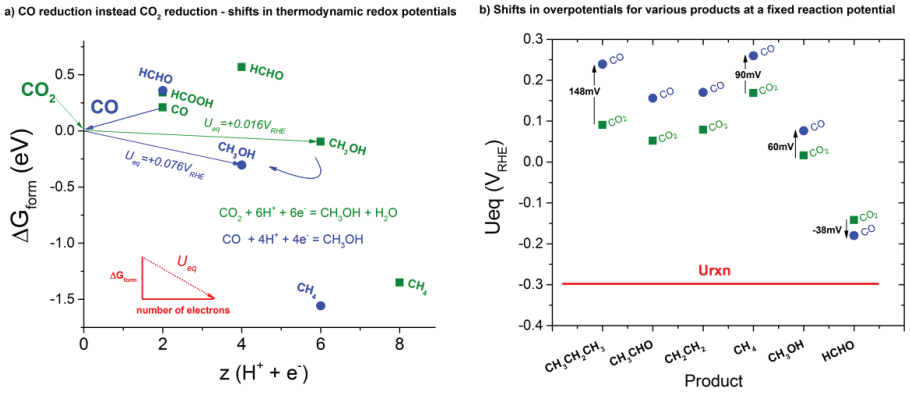

Figure 2.7: (a) Adapted Latimer-Frost plot comparing the reversible potentials for C1 products formed from CO_2 and CO; (b) The shifts in reversible potentials relative to the fixed reaction potential due to the use of a different reactant gas – an illustration of the shifts in practically applied overpotentials. Enthalpies of formation from[13].

When CO is used as reactant, the Gibbs formation energies as well as the number of electrons required decrease, resulting in changes in reversible potentials. Practically, this implies, that performing the CO electrolysis at a same fixed potential with respect to the RHE scale, results in change of applied overpotentials for all products with respect to CO_2 electrolysis, as shown in plot (b) of Figure 2.7. For instance, at a potential of -0.3 V RHE, the overpotential for methanol production from CO_2 is 0.316 V, whereas with CO as a starting reactant it is 0.376 V.

2.2.2 State-of-the-art understanding of CO_2 reduction electrocatalysis

The reversible potentials for formation of all the products from CO_2, which are in the range from -0.2 V to +0.2 V vs. RHE, indicate that it is thermodynamically possible for these reactions to occur below these given potentials. Since hydrogen evolution reaction has by definition its standard potential at 0 V vs. RHE, it will compete with CO_2 reduction at all negative potentials. Hence, an ideal CO_2 electro-reduction catalyst shoud be virtually inactive for hydrogen evolution, but reduce CO_2 to a single valuable product at lowest possible overpotential. The number of protons and electrons

transferred during CO_2 reduction may vary from 2 as for CO or formic acid, up to even 30 for hydrocarbon products such as propane.

An insightfull representation of the trends in CO_2 reduction can be obtained from the pioneering work of Hori and co-workers.[15,38] They measured Faradaic efficiencies towards CO_2 electro-reduction on many different metals, as shown in Table 2.2. These measurements were performed using chronopotentiometry, i.e. by applying a constant current density (of -5 $mA.cm^{-2}$). The activity of the catalyst is then defined by the value of the stable potential for obtaining this current density – highly active metals exhibit less negative potentials (lower overpotentials).[15]

Table 2.2: Product distribution for the CO_2 electrochemical reduction on various metals. (Adapted from[15])

Metal	***U***	***j***	**Faradaic Efficiency (%)**							
	V vs. RHE	$mA.cm^{-2}$	**CH_4**	**C_2H_4**	**EtOH**	**PrOH**	**CO**	**$HCOO^-$**	**H_2**	**Total**
Ni	-1.18	5	1.8	0	0	0	0	1	89	92
Fe	-0.57	5	0	0.1	0	0	0	0	95	95
Pt	-0.67	5	0	0	0	0	0	0	96	96
Ti	-1.20	5	0	0	0	0	tr	0	100	100
Pb	-1.23	5	0	0	0	0	0	97	5	102
Hg	-1.11	0.5	0	0	0	0	0	99	0	100
Tl	-1.20	5	0	0	0	0	0	95	6	101
In	-1.15	5	0	0	0	0	2	95	5	100
Sn	-1.08	5	0	0	0	0	7	88	5	100
Cd	-1.23	5	1.3	0	0	0	14	78	9	103
Au	-0.75	5	0	0	0	0	87	1	10	98
Ag	-0.97	5	0	0	0	0	81	1	12	95
Zn	-1.14	5	0	0	0	0	79	6	10	95
Pd	-0.80	5	2.9	0	0	0	28	3	26	60
Ga	-0.84	5	0	0	0	0	23	0	79	102
Cu	**-1.04**	**5**	**33.3**	**25.5**	**5.7**	**3**	**1.3**	**9**	**20**	**103**

The product selectivities, reported as Faradaic efficiencies in the Table 2.2, allow us to classify the metals in several groups. There are metals, such as Pt and Fe, that are inactive for CO_2 electro-reduction, but are highly active for hydrogen evolution reaction. These catalysts possess strong binding towards CO, so instead protonation of CO, the protons are preferably reduced to molecular hydrogen. The next group of metals, consisting of metals as Sn, In, Pb, Cd, successfully reduces CO_2, but does not have the possibility of breaking the carbon-oxygen bond, hence, the major product is formate. Nevertheless, this group of metals is least active for hydrogen evolution. Most prominent

representatives of the third group of metals, which reduce CO_2 to CO are Au, Ag and Zn. However, their weak binding towards CO does not allow them to reduce CO any further.

Copper is a unique metal, which produces hydrocarbons with remarkably higher selectivities than any other transition metal. The main drawbacks of Cu as catalyst are in fact the variety of products it makes and a large overpotential. Moreover, we still possess a poor understanding about the factors that control the selectivities towards production of the most interesting compounds such as ethylene or methanol.[15]

CO_2 electro-reduction on copper

Being unique amongst transition metals that reduce CO_2 to hydrocarbons, copper has been extensively studied as an electrocatalyst.[38-48] Various studies have correlated the catalytic activity and selectivity of copper to different parameters and reaction conditions – surface structure, working potential, temperature, working electrolyte and its pH.[39,42-44,49]

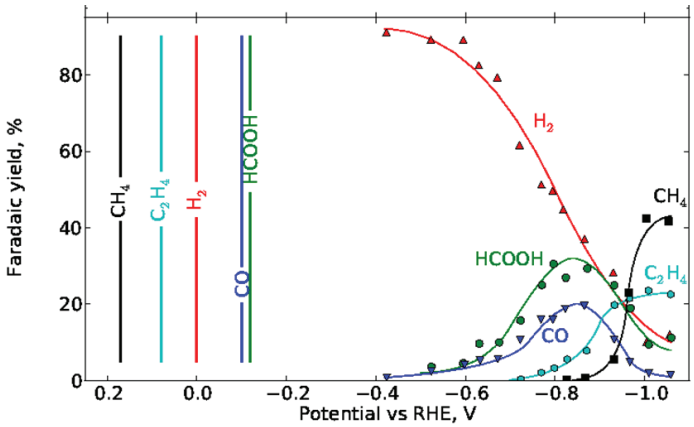

Figure 2.8: Product distribution as a function of potential measured by Hori and co-workers. (Figure reprinted from[50], data points from[38])

Initially, Hori and co-workers investigated the dependence of the product distribution on potential.[38] They reported hydrogen as the only detected product measured at potentials more positive than -0.4 V vs. RHE. CO_2 electro-reduction started when larger overpotentials were applied (Figure 2.8). Formation of CO and formate beings at ~ -0.6 V vs. RHE, reaching the highest Faradaic efficiencies at around -0.85 V vs. RHE. Hydrocarbons, predominately ethylene and methane, begin to be produced at -0.7 V and -0.85 V vs. RHE, respectively. Ethylene production reaches its maximum values at potentials below -0.9 V vs. RHE, whereby at -1.0 V vs. RHE methane becomes predominant product

reaching efficiencies of even 40 %. The corresponding overpotential for producing high hydrocarbons yields is in range of 1.0 V to 1.2 V, which is considered a significant energy input.

Recent work from Jaramillo and co-workers provides a more detailed insight into the product distribution as a function of potential during the electrocatalytic CO_2 reduction on copper electrodes.[39] Specific design of the electrochemical cell allowed them to use of high surface area electrodes inside a small volume of the electrolyte, inside which detectable concentrations of reaction products can build up. In combination with NMR spectroscopy as their main product analysis tool, they were able to quantify sixteen reaction products in total, whereby five of them were reported for the first time.

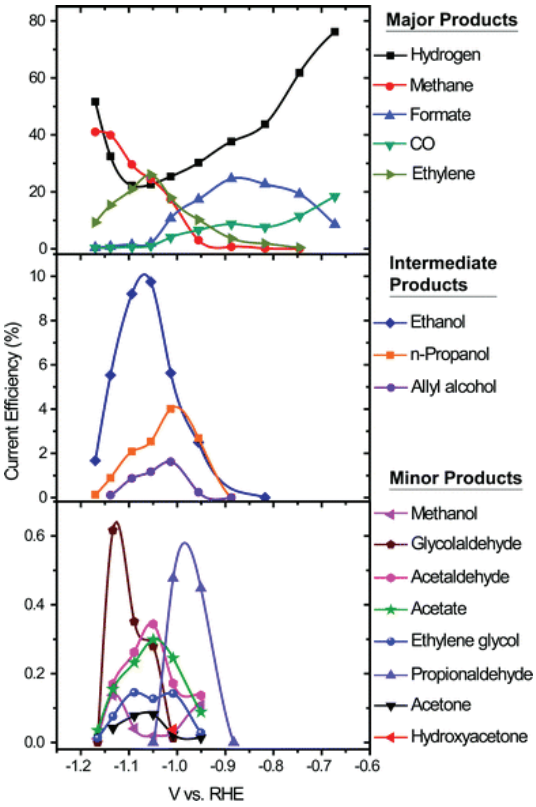

Figure 2.9: Product distribution as a function of potential obtained by Jaramillo and co-workers.
(Figure reprinted from[39])

The product distribution for the major CO_2 reduction products as a function of potential, shown on Figure 2.9, is consistent with the data from Hori and co-workers.[15] Furthermore, Jaramillo and co-workers found a similar potential dependence for the compounds possessing two or more carbon atoms. They report the maximum efficiency towards these products matches the maximum efficiency

towards ethylene (around -1.0 V). While the current efficiencies related to C2 products decay reaching -1.2 V, methane efficiencies still increase. This difference suggests that there might exist a different rate limiting step related to the production of these two compounds.

A similar product distribution as function of potential was observed experimentally upon reducing directly CO, instead of CO_2, on copper catalyst.[42] That suggests, that CO is an intermediate during CO_2 electro-reduction to hydrocarbons and that the reaction is limited by steps following the formation of CO. More detailed experimental studies of the reaction mechanism become challenging, since they should assume development of a technique capable of probing the reaction intermediates in situ.

A more recent paper by Li et al[48] presents results on roughened copper obtained by reducing a thick layer of Cu_2O. Using this preparation method they have achieved an extremely rough surface (roughness factor ~30) in which the reduction CO_2 to CO requires 0.2 V less overpotential than on polycrystalline Cu. Furthermore, on this surface the only hydrocarbons detected are C_2H_4 and C_2H_6, no methane.

Cook and co-workers measured Faradaic efficiencies for CH_4 and C_2H_4 as high as 79 % using in situ electrodeposited copper on glassy carbon electrodes. They propose a mechanism, which proceeds through a weakly adsorbed CO_2 and electrochemically generated chemisorbed hydrogen at the copper surface. The subsequent reduction of adsorbed CO_2 results in bridged CO, which can either desorb or be further reduced, as they suggest.[49] In addition, Ogura and coworkers report selectivity of 69 % for C_2H_4 production at -1.8 V vs. Ag/AgCl (-1.53 V vs. RHE) in 3 M KCl electrolyte with adding 1 mM of $CuSO_4$. They discuss that Cu^{2+} deposition performed along with CO_2 electrolysis gives rise to such high Faradaic efficiencies for ethylene.[51]

Hori and coworkers[41,52] showed that the crystal orientation of copper has a strong effect on its catalytic activity. Their work has been carried out at a constant current; consequently the local pH does not play a role since it should be the same on all the studied surfaces. Hori et al. observed that on stepped surfaces, like Cu(311), Cu(511) and Cu (711), the reaction occurs at lower potentials for a specific current density compared to the low index facets Cu(111) and Cu(100). They also concluded that the selectivity ratio between CH_4 and C_2H_4 depends strongly on the crystal orientation. They reported that Cu(111) produced CH_4 with a Faradaic efficiency of 50.5 % and C_2H_4 with an efficiency of 8.8 %. On the other hand, the stepped surface Cu(711) exhibited only a modest Faradaic efficiency of 3.8 % towards CH_4 and 51.6 % towards C_2H_4. These results indicate that steps are more selective towards ethylene production while terraces are more selective towards the formation of methane.

Insights into mechanism of CO_2 reduction on copper

Computational modelling of the electrochemical interface and the reactions taking place there would strictly speaking need to consider the electrolyte and the electric fields in the double layer.[53] Even so, the theoretical models in catalysis, developed based on density functional theory calculations, have been proven to be useful in elucidating the general trends.[50,54,55] The construction of an overall free energy diagram for a catalytic reaction is possible if the adsorption energies for all the reaction intermediates on that given catalyst are calculated. Moreover, the free energy diagram delivers a value of minimum theoretical overpotential necessary for the reaction to be thermodynamically viable.

The exact mechanism of CO_2 electro-reduction, in which hydrocarbons are produced, is still being debated. A detailed reaction pathway for reducing CO_2 to CH_4 on a Cu(211) model surface is proposed by Peterson et al.[50] The reaction steps corresponding to the lowest energy pathway for this reaction are shown in Figure 2.10. They identified the protonation of *CO to *CHO as the potential determining step, i.e. the step requiring the highest overpotential of all reaction steps.

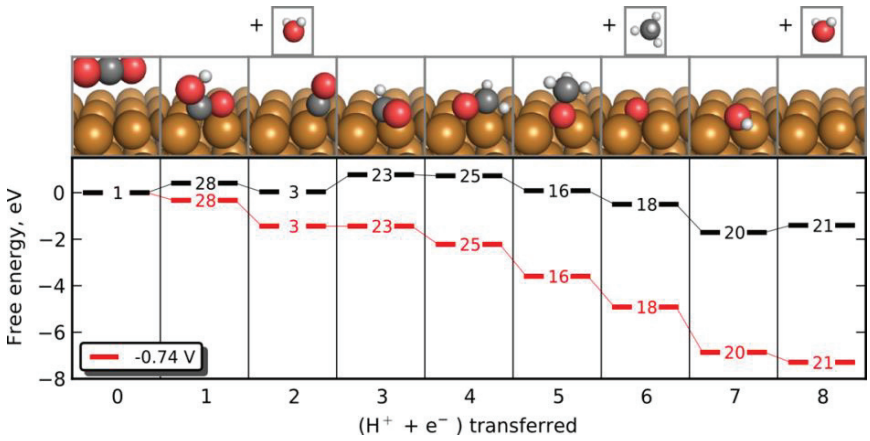

Figure 2.10: Proposed CO_2 electro-reduction pathway for methane formation on Cu(211) model surface. The free energy diagram is shown at 0V vs. RHE and at the minimum theoretical overpotential of -0. 74 V vs. RHE. (Figure reprinted from[50])

Recent study by Nie et al, included the kinetic barriers into the model. However, that indicated that the protonation of *CO to *COH is favored on Cu(111), instead the protonation to form *CHO.[50] Likewise, Nie et al propose further *COH reduction to methane, while *CHO intermediate would generate methanol.

A complete mechanism of CO_2 reduction should as well be capable of explaining the reaction pathway leading to the formation of ethylene. It should be consistent with the different experimental observations about methane and ethylene production regarding potential and pH dependence.

Koper and co-workers considered a scenario where C-C coupling happens early in the reaction via formation of a CO dimer.[43] Their studies show that the formation of methane depends on proton concentration, while the formation of ethylene is independent of pH.[56] This is consistent with *CO protonation being the limiting step for methane formation, but it also suggests that the limiting step for ethylene production should be a different one - involving no proton transfer (which could be dimerization of two moieties).

Nørskov and coworkers found the dimerisation of *CO kinetically unfavorable[57], opening space for discussion. In addition, they propose the protonation of *CO to *CHO to be the potential determining step in the formation of ethylene. They suggest that all C_2 products should be formed via a non-electrochemical reaction between the adsorbed intermediates at the surface.[57] According to their calculations, the coupling of adsorbed intermediates is more facile following protonation of adsorbed CO, for instance as coupling of *CHO to *OCHCHO*. Nonetheless, at present their calculations cannot reconcile the experimentally measured differences in product distribution at a constant potential with respect to RHE when varying electrolyte pH value.

CO_2 electro-reduction on gold

Results from Table 2.2 highlight gold as the transition metal with highest Faradaic efficiency towards CO evolution – being 87 % at -0.75 V vs. RHE (chronopotentiometry at fixed total current density of -5 $mA.cm^{-2}$).[15] Earlier studies by Hori et al[58] suggest indeed roughly an order of magnitude higher partial current densities for CO relative to H_2 over wide range of potentials, see Figure 2.11.

The electrochemical reduction of CO_2 was performed on polycrystalline gold electrode (roughened and cleaned by etching in aqua regia) in 1 bar CO_2 saturated 0.5 M $KHCO_3$ at 18°C over a range of potentials from -0.3 V to -1.1 V vs. RHE. The selectivity for CO formation reached even 91 % at -0.69 V vs. RHE, corresponding to a partial current of -3.7 $mA.cm^{-2}$.[58]

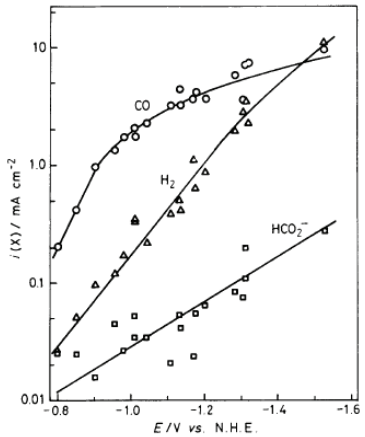

Figure 2.11: Partial current densities for CO, H_2 and $HCOO^-$ measured on polycrystalline gold surface plotted on the logarithmic scale against the normal hydrogen electrode (NHE). The measurements are performed in 0.5 M $KHCO_3$ with pH 7.5 at 18°C. Reprinted from[58]

Recently, Kanan and co-workers explored a method for roughening the gold surface by high frequency oxidation-reduction pulse.[59] Such pretreatment resulted in oxide-derived gold surface, as shown on SEM image in Figure 2.12 (a). Plot (b) indicates the Faradaic efficiency of such oxide-derived gold towards CO evolution at potential range from -0.2 V to -0.5 V vs. RHE. Oxide derived gold exhibits highly selective CO_2 reduction to CO in aqueous electrolyte at as low overpotential as 140 mV. This high activity was retained during 8 hours of electrolysis. Additionally, at -0.4 V vs. RHE they report Faradaic efficiency of 100 % towards CO evolution. Polycrystalline gold, as well as other nanostructured electrodes require higher overpotentials for reaching the same activity, which rapidly decreases during prolonged electrolysis. Their kinetic studies indicate that the enhancement in activity may be linked to stabilisation of $CO_2^{\bullet-}$ intermediate at oxide-derived gold surface.

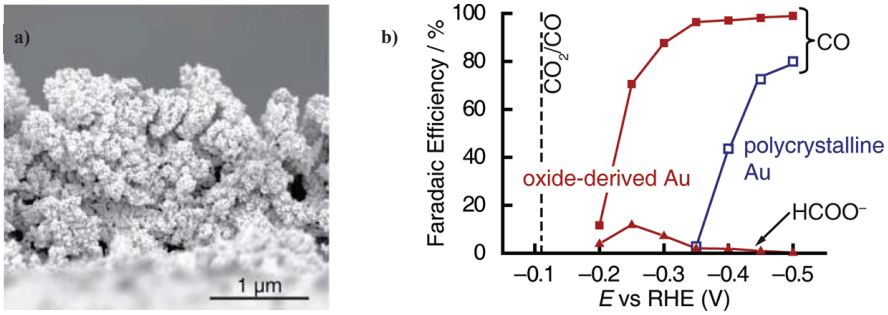

Figure 2.12: (a) cross-sectional SEM image of oxide-derived gold surface; (b) Faradaic efficiencies for CO and $HCOO^-$ production on oxide-derived Au and polycrystalline Au electrodes in range of potentials from –0.2 V to –0.5 V in 0.5 M $NaHCO_3$, pH 7.2. The reversible thermodynamic potential for CO is indicated with the dashed line.[59]

Insight into trends in activity based on theoretical modeling

Nørskov and co-workers focused on a model of CO_2 reduction to CH_4, whereby they employ DFT to calculate the adsorption energies of all reaction intermediates on various transition metals.[54,55] Conversion of CO_2 to methane involves transfer of eight proton-electron pairs, which results in seven intermediates adsorbed at the surface. Understanding of the mechanism is based on analysis of a seven-dimensional space. However, because of the strong correlations exisiting between the binding energies of adsorbates bound through the same atom, they were able to reduce the analysis to two-dimensional space – comparing the binding energies of all adsorbates bound via carbon atom with the binding energy of CO and comparing the binding energies of adsorbates bound via oxygen atom with the binding energy of OH. Figure 2.13 indicates the scaling relations of adsorbate binding energies in the proposed mechanism of CO_2 reduction to methane on fcc(211) facets of various transition metal surfaces. The plot on the left side shows the scaling relations among the first four reaction intermediates – *COOH, *CHO and *CH_2O – plotted against the binding energy of *CO. The plot on the right side shows scaling relations of *OCH_3 and *O plotted versus *OH binding energy.

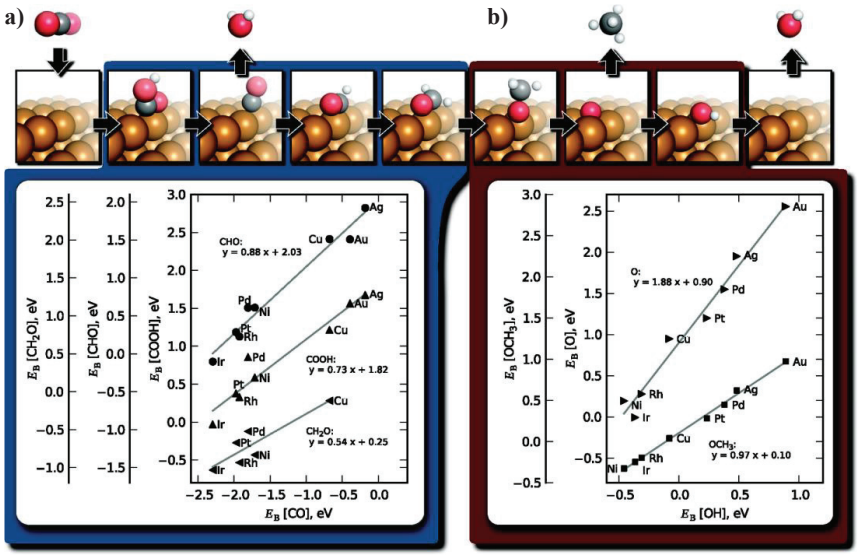

Figure 2.13: Scaling of adsorption energies on fcc(211) facets of transition metal surfaces – (a) Adsorption energies of adsorbates bound through carbon atom plotted against the binding energy of CO; (b) Adsorption energies of adsorbates bound through oxygen atom plotted against the binding energy of OH.[55]

Each of the transition metal surfaces possesses a limiting potential (U_L) – value representing a minimum required theoretical potential for the reaction step involving a single proton-electron

transfer to be exergonic, i.e. downhill in free energy. The limiting potential provides an approximate indication of the applied electrical potential at which that reaction step starts to have an appreciable rate.

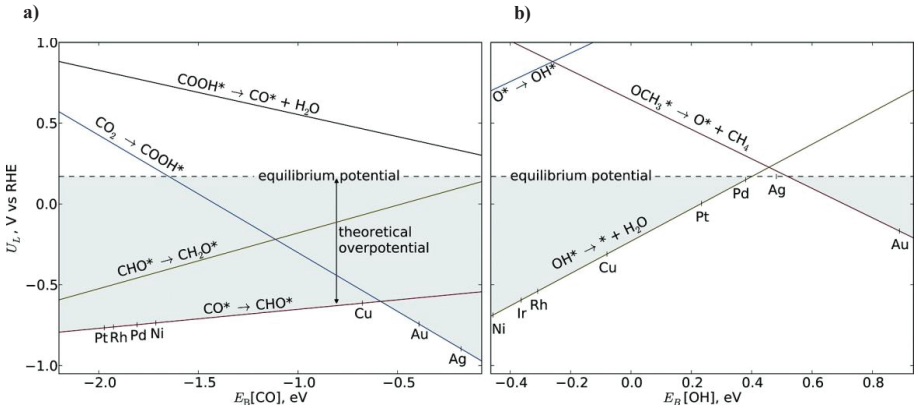

Figure 2.14: Limiting potentials (U_L) for elementary proton-electron transfer steps in the mechanism shown in Figure 2.9 – (a) Reaction steps involving an addition of proton-electron pair to the reactant bound through carbon atom plotted against the binding energy of CO; (b) Reaction steps involving an addition of proton-electron pair to the reactant bound through oxygen atom plotted against the binding energy of OH. Dashed line shows the reversible potential for CH_4 formation from CO_2 (+0.17 V vs. RHE). The theoretical overpotential for a given metal as catalyst can be represented as distance between the reversible potential and the line with the most negative limiting potential (highlighted in gray). [55]

On Figure 2.14, limiting potentials (relative to the reversible hydrogen electrode) for seven elementary reaction steps for various transition metal surfaces are plotted versus the binding energies of *CO and *OH. The reversible thermodynamic potential for CO_2 reduction to methane is represented as a dashed line at +0.17 V vs. RHE. The lines with most negative limiting potentials determine the value of the theoretical overpotential for a given catalyst – from the plots readily available as the distance between the reversible potential (dashed line) and the line corresponding to the most limiting reactions step. Figure 2.14 suggests that the protonation of the adsorbed *CO to form *CHO (red line on the left hand plot corresponding to $*CO + H^+ + e^- = *CHO$) represents the most limiting reaction for many transition metal surfaces including Pt, Rh, Pd, Ni and Cu, as shown previously.[50] Au and Ag possess most negative limiting potential values for the initial reaction step of CO_2 activation to *COOH. Copper lies closest to the top of the volcano made by these two lines.

The plot on the right hand side shows limiting potentials on various transition metal surfaces in relation to the intermediates bound through the oxygen atom. The values of limiting potential in all

cases are less negative than those on the reaction steps involving carbon atom bond intermediates. It is only for the metals with very strong binding towards *OH, such as Ni or Ir, that removal of adsorbed *OH may be the cause of large overpotentials. However, for most transition metals the catalytic effectiveness will be deterimined by the adsorbed *CO protonation.

The analysis employed for Figure 2.14 can now be considered for understanding the general trends observed experimentally by Hori and co-workers[15], shown in Table 2.2.

A value of 0.88 for the slope of the line connecting the limiting potentials for reaction step corresponding to *CO protonation to *CHO on considered transition metals describes high insensitivity of the reaction energetics to electronic properties of the catalyst (CO binding energy). This almost horizontal line indicates that regardless of the catalyst nature, due to scaling of the *CO and *CHO adsorption energies, the overpotentials cannot be reduced significantly.

In order to perform effective reduction of CO_2, they propose the use of an electrocatalyst with stronger binding energy towards *CHO relative to the binding energy for *CO. For the materials on the righ side of the volcano in Figure 2.14, a possible approach could be increasing the partial pressure of gas phase CO. Otherwise, there should be found other strategies for decouling the binding energies of *CO and *CHO. Peterson et al[55] suggest various decoupling strategies involving alloying, ligand stabilisation, tethering, addition of promoters. All strategies rely on employing an approach to tackle the different geometries of adsorbed *CO intermediate and the adsorbed *CHO intermediate. CO in adsorbed state has a linear geometry, whereby carbon tends to bind the catalyst surface. On the other hand, adsorbed *CHO possesses a planar geometry.

Alloying is often used in heterogeneous catalysis. Introduction of a solute element that has a higher affinity towards oxygen could preferentially stabilise *CHO without affecting the strength of *CO binding. The oxophilic element should also not inhibit the OH removal from the surface. Ligand stabilisation is a concept analogous to alloying, often exploited in homogeneous catalysis. An electrophilic chemical ligand capable to interact with a planar geometry of CHO stabilising it at the surface. Tethering involves using a ligand at an electrode surface – providing stabilisation of CHO adsorbate either through surface bound CHO interacting with the ligand or its direct bond to the ligand. Adding promoters to the catalyst surface can affect the adsorbates binding through electronic and structural effects. Other proposed approaches could involve stabilisation via hydrogen bonding or various solvent effects.[55]

Very recently, Nørskov and co-workers carried out a study, where they model the effects of adsorbates on binding energies of open and close-packed metal surfaces.[60] Adsorbate-adsorbate interactions have a larger impact, in terms of overpotential reduction, on open than on close-packed surfaces. They find that higher *CO coverages may have a larger effect on the metals at the strong

binding side of the volcano, than to Au or Ag. They emphasise that on the weak binding side, for Au and Ag, the relevant precursor to *CHO may rather be CO from the gas phase than adsorbed *CO. Additionally, breaking scaling relations between *CO and *H adsorption could decrease selectivities for hydrogen evolution.[60]

2.2.3 Alloying as a strategy for breaking scaling relations

In this work the main focus was on strategy of alloying as a concept to break the scaling of the binding energies of similar intermediates. This concept for stabilisation of the *CHO intermediate relative to the *CO by alloying a substrate metal with a solute metal of high oxygen affinity may have sense only for limited number of substrates. Improving the catalytic activity of copper is less attractive for this approach, since copper already binds oxygen strongly. In addition, copper possesses intermediate current efficiencies for HER, ranging from 40 % in the best case (at -1.1 V vs. RHE) up to 80-90 % in worst (potential region above -0.8 V and below -1.1 V)[15,39]. Metals that bind CO rather strongly, such as Pt, Ni, Fe etc. produce hydrogen with high current efficiencies in range of 90-100 %.[15,17] In this case, *CO acts as surface blocking species rather than an intermediate, since these metals do not possess favorable energetics for a further reduction of *CO to *CHO.

Evidently, gold is the most noble metal among all – it does not interact with oxygen over a wide range of potentials.[61] Moreover, gold and silver exhibit the lowest Faradaic efficiencies and hence lowest partial current densities towards HER among the transition metals.[27,58] Moreover, the observation that CO is the primary product during CO_2 reduction on Au is consistent with its rather weak binding towards CO, which would suggest that CO desorption is more kinetically facile than its further reduction.

Table 2.3: Selectivity for CO_2 reduction to CO on various adatom modified electrodes. Reprinted from [62].

Substrate metal	Potential (V vs. SHE)	Without adatoms	With adatoms				
			Cd	Sn	In	Pb	Tl
Au	−1.14	0.99	0.82	0.54	0.60	0.53	0.95
Ag	−1.37	0.99	0.92	0.59	0.40	0.39	0.05
Cu	−1.44	0.69	0.82	0.36	0.20	0.00	0.00
Zn	−1.54	0.93	0.19	0.08	0.03	0.01	0.01
Cd	−1.63	0.15					
Sn	−1.48	0.07					
In	−1.55	0.02					
Pb	−1.63	0.00	0.00	0.03			
Tl	−1.68	0.00					
Hg	−1.51	0.00					

CO selectivity, $r = CO/(CO + HCOO^-)$; current density for Hg: 0.5 mA cm^{-2}, other metals: 5 mA cm^{-2}, electrolyte: 0.1 M $KHCO_3$: temperature: 18.5 ± 0.5°C.

There are only few examples in the literature about the use of alloyed catalyst materials for electrochemical CO_2 reduction reaction. Hori et al[62] investigated the effect of addition of small amount of adatoms to various substrate metals, as shown in Table 2.3. These results indicate that the surface alloys of gold and silver change the initial substrate activity for CO evolution significantly, favoring formate production.[62]

Beyond the field of CO_2 electroreduction there are a large number of studies investigating the use of overlayer structures[63-65] and core-shell nanoparticles[66-70] as catalyst materials for electrochemical reactions. However, the true structure of these systems may not always be as expected.[71-73] For instance, Friebel and et al.[74] used X-ray absorption spectroscopy to confirm that Pt overlayer on Rh actually resulted in formation of three-dimensional islands, the structure which is in a better agreement with the measured activity towards oxygen reduction reaction. Additionally, under reactive conditions, bimetallic systems may modify their structure in effect of their interaction with the adsorbates.[75-77] These rearrangements of the catalytic surfaces cause changes in catalyst reactivity. Hence, it is becomes crucial to probe experimentally the surface structure under reaction conditions, in order to obtain have a complete understanding of the catalytic activity.

2.3. Electrolyte influence on catalytic processes

2.3.1 Local pH effect on product distribution

The influence of the electrolyte on the CO_2 electro-reduction was investigated as well by Hori and co-workers.[38] They established that the ratio between current efficiencies for CH_4 and C_2H_4 on copper electrodes becomes highly dependent on the working electrolyte. Production of ethylene and alcohols was enhanced in KCl, K_2SO_4, $KClO_4$ and diluted $KHCO_3$.[51] However, methane production prevailed in high concentration $KHCO_3$ and phosphate buffer solutions. Noda et al performed the electrochemical CO_2 reduction on Au in a phosphate buffer.[78] However, they did not achieve as high CO evolution efficiencies as Hori in bicarbonate buffer electrolyte.[58,78]

Different selectivities may be attributed to variations in local pH. Electrolytes possessing a low buffer capacity such as $KClO_4$ and diluted $KHCO_3$ change the pH value in the vicinity of the electrode surface significantly relative to the bulk pH value, as an effect of protons consumption in all reactions. Hence, in low buffer capacity electrolytes the electro-reduction of CO_2 practically occurrs in alkaline envorinment. Nevertheless, electrolytes possessing a higher buffer capacity tend to have more stable local pH.

The surface pH values in the vicinity of the cathode during CO_2 electro-reduction in $KHCO_3$ electrolytes are studied by Gupta et al.[79] Their results indicate significantly lower surface proton concentration significantly than in the bulk of the solution. Moreover, the local pH depends on the total current density at the electrode and the electrolyte buffer capacity. Gupta and co-workers presented Figure 2.15, showing local H^+ and CO_2 concentration as a function of buffer strength (concentration of $KHCO_3$) for current density of -5 $mA.cm^{-2}$.

From Figure 2.15, the local pH values close to the electrode surface are always higher than in the electrolyte bulk. The bulk pH values range from 6 for concentration of 0.03 M up to ~8 for 1.5 M concentrated $KHCO_3$. The discrepancy between the bulk and the surface pH is greater when the buffer capacity is small, reaching more alkaline local pH values at lower $KHCO_3$ concentrations. Studies of CO_2 electro-reduction in varied electrolyte ($KHCO_3$) concentrations have consistently shown enhanced ethylene formation in lower buffer capacity electrolytes. This is presumably a consequence of a higher local pH,[38] however the studies do not offer a mechanistic explanation why rather ethylene is formed over methane in more alkaline environment. Methane production was found to be related to the proton activity in solution, while ethylene production does not dependent on the pH.[56]

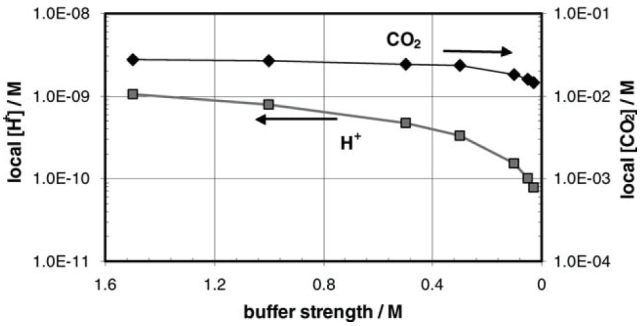

Figure 2.15: Proton and CO_2 local surface concentrations as a function of buffer strength (from 1.5 M $KHCO_3$ to 0.03 M $KHCO_3$) when the CO_2 reduction current is -5 $mA.cm^{-2}$. Reprinted from [79].

2.3.2 Non-covalent interactions

The effect of presence of different cations or anions on catalysis was studied extensively for oxygen reduction and hydrogen evolution reactions.[80-84] Their studies demonstrate how selectivities and activities can be varied in presence of various anions (CN^- or OH^-) adsorbed at the surface, or as function of cations (Li^+, Na^+, K^+, etc).

2.4 Brief summary of the literature overview

Copper is a unique electrocatalyst that reduces CO_2 or CO to hydrocarbons, however, at very high overpotentials of ~1 V.[38,40,42] Extensive studies have shown that many factors influence the reaction selectivity.[17,40,52] The density functional theory calculations interpret successfully the experimental observations on copper and other transition metal surfaces.[50] Changes in their reactivity reflect poorly onto their activity for the most limiting reaction step, protonation of the adsorbed CO.[55] Apart from a possibility to use highly undercoordinated surfaces as active and selective catalysts[59], other strategies are suggested, such as bifunctional catalysis.[55,85] Additionally, high surface roughness combined with high activity may result in large differences between the pH values at the surface and in the bulk of the electrolyte, being the reason for changes in selectivity.[79]

CHAPTER 3

3. Experimental methods

3.1. Approach – Bulk CO_2 electrolysis at ambient conditions

During CO_2 reduction several reactions run in parallel, including the hydrogen evolution reaction as a competitive reaction. Hence, initially, our approach was focusing on what controls the activity and the selectivity of the catalyst at a set of fixed parameters. The parameters are numerous and include temperature, pressure, catalyst surface morphology, mass transport inside the cell, type of electrolyte, its buffer capacity as well as its pH.[20,39-42]

In the case of CO_2 reduction reaction it is essential to not only measure the total current densities (monitored by the potentiostat), but also to perform both qualitative and quantitative analysis of all the reaction products coming from the entire catalyst surface. With this purpose we performed bulk CO_2 electrolysis in a closed volume at room temperature and 1 bar pressure of CO_2. After a given time the products are collected both in gas and liquid phase, to be analysed with suitable method and tools, such as gas and liquid chromatography, as well as nuclear magnetic resonance spectroscopy.

Experiments were usually run for up to 30 minutes, in cases of low current densities up to 60 minutes. Longer experiments would be more challenging, due to potential catalyst deactivation due to d changes in surface morphology, exposure to impurities and poisoning. Furthermore, care was taken to carry out product analysis shortly after the reaction. Otherwise, the products could be lost due to various reasons like leaks in the gas system, loss of volatile products from the liquid phase and various reactions catalysed in acidic or basic media.

3.2. Electrochemical setup and cells

3.2.1 The electrochemical three electrode setup

The typically used setup for studying electro-catalytic reactions is the electrochemical three-electrode setup (see Figure 3.1), which consists of working (WE), counter (CE) and reference electrode (RE). The counter electrode should ideally be a highly non-polarisable electrode, so that there is no change in potential on counter electrode when current is passed. This is achieved either by using a highly reversible counter electrode or by increasing the surface area of the counter electrode relative to the working electrode. Since it is the current density that is the cause of the potential change, in this way one can ensure smaller current density on CE relative to WE upon passing the same current.

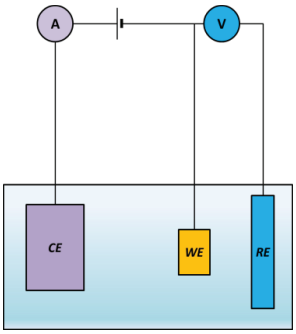

Figure 3.1: Scheme of electrochemical three-electrode setup

The reference electrode is usually made of materials with a stable standard electrochemical potential. Throughout this work, $Hg/HgSO_4/K_2SO_4$ reference electrode was used. The changes in potential of the working electrode are measured with respect to the reference electrode, where there is essentially no current passing. Basically, there are two separate circuits, one where polarising current is passing (WE-CE) and another where no current is passing enabling measurement of the potential change on WE. However, the potential on the CE can vary independently without any influence on WE potential. In the current investigation, we used *Bio-Logic VMP3* potentiostat with *EC-Lab Software*.

The potential of $Hg/HgSO_4$ reference electrode relative to the reversible hydrogen electrode scale was established in following procedure: a Pt wire was used as working electrode in 0.1 M H_2SO_4 saturated with 1 bar H_2. The open circuit potential indicated the value of 0.72 V. Considering the meaured pH value of 1, that implies a correction of 0.66 V relative to normal hydrogen electrode (NHE).

To avoid the oxidation of reaction products at the CE, the working and the counter electrodes are separated. As shown on Figure 3.2, a simple cell for running the short-term bulk electrolysis reactions consists of three electrode compartments. The WE and CE compartments are separated with a proton conduction membrane (Nafion), which works as a salt bridge, while a small porous ceramic frit ensures that no contaminations come to the WE from the RE compartment.

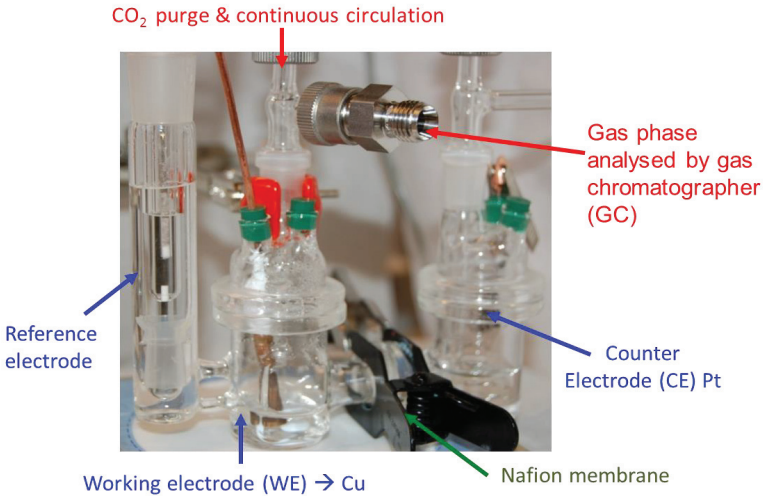

Figure 3.2: Photograph of the H-cell used for the studies on polycrystalline copper electrodes (Chapter 4).

The working electrode compartment is the reactor where CO_2 reduction occurs. Protons are supplied from the CE compartment and electrons passed through the catalyst upon applied cathodic (negative) potentials. The inlet for the gas reactant (CO_2 or CO) is connected to the gas bubbler, placed inside the WE compartment. The outlet is located at the top of it and the gas is transported further along the gas pipeline system to the gas chromatograph (GC) using a pump, as shown on Figure 3.3. The scheme on Figure 3.3 shows that the cell can be operated in *purge* and *loop* mode. The *purge* mode is used to remove oxygen and other dissolved gases from the electrolyte by purging with Ar or N_2. In addition one can saturate the electrolyte with the reactant gas. The *loop* mode is used during bulk electrolysis. A flow meter mounted in the vicinity of the pump inside the look enabled the monitoring of the reactant gas flux. Depending on the electrolysis conditions it varied in the range from 20 to 50 mL/min.

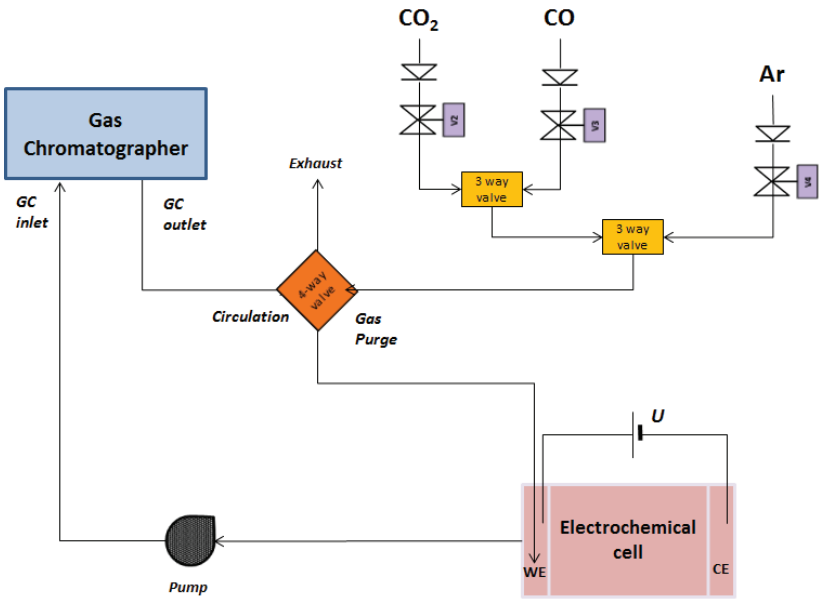

Figure 3.3: Schematic representation of the electrochemical setup connected to gas supply and online analysis systems.

3.2.2 *In-situ* electrodeposition cell

On Figure 3.2, a simple version of the H-cell used for electro-catalytic studies is shown. This cell was employed for studies on polycrystalline copper electrodes explained in more detail in Chapter 4. However, this cell was less convenient for work with alloyed catalyst (refer to Chapter 6 and 7) for several reasons. Adjustments to the cell were needed in order to allow the electrolyte exchange needed for in-situ preparation of the catalyst.[86] The cell design was adapted from a cell developed for previous investigations at our laboratory for single crystals. Another lack of the simple H-cell design was the difficulty to take the aliquiots for liquid product analysis after each batch reaction. For this reason we implemented a more complex cell to work with alloyed catalyst (Figure 3.4) A small WE compartment volume (in range from 6-10 ml) enables high catalyst area to electrolyte volume ratio.

The in-situ preparation of an alloy based catalyst required the possibility of introducing the solute metal solution to the cell where the solute metal would be deposited onto the substrate electrode. In the following step, the cell needed to be rinsed and filled with the working electrolyte. In order to achieve that, glass joints were added to the top and bottom of the working electrode compartment. An

electrolyte reservoir (glass beaker with a bubbler) was connected to the top, while an opening with a Teflon stopper was introduced to the bottom of the cell. These adjustments enabled saturating the electrolyte with a gas, passing it into the working electrode compartment for either purpose of electrode preparation of running the bulk electrolysis, as well as the collection of the working electrolyte samples after the reaction for the content analysis.

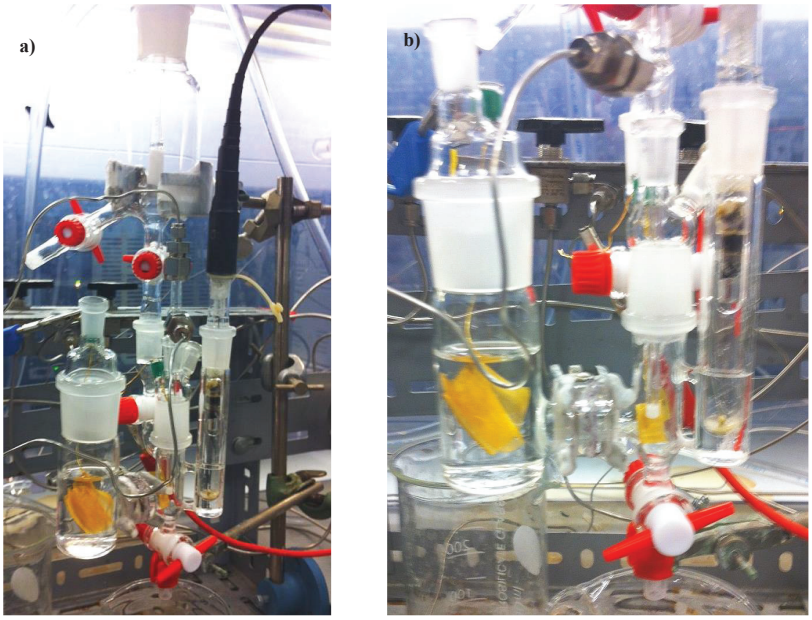

Figure 3.4: Electrochemical H-cell suitable for *in-situ* electrodeposition and bulk electrolysis: (a) Electrolyte reservoir with bubbler connected to the inlet to the WE compartment ending with the outlet at the cell bottom; (b) H-cell and showing three electrode compartments with Au-sheet as working electrode and Au-mesh as counter electrode.

3.2.3 Removal of contaminations and impurities

The electrochemical reactions we are interested in are proceeding at the electrode – electrolyte interface. Since CO_2 reduction reactions require cathodic potentials, where most of the metallic cations also adsorb and deposit to the surface, one must make sure that all the contaminations, organic as well as metallic are removed prior to the reaction from every part of the cell that is in contact with the electrolyte. Contaminations are preferably avoided during preparation of the glassware, electrodes, proton conducting membrane and electrolytes. However, most often it is necessary to apply additional treatments to remove the trace amounts of impurities from glassware, electrodes and electrolytes.

As organic impurities we consider different types of small molecules adsorbed on the glassware or at the electrode surface. The source of this type of contaminations is usually from the air (oxygen, hydrocarbons, etc.) or in contact with plastic, rubber or grease. Metallic impurities may come from various sources such as residual traces of metal cations inside electrolytes, as well as from a used cell residues of the working or counter electrodes. In addition, the glass itself is composed of amorphous phases containing metals as iron, silicon, magnesium, etc., which for instance under strong alkaline conditions may dissolve into the electrolyte and affect the catalyst surface during reaction.

Cleaning glassware

A standard procedure for glassware cleaning in general consists in storing the glassware inside the "piranha" solution (a mixture of 96 % H_2SO_4 and 30 % H_2O_2 in ratio 3:1) for 24 hours with subsequent rinsing in ultrapure water (Millipore Synergy Pak UV>18.2 MΩcm, 22±2ºC). This removes both organic and metallic impurities. Multiple rinsing and sonication in an ultrasound water bath at 50ºC removes the sulfates from the glassware.

In order to remove Au or Pt from the cell, "Aqua Regia" solution, a 3:1 mixture of conc. HNO_3 and conc. HCl was used. Prior to measurements in alkaline solution, a pretreatment was performed in 10 M KOH prior to the "piranha" cleaning. This was to ensure limited corrosion under less alkaline conditions.

Proton membrane preparation

For purpose of separation of working and counter electrode compartments we used proton conducting membranes. The ionic conductivity of Nafion based membranes is high enough to provide a fast transport of H+ from the CE, where they are produced in Oxygen Evolution Reaction (OER), to the WE compartment where they are consumed in CO_2 reduction reaction. We used *Nafion 117 perflourinated membrane*, 0.007 in. thick from Sigma Aldrich. The membrane is carefully cut into pieces of appropriate size. The pieces of membrane are then cleaned in 3% water solution of H_2O_2 by boiling for 1 hour. Afterwards, the Nafion is boiling in 0.1 M H_2SO_4 for 1 hour, following by several rinsing in ultrapure water. The membrane pieces as prepared contain an excess of protons. In contact with the working electrolyte, this proton excess could easily shift the pH value of the electrolyte to lower values. To avoiding this, the cleaned membrane pieces were sonicated for 1 hour in 0.1 M $KClO_4$ solution in order to exchange the excess H^+ by K^+.

Cleaning electrolytes

The electrolytes used for the bulk electrolysis were purchased with the highest purity available (please refer to the materials and suppliers list at the end of this chapter). Special attention was paid to preparation of clean $KHCO_3$. For this purpose we used the pre-electrolysis cell (Figure 3.5). Ultrahigh purity water was saturated with 1 bar CO_2 prior to the addition of the weighed amount of KOH. The KOH was added gradually, so that the solution does not reach high pH values and dissolves possibly contaminants from the glassware.

Additionally, the metallic traces were removed by performing *pre-electrolysis*.[15] This consisted in employing a three-electrode setup where the working electrode would be an auxiliary electrode, as shown in Figure 3.5. The auxiliary electrode is set to cathodic potentials in a stirred, CO_2 or Ar-bubbled electrolyte solution for several hours. This treatment enables fast convective transport of the metallic impurities to the auxiliary electrode, onto which they deposit. Subsequently, the auxiliary electrode is carefully taken out of the solution under potential-control.

The pH value of the electrolytes as prepared prior to use and post-reaction was measured using a pH meter.

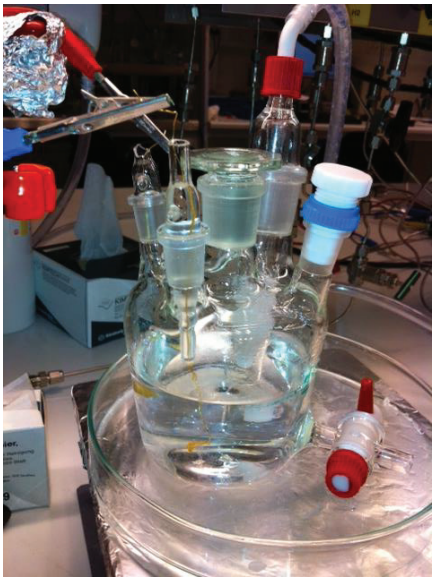

Figure 3.5: Pre-electrolysis cell for preparing clean electrolyte ($KHCO_3$).

3.2.4 Electrode preparation

We employed a variety of methods for preparing clean catalyst materials prior to testing their electrocatalytic activities. The methods varied depending on the nature of the electrode material, as well as our major aims, such for instance obtaining certain surface morphology. Apart of common organic contaminations at the surface, electrodes may also contain surface or bulk metallic impurities due to the technology of their production or affinity to alloy to other elements.

Polycrystalline copper – Cu:

- *Electropolishing* (Chapter 3 and 4) – Electropolished Cu is prepared by electrochemical anodisation, applying a potential of +2 V between the copper electrode and a platinum cathode in phosphoric acid (1 M) for 20 minutes, followed by rinsing of the copper electrode with ultrahigh purity deionised water (18 MΩ).
- *Sputtering* (Chapter 4) – Sputtered copper is prepared by argon-sputtering of an electropolished copper surface. High energy ionised Ar is hitting the sample atoms causing them to sputter off the surface. The rate of sputtering and the time determines the amount of monolayers removed during such procedure. Incidently, Cu sample was bombarded with 3 keV Ar^+ ions and 4 μA emission current for 10 min, removing approximately 30 monolayers (~10 nm) from the surface. When the Ar^+ ions hit the sample, they remove copper from the surface.

Polycrystalline platinum wire – Pt:

- *Flame annealing* of Pt wire removed organic contaminations from the surface.
- *Electropolishing* – Pt wire is subjected to the by electrochemical anodisation by applying a potential of +2 V between the wire and a platinum mesh in 0.1 M HNO_3 for 20 minutes, followed by rinsing with ultrahigh purity deionised water (18 MΩ).

Single crystals of platinum – Pt(111) and Pt(211):

- *Thermal annealing under reducing atmosphere* (Chapter 5) – Disc shaped (10 mm diameter) single crystalline Pt electrodes were thermally annealed using induction heater inside an electrochemical cell purged with 5 vol. % of H_2 in Ar.[86-88] During this process the temperature was monitored and kept below the melting point of Pt.

Copper overlayers on platinum single crystals – Cu/Pt(111) and Cu/Pt(211):

- *Cu underpotential deposition* (Chapter 5) – Copper was deposited from a 3 mM $Cu(ClO_4)_2$ solution in 0.1 M $HClO_4$ by performing cyclic voltammetry and holding at 0.4 V vs. RHE for several minutes.

Polycrystalline gold – Au(pc):

- **Disc shaped polycrystalline gold electrode** (diameter 5 mm) for RDE studies (Chapters 6 and 7) and smooth gold sheet (Chapter 6 - Section 6.2):
  - *Flame annealing* consisted in heating up the gold disc or sheet to high temperatures to remove organic contaminations from the surface by burning them. The procedure was conducted in darkness for better visibility of the red glow in order to avoid melting the gold crystal.
  - *Electrochemical anodisation* involved applying +10 V to the gold disc or sheet relative to Au mesh counter electrode in 0.1 M H_2SO_4 for 10 seconds, followed by immersion of the Au sheet in 0.1 M HCl to reduce the oxidised parts of the surface.

- **Polycrystalline gold sheet** (Chapters 6 and 7):
  - *Chemical etching* in "aqua regia" solution prepared from highest purity acids (conc. HCl : conc. HNO_3 in ratio 3:1) for 30 seconds.

Bulk alloy Au_3Cd (Chapter 7):

- *Polishing* – As received Au_3Cd sheet was polished using 0.25 mm grain size diamond paste on a *MD Nap* cloth (further details in the list of materials and suppliers at the end of this chapter). After polishing the sample was unltrasonicated in acetone, ethanol and ultrahigh purity water multiple times.
- *Sputtering* – The procedure involved bombardment of the Au_3Cd sheet with 1 keV Ar^+ ions and 1 μA emission current until no carbon or oxygen contamination were observed, which usually lasted for 20 min. The UHV sputtering setup is shown in Figure 3.6.

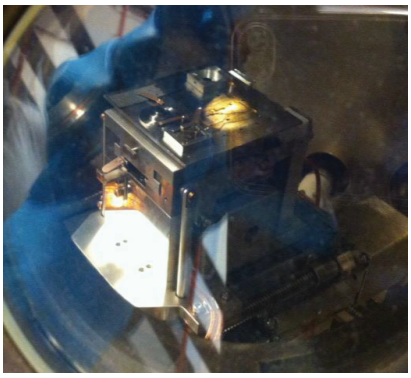

Figure 3.6: Sputter cleaning of the electrode in an ultra-high vacuum (UHV) chamber

It was essential to immerse the freshly sputter-cleaned Au_3Cd under potential control, meaning that immediately before that all electrodes, reference and counter were set in place, as well as an additional clean gold wire in working electrode compartment – serving as an auxiliary working electrode to stabilise the potentiostat. The potential was set to 100-150 mV below the reversible Cd dissolution potential at a given pH. The Au_3Cd sheet is introduced under these conditions, so that no surface cadmium is lost upon contact with the electrolyte. Upon immersion of the sheet, the auxiliary gold wire was removed from the working electrode compartment so that the cell can be further utilised for electrolysis.

Surface alloy Cd/Au – (Chapter 7):

- *Cd underpotential deposition* – A polycrystalline gold sheet, prepared as described above, was cycled in Ar-saturated 0.1 M H_2SO_4 to improve its cleanliness and obtain an estimation of the surface area. Although the electrolysis measurements are carried at pH 7 for CO_2 reduction in bicarbonate and pH 13 for CO reduction in KOH, Cd can only be deposited at pH below 7 (Cd is insoluble at pH above 7).[37] In order to maintain potential control, the electrolyte in the reference and counter compartments could be not be exchanged. Within these two latter compartments, a 0.25 M phosphate buffer was used (0.25 M K_2HPO_4 + 0.25 M KH_2PO_4). An Ar-saturated solution of 0.1 mM $CdSO_4$ dissolved in 0.1 M H_2SO_4 was introduced into the working electrode compartment and potential was cycled between +0.74 V and 0 V or -0.05 V vs. NHE, as shown in Figure 3.7. The deposition potential, hold time and

scan rate were chosen emipirically in order to achieve a specific coverage of Cd. A low Cd concentration in solution means that a longer hold time may be needed to achieve the same deposition charge, which is correlated to coverage based on the surface charge estimations obtained for Cu upd on Au, shown in Figure 6.2. For achieving very lower Cd coverages, a fast scan rate was used.

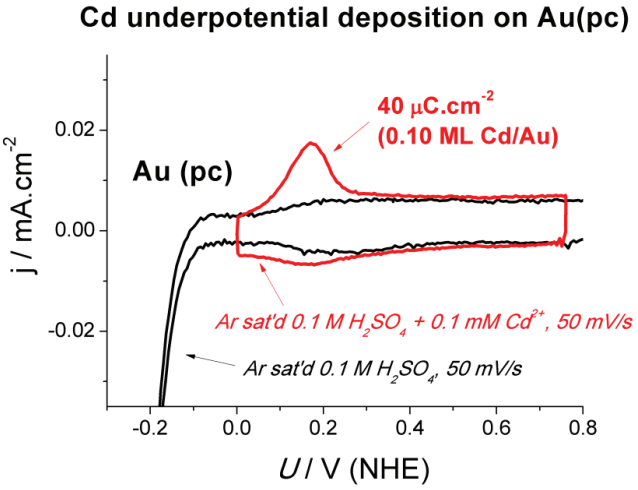

Figure 3.7: Cyclic Voltammograms of *underpotential deposition* of Cd on polycrystalline Au electrode in solution containing 0.1 mM $CdSO_4$ in 0.1 M H_2SO_4 (red line) and reference CV of polycrystalline gold in Cd-free 0.1 M H_2SO_4 solution (black line). Integrated oxidation charge of Cd^{2+} normalised for the geometric area and roughness factor of electrode indicates the coverage of Cd at the surface, corresponding to ca. 0.1 monolayer of Cd on Au. Specific charge for a monolayer obtained in 2 electron process is established in Figure 6.2, Chapter 6. Roughness factor of Au(pc) used here was 1.5.

Following this, the potential is held at certain value and a Cd-free 0.1 M H_2SO_4 is passed through the working electrode compartment of the cell. Aprroximately 100 mL of Ar saturated Cd-free solution was passed through the cell, to ensure complete Cd^{2+} removal from the inside of the cell. Following this, oxygen-free working electrolyte ($KHCO_3$ or KOH) was introduced at potentials where Cd would be stable at the working pH.

High surface area catalysts – (Chapters 6 and 7):

- **Au nanoparticles** – Various inks were prepared containing different amounts of 5 nm Au particles dissolved with Nafion and isopropanol. The ink was sprayed onto carbon cloth and dried in Ar purge. Au nanoparticles were prepared by Ana Sofia Varela.

- **Oxide derived Au** – Following instructions for preparation from work of Chen et al[59]. Preparation of oxide-derived Au was carried out by Arnau Verdaguer-Casadevall.

- **Nanoporous gold leaves** – Following and adapting the instructions from work of several groups.[89,90] Gold-silver alloy (in ratio 1:1) shaped in 100 nm thin leaf was initially rolled onto a polycrystalline gold rod. Silver was leached out by various methods – either by using conc. HNO_3 leaching or by electrochemical cycling in 0.5 M HNO_3.

3.3. Electrochemical techniques for electrode characterisation and catalytic activity testing

3.3.1. Cyclic Voltammetry

Pre- and postreaction electrode characterisation is a crucial step in understanding the catalytic results. In general, one can use a variety of techniques to prove the cleanliness of the catalyst surface, the oxidation state of the elements, bulk crystallographic structure, as well as the surface morphology including the possibility to estimate the surface area. In this section particular attention is paid to electrochemical, UHV and microscopy techniques used for catalyst characterisation in this work.

Cyclic voltammetry is an electrochemical technique widely used for electrode characterisation. It consists in sweeping the potential along a triangular wave between two values using a certain scan rate (dU/dt) while measuring the current response (see Figure 3.8). The outcome current comes as consequence of all the processes occurring at electrode at a specific potential. A positive current is recorded if the processes at the working electrode assume net shuffling of electrons in direction from the WE to the CE. Similarly, negative currents are measured in a CV if the processes occurring on the WE involve transfer of electrons from its surface. This means that not only processes of oxidation or reduction of the electrode surface are possible to identify, but also all other processes that involve transfer of electrons such as oxidation or reduction of atoms (metals) or molecules (gases or organic impurities), electrolyte adsorption, surface reconstructions, as well as changes in double layer capacitance.

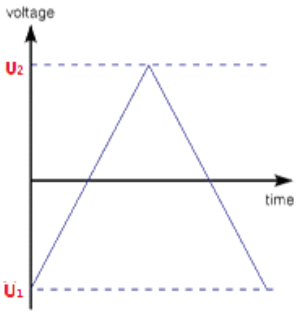

Figure 3.8: Cyclic Voltammetry - Potential waveform. The slopes of the lines are determined by the scan rate. Figure reprinted from.[91]

This is a very powerful technique since under certain conditions (fixed set of parameters) one can isolate the object of the study and use the CV as a fingerprint of the studied surface under given conditions. In electrocatalytic studies we used it widely to qualitatively (cleanliness) and quantitatively (surface area) characterise the catalyst surface, clean it from organic impurities or use it as a tool for surface roughening at very high scan rates. However, cyclic voltammetry can be as well used for studying catalyst activity, for example for the oxygen reduction reaction.[92]

3.3.2. Surface Area Measurements via Electrochemical Impedance Spectroscopy

As alternative to upd methods used for surface area estimations of pure metals, we present here a technique used for estimations of surface area on bimetallic surfaces. The electrochemical impedance spectroscopy (EIS) is a non-invasive and very sensitive method for investigation of the solid-electrolyte interface. The principle we use in accessing the roughness factor using the EIS is based on measurement of the capacitance of the double layer for a given electrode-electrolyte system. The double layer capacitance depends on electrolyte, its concentration, pH and possibly as well on the dissolved gases. On the other hand, it also depends on the nature of electrode, its potential and its roughness, i.e. surface area.[93]

The electrochemical impedance spectroscopy measures the system response to the application of a small periodic ac signal. The measurements are performed at different ac frequencies. The interpretation of the system response contains information about the electrode-electrolyte interface, its structure and the reactions taking place there. In short, the system response is plotted as Nyquist plot, shown in Figure 3.9.

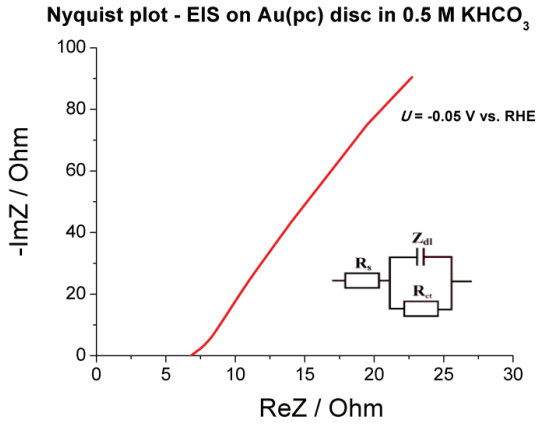

Figure 3.9: Nyquist plot Equivalent circuit used for the data analysis and parameters fitting. Inset figure reprinted from[94].

To interpret the Nyquist plot, we used a suitable equivalent electric circuit consisting of a resistor (solution resistance) connected in series with the constant phase element (CPE), modelling the behaviour of the double layer and a resistor (charge transfer resistance) in parallel, as shown in the inset of the Figure 3.9. The solution resistance can be obtained from the x-axis of the Nyquist plot. Charge transfer resistance can be deduced from the radius of the semi-circle. The impedance (Z) is expressed through the following equation:

$$Z = Q^{-1}(j\omega)^{-a} \qquad \textbf{(3.1)}$$

whereby Q is the pre-exponential parameter of the CPE, which is proportional to the double layer capacitance of pure capacitive electrodes, the exponent a is a parameter ($0.5 \leq a \leq 1$). The EIS data analysis was performed with the built-in EC-Lab software (EIS, Z fit). The quality of the fit was estimated via the rootmean-square deviation.[95]

3.3.3. Chronoamperometry

In general, the catalyst activity can either be expressed in terms of potential at which a certain current density is achieved, as often reported by Hori and co-workers[15], or in terms of current densities at a given potential. The measurement is carried out by holding the potential during a certain reaction time, while the current is recorded. This techniques is called chronoamperometry and it was used through this work. On the other hand, the advantage of using chronopotentiomentry (where a current is set and the potential is measured) is based on having a fixed current density at the electrode surface which ensures the same ohmic losses for various types of electrodes regardless their morphology or composition. As well, it means that the effects of electrolyte, its buffer capacity and local changes in pH are the same.

Prepared for the catalytic studies, the catalyst material was placed into the working electrode compartment, attached to a wire (0.5 mm diameter) of same nature as the studied electrode (cathode). As counter, usually a Pt or Au mesh were used. The potential was measured relative to a $Hg/HgSO_4$ reference electrode. The electrode potential was corrected for the IR drop between the ceramic frit separating the reference electrode and the cathode compartment.

3.3.4 Ohmic losses corrections of potential

The accuracy of measuring the potential during electrolysis may to great extend be affected by the electrolyte resistance. The drop in voltage created between the working and the reference electrode is proportional to the current passing at the working electrode. In order to produce high enough concentrations of liquid products to meet the detection limits of the analysis methods, the total average currents during electrolysis were sometimes reaching rather high values of ca. -50 mA.

For estimating the solution resistance in this work we employed the potentiostatic electrochemical impedance spectroscopy. This method consists in performing the EIS measurement at the ac frequency where other contributions of impedance can be neglected and only resistance is measured. By sweeping the frequency from 50 Hz to 1 MHz at open circuit potential we obtained a particular case of the Nyquist plot, from which we extrapolated the value of the frequency relevant for resistance measurement to be 3 kHz. Using this value, typically measured values for the solution resistance are in range of 16-17 Ω (for 0.1 M $KHCO_3$) and 7-8 Ω (for 0.5 M $KHCO_3$).

The potentiostat was set to automatically correct for the 85 % of the ohmic losses, whereby the rest must be corrected afterwards using equation 3.2:

$$U_{corr}^{100\%} = U_{corr}^{85\%} - 0.15\, IR_{sol} \qquad \textbf{(3.2)}$$

The equation 3.2 shows that a lack of correction assuming high average currents would give rise to a discrepancy between the measured and the real potential in the range of ca. 0.4 V in case of higher and even up to even 0.8 V in case of lower electrolyte concentration.

Accurate determination of the actual working potential is crucial for comparing the data among various research groups.[96]

3.3.5 Calculations of the activity and the selectivity

Catalytic activity – Partial current density – j / mA.cm^{-2}

The values for partial current densities are obtained using Faraday's law of electrolysis, which correlates the amount of the product formed during the bulk electrolysis (in moles) to the charge transferred in the process:

$$n_i = \frac{Q_i}{zF} \quad \textbf{(3.3)}$$

whereby n_i - represents the amount of product in moles, Q_i – charge used to produce the product, z - number of transferred electrons for obtaining one molecule of the product and F – *Faraday constant* being 96485,34 C/mol.

From Faraday's law and equation 3.4:

$$Q_i = I_i t = j_i S_{geom} r t \quad \textbf{(3.4)}$$

whereby: j_i represents the current density, S_{geom} – geometric surface area of the electrode, r – roughness factor and t – time, follows the expression for the partial current density (j_i) corresponding to product *i*:

$$j_i = \frac{n_i z F}{S_{geom}\, r\, t} \quad \textbf{(3.5)}$$

whereby we access n_i from the product concentration in gas or liquid phase (described separately for gas and liquid analysis in following sections).

Partial current density is hence the current consumed in order to form a certain product per unit of the catalyst active area. It describes the activity of the given catalyst for the formation of a certain product.

Selectivity – Faradaic efficiency - ε (%)

Observing a partial current density with respect to the total current density within a single reaction one may obtain the current efficiency or so called Faradaic efficiency, since it is attributed only to Faradaic currents from the electrolysis process. It does not take into account other usually much smaller currents, which correspond to surface adsorption – desorption processes.

For the calculation of the Faradaic efficiencies (ε_i) for various gaseous products we used the following equation:

$$\varepsilon_i(\%) = \frac{j_i}{j_{tot}} \quad \textbf{(3.6)}$$

The total current is the average current during the bulk electrolysis, obtained as ratio of total charge and time of reaction per unit active surface area.

3.4 X-ray Photoelectron Spectroscopy (XPS)

X-ray Photoelectron Spectroscopy (XPS) is commonly used technique for surface characterisation. It is based on the photoelectric effect, whereby a photon of certain energy hits the sample and interacts with its electrons. The electrons are then emitted outside the sample with kinetic energies that can be measured.[8] More precisely, an X-ray source with two lines – *Mg Kα* (hv =1253.6 eV) and *Al Kα* (hv=1486.3 eV) generates an incident X-ray beam, which has a large depth of penetration into the sample. The X-rays excite the electrons with different binding energies deep in the sample below the vacuum level (see Figure 3.10 a). One can use a detector to measure the kinetic energy distribution of the electrons emitted from the sample. From this measured kinetic energy one can determine the electron binding energies using following equations:

$$E_{kin} = h\upsilon - E_{bin} - \phi_{analyzer} \qquad \textbf{(3.7)}$$

Even though the X-rays used in the measurements penetrate several nanometers into the sample, according to the universal curve (Figure 3.10 b), the emitted electrons have the mean free path of only 0.5 – 2 nm. This is the reason why XPS is a very surface sensitive technique, since only these electrons originating from few atomic monolayers can be detected.

XPS is very useful for identifying the surface composition: it gives the surface density of electrons at a specific binding energy, which is a unique characteristic for an electron transition inside an element.

As well, XPS provides information about the oxidation state of an element, since its core level electrons binding energy is dependent on the chemical environment around the atom.

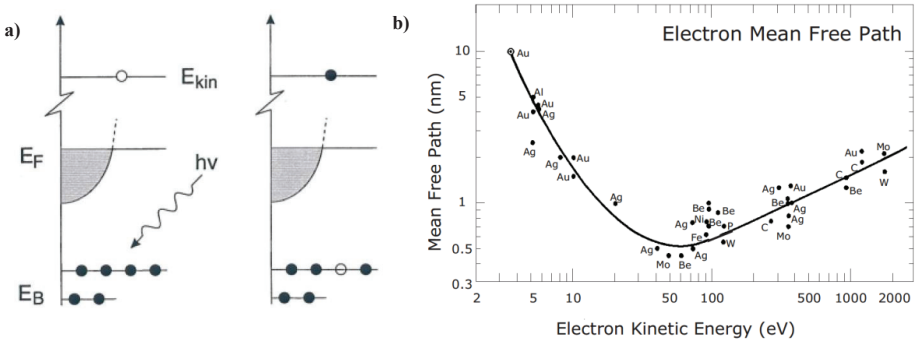

Figure 3.10: (a) Photoelectric effect – Electron obtains kinetic energy upon its interaction with a photon of energy hv. EB is binding energy and EF is Fermi level. Reprinted from[97] (b)Universal curve – electron mean free path. Figure adopted from[98].

Angle resolved XPS (AR-XPS)

Furthermore, the surface sensitivity of an XPS measurement can be tuned by varying the angle between the X-ray incident beam and the normal to the sample. By changing the angle one is influencing the effective mean free path of electrons, hence, recording the kinetic energies of electrons from different penetration depths (Figure 3.11). Based on this principle, it is possible to make a non-destructive depth profile of the sample. The data collected at all angles are converted into a sample depth profile.

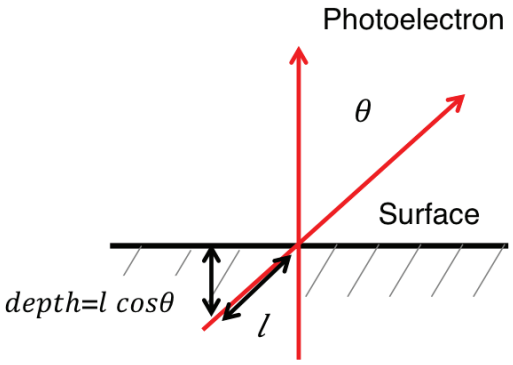

Figure 3.11: Angle Resolved XPS -Scheme representing the relationship between the incident beam angle and the depth of the probed electrons. Adapted from[99].

Equipment details: The XPS equipment (*Sigma Probe, Thermo Scientific*) uses monochromated *Al Kα* line as X-ray source and a six channel detector for the detection of emitted electrons.

3.5. Scanning Electron Microscopy (SEM)

Scanning electron microscopy provides the possibility of imaging the surface. An SEM measurement consists in irradiating the sample in an ordered manner with a beam of high-energy electrons (primary electrons). As an effect of the interaction between the primary electrons and the sample, the secondary electrons are emitted along with the backscattered electrons. The secondary electrons come from the near surface region and contain topographic information about it. They can be used to generate an image of the sample surface (Figure 3.12).

Equipment details: This thesis contains images obtained using an FEGSEM 200F digital scanning microscope.

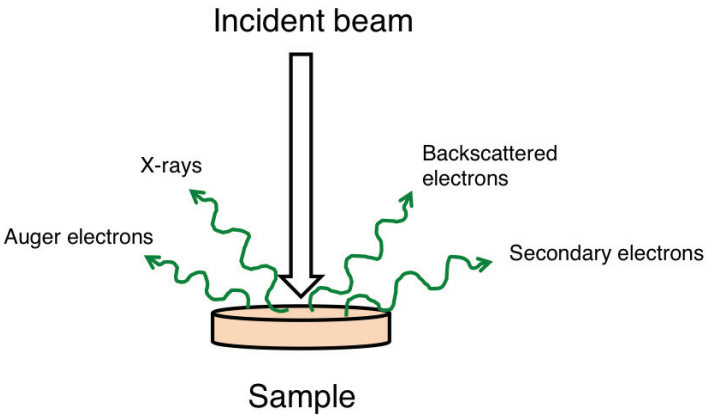

Figure 3.12: Electron beam – sample interaction in Scanning Electron Microscopy.

3.6. Qualitative and quantitative products analysis

The information about the catalyst selectivity, thus on partial activities towards specific compounds in relation to CO_2 reduction, relies on identification, detection and quantification of all reaction products. A valuable indication of the accuracy of product quantification is obtaining the full total balance between the integrated charge measured by potentiostat and the charge that would be necessary for the formation of all the detected gaseous or liquid molecules. There are several techniques that can be used for analysis of CO_2 electro-reduction products[100] in order to access the total charge such as gas chromatography (useful for identification of gaseous products like hydrogen and hydrocarbons, as well as oxygenated products as alcohols, aldehydes or ketones in connection to the headspace analysis equipment), liquid chromatography (useful for quantification carboxylic acids, as well as alcohols) as well as nuclear magnetic resonance spectroscopy (useful for all products, especially identification of new products).

3.6.1. Gas phase product analysis

The major gas phase products of the bulk CO_2 electrolysis are hydrogen, carbon monoxide and hydrocarbons, among them mostly methane and ethylene. In this study, these were detercted using gas chromatography. The most important feature of the gas chromatography as analytical technique is a good separation of the products and their quantification with rather high sensitivities.[100]

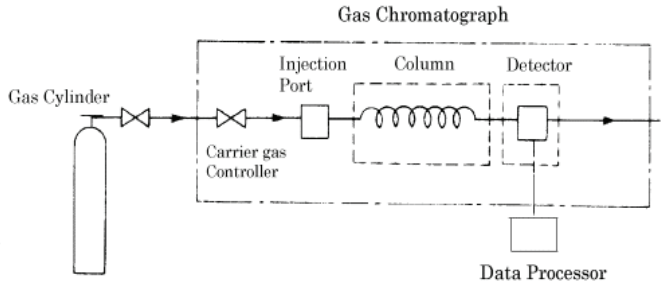

Figure 3.13: Gas Chromatograph – schematic representation of the analysis principle. Figure from[101]

The separation process takes place inside the column and it is based on principles of chromatography, whereby different species possess different retention times due to their interaction with the material inside the column, also known as stationary phase. After performing the bulk CO_2 electrolysis, a small

fraction of the gas mixture containing the gaseous products is injected into the GC loop and carried to the column with the carrier gas (inert gas as He or Ar), which represents the mobile phase.

The compounds with weaker interaction with the column material are retained shorter, while compounds with stronger interaction with the stationary phase stay longer in the column. In order to provide the best separation of the gas mixture, one can vary the retention times by changing the temperature of the column or the flux of the carrier gas. The columns have length of ca. 30 m giving enough time for all the gas molecules to interact with the stationary phase. Following the column an appropriate detector should be used for an optimal quantification (see Figure 3.13).

There are two different detectors used in our setup:

1. **Thermal Conductivity Detector (TCD)** – The principle of detection is based on measuring the changes in thermal conductivity of the mobile phase, i.e. changes caused by dissolving the sample inside the carrier gas relative to its own thermal conductivity. This detector was employed for detection of hydrogen and CO as products and as well oxygen and nitrogen in case they would leak in from the air. In principle, this detector can be used for organic compound detection as well.
2. **Flame Ionisation Detector (FID)** – Organic compounds, such as alcohols, aldehydes and hydrocarbons are detected using FID. The mobile phase is exposed to H_2 flame, by which the gas compounds become ionised and measured in that form. Since this is a destructive method, it is preferable to analyse the gas first using TCD followed by FID.

Calibrations and interpretation of the data

The area of the detected signal for each product is linearly proportional to its gas phase concentration. We calibrated the GC using corresponding calibration mixtures:

- For hydrogen we used 5%H_2 in Ar (supplier *AGA*).
- For CO and hydrocarbons we used a mixture of 1% CO, 0.2%CH_4, 0.25% C_2H_4, 0.15% C_2H_6, 0.15% C_3H_8 and 0.1% C_3H_6 (from supplier *AGA*).

The calibration of products for quantification purposes was performed by passing the calibration gas mixtures (of known concentrations) through the electrochemical cell in use at a fixed flux, set previously by choice of suitable gas inlet pressure and pump power. We injected the samples while having the sample gas in the loop mode, whereby the pump is used to establish the circulation of the sample gas with a constant flux. In such way, the coefficients for 1% (volumetric) are obtained for all products. Higher value of the $K_i(1\%)$ means better sensitivity for that specific product.

The volumetric concentration x_i is expressed by equation 3.8:

$$x_i = \frac{A_i}{K_i(1\%)} \quad \textbf{(3.8)}$$

whereby A_i represents a signal measured by gas chromatography for a specific product i and $K_i(1\%)$ the calibrated value for each product for 1% volumetric concentration.

For gaseous products n_i is calculated from:

$$n_i = x_i n_{tot} \quad \textbf{(3.9)}$$

whereby the total amount of the gas must fulfil the ideal gas law:

$$n_{tot} = \frac{pV_{gas}}{RT} \quad \textbf{(3.10)}$$

In this equation: p – pressure, V_{gas} – gas phase volume circulating through the electrolyte inside the cell, R – universal gas constant and T – temperature. V_{gas} is calculated as difference between the total system volume and the volume of electrolyte inside the cell.

For obtaining a full total balance between the gaseous and liquid products of one reaction, the electrolysis was performed as batch experiments in a closed system with a specific volume. An accurate calculation of all the Faradaic efficiencies, hence all the partial current densities relies on a good estimation of the volume of the system.

To obtain an accurate value of the system volume, which assumes the headspace volume inside the cell and all the tubings, flow meter, pump as well as the GC loop volume. We accessed this value by performing the hydrogen evolution reaction on polycrystalline Pt wire in Ar-saturated 0.1 M H_2SO_4 (since we adopt its Faradaic efficiency on Pt is 100 % towards hydrogen evolution).

At the constant flux, the gas phase volume for a specific cell can be calculated following equations shown below:

$$Q_{H2} = n_{H2} zF \quad \textbf{(3.11)}$$

$$n_{H2} = x_{H2} \frac{V_{gas}}{V_m} \quad \textbf{(3.12)}$$

$$x_{H2} = \frac{A_{H2}}{K_{H2}(1\%)} \quad \textbf{(3.13)}$$

By plugging all in, one obtains:

$$A_{H2} = Q_{H2} \frac{RT\, K_{H2(1\%)}}{p\, V_{gas}\, z} \qquad \textbf{(3.14)}$$

Recording the hydrogen signal data from the gas chromatograph (TCD) against the total reaction charge provides a linear dependence with a slope containing information about the volume of the gas phase (Figure 3.14, Equations 3.14 and 3.15).

$$V_{gas} = \frac{RT\, K_{H2(1\%)}}{p\, z\, \alpha} \qquad \textbf{(3.15)}$$

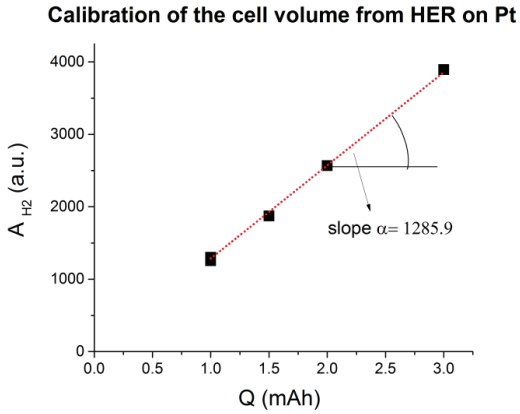

Figure 3.14: Experimental determination of the reactor volume - calibration plot –intergrated signal of H_2 detected by GC-TCD produced on a Pt wire at -0.5 V vs. RHE assuming its 100 % selectivity towards the hydrogen evolution reaction, plotted versus the total reaction charge. The derivation of the physical meaning of the slope is obtained using equations 3.11 – 3.15).

Equipment details:

As previously shown on Figure 3.3, the electrochemical cell as a reactor was connected directly to the gas chromatograph (GC). We used gas chromatograph of type Agilent 6890. The front and back inlets are connected to the sample loop, which injects a volume of 250 µL of sample into the column. We used two different columns, one of type *HP/Molesieve* for separation of H_2, O_2, N_2 and CO and another of type *SUPEL-PLOT/Q* for the separation of all the hydrocarbon species such as CH_4, C_2H_6, C_2H_4, C_3H_8 and C_3H_6.

Following separation, the products continue towards detectors. For detection of H_2, O_2, N_2 and CO we employed the thermal conductivity detector, while for the hydrocarbons a flame ionization detector is used.

3.6.2. Liquid phase product analysis

Apart from the gaseous products, electrocatalytic reduction of CO_2 gives products in liquid phase, however with generally low current efficiencies, meaning that only very small concentrations are produced. On pure polycrystalline Cu or Au, the liquid product which is produced at the highest efficiency is formate.[15,39,58] Other products observed include carboxylic acids aldehydes, alcohols, and ketones. Consequently, not one single method can be used to detect all products.[100]

In case of liquid products, the value for n_i related to calculations of activity and selectivity is obtained from concentration of the product and the volume of used electrolyte:

$$n_i = c_i V_{el} \qquad \textbf{(3.16)}$$

Whereby c_i represents the concentration of the product in the liquid phase (determined using one of the methods described below) and V_{el} is electrolyte volume.

To access the catalytic activities towards different products partially, one must produce all products with concentrations higher than the detection limits of the analysis method. Comparing the equations 3.4 and 3.16, one can easily conclude that there are three major parameters influence the concentration of liquid products in solution: total reaction charge (at constant j dependent on the electrode roughness factor and the reaction time) and the electrolyte volume. The minimum electrolyte volume is fixed by the analysis equipment. Hence, either high surface area catalyst or longer reaction times may ensure meeting the required concentrations, necessary for the reproducible and reliable product analysis. Electrolysis extended in time may provide enough high products concentrations, however, this also introduces possibilities for other, unwanted processes, such as catalyst deactivation. It becomes clear that having high roughness factor catalyst would ensure reaching the detection limits of our methods and the accuracy of the quantitative analysis.

In this study, three different techniques were used for the detection of liquid products, high performance liquid chromoatography, static headspace gas chromatography, both of which were carried out in-house, unlike the nuclear magnetic resonance spectroscopy.

I - High Performance Liquid Chromatography (HPLC)

In this study, liquid chromatography has been employed primarily for detection of carboxylic acids, such as formic and acetic acid.

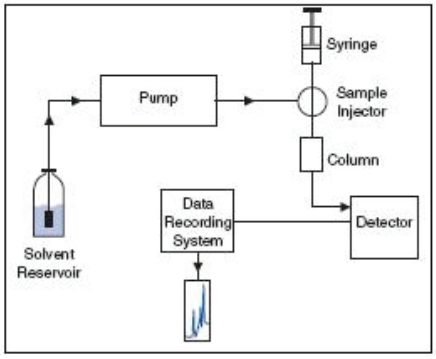

Figure 3.15: Flow chart of the HPLC (high performance liquid chromatograph) system. Figure reprinted from[102].

Similarly to the gas chromatography, liquid chromatography relies on interaction between the stationary and the mobile phase, whereby here the mobile phase is liquid.

The principle of separation of the products in liquid phase depends on the column in used, in our work it was based on different polarity of the compounds. A small amount of liquid (1-10 μL) is sampled from the 2 mL sample vials by the needle. The needle injects the aliquot to the mobile phase which passes through the column for products separation (follow Figure 3.15). A good separation is achieved by setting the optimal values for temperature of the column, flow of the mobile phase, as well as its composition, pH value, etc.

Upon leaving the column, the separated compounds should be detected by an appropriate type of detector. In this work, two types of detectors were used:

- Diode Array Detector (DAD) – The principle behind compound detection is based on the differences in their UV or visible light absorption. This detector contains an array of photodiodes, which enable obtaining information from a wide range of wavelengths. This type of detection is suitable for unsaturated compounds having strong absorption in UV region. However, this detector does not show very good sensitivities towards alcohols.
- Refraction Index Detector (RID) – The differences in refractive index between the mobile phase and the sample allow the detection and quantification by this method. Figure 3.16 shows a beam of light shining onto a dual compartment flow cell. Through one of the compartments flows the pure eluent with its reference refraction index. Through the other

compartment flow both the eluent and the eluate (the mobile phase). A signal is obtained when a difference in refraction indices is measured.

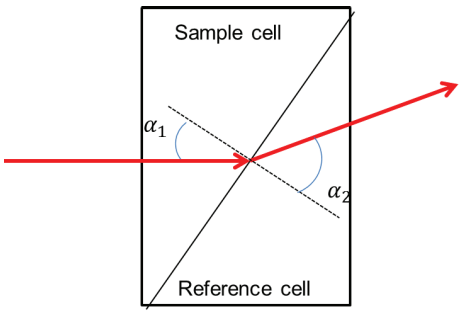

Figure 3.16: Principle behind detection in Refractive Index Detector (RID) in HPLC system. Figure adapted from[103]

Calibrations of the HPLC

The peak area in liquid chromatography is proportional to the compound concentration. We calibrated the HPLC using known concentrations of various possible products such as carboxylic acids (formic and acetic), alcohols (methanol, ethanol) in our working electrolyte (0.5 M $KHCO_3$ or 0.1 M KOH).

Equipment details: HPLC used for data in this thesis is of type *Agilent 1200 Series* equipped with an autosampler, degasser, quaternary pump, as well as both refractive index and diode array detectors. We used column purchased from *BIORAD*, *Aminex HPX-87H*. Samples were analysed both at room temperature and slightly elevated temperatures (30ºC) using 0.005 M H_2SO_4 as eluent at flow rate of 0.6 mL/min. Injection volume was 30 µL.

Formaldehyde detection

Formaldehyde is a challenging product for detection. The use of HPLC for detection of trace amounts of formaldehyde may be feasible, however, it relies on applying a derivatisation method. Namely, aldehydes are reacted with an aromatic compound with a strong signal in UV-VIS region, which ensures high sensitivity of detection.[104] Such typical reaction with a *2,4-dinitrophenylhydrazine* (DNPH) is shown in Figure 3.17.

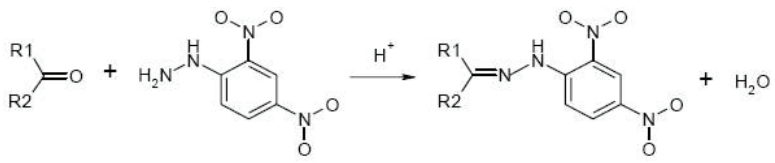

Figure 3.17: Principle reaction behind the derivatisation method for aldehydes detection.

However, in our case, analysis of formaldehyde in an alkaline solution posed an additional challenge, since many organic reactions could occur simultaneously – of which the most prominent could be a base catalysed disproportionation reaction.[105,106]

II Static Headspace Gas Chromatography

Specifically for the current thesis, we established the use of static headspace gas chromatography at our laboratory. This allows quantitative analysis of the volatile organic compounds with very high sensitivities, similar to those of dynamic purge and trap analysis[107]. The detection limits of this method can be optimised to reach concentrations of several μM for compounds such as methanol, ethanol or acetone. The technique is rather simple since it does not involve any extraction nor concentration methods. It is based on sampling the volatile compounds directly from the headspace over a liquid sample inside the vial, which makes it both less time consuming and inexpensive.

A typical sample for this technique is prepared in a vial of specific volume, which contains liquid sample and the headspace above. A liquid sample is placed into the vial directly from the cell following the reaction. The volatile compounds start to diffuse into the gas phase immediately even at room temperature. The vial is heated up to a higher temperature but below the boiling point of water (80-95ºC) and kept for certain amount of time until the equilibrium between the vapor and the liquid is reached. Following this, the gaseous sample is taken from the headspace of the vial and injected further to the GC column), where the separation and detection of the components occurs. Once the products are out of the column they are analysed, in this case with an FID detector (schematically shown on Figure 3.18).

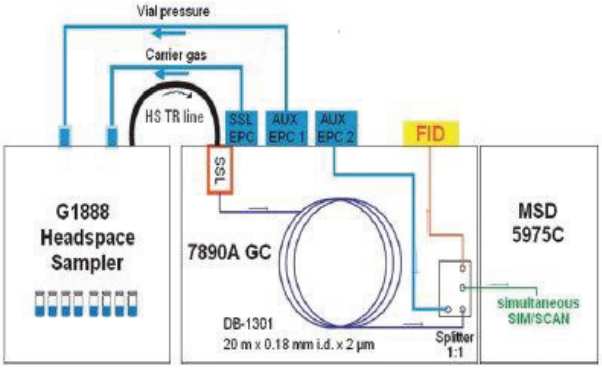

Figure 3.18: Headspace sampler in connection to the gas chromatograph. Reprinted from[108].

The best performance of this technique is achieved considering careful sample preparation and optimal equipment settings. The key issue related to the instrument settings is how to achieve the maximum concentration of the volatile compounds in the headspace of the vial.

An optimal choice for sample preparation should maximise the concentrations of the volatile components in the gas phase and minimise the undesired contaminations from other compounds in the sample matrix. The equilibrium concentration distribution of the analyte between the liquid and the gas phase is given by the partition coefficient, defined as ratio of liquid and gas concentration of a given compound. Hence, low values of partition coefficient mean that the compound will tend more readily to leave the liquid and move into the gas phase, resulting in relatively low limits of detection. On the other hand, the components with high partition coefficient values will have relatively low response and result in high detection limits. Partition coefficient can be lowered by changing the temperature where the vial is equilibrated or by adding some salts into the sample matrix.[107]

Calibrations for the static headspace analysis

On Figure 3.19, a typical chromatograph obtained during the calibration of the FID signal area for mixture of products of 0.1 mM concentration. The initial spike corresponds to trace amounts of H_2 and CH_4 dissolved in the aliquot. The retention times of the products are as follows: methane (2.4 min), methanol (3.9 min), acetaldehyde (4.2 min), ethanol (7.5 min), acetone (10.5 min), n-propanol (22 min), see Figure 3.19. Figure 3.20 provides a full calibration obtained for the major volatile products possibly emerging in the liquid phase – methanol, acetaldehyde, ethanol, n-propanol and acetone, at four different concentrations, dissolved in 0.1 M KOH matrix.

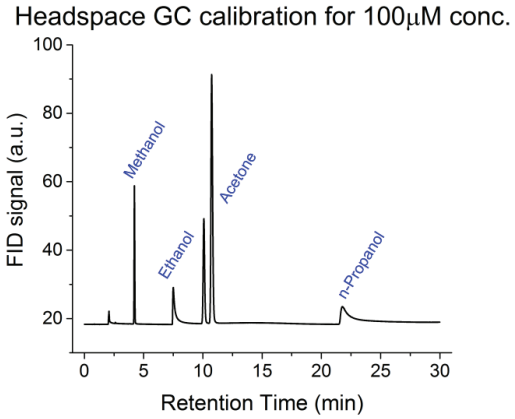

Figure 3.19: Static headspace analysis - FID chromatograph of calibration for mixture of products at 100 μM concentration in 0.1 M KOH matrix.

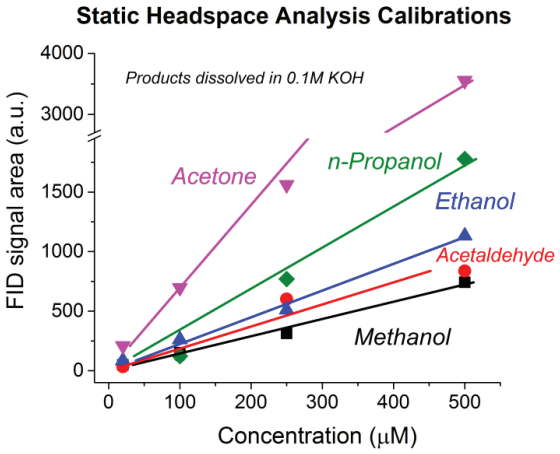

Figure 3.20: Static headspace analysis – calibration lines for various products in 0.1 M KOH matrix.

Additionally to these calibrations, we provide a test electrolysis measurements on an electropolished polycrystalline copper electrode under various reaction conditions: (a) CO_2 reduction reaction in 0.1 M $KHCO_3$ at -1.1 V vs. RHE (potential was chosen from Figure 2.9, where as reported by Kuhl et al[39], Cu produces significant amount of ethanol, n-propanol, allyl alcohol and trace amounts of acetaldehyde, acetone and methanol); (b) CO reduction in 0.1 M KOH at -0.75 V and (c) -0.35 V vs. RHE.

Plot (a) in Figure 3.21 shows the overall comparison of the three chromatograpy analyses. The most pronounced feature at this plot corresponds to methane, forming a peak at retention time of 2.4 min. The initial spike corresponds possibly to the trace amounts of H_2 dissolved in the aliquot.

Plots (b) in Figure 3.21, however, provides a clearer insight into the liquid phase products. We observe many of the same products as those reported by Kuhl et al, collected under similar conditions.[39] CO_2 reduction at -1.1 V (blue solid line) on electropolished Cu(pc) showed ethanol, acetone, acetaldehyde and few other peaks, as expected. Chromatographs obtained after CO reduction at less negative potentials (red and black solid lines), also show clear detection of acetaldehyde and ethanol.

These test results confirm the capability of the technique to detect and quantify accurately the volatile organic compounds at low concentrations. The same method was employed further on in Chapters 6 and 7 on Au and alloyed Au samples.

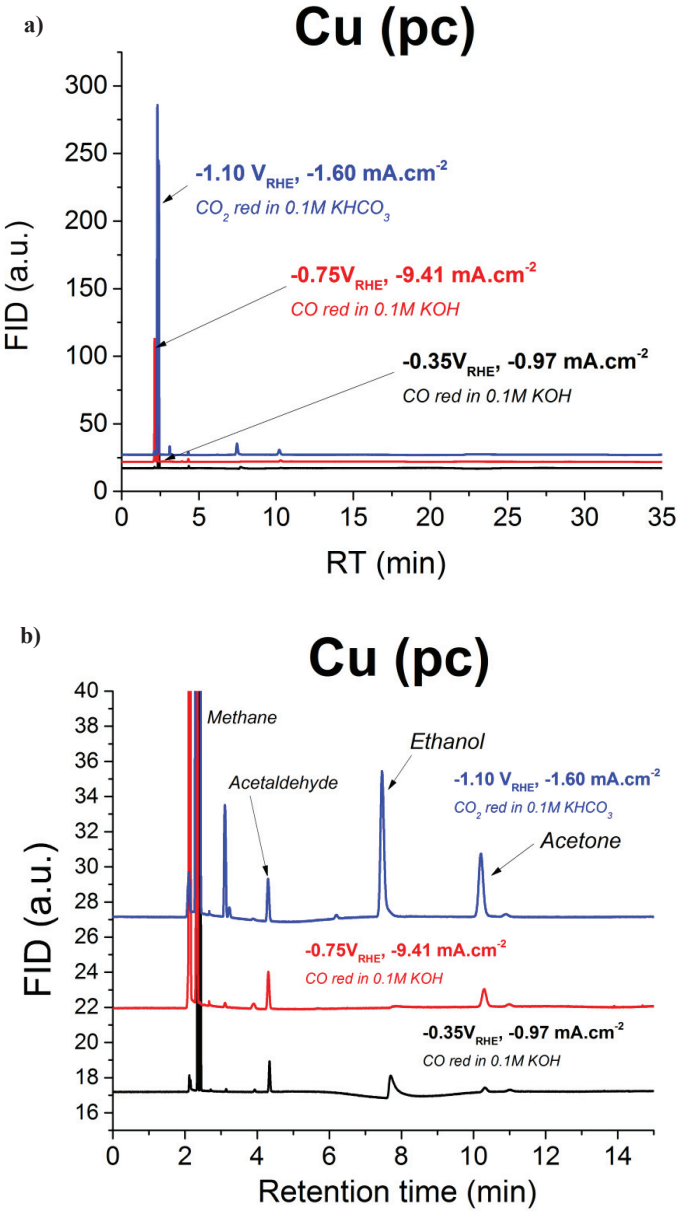

Figure 3.21: The example of use of high sensitivity static headspace analysis connected to the flame ionisation detector (gas chromatograph): (a) Chromatograph made on aliquots from CO electrolysis at -0.35V, -0.75V and CO_2 electrolysis at -1.10V on polycrystalline Cu electrode. (b) a zoomed chromatograph with sharp features with corresponding products confirming high sensitivity of this method.

Equipment details: We used the *Agilent Headspace Sampler 7694E* in connection to our GC of type *Agilent 7890A.*

III Nuclear Magnetic Resonance Spectroscopy (NMR)

Quantification of liquid phase CO reduction products in alkaline media

NMR spectroscopy is a unique technique for identification of the compounds, based on the magnetic properties of a given nuclei. In particular ^{1}H-NMR, spectroscopy allows the identification of different types of protons on a given sample. Moreover, the signals observed in NMR are proportional to the concentration of each compound, so it facilitates an acceptable quantification of almost all compounds with low detection limits. For this reason we employed ^{1}H-NMR spectroscopy as means of quantification of the products from CO electro-reduction in alkaline media. This study involved strict considerations of cleanliness, use of internal standards and chemical shift references, sample shipping and preparation, as well as obtaining the calibration curves for some of the most interesting products and detection and quantification on the unknown samples.

Cleanliness: it turns out that NMR was able to detect traces of organic impurities coming from fingerprints, various types of plastics, gloves, etc. For purpose of obtaining clean spectra, all the glassware, weighing cups, plastic pipettes and tubes used for accurate measuring, weighing and storage of standard solutions should be cleaned of organic impurities (glassware best by using previously described method with piranha solution; plastics by multiple sonication in heated ultrapure water).

NMR - sample preparation – internal standard:

The absolute peak area in an NMR spectrum depends on several factors. That is the reason why the peak areas in NMR must be compared to the peak area of an internal standard of known concentration to find the accurate concentration of a specific product. Apart from use of internal standard, aliquots based on aqueous solutions need to be added deuterized water (D_2O) in order to suppress the wide peak coming from water.

For each measurement, 1 mM phenol solution was used as internal standard. Phenol stock solution was made by dissolving a corresponding amount of phenol to 0.1 M KOH to obtain 12 mM phenol solution in 0.1 M KOH. All samples have been made up as follows:

- 275 µl of sample
- 25 µl of internal standard (12 mM phenol solution in 0.1 M KOH)
- 25 µl D_2O

This ensured 12 times dilution of the internal standard, to obtain 1 mM peak areas in each measurement. In principle one could go for twice these volumes if necessary, but in this case smaller sample volumes were favored for accurate temperature control.

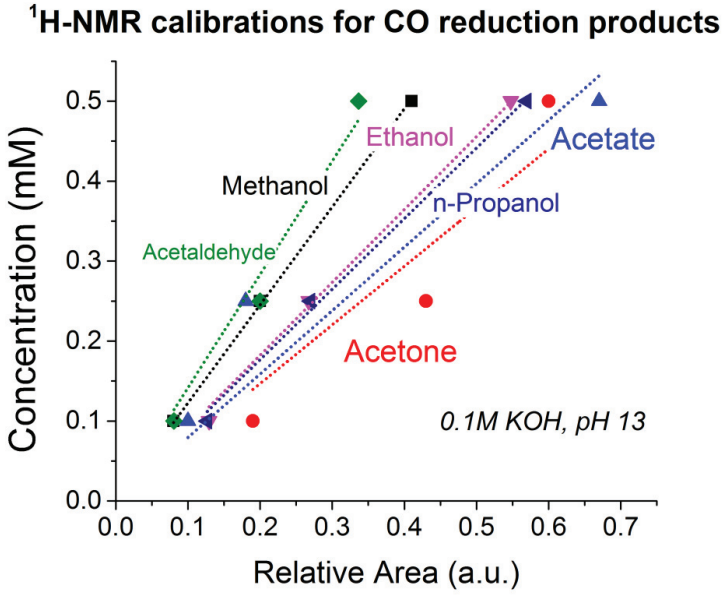

Figure 3.22: [1]H-NMR calibrations for various products of electrolysis in alkaline environment.

Preparation of NMR standards for calibration purposes:

NMR standards are prepared by making solutions of known concentration, mixing them with the internal standards solution, and collecting an NMR spectrum with the same parameters to be used to quantify the actual samples.

All the standards are made in the working electrolyte (most cases 0.1 M KOH). An accurately measured amount of high purity compound (liquid) was added in order to make solutions of 5 mM, or in some cases 10 mM (to match the volume of ca. 50-100 µL for pipette's accuracy). These starting solutions were further diluted to obtain 0.5 mM, 0.25 mM and 0.1 mM solutions, and subsequently used for NMR measurements in order to obtain the calibration curves (see Figure 3.22).

In order to avoid interactions between the different components of the standards, standard solutions were made for each separate possible product, as follows:

- Carboxylic Acids: Formic and Acetic Acid – Since these acids are not stable in this form under alkaline conditions, we used their potassium salts: potassium formate and potassium acetate.
- Alcohols: Methanol, Ethanol, 1-Propanol
- Aldehydes: Acetaldehyde.

Due to high volatility of some of the products, i.e. their high vapor pressures, it was important to work fast and precise when preparing these standard solutions. Some of the components, such as aldehydes may undergo various organic reactions, usually catalysed in acidic or alkaline media.[106] For these reasons, the standard solutions were prepared each time fresh and shipped the same day in thermally insulated packaging containing dry ice. For short-term storage, a fridge or a freezer was used.

Unknown concentration sample analysis

Samples with unknown concentrations of compounds were stored for short-term before the shipping to the NMR facility, where phenol was added as internal standard to reach a concentration of 1 mM. After the measurement, the obtained peaks are identified and integrated and their areas expressed relative to the internal standard peaks areas. The calibration curves are then used to determine the unknown concentrations of the compounds detected.

Sample shipping: Both standard solutions for calibrations and unknown sample as produced were shipped to the NMR facility. Shipping was done using thermally insulated packaging containing dry ice to avoid evaporation of the volatile products or their possible degradation at elevated temperatures.

Equipment details:

^{1}H-NMR, 600MHz, Queen Mary University of London, London, UK.

List of materials and chemicals used in this work:

Electrodes

- Cu – polycrystalline sheet, size: 25.0 mm x 12.5 mm x 1.0 mm, Goodfellow 99.999%
- Pt – wire, 0.5 mm diameter, ChemPar
- Au – polycrystalline disc, PINE Research Instruments, 5 mm diameter, 4 mm.
- Au – polycrystalline sheet, 25.0 mm x 25.0 mm x 0.5 mm, Goodfellow 99,995%
- Au – nanoporous gold-silver leaves, Genuine Gold Leaf, 12Kt White, Monarch, Sepp Leaf Products, Inc.
- Au – mesh, Goodfellow 99.9%
- Au_3Cd – bulk alloy sheet, 12.0 mm x 10.0 mm x 0.5 mm, MaTeck.

Chemicals

- H_2O_2 – Merck, EMSURE, for analysis, 30 %
- H_2SO_4 – Merck, Suprapur, 96 %
- $HClO_4$ – Merck, Suprapur, 70%
- $KOH.H_2O$ – Merck, Suprapur, 99.995 %
- HNO_3 – Merck, Suprapur, 65 %
- HCl– Merck, Suprapur, 30 %
- K_2HPO_4 – Merck, Suprapur, 99.99 %
- KH_2PO_4– Merck, Suprapur, 99.99 %
- $KClO_4$ – Sigma Aldrich, 99.99 %
- Phenol – Sigma Aldrich, purified by redistillation, >99 %
- $CdSO_4.8H_2O$ – Merck, EMSURE (ACS), for analysis
- CuO – Alfa Aesar, 99.9995 %

Product calibrations

- Hydrocarbons gas mixture for GC calibrations - AGA
- Formic acid – Sigma Aldrich, LC-MS Ultra
- Pottasium formate – Sigma Aldrich, purum, p.a. >99 %
- Formaldehyde – Merck, 37 %w/w in water, with about 10 % methanol
- Methanol – Sigma Aldrich, CHROMASOLV, for HPLC, >99.9 %.
- Acetaldehyde – Sigma Aldrich, ACS reagent, >99.5 %
- Potassium acetate – Sigma Aldrich, purum, p.a. >99 %
- Ethanol – Sigma Aldrich, ACS reagent, puriss. p.a. , >99.8 %

- n-Propanol – Sigma Aldrich, CHROMASOLV, for HPLC, >99.9 %.
- Acetone – – Sigma Aldrich, CHROMASOLV, for HPLC, >99.9 %.

Other materials

- Polishing disc – NP MAP, Struers
- Diamond paste – Struers-DK, DP Paste P ¼ μm
- Nafion membranes – Sigma Aldrich, perflourinated membrane 117, 0.007 in. thickness

CHAPTER 4

4. Copper surface morphology and CO_2 electro-reduction catalysis

4.1. Scope of the study - parameters in control of activity and selectivity

Earlier works, in particular those of Hori and coworkers, established that copper is an unique catalyst for production of various hydrocarbons by the electoreduction of CO_2. This chapter builds upon those works to understand the parameters the influence of Cu surface morphology on the selectivity for the reaction.

There are several reports in the literature suggesting that surface morphology may play an important role for the selectivity towards CO_2 reduction, with respect to the competitor reaction, hydrogen evolution.[17,41,60] Moreover, the surface structure may determine exactly which CO_2 reduction products are formed. However, there may be other relevant factors closely related to surface structure that influence the overall product distribution.

Herein, the influence of the surface morphology of polycrystalline copper on its catalytic activity towards electro-reduction of CO_2 was investigated by comparing three different copper electrodes. The surface morphology of the electrodes was studied by scanning electron microscopy (SEM), while the composition was confirmed by X-ray photoelectron spectroscopy (XPS). Cyclic voltammetry was used as an initial evaluation of the catalytic activity of the electrodes. Additionally, bulk CO_2 electrolysis was performed to access the selectivity of the reaction on various surfaces. These catalytic studies showed a strong effect of copper surface morphology on its activity and selectivity for CO_2 electro-reduction. These results are discussed based on the effect of local pH and considering the mechanism insight from density functional theory.[20]

4.2. Copper activation by cycling

We present a study on three different surface morphologies of copper in this Chapter. The preparation of the electropolished and sputtered copper are described in detail in Chapter 3, Section 3.2.4. During the electropolishing procedure the surface impurities and part of the copper itself are oxidised and dissolved into the electrolyte. The protruding parts of the surfaces will dissolve easily, resulting in a smooth clean surface, as reported in scanning tunneling microscopy (STM) studies.[109-111] Sputterring is typically generating a rough surface, with a significant number of defects and undercoordinated sites.[110,112] This treatment should give rise to a slightly rougher surface with respect to the electropolished one. Nanoparticle-covered copper was prepared *in situ* following two-step procedure. First, an electropolished copper electrode was cycled between -0.6 V and +1.15 V vs. RHE at 20 mV/s in N_2 saturated 0.1M $KClO_4$. The pH of the solution was measured before and after the experiment. The initial pH was 7, whereas the final pH was 10.5.

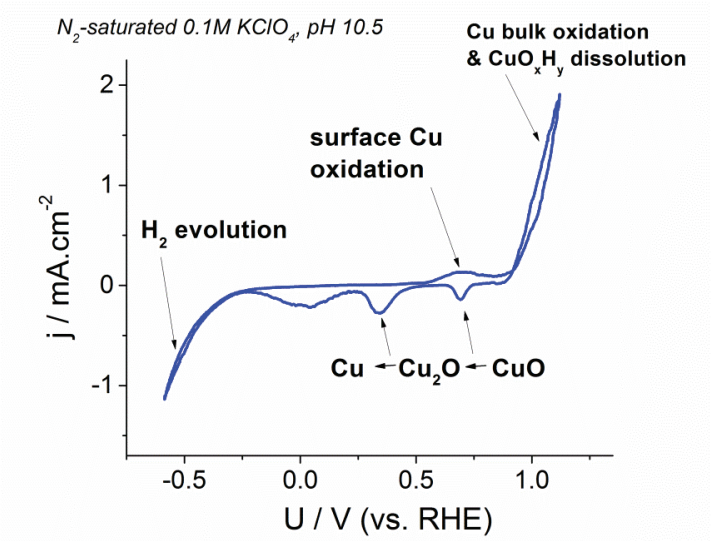

Figure 4.1: Cyclic voltammogram performed on a Cu foil in N_2-saturated 0.1 M $KClO_4$ at pH 10.5 (a first step in the formation of Cu nanoparticles). Current density is obtained by normalizing current to the geometric area of the electrode.

Since the cyclic voltammetry was performed on a non-buffered solution, the bulk pH of the electrolyte shifted from 7 to ~10.5 due to proton consumption during hydrogen evolution reaction at potentials below 0 V vs. RHE.

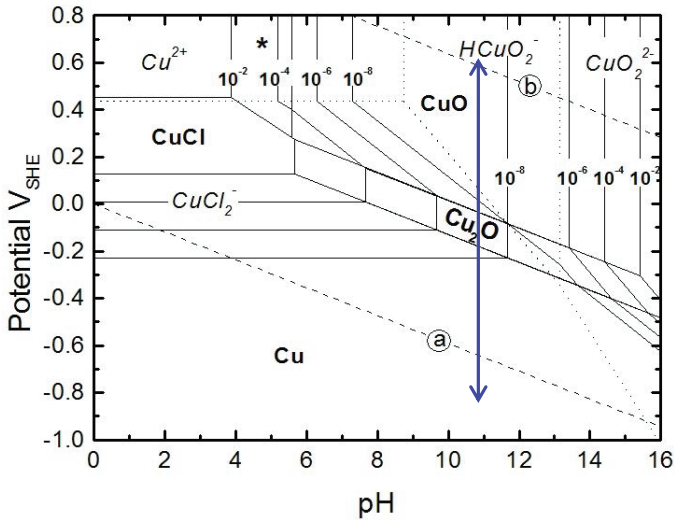

Figure 4.2: Pourbaix diagram for copper in water at 25°C. The blue arrow indicates the potential range where the Cu electrode was cycled during the first step of the nanoparticles formation. (Adapted from[113])

On Figure 4.1 a cyclic voltammogram obtained at pH 10.5 is shown. Based on the Pourbaix diagram[37,113], we can assign the origin of the different peaks. This CV shows a wide oxidation peak starting at +0.55 V vs. RHE, which we attribute to Cu oxidation. The increase in current density at more positive potentials could be assigned to both copper dissolution and porous bulk oxide formation. On the cathodic scan, the first reduction peak, at +0.7 V vs. RHE, most likely corresponds to the reduction of copper (II) oxide phase (CuO) to copper (I) – oxide (Cu_2O), in agreement with the thermodynamic potential predicted by the Pourbaix diagram (Figure 4.2). The second peak at +0.35 V vs. RHE is attributed to the reduction of Cu_2O to metallic Cu. The third reduction peak, centered around +0.05 V vs. RHE, could be assigned to removal of adsorbed hydroxide species before hydrogen evolution occurs. Finally, hydrogen evolution appears as an exponential increase of the cathodic current, which also causes a pH shift towards higher values.

During cycling the electrolyte changed to a yellow-brown colour. This can be attributed to the formation of CuO_xH_y, which is the stable solution species at pH 10.5, as shown in the Pourbaix diagram of copper on Figure 4.2.

Figure 4.3: Cu electrode as received (left) and Cu electrode covered with nanoparticles (right).

In the second step, the copper species in solution were re-deposited by applying a negative potential of -1.3 V vs. RHE in the same $KClO_4$ solution saturated with CO_2. The pH of the electrolyte, measured following this step, had lowered to a value of ~6. This procedure results in the formation of a rough copper surface due to the formation of copper nanoparticles at the surface, giving the electrode a dark appearance as shown in Figure 4.3.

4.3. Surface characterisation

4.3.1. Scanning Electron Microscopy (SEM)

The surface morphology of the different electrodes was analysed using SEM. The results show a clear difference in the roughness of the three samples (Figure 4.4).

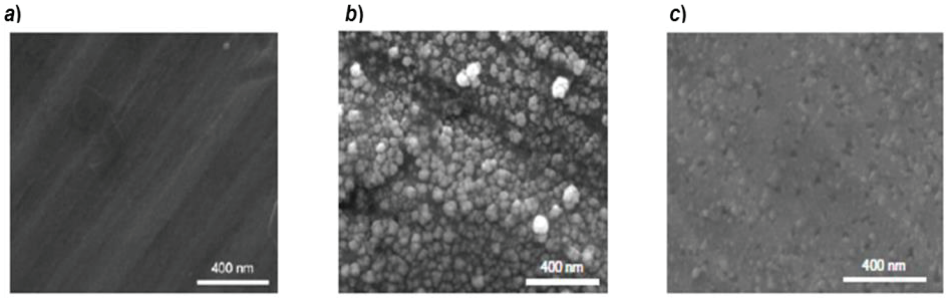

Figure 4.4: Scanning Electron Microscopy of the three electrodes: (a) electropolished surface, (b) copper nanoparticles-covered surface and (c) sputtered surface.

The SEM-image of the electropolished copper (a) shows a smooth surface, where a low number of defects is expected relative to the other two samples. Based on this image and on previous STM studies[114,115], we anticipate that the electropolished surface is mainly dominated by low indexed terraces such as (111) and (100), but also may contain a significant number of undercoordinated surface sites, such as steps and kinks.

The nanoparticles-covered copper image (b) exhibits a surface covered with nanoparticles in size range of 50 to 100 nm. Estimated from the micrograph, the surface area of Sample B is greater than the geometric surface area of the electrode by a factor of 2-3. This surface should contain a significantly larger amount of under-coordinated sites.

Finally, an SEM-image of a sputtered (or sputter-cleaned) copper (c) shows a surface with an intermediate roughness factor ranging between the electropolished and the nanoparticles-covered sample.

4.3.2 X-Ray Photoelectron Spectroscopy (XPS)

The surface composition of the three samples was analysed by XPS. The sputtered copper only shows the signals belonging to clean metallic copper, with practically no oxygen present. This result is not surprising since sputter-cleaned sample has been prepared under Ultra High Vacuum (UHV) conditions and has not been exposed to the air before the XPS measurements. On the other hand, the electropolished and nanoparticles-covered copper, which were prepared electrochemically and transferred to the UHV chamber under ambient conditions, show a clear peak at 352 eV, consistent with the presence of oxygen at the surface (Figure 4.5a). In addition, all three surfaces exhibit the following signals for copper: $Cu\ 2p_{3/2}$ at 932.4 eV and $Cu\ 2p_{1/2}$ at 952.2 eV, corresponding to metallic copper or copper (I) (Figure 4.5b). To distinguish between the metallic Cu and Cu_2O, we focus on the Auger signal[116] provided in Figure 4.5 (c). Consistently with the lack of oxygen, the Auger spectrum of the sputtered sample (green line) corresponds to clean metallic copper. The Auger signal of the electro-polished sample (blue line) also corresponds to metallic copper, whereas the nanoparticles-covered surface (red line) shows an Auger peak associated with the presence of Cu_2O. These last two samples were both transferred in air, suggesting that the formation of Cu_2O is not only related to the air exposure, but as well to the surface preparation method.

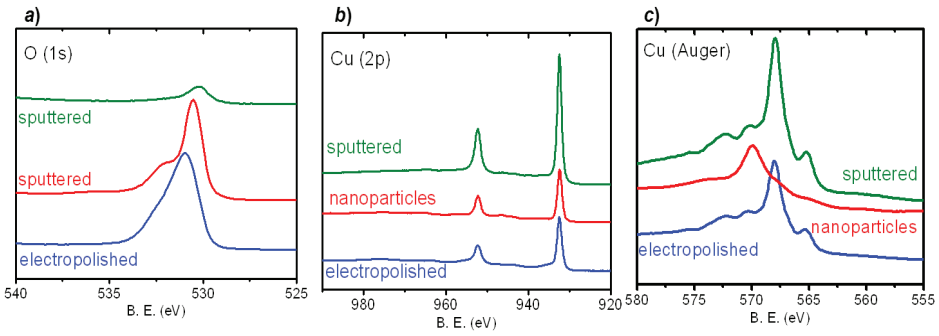

Figure 4.5: XPS spectra of the three surfaces (electropolished, nanoparticles-covered and sputtered): (a) O(*1s*) signal, (b) Cu(*2p*) peak (c) Auger peak.

The electropolished copper was prepared by applying a positive potential in phosphoric acid solution (pH 1.5), in conditions under which, according to the Pourbaix diagram of copper, Figure 4.2, the stable species should be Cu^{2+} and no oxide species are expected. The nanoparticles-covered copper was prepared in 0.1 M $KClO_4$ solution in alkaline pH range, where Cu_2O can be formed. Prior to the XPS measurements all samples were rinsed using degassed *MiliQ* water.

From these XPS measurements we cannot conclude whether the nanoparticles remained oxidised even after the re-deposition step and during reaction, or simply were oxidised following the reaction at 0 V vs. RHE in alkaline solution or by the exposure to air upon sample transfer to the UHV chamber.

Aiming to clarify the stage at which Cu_2O was formed, we studied the Auger signals on the sputtered sample in the following cases: as prepared under UHV conditions, upon air exposure for 30 min. and after being dipped into Ar-saturated alkaline solution of 0.1 M $KClO_4$ and transferred in air afterwards (Figure 4.6). The XPS spectra of these three samples show that the exposure of copper sheet to air leads to a slightly oxidised surface. On the other hand, dipping of the sputtered sample into the alkaline electrolyte and transferring it in air clearly forms significant amounts of Cu_2O on the surface. The last treatment resembles the nanoparticle formation treatment since in both cases the Cu sheet is in contact with alkaline electrolyte and air.

This means that the XPS measurements presented here are insufficient to determine whether there was also Cu_2O formation while the nanoparticles were prepared. XPS would only be able to identify the oxidation state if it was performed *in-situ*[117], or if the sample was transferred from the electrochemical cell to vacuum under a clean, inert atmosphere.[118] Unfortunately, such measurements are beyond the scope of the current investigation. It is highly unlikely, however, that the active phase is a form of copper oxide, rather than metallic Cu, as there is a significant driving force for the reduction of copper

oxide under reaction conditions, i.e. ~ -1.5 V of overpotential relative to the Nernst potential of the reduction of Cu_2O to metallic Cu at pH ~6 (at -1.1 V vs. RHE). *In situ* STM studies have shown that at the most ~-1 V overpotential is required to completely reduce Cu oxide to form ordered Cu(111) terraces in 0.1 M NaOH[109], suggesting that at our working conditions (~-1.5 V overpotential) the surface should be fully reduced. Moreover, Le et al.[119] found that a Cu-oxide catalyst was reduced to metallic Cu at an overpotential of -1.3 V relative to the Cu/Cu_2O reversible potential in CO_2 saturated 0.5 M $KHCO_3$.

Figure 4.6: Auger peak for a sputtered sample as prepared, sputtered sample after its exposure to the air for 30

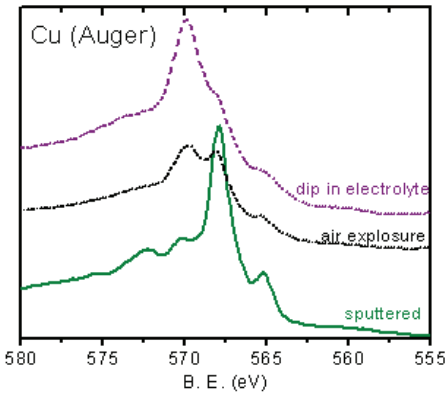

min and sputtered sample after immersion into alkaline electrolyte. The results indicate that Cu_2O is mainly formed when copper is immersed into the alkaline electrolyte, however its transfer in the air does not exclude

4.4 Electrochemical characterisation

The three surfaces were also characterised by cyclic voltammetry in CO_2 and N_2 saturated 0.1M $KClO_4$. Since the experiments were carried out in a non-buffered solution, the pH value had to be monitored throughout all the steps of the electrochemical process. The as-made electrolyte has a pH of 7±0.5. The electrolyte was cleaned by pre-electrolysis to remove traces of impurities by applying -1.0V to a Pt wire during 2 hours. After the pre-electrolysis, the pH shifted to values close to 8 due to proton consumption. As we are studying a reduction process, the samples were cycled to negative potentials where hydrogen evolution takes place, resulting in a decrease of proton concentration nearby the electrode surface. Surprisingly, the protons formed at the counter electrode do not diffuse fast enough from one compartment to the other, causing a shift of the electrolyte bulk pH value in the working compartment to higher values. As a result of this pH change, the CVs in N_2 were recorded at

pH values of 11±0.5. This demonstrates the importance of keeping track of the pH value of the electrolyte when working with non-buffered solutions, especially when high current densities are involved.

When the solution was saturated with CO_2, the pH value shifted again to 6±0.5, due to the formation of carbonic acid. It is well known that CO_2 reacts with water to form H_2CO_3, a diprotic acid that is in equilibrium with the deprotonated species[79] (see equations 2.3 to 2.5 in Section 2.2).

To make a fair comparison of the onset reduction potentials in saturated N_2 and CO_2 electrolyte, it is crucial to plot the cyclic voltammograms in the reversible hydrogen electrode (RHE) potential scale, to account for the pH difference. According to the Pourbaix diagram of Cu (Figure 4.2) these peaks appear at the same potential against RHE regardless of the pH. The Cu(I)-oxide formation peak is easily identified in the CVs performed in N_2 saturated electrolyte, where an oxidation process due to the formation of copper oxide (I) is observed at around 0.65 V and its reduction is observed during the cathodic scan at ~0.3 V vs. RHE. The previous potential values are consistent with the thermodynamic potential of Cu to Cu_2O at 0.47 V vs. RHE.

Both CO_2 electro-reduction and hydrogen evolution reaction (HER) are occurring at negative potentials relative to the reversible hydrogen electrode. When the electrolyte is saturated with N_2, the cathodic current observed below 0 V vs. RHE can only be attributed to hydrogen evolution. Figure 4.7b shows the N_2 voltammograms for the three studied surfaces, where it can be seen that the onset potential for the HER is clearly affected by the surface morphology. Comparing the potentials at fixed current density of -5.0 $mA.cm^{-2}$, we can observe that the electropolished copper electrode needs a potential of -0.75 V vs. RHE to produce such currents. On the other hand, the other electrodes, sputtered and nanoparticles-covered, can achieve these current densities at more positive potentials.

Moreover, we can also observe a difference in current densities at fixed potentials. Since the currents are only normalized by geometric area of the electrodes and not by the active surface area, one could think that only this explains the increasing current densities on rougher surfaces. However, the surface area contribution is not that much if we consider that the roughness for the Ar-sputtered and nanoparticles-covered sample differ by factors of 1-2 and 2-3 compared to the electropolished sample, respectively.

However, the main proof of the activity differences among the studied surfaces should be provided by the bulk CO_2 electrolysis measurements, which can indicate additionally differences in selectivity.

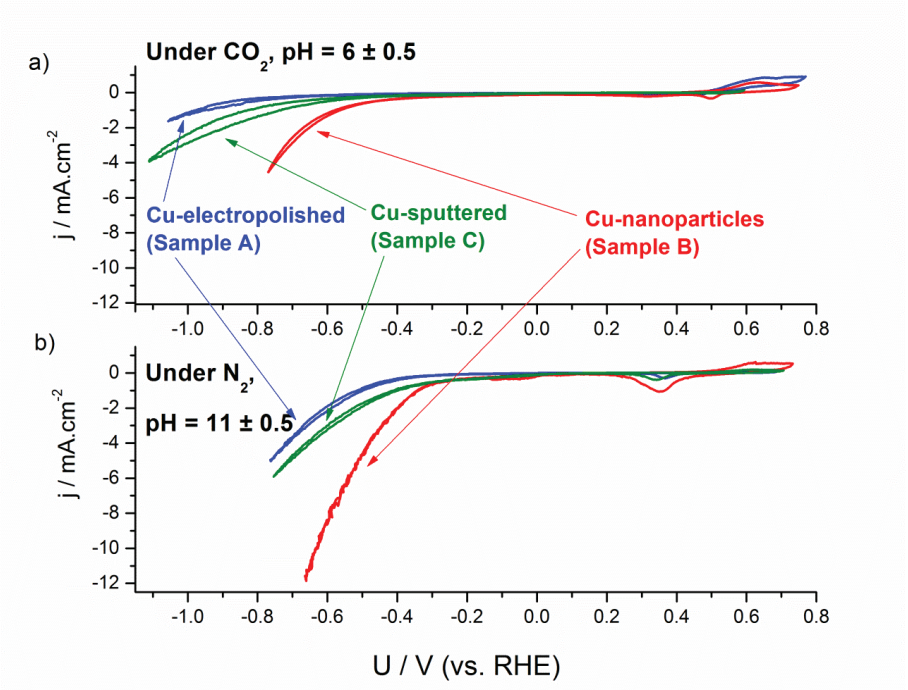

Figure 4.7: Cyclic voltammogram of the electropolished copper surface, copper-nanoparticles-covered surface and sputtered copper surface in 0.1 M $KClO_4$ purged with CO_2 (a) and N_2 (b). The current density is obtained by normalising the current to the geometric area of the electrode.

When the CVs are recorded under CO_2 (pH 6.0±0.5), we observe a cathodic current due to a combination of various reduction processes, HER and CO_2 electro-reduction reactions (Figure 4.7a). On the CVs recorded under CO_2, the onset potentials (compared, as previously, at -5 mA.cm^{-2}) are moving towards more positive potentials when the surface is rougher.

Furthermore, the onset potentials on all surfaces in CO_2 saturated neutral solutions are all more negative than the corresponding ones in N_2 saturated alkaline solutions. Neglecting the differences in HER in different media, which do exist, these results could indicate the adsorption of the species during CO_2 reduction, which block the active sites for hydrogen evolution, thus suppressing it. According to Hori et al[56] the CO_2 reduction reaction proceeds with the formation of adsorbed CO as an intermediate product.

At low overpotentials the Faradaic current is provided by two competing reactions[15,42,56]:

$$CO_2 + 2H^+ + 2e^- = CO + H_2O \quad (4.1)$$

$$2H^+ + 2e^- = H_2 \quad (4.2)$$

However, at high overpotentials, further reduction of adsorbed CO may occur to give variety of products – a mixture of hydrocarbons.

4.5 Electrocatalytic results

4.5.1 Surface morphology effect on product distribution

For purpose of studying the activity and selectivity of the three copper surfaces as electro-catalysts for CO_2 reduction, we employed chronoamperometry (applying a constant potential and measuring current) in CO_2 saturated electrolyte (0.1 M $KClO_4$). As outcome, the gaseous products are detected and quantified after the reaction using gas chromatography.

On Figure 4.8 current (Faradaic) efficiencies (a) and partial current densities (b) for different gaseous products measured after 15 min reactions at -1.1 V vs. RHE are shown. The currents are normalised to the geometric area of the electrodes.

After this short reaction time, it was not possible to detect any liquid products, given the high detection limits of the liquid chromatography method (HPLC) we employed. In order to quantify the liquid products, we ran a reaction in duration of 24 hours on the electropolished sample. According to the subsequent HPLC analysis, the only identified liquid product was formate, produced with a faradaic efficiency of 7.5 %.

On Figure 4.8 (b) one can observe some differences in catalytic activity of the three surfaces. The nanoparticles-covered sample exhibits the highest total current densities (nanoparticles-covered sample ~-5.4 $mA.cm^{-2}$, sputtered ~-3.5 $mA.cm^{-2}$ and electropolished ~-2.3 $mA.cm^{-2}$) as expected from previous considerations on Figure 4.7. If we focus on the activity for hydrogen evolution reaction (Figure 4.8b), we notice similar values for all three samples. However, taking into consideration that the normalisation is performed only relative to the geometric area, we have lower activities towards HER on sputtered and nanoparticles-covered samples when we consider the real active area. Looking at other products in the same plot, especially ethylene and CO, one can notice their partial current densities increase on rougher surfaces. This is not only due to their slightly higher roughness factors relative to the electropolished sample, but also due to the activity enhancement towards the reduction of CO_2 on undercoordinated sites.

***a*) Faradaic Efficiencies after 15 min. reaction at -1.1 V vs. RHE**

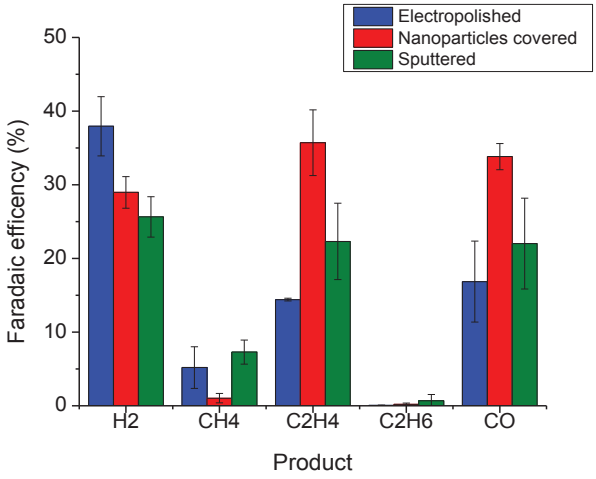

***b*) Partial Current Densities after 15 min. reaction at -1.1 V vs. RHE**

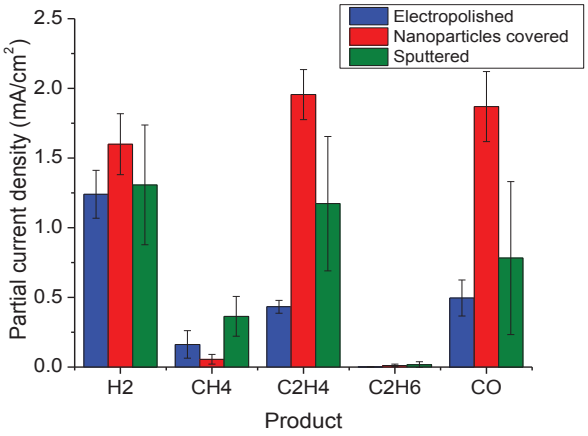

Figure 4.8: (a) Faradaic Efficiencies and (b) Partial Current Densities for the products of CO_2 electro-reduction on three surface morphologies of copper in CO_2-saturated 0.1 M $KClO_4$ at -1.1 V vs. RHE.

To illustrate this further, one should focus on the analysis of the reaction products in terms of current efficiencies (Figure 4.8a). These current (Faradaic) efficiencies are obtained as a ratio of partial current densities of each product and the total current density within a single bulk electrolysis measurement. Performing the bulk CO_2 electrolysis measurements on rough surfaces obviously decreases the selectivity towards hydrogen production and favors CO_2 reduction. In addition,

differences in surface morphology induce changes of selectivities for various products. The electropolished surface produces C_2H_4 with the Faradaic efficiency of 14 % and CH_4 with 5 %. On the other hand, on the nanoparticles-covered surface ethylene formation is enhanced to a 36 % Faradaic efficiency, while the selectivity towards methane fell to only 1 %. Sputtered copper, having an intermediate roughness between that of electropolished and the nanoparticle-covered sample, exhibits intermediate selectivity towards C_2H_4 (26 %) and the highest Faradaic efficiency towards CH_4 (8 %) of all three surfaces. In addition, the methane/ethylene ratio is different on the studied surfaces, our results indicate that the formation of CO and the formation of ethylene follow the same trends. Higher CO production seems to favor the formation of ethylene, suggesting a correlation of these two products.

Another noteworthy bulk electrolysis result is that the ethylene formation is favored over methane on all studied surfaces. Our results also show higher current efficiencies for ethylene relative to methane on roughened Cu surfaces. Our observations are consistent with already published results suggesting a dependence of the catalytic activity of copper on its surface morphology: Branco and co-workers showed that by modifying a copper electrode through copper electrodeposition, i.e. making it rougher, methane formation was suppressed.

Hence, discussions above suggest that different facets present in each surface play a key role in the catalytic activity. Results from Hori and coworkers[41,52] indicate higher selectivity of steps towards ethylene production, while terraces are more selective towards the formation of methane.

4.5.2 DFT insight into surface morphology influence on catalytic activity

In order to obtain better understanding about the differences in catalytic activity of the various crystal orientations, we can use the input from theoretical calculations based on density functional theory (DFT). DFT studies on the HER and CO_2 reduction to methane at different copper facets (fcc(111), fcc(100) and fcc(211)) provide insight into the reaction pathways based on the free energy diagrams of reactants, reaction intermediates and products.

We studied the CO_2 electrochemical reduction using the mechanism proposed by Peterson et al[50], where the elementary proton-electron transfer steps have been proposed for the process of reducing CO_2 to methane on a (211) copper surface. They have proposed that the rate limiting step is the reduction of *CO to *CHO. Based on these calculations, we used the free energies of the transformation of *CO to both *CHO and *COH with the aim to understand the different catalytic activity of different copper surfaces. Figure 4.9 compares the energetics of *CO protonation on the

(111), (100), and (211) surfaces at 0 V vs. RHE. It can be seen, that according to the thermodynamic analysis, on all surfaces the route to *CHO is favored over the route to *COH. Additionally, the (211) surface facilitates the formation of *CHO relative to (111) and (100) facets.

These results indicate that if the potential limiting step in hydrocarbon formation is the protonation of *CO to *CHO, roughened surfaces should be more active towards CO_2 reduction, thus explaining the higher current densities towards CO and ethylene obtained on the nanoparticles-covered sample. One should however bear in mind that this is purely a thermodynamic analysis and no kinetic barriers were considered.

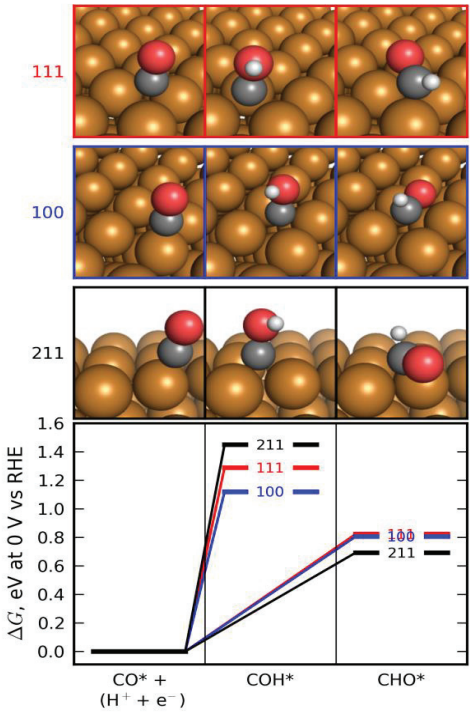

Figure 4.9: Calculated free energies, at 0 V vs. reversible hydrogen electrode (RHE), of the protonation of adsorbed CO to form adsorbed COH or CHO on the (111), (100), and (211) facets of the face-centered cubic copper crystal. The protonation proceeds most favorably on the (211) facet to the CHO adsorbate.

One possible explanation of the high selectivity towards C_2H_4 and the suppressed CH_4 formation on the rough surfaces could be that rough surfaces have a higher coverage of C-containing species, which facilitates the C-C coupling.

For HER, the only intermediate is adsorbed hydrogen (*H), meaning that the theoretical activity of a given surface depends only on the free energy of *H. The work of Durand et al[120], (Figure 4.10), predicts that the stepped sites (211) have higher activity for HER than the (111) and (100) terraces, since adsorbed hydrogen intermediate is closer in free energy to the initial and final states of reaction

on Cu(211) with respect to Cu(111) and Cu(100). The prediction of higher activity for a stepped surface is in agreement with the higher current obtained during cyclic voltammetry of the nanoparticles-covered sample, which has a higher density of steps and kinks. However, these thermodynamic considerations may after all have less effect on the onset potentials in this system due to a possible OH poisoning of the surface. Namely, the copper surface might be inaccessible for hydrogen to adsorb in the region from 0 to -0.31 V vs. RHE. Figure 4.11 shows how OH adsorption on Cu(211) and Cu(100) surfaces proceeds spontaneously at 0V vs. RHE, thus blocking the surface. Calculations suggest that a potential of -0.31 V vs. RHE is needed to remove the adsorbed OH from the step edge. This is in accordance with the third reduction peak observed during the first part of the preparation of nanoparticles-covered sample (Figure 4.1).

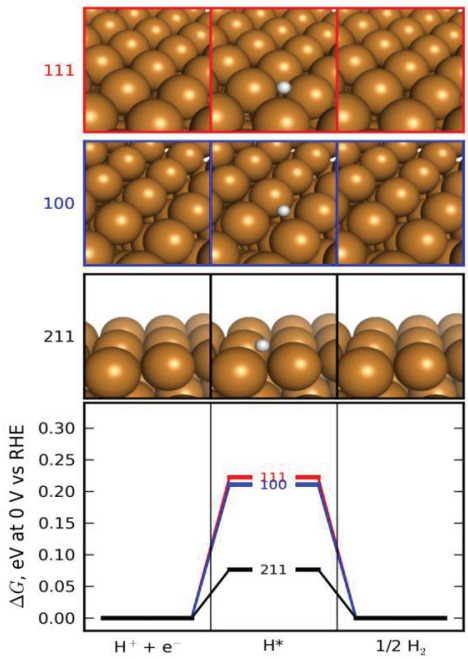

Figure 4.10: Calculated free energies of the hydrogen evolution reaction on the (211), (111), and (100) surfaces of a Cu fcc crystal.

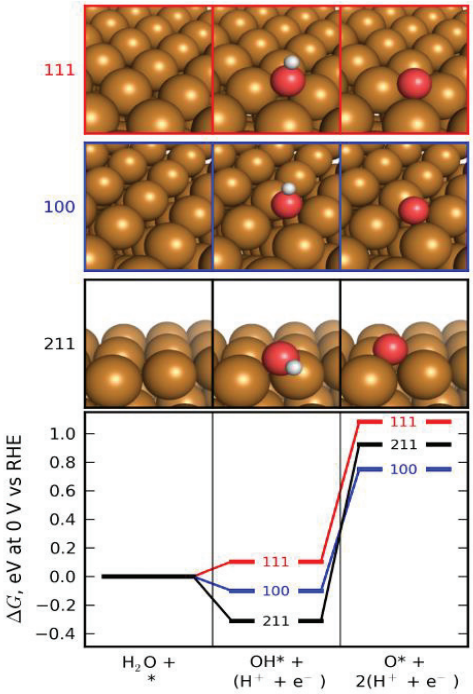

Figure 4.11: Calculated free energies of water oxidation on the (211), (111), and (100) surfaces of a Cu fcc crystal. According to these calculations, a potential of -0.31 V vs RHE is necessary to reduce the (211) step sites to enable hydrogen evolution.

Extremely rough surfaces like these studied by Kanan and co-workers[48], where high current densities are obtained, the effect of the local pH should play a more important role than on moderately roughened surfaces. On the surfaces studied here we could anticipate a significant variation in the local pH, which can be attributed to a very low buffer capacity of the electrolyte, rather than to a high total current density. The experimental observations we obtained on the nanoparticle-covered surface illustrate how low buffer capacity of electrolyte, even with insignificant current increase, can influence the selectivity of the reaction, favoring ethylene formation relative to methane formation.

The increase in production of compounds containing two carbon atoms (such as ethylene, ethane) on rough surfaces can partially rationalised considering the effect of changes in local pH value of the electrolyte. Rough surfaces exhibit higher geometric partial current densities relative to the the smooth ones. Hence, a higher local pH values can be assumed on the rough in comparison to the smooth surfaces, which consequently inhibits the production of methane. The accurate value of the local pH can vary depending on the system since it is established as an effect of high current densities of proton consuming reactions, the buffer capacity of the electrolyte and mass transport in the solution (diffusion layer thickness).

4.6 Summary and conclusions

Summarising, the experimentally observed improvements in CO_2 reduction activity relative to competitive reaction - hydrogen evolution - can be understood as a consequence of higher catalytic activity of the undercoordinated sites towards the reduction of CO_2. Nevertheless, the changes in ratio among the CO_2 reduction products can partially be rationalized by taking into account the effect of the change in the local pH value of the electrolyte in the catalyst surface vicinity. This may be called a side effect of an increase in roughness, leading to the increase in total currents, which consume protons and locally changes the proton concentration to significant extent. Nevertheless, it is an additional catalytic effect, whose intrinsic nature is still not well understood. Further mechanistic studies are necessary for better understanding of the phenomena at the electrode-electrolyte interface.

i. This work introduces a facile *in situ* electrochemical method for activation of polycrystalline copper electrodes and taking control of selectivity towards the production of ethylene by surface roughening.

ii. Surface pretreatment, thus surface morphology of copper electrode affect both activity and selectivity for the CO_2 electroreduction in aqueous solutions. Rough surfaces exhibit higher activities and higher selectivity toward CO_2 reduction products, in particular ethylene. On the other hand, rough surfaces exhibit lower selectivity towards the production of hydrogen.

iii. Working with neutral non-buffered solutions requires extreme care to establish the correct pH under working conditions. The bulk pH in a CO_2 free electrolyte is extremely sensitive to high current densities, which affects the equilibrium between H_2O, H^+ and OH^-. In CO_2 saturated electrolyte the formation of carbonic acid permits to keep the bulk pH constant. The buffer capacity of the electrolyte, however, would be low causing important differences in local pH, which should be taken into account when interpreting the reactions.

iv. The effect of surface morphology can be explained by considering the different facets present at each surface. Smooth surfaces contain predominately low index facts such as (111) and (100), while roughened surfaces have a greater number of undercoordinated sites. According to DFT calculations, undercoordinated sites simulated using a (211) surface are more active towards HER and CO_2 reduction. Further modeling of different facets may provide more insight to the effect of coordination on the activity of stepped surfaces.

v. To get a better understanding of the difference in selectivity towards methane an ethylene, it is necessary to make a detailed mechanistic study of the C-C bond formation and consider other factors such as the local pH.

CHAPTER 5

5. Tuning the catalytic activity and selectivity of copper for CO_2 electro-reduction via overlayer structures

The focus of this chapter is on the catalytic activity and selectivity for the electrochemical CO_2 reduction of underpotentially deposited overlayers of copper on platinum single crystals. We studied smooth surfaces – Pt(111) and Cu/Pt(111), as well as surfaces with higher density of steps – Pt(211) and Cu/Pt(211) with aim to explore their catalytic behavior for CO_2 electro-reduction. An expanded copper surface has a higher reactivity relative to the pure copper.[55] Additionally, at the outset we anticipated that a Cu monolayer on Pt(111) could be more stable than a bulk Cu(111) single crystal, which can reconstruct and facets under reaction conditions.[111] Comparing (111) and (211) orientations, we expect to gain more knowledge about the role of undercoordinated sites in CO_2 electro-reduction.

The catalytic activity and selectivity of the copper overlayers were investigated using electrochemical methods: cyclic voltammetry and bulk electrolysis. Furthermore, we present experiments using electrochemical scanning tunneling microscopy (EC-STM) useful for studying stability of the overlayers under reaction conditions.

More details about this work can be found in PhD thesis of Ana Sofia Varela.[121]

5.1. Electrochemical preparation and characterisation of copper overlayers on platinum single crystals

For the present study, we used Pt(111) and Pt(211) single crystals, in size of 10 mm in diameter. Intentionally, we chose electrodes with larger surface area in order to achieve high currents and thus facilitate the quantification of the products.

Prior to carrying out any reactions, single crystals of platinum were thermally annealed at 850±20 °C in gas mixture containing 5 % of H_2 in Ar for 3 min, followed by the annealing in a gas mixture consisting of 1% CO in Ar for 1 min. Following annealing, single crystals were studied using cyclic voltammetry in Ar-saturated 0.1 M $HClO_4$ at pH 1, between 0.05 V and 1.0 V vs. RHE (Figure 5.1).

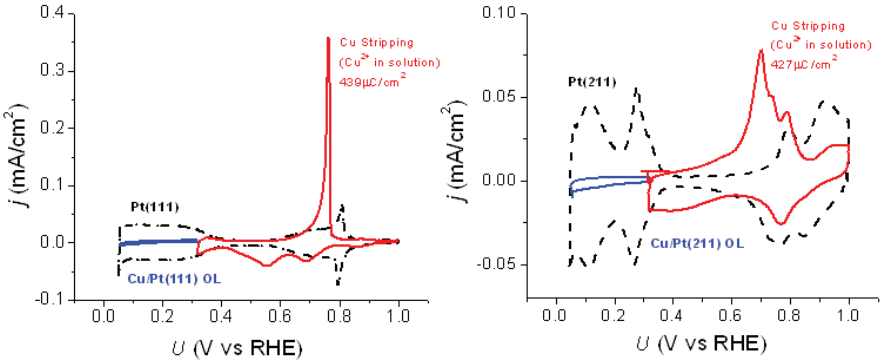

Figure 5.1: Characterisation of Pt single crystals and preparation of the corresponding Cu overlayers by cyclic voltammetry (CV). Pt(111) is shown on the left side and Pt(211) on the right side. Colour legend: (1) *black dashed line* – CVs on Pt(111) and Pt(211) in 0.1 M $HClO_4$ at 50 mV/s following thermal annealing; (2) *red solid line* – CVs on Pt(111) and Pt(211) in 0.1 M $HClO_4$ solution containing 3 mM $CuClO_4$ at 20 mV/s after holding the potential for 2 minutes at 0.32 V vs. RHE (charges for Cu upd on Pt(111) and Pt(211) are 439 $\mu C.cm^{-2}$ and 427 $\mu C.cm^{-2}$, respectively); (3) *blue solid line* – CVs in Cu-free 0.1 M $HClO_4$ solution at 50 mV/s on Cu/Pt overlayers following Cu deposition. Figure made by Ana Sofia Varela.

The cyclic voltammograms in $HClO_4$ for both surfaces are consistent with the literature.[122,123] In the potential region between 0.05 V and 0.4 V, traditionally known as the hydrogen *upd* region, we observe clearly different peaks for the two crystal orientations – Pt(111) exhibits a broad feature, flat at the top, while on Pt(211), we distinguish two peaks centered at approximately 0.1 V and 0.3 V. At

higher potentials, Pt(111) exhibits a characteristic reversible peak pair correlated to the *OH adsorption between 0.6 V and 0.8 V.

Copper was deposited by underpotential deposition (*upd*)[33,124] onto the Pt crystals. To ensure the formation of a single monolayer, the potential was kept at 0.32 V vs. RHE, for 2 minutes. These conditions should lead to the formation of a pseudomorphic Cu overlayer on Pt. The amount of Cu deposited on Pt was controlled by integration of the charge necessary for the anodic dissolution of the Cu overlayer when potential is swept positively (see red solid line in Figure 5.1).

Formation of a pseudomorphic overlayer during Cu *upd* means that each Cu atom positions on top of a Pt atom, resulting in a Cu surface with retained lattice parameter of Pt. Since lattice parameter of Pt is larger compared to Cu, the Cu/Pt overlayer is expanded relative to pure Cu. On such an overlayer structure, the reactivity of copper is modified due to both ligand and strain effects. As discussed in Chapter 2, the d-band of Cu is shifted upwards when deposited onto Pt. This makes the copper surfaces under tensile strain more reactive with respect to the copper surfaces in bulk copper electrodes.

Figure 5.1 shows the oxidation ("stripping") CV of copper, after holding the potential at 0.32 V for two minutes in containing perchloric acid containing 3 mM $Cu(ClO_4)_2$. Copper dissolution appears shifted by ~0.42 V positively than the Nernst potential for Cu oxidation on Pt(111), being consistent with Cu overlayer being more stable on Pt substrate. The CV exhibits an extremely sharp feature suggesting a strong attractive interaction between copper atoms.[125] After removal of the first copper atom, the whole overlayer becomes less stable and becomes imminently oxidised, in very narrow potential range. On the other hand, on Cu overlayer on Pt(211) a broad anodic feature is recorded. Furthermore, Cu oxidation starts already at 0.4 V, which is expected on stepped sites.[126] Following the formation of the Cu overlayer by Cu *upd*, the Cu containing solution was removed and exchanged to Ar-saturated 0.1 M $HClO_4$ under potential control, at 0.32 V vs RHE. The overlayers of Cu on Pt were characterised using cyclic voltammetry, in potential range between 0.05 and 0.32 V where we can observed suppression of the hydrogen *upd* region, typically seen on Pt.[127]

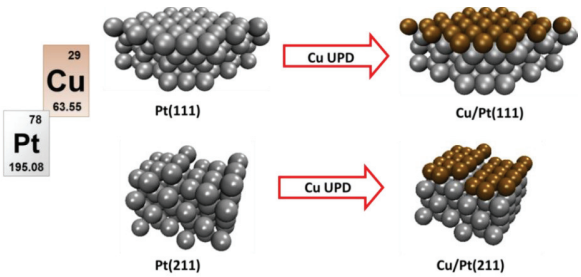

Figure 5.2: Schematic representation of the formation of the Cu overlayers on Pt(111) and Pt(211) single crystal. Figure made by Ana Sofia Varela.

5.2 CO_2 bulk electrolysis on Cu overlayers on Pt single crystals

The potentiostatic bulk electrolysis experiments were conducted in CO_2-saturated 0.1 M $KHCO_3$, at potentials in range from -0.7 V to -1.3 V vs. RHE, with each experiment lasting 15 minutes. For each measurement at a different potential, a fresh Cu overlayer was prepared to ensure that the adsorbates from the previous reaction do not influence the catalytic results. These bulk electrolysis measurements were compared with the obtained results on polycrystalline Cu in the same setup.

Pt(211), used as a catalyst, produces hydrogen as the major product, accompanied with traces of methane (Faradaic efficiencies less than 0.2 %). On the other hand, during electrolysis on Cu/Pt(111) and Cu/Pt(211), hydrogen and methane were detected as major products, as well as traces of ethylene (Faradaic efficiencies below 0.6 %). The presence of CO was not confirmed, however, the detection limit of the GC method does not reach below volumetric CO concentrations lower than 0.1 %. Therefore, when using a large volume electrochemical cell (ca. 200 ml), as the one used in the single crystal studies, it was not possible to detect any CO unless its partial charge reaches 1.7 C, corresponding to the partial current densities of 2.4 $mA.cm^{-2}$ (for electrolysis of 15 min). Hence, the unbalanced Faradaic efficiencies are attributed mainly to the undetected CO, as well as to $HCOO^-$ in the liquid phase.

Figure 5.3 shows the potential dependence of H_2 and CH_4 production in terms of both Faradaic efficiencies and partial current densities. The high dispersion of the results is partially caused by wetting of the edges of the crystal. The bubbling during the electrolysis poses additional challenge in keeping the edges of the electrode dry, so in some cases, they contribute to the total current. Since the edges consist of Pt that efficiently produces hydrogen, we expect that the crystal edge wetting may be the reason for higher hydrogen partial current densities.

The analysis of the plots in Figure 5.3 indicates Pt(211) as the most active surface for HER, while polycrystalline copper exhibits lowest HER activities. In addition, Pt(211) does not catalyse formation of any other products, being almost 100 % selective towards the hydrogen evolution. On the other hand, selectivity towards H_2 on polycrystalline copper is in range of 40% to 80 % and depends strongly on the potential, reaching a minimum value at -1.0 V. The H_2 selectivity of Cu/Pt (111) and Cu/Pt(211) are intermediate and are less dependent on potential, with Faradaic efficiencies of around 80%.

On the overlayers, CH_4 begins to form at around -0.7 V, as on polycrystalline copper, with increasing Faradaic efficiencies and partial current densities at more negative potentials. However, the activity of the overlayers is much lower than on polycrystalline copper.

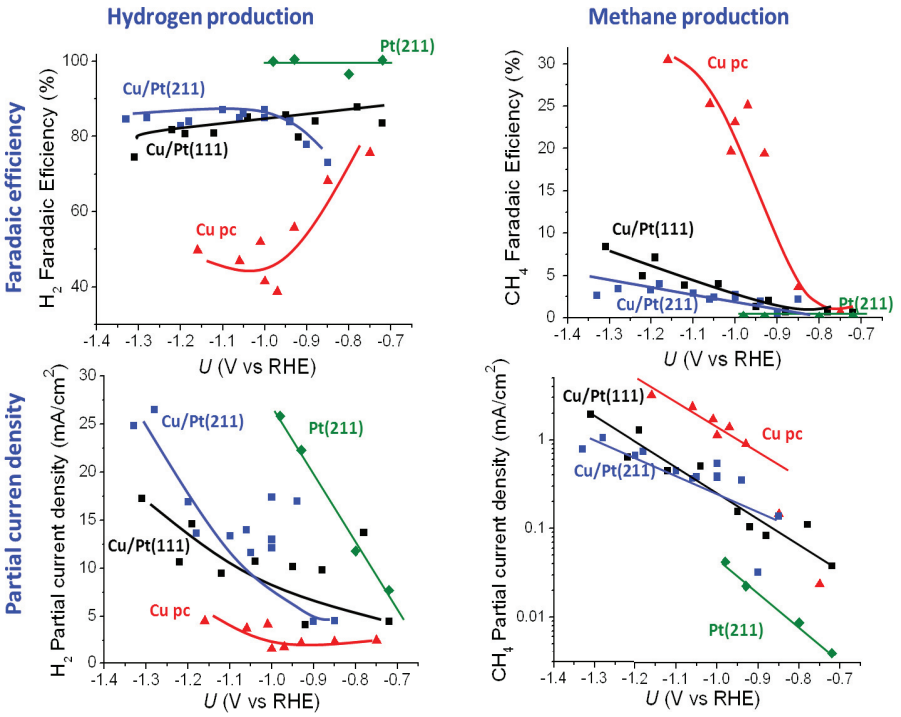

Figure 5.3: Faradaic efficiencies and partial current densities towards CH_4 and H_2 as function of potential on Pt(211) (green), Cu/Pt(211) (blue), Cu/Pt(111) (black) and polycrystalline Cu (red) after 15 minutes of bulk electrolysis in CO_2 saturated 0.1 M $KHCO_3$ (Lines are shown to guide the eyes). Figure made by Ana Sofia Varela.

5.3 Post electrolysis surface characterisation

5.3.1 Angle Resolved XPS

In order to confirm the catalyst surface composition during CO_2 reduction, we employed angle resolved X-Ray photoelectron spectroscopy (XPS) on Cu/Pt(111) after 1 hour of electrolysis. The depth profile shown in Figure 5.4 indicates presence of the electrolyte constituents (K, C and O) at the very surface. Metallic Pt and Cu were detected on the surface in similar ratio, suggesting no other unexpected contaminants. Nevertheless, this result is more consistent with both Cu and Pt being at the surface, rather than only Cu, as initially anticipated for pseudomorphic overlayers. This XPS analysis, however, is not sufficient to conclude about the surface structure. For this reason, further studies were carried out on Cu/Pt(111) under reactive conditions.

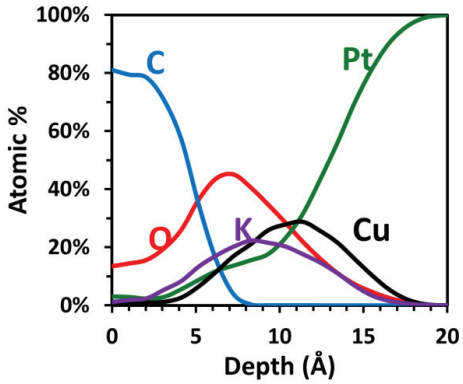

Figure 5.4: Depth profile obtained by Angle resolved X-ray Photoelectron Spectroscopy on Cu/Pt(111) after 1 hour of bulk CO_2 electrolysis. Figure made by Paolo Malacrida.

5.3.2 Scanning Tunneling Microscopy (STM) studies

An electrochemical scanning tunneling microscope (EC-STM) was employed to study, in particular, the effect of CO on the structure of the Cu overlayer on Pt(111). Figure 5.5 shows an STM image, obtained on Cu/Pt(111) in Ar-saturated 0.1 M $HClO_4$ at ~0.26 V vs. RHE. Recording STM images at more negative potentials was challenging due to HER occurring on the studied surface and on the STM tip.

Since the surface may suffer certain structural changes during HER, the STM images were recorded after cycling the potential to ~-0.4 V. The obtained image shows a smooth surface, consistent with a pseudomorphic Cu overlayer on Pt(111).

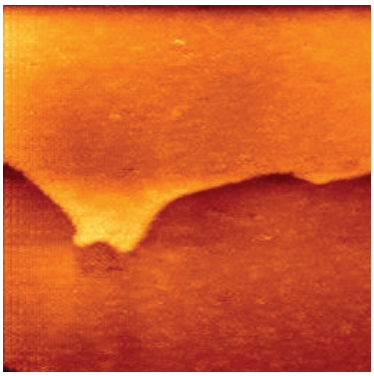

Figure 5.5: EC-STM image of Cu/Pt(111) in Ar-saturated 0.1 M $HClO_4$, image $(337.32\ nm)^2$, E = 0.2 V vs. NHE (~0.26 V vs. RHE), U_B = 249 mV, I_T = 1 nA. Figure made by Christian Schlaup.

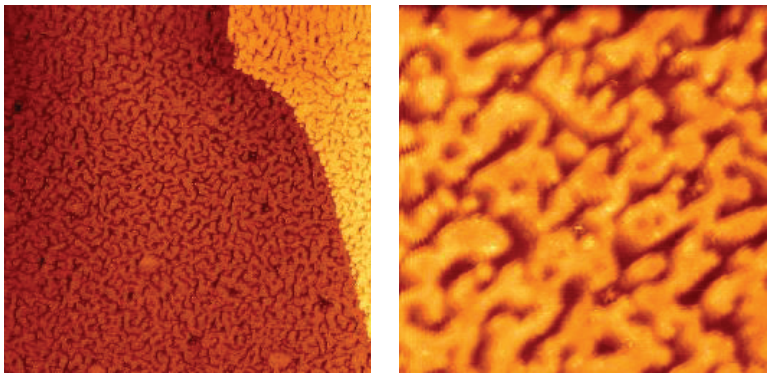

Figure 5.6: EC-STM image of Cu/Pt(111) in CO-saturated 0.1 M $HClO_4$: a) $(346.82\ nm)^2$, E = 0.25 V vs. NHE, U_B = 9 mV, I_T = 3 nA b) $(111.49\ nm)^2$, E = -39 mV vs. NHE, U_B = 102 mV, I_T = 1 nA. Figure made by Christian Schaup.

On the other hand, the STM images of Cu/Pt(111) obtained in CO-saturated 0.1 M $HClO_4$, as shown in Figure 5.6, clearly suggest changes in surface structure, from smooth to granulate. From these EC-STM images, we can deduce, that for Cu/Pt(111), copper remains on the surface when exposed to CO at the working potentials. However, the structure of the overlayer is no longer pseudomorphic, but more likely corresponds to a disordered layer with interatomic distances between those of pure Cu and pure Pt. As an effect of the compression of Cu relative to the Pt lattice constant, Pt atoms are exposed to the electrolyte. Moreover, in some cases, the Cu islands have a height of 2 or 3 atoms, resulting in a higher exposure of the Pt surface.

A high binding energy between Pt surface and CO molecules is the driving force for the transformation of bimetallic particles to core-shell nanoparticles consistent of a Pt outer shell.[76,128] Similarly, we take the view that the observed surface structure changes on Cu overlayers on Pt are induced by much higher binding energy of CO to Pt relative to Cu, which favors the reconstruction of the overlayer. In the presence of CO, Cu atoms are pushed together to expose the Pt surface to CO.

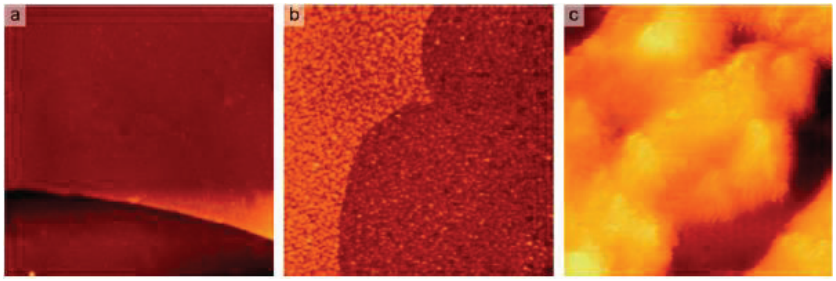

Figure 5.7: EC-STM images of Cu/Pt(111) in 0.1 M $KHCO_3$: a) Atomically flat Cu overlayer in CO-free electrolyte, (499 nm)^2, E = 0.02 V vs. RHE, U_B = 292 mV, I_T = 1 nA; b) Granular morphology of the Cu overlayer after its exposure to CO-saturated electrolyte, (499 nm)^2, E = 0.01 V vs. RHE, U_B = 356 mV, I_T = 10 nA; c) Disordered Cu overlayer with (2 × 2)-CO structure inside the vacancies, (13.6 nm)^2, E = 0.01 V vs. RHE, U_B = 356 mV, I_T = 10 nA. Figure made by Christian Schlaup. Reprinted from[87].

Figure 5.7 shows the STM images obtained in the working electrolyte, 0.1 M $KHCO_3$. They show how Cu overlayer retains its atomically flat morphology in CO-free 0.1 M $KHCO_3$, as shown in Figure 5.7 (a). This indicates that the electrolyte exchange, whereby as well the pH changes from 1 to ~9, does not influence the structure of the overlayer. However, the morphology of the Cu overlayer on Pt changes considerably upon its exposure to CO, as shown in Figure 5.7, (b) and (c), appearing granular, as recorded in CO-saturated 0.1 M $HClO_4$.

5.4 Discussion of the catalytic results

Overall, the bulk electrolysis results suggest that the copper overlayers do not exhibit an improved catalytic activity for CO_2 reduction with respect to pure copper. Moreover, there is no significant difference between Cu/Pt(111) and Cu/Pt(211) surfaces.

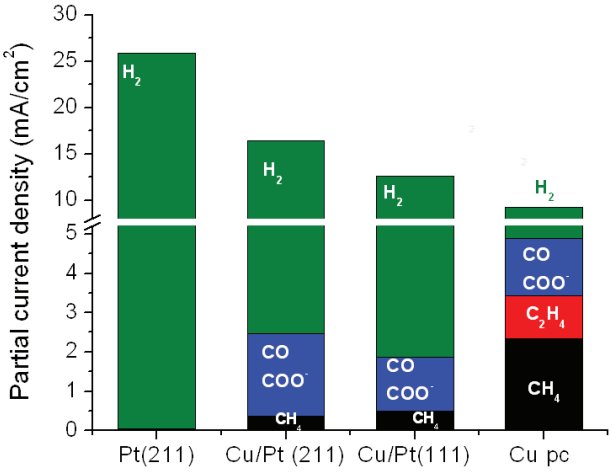

Figure 5.8: Comparison of activities towards various reaction products during CO_2 bulk electrolysis at -1.0 V vs. RHE on Pt(211), Cu/Pt(211), Cu/Pt(111) and polycrystalline Cu in CO_2-saturated 0.1 M $KHCO_3$ at pH 6.8.

Figure 5.8 shows a comparison of the partial current densities towards all reaction products at -1.0 V vs. RHE. The catalytically most active surface during CO_2 bulk electrolysis is Pt(211), however, completely selective towards the competitor hydrogen evolution. Cu overlayers on Pt(211) and Pt (111) exhibit similar activities for methane production. The partial current density towards CH_4 is comparable on both Cu overlayers, however, considerably lower than on polycrystalline copper. Additionally, our measurements indicate a 4-fold higher methane production activity of polycrystalline Cu with respect to the copper overlayers. It is also noteworthy, that the polycrystalline copper produces ethylene as one of the major products, whreby Cu/Pt (111) and Cu/Pt(211) produce only traces of ethylene.

The CO-induced structural changes of the Cu overlayers on Pt should be taken into account when analysing their catalytic activities for CO_2 reduction. Similarly to the established structural changes of the Cu/Pt(111), one can expect these as well for the Cu/Pt (211). Therefore, instead of assuming the

expanded copper overlayers, we may rather consider interpreting these surfaces as Pt single crystals partially covered by polycrystalline copper islands. Another fact, implying the validity of the described structural changes, is the extent of similarity in the catalytic activity of Cu/Pt (111) and Cu/Pt(211). This indicates that the resulting copper islands have a similar structure on Cu/Pt(111) and Cu/Pt(211). Surprisingly, the product distribution on Cu overlayers is very different than for the polycrystalline Cu, suggesting that Cu on top of Pt possesses a different catalytic activity relative to the bulk Cu.

This study represents a pertinent example of how important it is to have an *in situ* characterisation of the catalyst surface. A direct insight into the catalyst surface structure under reaction conditions can be crucial for the understanding of the catalyst reactivity, especially involving the bimetallic systems prone to surface segregations.

5.5 Summary and conclusions

i. Cu/Pt(111) and Cu/Pt(211) surfaces exhibit the catalytic activities in-between those of bulk Pt and bulk Cu. A higher total catalytic activity of the Cu/Pt structures with respect to pure copper can be attributed to enhanced hydrogen evolution activity. On the other hand, the activity and selectivity of these structures towards methane is significantly lower relative to bulk copper.
ii. EC-STM images indicate how presence of CO destabilises Cu/Pt(111). The structure of the Cu overlayer, however, changes to a granular structure in the presence of CO, exposing a part of the Pt surface.
iii. The structural changes induced by CO are key factor in understanding the catalytic activity of the bimetallic overlayer surfaces. The exposure of the Pt surface accounts for the high activity of these structures towards HER and their poor selectivity towards the reduction of CO_2.
iv. These results illustrate the importance of *in situ* surface characterisation to gain an insight into the catalyst surface structure under reactive conditions.

5.6 Outlook

The CO-induced rearrangements of copper overlayers on platinum, suggests different strategies are required towards the improvmenet of CO_2 reduction using bimetallic catalysts. The instability in the presence of CO may be overcome, if a metal substrate with weaker CO binding energy is used instead of the strong CO binding metals, such as Pt. Au based surfaces may be ideal surfaces for this purpose.

On the other hand, as discussed in Section 2.2.2, the CO_2 reduction activity of Cu would benefit from compressive, rather than tensile strain. Since Cu(211) is on the strong binding side of the volcano, the formation of a compressed Cu overlayer would push its d-band centre upwards; assuming perfect scaling between the d-band centre and *CO and *CHO binding energies[32], this would decrease the overpotential of *CO protonation to *CHO (see Figure 2.14).[55] However, Figure 2.4 implies that there is a rather limited choice of substrate metals that would provide such an upward shift in the d-band centre of Cu.

CHAPTER 6

6. CO_2 and CO electro-reduction on polycrystalline gold

In this chapter we present our results from electrocatalytic reduction of CO_2 and CO on polycrystalline gold electrodes in aqueous media.

We describe here the electrochemical methods for surface characterisation and determination of the active surface area of gold by using underpotential deposition of copper.

Although polycrystalline Au has been tested in the literature in different electrolytes, in particular $KHCO_3$ and phosphate buffer, it has not been systematically studied in a single study.[58,78]

Consequently, we investigated the catalytic activities and selectivities for the hydrogen evolution reaction and CO_2 reduction on smooth, flame-annealed polycrystalline gold electrode using aqueous bicarbonate and phosphate buffer solutions as working electrolytes.

Ultimately, we are interested in confirming the values reported in the literature by Hori et al[58], related to the CO_2 electro-reduction on gold in bicarbonate buffer. Moreover, we also attempt to reduce CO reduction on polycrystalline Au in alkaline media; this has not previously been reported in the literature. Both data from CO_2 and CO reduction reactions on polycrystalline gold are useful as reference for the interpretation of the data obtained in work with alloyed gold catalyst, described in detail in Chapter 7. In order to obtain mechanistic insight into the reaction, we perform stripping experiments following the bulk electrolysis.

6.1 Electrochemical surface characterisation of polycrystalline gold

6.1.1 Cyclic Voltammetry on Au

Prior to the bulk electrolysis measurements on polycrystalline gold electrodes, we characterise them by performing the cyclic voltammetry in potential range from -0.3 V to 1.6 V vs. RHE. Figure 6.1 shows typical cyclic voltammograms (CVs) obtained on polycrystalline gold electrode prepared as described in the Experimental Methods (Chapter 3). The plot shows CVs performed on gold with scan rate of 50 mV/s in Argon saturated 0.1 M H_2SO_4 with pH 1 (red line) and in 0.1 M KOH with pH 12.8 (blue line).

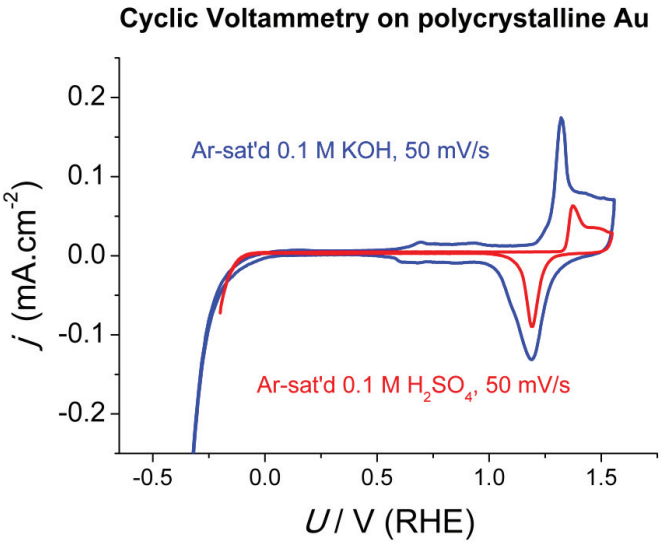

Figure 6.1: Cyclic voltammograms on polycrystalline gold electrodes in Ar-saturated 0.1 M H_2SO_4, pH 1 (red line) and Ar saturated 0.1 M KOH, pH 12.8 (blue line) at 50 mV/s.

6.1.2 Gold surface area measurements using copper underpotential deposition

In order to access the unknown roughness factor of a gold electrode or the active surface area on gold nanoparticles, we used underpotential deposition of copper.[33,73,129] Provided the deposition charge per

unit active area is known, the oxidation charge of copper monolayer on an unknown sample can be used to estimate the active surface area, i.e. the roughness factor. This is preferable to the oxide reduction method used in the literature[130], as the coverage of O* or HO* during Au oxidation is ill-defined in comparison to Cu deposition on Au.[111,131]

A polycrystalline gold surface, would mainly be exposed with close packedly fcc surface – Au(111) – which has a hexagonal geometry, as it is the facet with the lowest surface energy.[132] Therefore, we can use equation 6.1 to express the area of a single surface unit cell (S_{Ucell}) with lattice parameter a_{Ucell}. Hence, the total number of the unit cells on a surface with roughness factor r and geometric area S_{geom} can be calculated as a ratio of total surface area and the surface area of a single unit cell (see equation 6.1 and 6.2).

$$S_{Ucell} = a_{Ucell}^2 \cos 60 \qquad \textbf{(6.1)}$$

The charge exchanged during copper two electron *upd* is defined by following equation:

$$Q = ze\theta \frac{S_{geom}}{S_{Ucell}} r \qquad \textbf{(6.2)}$$

The charge Q of the *upd* corresponds to a multiplication of a single electron charge (e=1.6.10^{-19} C) by the number of electrons per atom involved in the deposition process (in case of Cu z=2), coverage of the solute metal atoms per unit cell ($0 < \theta < 1$) and number of the unit cells, as shown in equation 6.2.

To experimentally access the charge per unit area involved in Cu upd, which follows from equation 6.3, we had to make a measurement on an electrode where roughness factor is unity.

$$\frac{Q}{S_{geom}} = r \frac{ze\theta}{a_{Ucell}^2 \cos 60} \qquad \textbf{(6.3)}$$

For that reason, a clean gold electrode in form of disc is prepared by flame-annealing and cooling in Ar flow, similarly to the method commonly used for single crystal electrodes preparation.[133-135] The electrode is then placed into the rotating disc electrode setup in order to expose only the flat area to the working electrolyte. Figure 6.2 shows cyclic voltammetry performed on such smooth polycrystalline gold disc electrode of 5 mm diameter in a solution containing 1 mM CuO in 0.1 M H_2SO_4. A measured oxidation charge of 77±1.5 μC implies a value of 394±6 μC.cm^{-2} coupled with the two electron process of copper deposition. This value was used for the estimation of the active surface area of all gold electrodes used in this work. Except for the electrolyte studies in Section 6.2, where we used smooth gold electrodes, the preparation procedures we followed produced roughened gold with a measured value of roughness factor of 1.5±0.1. This value was used for current normalisations for gold electrodes throughout this and the following chapter.

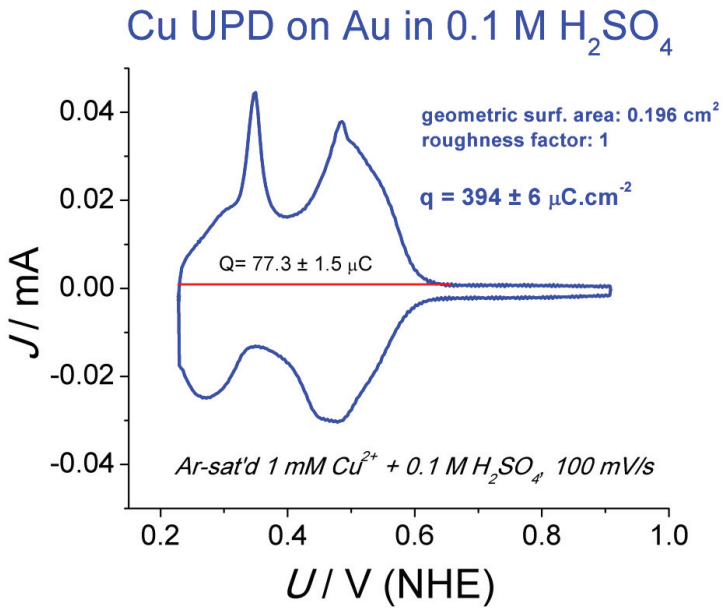

Figure 6.2: A cyclic voltammogram (scan rate 100 mV/s) showing underpotential deposition of copper on a smooth polycrystalline gold disc electrode with diameter 5 mm (solid blue line). The potential is shown relative to the normal hydrogen electrode (NHE). Underpotential deposition was performed at +0.23 V vs. NHE for 30 seconds (corresponding to +0.29 V vs. RHE, at pH 1). A solid red line represents the lower limit of the integrated area corresponding to the total charge of copper oxidation.

6.2 Study of the electrolyte effect on CO_2 electro-reduction on smooth polycrystalline Au electrodes

There are separate reports in the literature about the use of phosphate buffer[78] and bicarbonate buffer[58] solutions as working electrolytes in CO_2 electro-reduction on gold. Based on these reports, the Faradaic efficiencies towards CO evolution are much lower in phosphate based electrolyte. However, it remains unclear whether this is due to differences in experimental procedures, for example the treatment of the electrode surface prior to the bulk electrolysis of CO_2.

In order to investigate these differences, we carried out a study using a bicarbonate buffer at pH 7.7 (0.5 M $KHCO_3$) and using a phosphate buffer at pH 6.6 (0.25 M K_2HPO_4 + 0.25 M KH_2PO_4). On Figure 6.3 we show cyclic voltammograms performed in the range from +0.2 V to -0.5 V vs. RHE at scan rate of 50 mV/s on a smooth polycrystalline gold electrode using the two mentioned electrolytes. The smooth electrodes, prepared by flame-annealing were chosen in order to provide a better insight into the effect of possible specific anion adsorption (on terraces) on our electro-catalytic results.

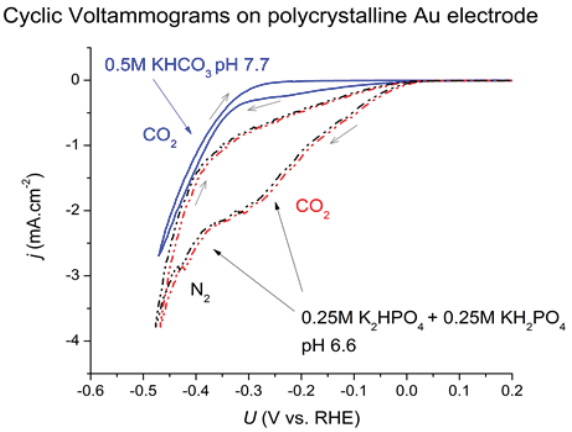

Figure 6.3: Cyclic Voltammetry on a smooth polycrystalline gold electrode in two different working electrolytes: CO_2 saturated bicarbonate buffer at pH 7.7 (solid blue line) and in phosphate buffer at pH 6.6 saturated with N_2 (dash-dotted black line) and CO_2 (dash-dotted red line).

The phosphate buffer exhibits an earlier apparent onset potential for either hydrogen evolution or CO_2 reduction reactions than the bicarbonate buffer. The cathodic peak centered at ca. -0.25 V vs. RHE in both CO_2 and N_2 saturated phosphate buffer could indicate a process related to the solution species,

for instance desorption of the phosphate anion. Phosphate anion adsorption on gold in this potential region has been previously reported in the literature.[111,136,137]

Moreover, in order to explore if these differences in onset potentials indeed have an effect on CO_2 reduction, we performed the bulk electrolysis measurements. Figure 6.4 compares electrolysis measurements made in two buffer electrolytes at -0.6 V vs RHE at various reaction times. In particular, we focus on gas phase product analysis, involving H_2 and CO, without considering formate production.

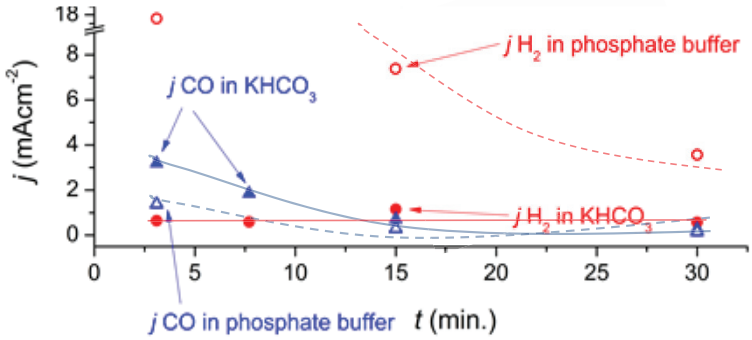

Figure 6.4: Data points obtained during three separate electrolysis measurements for each bicarbonate (filled circles, solid lines) and phosphate buffer (open circles, dashed lines). The partial current densities for CO (in blue) and H_2 (in red) formation on smooth polycrystalline gold at -0.6 V_{RHE} are plotted versus the reaction time (time of product analysis) and correspond to the cumulative values averaged over the entire reaction time. The lines have purpose of guiding the eye.

The plot on Figure 6.4 shows partial current densities for CO (blue) and H_2 (red) measured during three separate electrolysis measurements with different reaction times at -0.6 V vs. RHE, both in bicarbonate (full circles, solid lines) and phosphate buffer (empty circles, dashed lines). The activity of gold for hydrogen evolution in phosphate buffer is generally much higher than in bicarbonate, initially reaching partial current density of -18 $mA.cm^{-2}$, after 3 minutes of reaction. On the contrary, in bicarbonate, hydrogen evolution proceeds at very low current densities, not higher than -1 $mA.cm^{-2}$. The effect of pH difference may play an important role for hydrogen evolution, but it does not account for the huge differences observed here[138]. On the other hand, CO evolution prevails in bicarbonate buffer, with an initial partial current density of ca. -3 $mA.cm^{-2}$. CO evolution in phosphate buffer proceeds initially with lower current densities than in bicarbonate.

Observed on the time scale, the only significant decrease in current density occurs for hydrogen evolution in phosphate buffer, whereby the activity for H_2 evolution in bicarbonate remains low and

does not vary with time. The activities for CO evolution in both bicarbonate and phosphate buffer decrease gradually, eventually reaching similar values.

The higher activity and selectivity for hydrogen evolution on gold electrodes in phosphate buffer with respect to the bicarbonate buffer may be attributed to a higher buffer capacity, as described previously in Chapter 2. The data matches well with previously reported CO_2 reduction on gold in phosphate buffer.[78] However, the time resolved data indicate an intitial decrease in activity of smooth gold for CO evolution, showing discrepancies with respect to the activities, and hence as well selectivities, obtained on the roughened gold electrodes by Hori[58] and in our own measurements later (see Figure 6.5).

Nevertheless, these initial measurements in bicarbonate and phosphate buffers using smooth gold electrodes indicated two important conclusions: (1) Faradaic efficiencies for CO evolution are much more favourable in bicarbonate compared to the phosphate buffer, being mainly consequence of its high buffer capacity effecting in high hydrogen evolution partial current densities; and (2) smooth, flame-annealed gold electrodes show a decrease in CO_2 reduction activity over time.

6.3 Bulk Electrolysis on rough polycrystalline gold

This section of the chapter focuses on bulk electrolysis measurements performed in CO_2 saturated 0.5 M $KHCO_3$ and CO-saturated 0.1 M KOH, using roughened polycrystalline gold sheets as electrodes. Hereby, we use chromatography analysis tools to determine the activity and the selectivity of roughened gold as catalyst for CO_2 and CO reduction reactions. The free energy diagram for Au(211) is contrasted to Cu(211), explaining the differences in binding of intermediates, the advantage of performing CO reduction and identifying possible expected products. We employ cyclic voltammetry post-reaction to obtain insight into the presence of adsorbed species.

6.3.1 CO_2 electro-reduction on polycrystalline gold

In order to compare our data to the literature and ensure that we perform the electrolysis measurements correctly, we performed the CO_2 reduction on roughened Au(pc) under conditions very close to those of Hori and coworkers[58]. Figure 6.5 illustrates a good match of our data (filled circles) with Hori's data (open circles) in terms of (a) Faradaic Efficiencies and (b) Partial Current Densities, from -0.35 V to -1 V vs. RHE. Despite the difference in temperature at which the electrolysis was carried out, there is an excellent agreement between both data sets, demonstrating that we have established appropriate experimental conditions.

As expected, our data show high current efficiencies on roughened gold for CO evolution, of ~80-90%, over a wide potential range. The second major product is hydrogen, accounting for 15-35% of current efficiency, depending on the potential. The third product measured by Hori was formate. We plotted here the unbalanced Faradaic efficiencies, since the product analysis using HPLC was not performed on all aliquots. Instead, we analysed aliquots from the bulk electrolysis at selected potentials: -0.49 V, -0.68 V and -0.88 V vs. RHE, which showed Faradaic efficiencies for formate production of 1.8 %, 4.2 % and 5.7 %, respectively. Both Hori's data and the data presented here show that ~100 % of the charge can be accounted for by CO, formate and H_2 production.

Interestingly, it is worth reporting that we were only able to achieve this high selectivity towards CO when gold was treated in the same manner as reported by Hori and coworkers,[58] i.e. etched briefly in aqua regia. Preliminary measurements on smooth, flame annealed electrodes lead to higher selectivity for hydrogen evolution, and decreased activity for CO evolution (shown in Section 6.2).

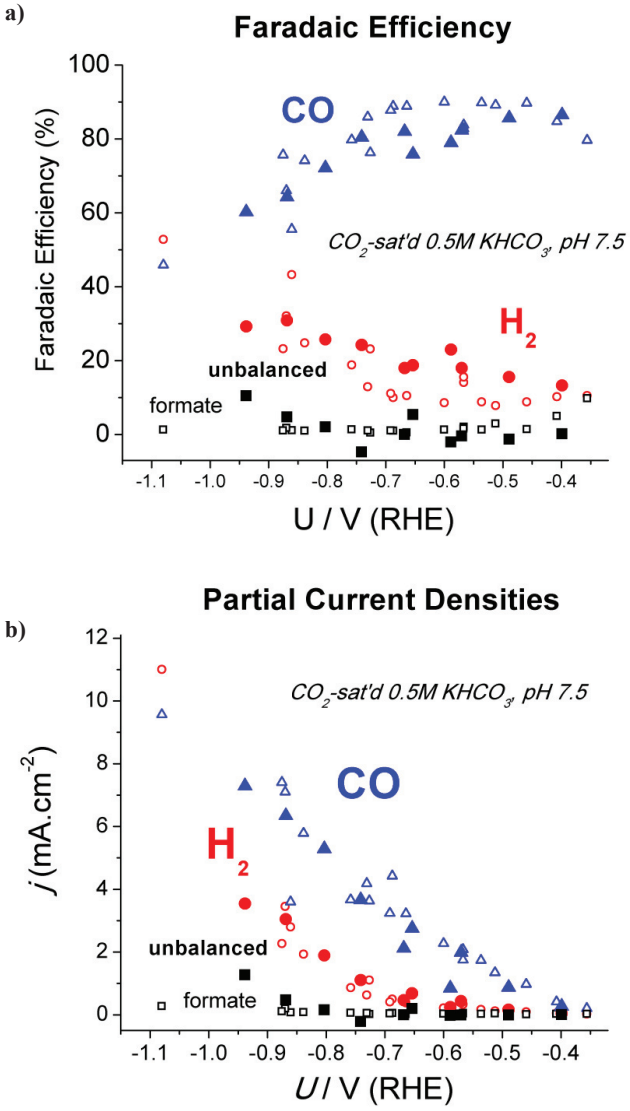

Figure 6.5: (a) **Faradaic Efficiencies** for major products of electrochemical CO_2 reduction on roughened polycrystalline gold electrodes; (b) **Partial Current Densities** for major products of electrochemical CO_2 reduction on roughened polycrystalline gold electrodes. Plots provide the comparison of the data from this work (fil*led data points*) with the digitised data from Hori and coworkers[58] (*open data points*). Hori's data contain formate analysis, while we present the unbalanced efficiencies. HPLC was used for product analysis only at selected potentials to confirm the production of formate.

6.3.2 CO electro-reduction on polycrystalline gold

On Figure 6.6, a comparison of the free energy diagrams for Cu(211) and Au(211) is at -0.77 V vs. RHE, the limiting potential of the potential determining step on Au(211), which is CO_2 activation. The binding energies are calculated by Heine A. Hansen using DFT calculations, assuming CO_2 pressure of 1 bar and CO pressure of 1 mbar.[60]

The plot shows, that at -0.77 V, all the reaction steps on Au(211) are exergonic. As discussed in Chapter 2, Cu has limiting potential of -0.74 V, however for the third electron transfer reaction, corresponding to the protonation of adsorbed CO. Additionally, the free energy diagram indicates towards a difference in selectivities of the two electrodes. In case of possible further reduction of CO on gold, one could expect to produce formaldehyde, as four electron transfer product, or methanol, as six electron transfer product of CO_2 reduction. According to these calculations, it would be energetically more favored for Au(211) to produce methanol rather than methane, as it is case for Cu(211). This difference is brought about by the different oxygen binding energies of these metals, playing important role at the sixth electron transfer (see Figure 6.6). The selectivity depends on whether the catalyst would reduce *OCH_3 intermediate to form CH_3OH (as predicted for gold) or would rather favor keeping the atomic oxygen at the surface, followed by the formation of CH_4 (as in case of copper).

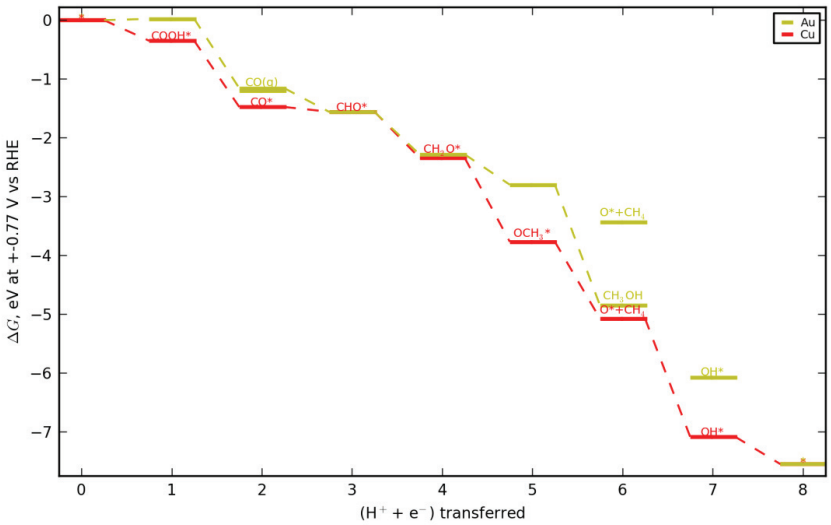

Figure 6.6: Comparison of the free energy diagrams for Cu(211) in red and for Au(211) in yellow at -0.77 V vs. RHE, limiting potential for the initial reaction step CO_2 to *COOH on Au(211). The binding energies are calculated assuming 1 bar CO_2 pressure and 0.001 bar CO pressure at 298.15 K. Figure made by Heine A. Hansen.

As shown on Figure 6.6, the free energy diagram for CO_2 reduction on Au(211) suggests that at sufficiently negative potential (-0.77 V vs. RHE), it should be thermodynamically downhill to form more reduced products, in particular formaldehyde and methanol. Nevertheless, CO_2 reduction does not give any more reduced products of CO. Moreover, even at lower potentials, gold exhibits substantial activity for CO evolution, confirmed by both Hori's and our own measurements.[58] This might be a consequence of rather fast kinetics of *CO desorption. Hence, further electrochemical reduction of *CO to methanol would be competing with CO evolution. It is challenging to address the selectivity question here because one step is chemical and the other electrochemical. The fact that CO(g) re-adsorption might be important and that the CO(g) concentration in the vicinity of the electrode-electrolyte interface is not well established complicates the analysis further. This could however imply, that CO reduction, if CO is coming from the gas phase, may even be thermodynamically possible at more positive potentials, i.e. at -0.59 V vs. RHE. This is the potential where CO(g, 1mbar) to *CHO step is thermoneutral on Au(211). Comparing this value to the limiting potential for the step of CO_2 reduction to *COOH(-0.77 V), would suggest, that CO could be further reduced, however, such a comparison assumes similar additional barriers for the two processes. It could be possible that the barrier for the *CO to *CHO step is considerably larger.

Hence, the most trivial explanation for why there is no detection of more reduced products of CO during CO_2 reduction, is that the rate of CO evolution (which is a chemical step), by far exceeds the rate of CO reduction. This notion can be easily justified based on DFT calculations suggesting that CO adsorption is close to thermoneutral on Au(211).

However, by using CO as the initial reactant, i.e. increasing pressure of CO in the vicinity of electrode surface, it seems plausible that CO adsorption would be favoured, which also means that its further reduction could be facilitated. The limiting potential for obtaining *CHO from 1 bar CO(g) on Au(211) is calculated to be -0.41 V vs. RHE. Presumably, a pressure of 1 bar of CO would result in a higher *CO coverage at the surface. In addition, Koper and coworkers report that alkaline environment was reported to enhance CO adsorption on Au surfaces.[139-142] Consequently, conducted the bulk electrolysis measurements in CO-saturated 0.1 M KOH at pH 12.8.

Our bulk CO electrolysis measurements showed that no other major products apart from hydrogen, over a wide range of potentials. Minor products as formate and formaldehyde are detected.

Figure 6.7 compares the partial current densities of gold for hydrogen evolution in CO-saturated 0.1 M KOH and in CO_2–saturated 0.5 M $KHCO_3$ (i.e. the data shown in Figure 6.5b). From -0.4 V to -0.7 V, the current densities are very similar in magnitude between the two experiments. On the other hand, at more negative potentials, the current in KOH is significantly higher.

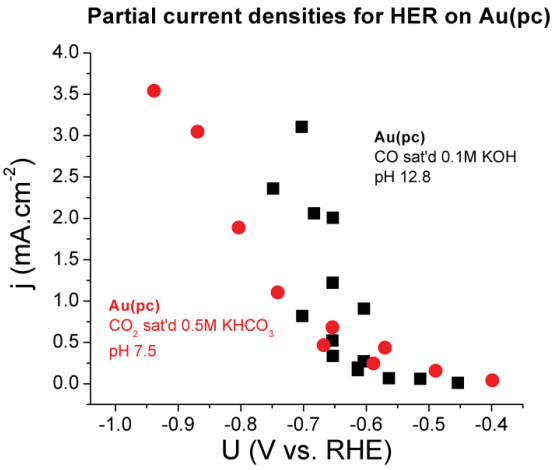

Figure 6.7: Partial current densities for hydrogen evolution reaction on polycrystalline Au during CO_2 bulk electrolysis (0.5 M $KHCO_3$, pH 7.5) and during the CO bulk electrolysis (0.1M KOH, pH 12.8).

The trend towards increased hydrogen evolution in CO-saturated KOH, relative to CO_2 saturated $KHCO_3$, could, at first glance, seem counterintuitive. Typically, at any given potential with respect to the RHE, hydrogen evolution is favored at lower pH values.[84,143,144] However, it is worth bearing in mind that the total current density is around an order of magnitude higher in CO_2-saturated solution (see Figure 6.5b). The implication of this is that in neutral solution, at high current densities, the local pH would shift considerably to higher values.[79,143] This effect would be difficult to account for quantitatively in the cell used for the current study, as the flow around the electrode is likely to be turbulent (greater control of mass transport would be afforded by the use of a rotating disk electrode, for instance[145]).

In following paragraphs, we present the effect of phosphate anion adsorption on the hydrogen evolution activity of gold. We support our observations through data from cyclic voltammetry and electrolyses measurements.

Namely, for the preparation of surface alloys (Cd/Au) in-situ, described in more detail in Chapter 3 and Chapter 7, prior to the electrolysis, we needed to ensure that the working electrolyte would not have an effect on the pH of the electrolyte in counter and reference electrode compartments. We achieved that by using a neutral phosphate buffer solution with 0.25 M concentration of K_2HPO_4 and KH_2PO_4. However, the presence of phosphate anions has been detected in the working electrode compartment as well, by means of liquid chromatography and cyclic voltammetry, both on pure polycrystalline Au electrodes presented here and during post-reaction stripping measurements on surface alloys (Cd/Au), presented in Chapter 7. Figure 6.8 below shows the effect of phosphate anion adsorption on Au.

The CV on Au obtained in the cell containing purely KOH (blue solid line) shows typical gold surface oxidation and reduction peaks followed by the hydrogen evolution onset at the potential of -0.1 V. On the contrary, the CV on Au electrode obtained in an H-cell containing phosphate buffer in counter and reference electrode compartments (shown in red), exhibits smaller gold oxidation and reduction peaks, possibly due to the phosphate anion adsorption at positive potentials. A small cathodic peak is observed at -0.1 V, which is most likely assigned to phosphate anion desorption. The onset of ydrogen evolution onset is shifted negatively.

Moreover, in Figure 6.9 we provide the comparison of partial current densities for the hydrogen evolution during CO bulk electrolysis on polycrystalline Au surface at three different potentials. In the case when phosphate buffer was added to CE and REF cell compartments (red circles), the HER activity is slightly lower relative to the situation when KOH is used in all cell compartments (blue circles). Both measurements detected the amount of hydrogen balancing 100 % of passed reaction charge. The pH values of working electrolytes in both cases are established to be the same, 12.8.

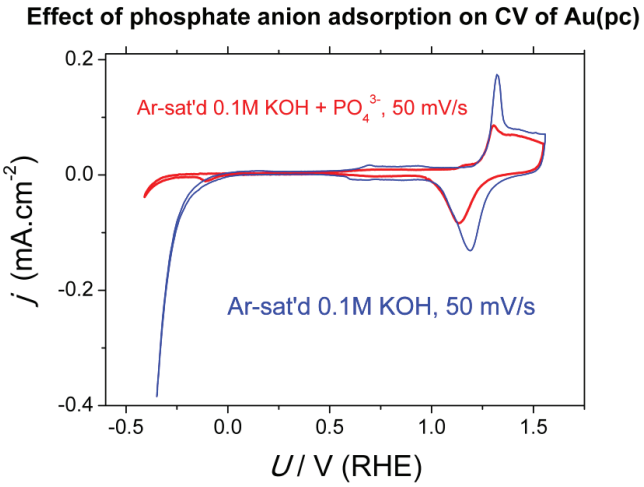

Figure 6.8: The effect of phosphate adsorption illustrated by Cyclic Voltammetry on a rough polycrystalline gold electrode in two different working electrolytes: Ar-saturated 0.1 M KOH at pH 12.7 (solid blue line) and Ar-saturated 0.1 M KOH containing phosphate anions at pH 12.8 (solid red line).

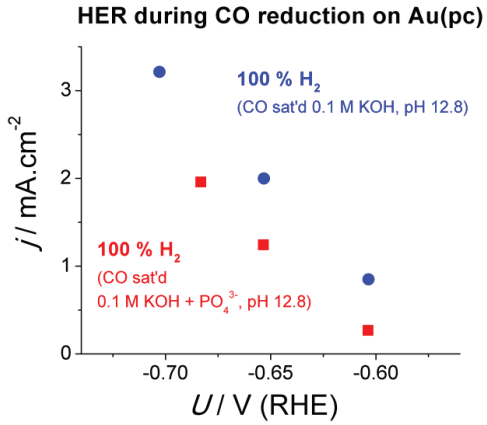

Figure 6.9: The effect of phosphate adsorption illustrated by the hydrogen evolution activity during bulk CO electrolysis on a rough polycrystalline gold electrode in two different working electrolytes: Ar-saturated 0.1 M KOH at pH 12.7 (blue dots) and Ar-saturated 0.1 M KOH containing phosphate anions at pH 12.8 (red squares).

In CO-saturated 0.1 M KOH, HPLC measurements suggested formate production, as shown in Figure 6.10. Formate was presumably formed from residual amount of CO_2 dissolved in the KOH in the form of CO_3^{2-} anion.[146]

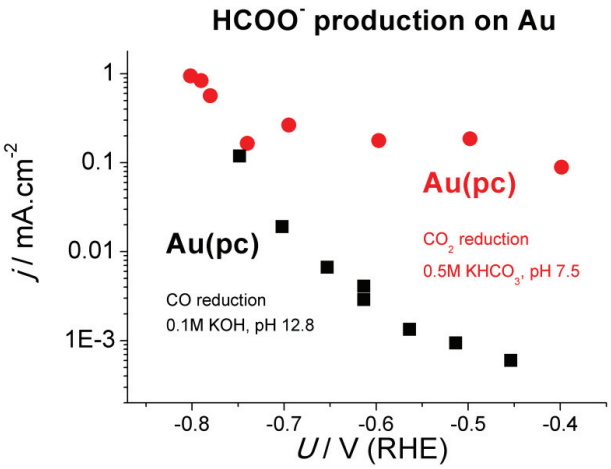

Figure 6.10: Faradaic efficiencies for formate production on polycrystalline Au during CO_2 bulk electrolysis (0.5 M $KHCO_3$, pH 7.5, red dots) and during CO bulk electrolysis (0.1 M KOH, pH 12.8, black squares). Each point represents an individual, independent measurement.

During some experiments, the HPLC analysis detected trace amounts of formaldehyde, likely produced from the reduction of CO. However, it was close to the limit of detection (as described in more detail described in Section 3.6). Nonetheless, the observation that formaldehyde is formed on some occasions led us to investigate whether it was reduced further, for instance to methanol (see the free energy diagram at Figure 6.6).

In order to increase the likelihood that trace liquid products could be detected, we prepared high surface area gold electrodes, i.e. a thin nanoporous gold leaf rolled onto a polycrystalline gold rod (described in detail in Section 3.2.4). The liquid products were measured using the static headspace chromatography on aliquots obtained on high surface area gold electrodes.[89,90] Plot (a) in Figure 6.11 provides an estimation of the roughness factor of a nanoporous gold electrode by comparing the double layer capacitance and the hydrogen evolution current densities at -0.25 V vs. RHE from cyclic voltammetry. The capacitance increased by roughly two orders of magnitude. On plot (b) in this figure, the chromatographs show FID signals obtained from the analysis of aliquots produced in CO bulk electrolysis experiments on high surface area nanoporous gold leaves. The calibration chromatograph is plotted along with the aliquots from reactions at four different potentials. Apart from consistent detection of the trace amounts of CH_4 from the air, no significant concentrations of methanol were detected. Trace amounts of methanol correspond to Faradaic efficiencies less than 0.1 %.

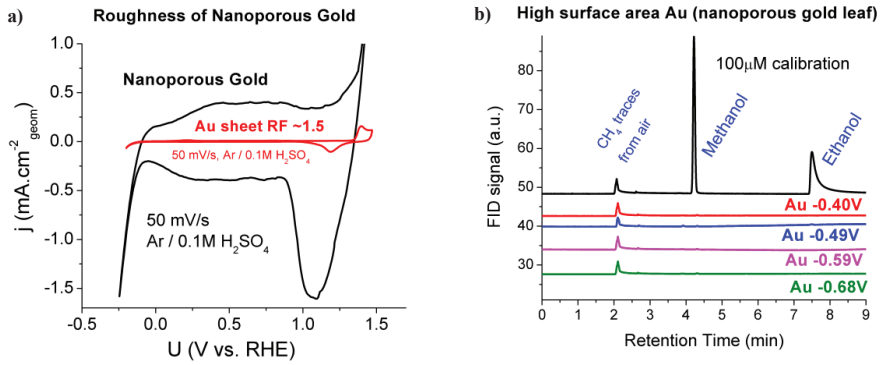

Figure 6.11: (a) Cyclic Voltammograms performed on Au sheet with roughness factor 1.5 (red line) and on nanoporous gold leaf (black line). The CV indicates high roughness factor of nanoporous gold electrode. (b) Chromatographs showing the FID signal obtained from aliquot analysis from CO bulk electrolysis on high surface area nanoporous Au at various potentials in 0.1 M KOH (pH 12.8). The chromatographs are contrasted with the calibration chromatograph obtained using a known concentration of products (shown here: 100 μM methanol and 100 μM ethanol signals from flame ionisation detector-FID). Apart from methanol and ethanol signals, there is a signal at retention time 2.1 min, corresponding to the traces of CH_4 present in air.

6.4 Post-reaction electrochemical characterisation of rough polycrystalline gold

6.4.1 Stripping on gold after CO_2 reduction in neutral media

The stripping experiments was performed immediately after the electrolysis measurements on gold in CO_2-saturated 0.5 M $KHCO_3$ at -0.69 V vs. RHE. After 15 min of electrolysis, the potential was kept at +0.1 V vs. RHE, while Ar was purged through the cell for 20-30 min to remove any dissolved CO from the solution, whereby the pH value of the electrolyte stabilised at values between 8.7 and 9. These experiments were performed with the intention of electrochemically detecting the reaction intermediates at the surface undergoing oxidation at positive potentials.

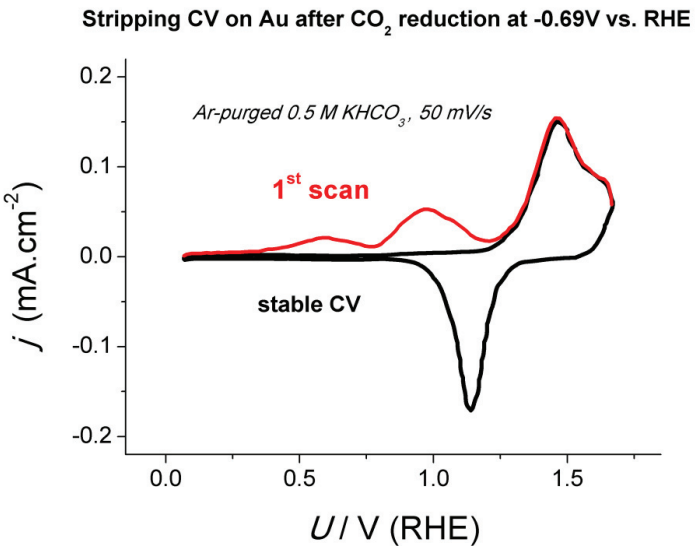

Figure 6.12: Cyclic Voltammetry on Au(pc) in 0.5 M $KHCO_3$. CVs recorded in following procedure: (1) performing CO_2 reduction at -0.69 V for 15 min, (2) purging for 20-30 min with Ar while holding at +0.1 V vs. RHE and (3) ramping the potential to 1.6 V vs. RHE. The potentials are corrected for measured pH value of the 0.5 M $KHCO_3$ after Ar purge being ~9. The total stripping charge corresponds to 260 $\mu C.cm^{-2}$.

On Figure 6.12, two peaks are arising after 15 min of CO_2 reduction reaction at -0.69 V vs. RHE. The first peak is smaller in charge and appears at broader range of potentials with the center around +0.6 V. The second peak is more pronounced and is centred at ~ 1.0 V. Given that both CO and formate are products of the reaction, it seems plausible that the peaks correspond to the oxidation of the irreversibly adsorbed form of these species. CO is adsorbed on Au surfaces both in acid and in base, although the saturation coverage is generally much higher in the alkaline solutions.[147] The peak at 1 V is consistent with CO adlayer oxidation experiments in base and acid on different Au surfaces.[139-141,147-149] The earlier peak centred at 0.6 V coincides with the region where the bulk oxidation of formate takes place;[150] we may tenatively assign it to the oxidation of an irreversibly adsorbed formate adlayer.

6.4.2 Stripping on gold after CO reduction in alkaline media

To explore if there are any intermediates formed at the surface of gold during the CO electrolysis in alkaline media, we performed cyclic voltammetry after a CO reduction reaction on gold at -0.7 V vs. RHE, as shown in Figure 6.13.

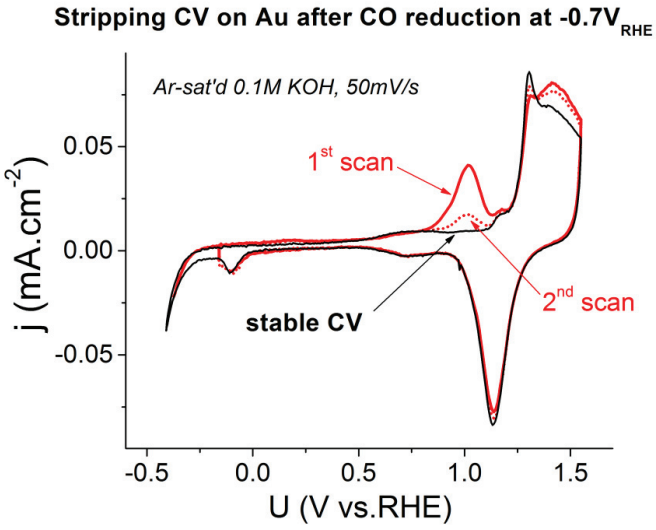

Figure 6.13: Cyclic Voltammetry on Au(pc) in 0.1 M KOH – oxidation of intermediates after CO reduction for 60 min on Au at -0.7 V vs. RHE. Red line represents the first scan following the electrolysis obtained after holding 20-30 min at -0.15 V vs. RHE while purging Ar, corresponding to the surface charge of 70 $\mu C.cm^{-2}$; black line is a stable CV after several cycles.

The stripping CV in Figure 6.13, exhibits an oxidation current peaking around 1 V, and an oxidation charge of 70 μC cm^{-2}. The position of the peak is consistent with CO adlayer oxidation experiments on polycrystalline Au, measured by Kita et al[147]. The charge is somewhat smaller, as it is very sensitive to the experimental conditions, including pH and adsorption potential[141], time and the conditions under which the electrolyte is purged of CO.

6.4.3 XPS surface characterisation

XPS surface characterisations following various CO_2 and CO bulk electrolysis measurements confirmed the presence of only metallic Au with some traces of adventitious oxygen and carbon, as well as potassium traces coming from the electrolyte. No metallic contaminants were found.

6.5 Discussion and conclusions

The electrolysis measurements using CO_2 and CO as initial reactant gases, theoretical considerations based on DFT calculations, as well as the post-reaction oxidation CVs indicate towards few important conclusions:

(1) CO_2 reduction forms only CO and formate as products, within detection limits.

(2) During CO reduction in KOH, only trace amounts of CO are reduced, to formaldehyde, at the limit of detection (<0.5% Faradaic efficiency). High surface area gold showed trace amounts of methanol, less than 0.1 % Faradaic efficiency.

(3) DFT calculations on Au(211) suggests that the electrochemical reduction of 1 bar CO (g) to formaldehyde and methanol should be downhill in free energy at a potential negative of -0.41 V. However, on the basis of the DFT calculations, a plausible reason that CO does not reduce further would be because it simply desorbs.

(4) Despite (3), above, the stripping experiments following CO electrolysis and CO_2 electrolysis measurements at -0.7 V suggest that a significant coverage of an adsorbate derived from CO_2 or CO is formed during the reaction. In alkaline electrolyte, it seems reasonable to assume that the adsorbate is CO, consistent with very similar experiments by Kita et al. Few studies, if any have addressed CO adsorption under neutral conditions. However, CO also adsorbs in acid, albeit rather more weakly[148,151] Consequently, we conjecture that in neutral solution CO is also adsorbed at the surface, tentatively in combination with adsorbed formate.

Given that CO is known to adsorb from the gas phase onto Au both in alkaline and in acid, it seems reasonable to assume that at least part of this coverage is due to adsorbed CO, and the remainder due to the adsorbed formate. However, the notion that an irreversibly adsorbed CO adlayer is formed is not completely consistent with (3) above, suggesting fast CO desorption kinetics. Given the high rate at which CO desorbs under reaction conditions, it is somewhat surprising that CO remains on the surface during the 20-30 minutes between the end of the electrolysis measurement and the commencement of the stripping experiment, during which time the electrolyte is purged with argon. For instance, at a potential of -0.69 V, in neutral media, CO is evolved at a partial current density of ca. -2 $mA.cm^{-2}$; at this rate, it would only take ~0.1 seconds to desorb all the adsorbed *CO detected during the stripping experiment (assuming that all stripping charge from peak at 1.0 V in Figure 6.10, 195 $\mu C.cm^{-2}$, corresponds to CO).This would suggest that the precursor to the CO that is evolved

during electrolysis is a more weakly bound CO than the CO that is oxidised during the stripping experiment.

Similarly, Rodriguez et al observed that bulk CO oxidation proceeds at much more negative potentials than CO adlayer oxidation, indicating the presence of two types of CO.[139,142] Thus, the CO that is oxidatively stripped could be on a different, stronger binding site than the CO that is evolved. Alternatively, under reaction conditions, there is a high coverage of CO at the active site, which could also lead to weaker bound CO, due to repulsive adsorbate-adsorbate interactions.[152] Koper and co-workers also reported the existence of "physisorbed" and "chemisorbed" CO in experimental and theoretical studies.[141,153] Moreover, experiments by several groups made analogous observations regarding CO oxidation: in the presence of CO in the solution, under which conditions the CO coverage could be higher, CO oxidation occurs at a much higher rate; this is consistent with the notion that a weaker bound form of CO exists at high coverage.[141,147,151] The actual absolute CO binding energy on Au may be slightly lower than initially estimated by DFT calculations. However, the consequences of this for the CO coverage on gold surface and the kinetics of CO evolution require further investigations.

(5) Based on the free energy diagram on Figure 6.6, should there be a significant coverage of CO at the surface of Au(211), it would get reduced further at -0.41 V. However, only negligible amounts of more reduced products were observed. Importantly, this suggests that there are some additional kinetic barriers preventing the reduction of adsorbed CO, which are not captured by the thermodynamic analysis in the free energy diagram in Figure 6.6.

6.6 Summary of CO_2 and CO reduction on rough polycrystalline gold

CO_2 electro-reduction on polycrystalline gold in bicarbonate based electrolyte confirmed the activity for formation of three major products: hydrogen, CO and formate. Highest current efficiencies of ca. 90 % were measured in potential range from -0.4 V to -0.7 V vs. RHE. Formate is produced with efficiencies ranging from 0 - 10 %.

Opposite to copper, DFT calculations predict a possible methanol production on gold, if CO is reduced further. The standard redox potential for CO reduction to CH_3OH is +0.076 V (see Latimer-Frost plot in Chapter 2, Figure 2.7). Since Au binds *CO weakly (see Figure 6.6), the chemical step of CO(g) adsorption is considered to govern the formation of *CHO at the surface. At 1 bar CO (during CO electrolysis) relative to 0.001 bar CO (during CO_2 electrolysis), DFT predicts a slightly less negative limiting potential, shifting from -0.59 V to -0.41 V (the limiting potentials for Au(211) are summarised in Table 7.1, Section 7.1).

However, the electrolyses performed in CO saturated 0.1 M KOH with pH 12.8 showed almost 100 % efficiencies for hydrogen evolution reaction. Occasionally, at -0.5 V and -0.6 V, trace amounts of formaldehyde were measured, at the limits of detection limit of the HPLC. Even in alkaline media, formate was formed during bulk electrolysis conditions, produced from CO_2 originating from the chemical decomposition of CO_3^{2-}. Stripping voltammetry performed post reactions in CO-free electrolyte, indicated that a significant coverage of adsorbates are formed during the reaction, presumably CO, consistent with experiments by others showing that CO adsorbs onto Au surfaces under neutral or alkaline solutions. That implies a possibility of existence of two types of CO: in high coverage regime – CO binding weakly and in low coverage regime – the stronger bound CO.

CHAPTER 7

7. Alloyed gold for CO_2 and CO electro-reduction

This chapter introduces the concept of breaking scaling relations via alloying in more detail. We provide an introduction into the theoretical modelling based on DFT calculations. The DFT methods used in search for new active and selective model catalysts for CO_2 electro-reduction are presented. Furthermore, we present extensive experimental work carried out on the Au_3Cd catalyst, identified as the most promising candidate for efficient methanol production, in the worst case possessing highest CO evolution activity. Finally, we contrast the obtained results with the initial theoretical model, in order to improve it and understand the additional processes governing the overall activity of Cd-alloyed Au electrodes under reactive conditions.

7.1. Density Functional Theory Calculations

7.1.1. Breaking scaling relations via alloying

One of the strategies for breaking the scaling relations and thus, achieving less negative limiting potentials, suggested by Jens Nørskov and coworkers[55], involves using a catalyst with bifunctional properties. Similar approaches have been used with other related electrochemical reactions: for example PtRu or PtCu for methanol oxidation and CO oxidation.[88,154-159]

As previously described in Chapter 2 on Figure 2.13, the origin of overpotential for CO_2 reduction on metals at the strong CO binding side of the volcano - eg. Pt, Ni - is the protonation of the adsorbed *CO.[55] However, for metals that bind CO weaker (such as Cu, Au and Ag), the very first protonation of the CO_2 molecule is the reaction step most uphill in free energy.

$$CO_{2(g)} + * + e^- + H^+_{(aq)} \rightarrow *COOH* \quad \textbf{(7.1)}$$

$$*COOH* + e^- + H^+_{(aq)} \rightarrow *CO + H_2O_{(l)} \quad \textbf{(7.2)}$$

$$*CO \rightarrow CO_{(g)} + * \quad \textbf{(7.3)}$$

Equations 7.1, 7.2 and 7.3 describe the steps and intermediates involved in the electrochemical reduction of CO_2 to CO. A kinetic two-dimensional volcano plot on Figure 7.1 shows theoretically predicted partial current densities for CO evolution.[85] The volcano identifies numerous transition metals and bimetallic alloys included in the screening following strong scaling relations between the binding of *COOH and *CO. In other words, these metals have limited activity, since they cannot have a fast initial CO_2 activation without being limited by *CO removal.

The screening of bimetallic alloys performed by Nørskov's group included a large number of transition metals forming alloy compositions in ratio of 3:1 (of type X_3Y). Among several alloys that potentially have higher activity for CO evolution (red region on the volcano) one of the most promising is Au_3Cd, because it has a respectable stability under reaction conditions.

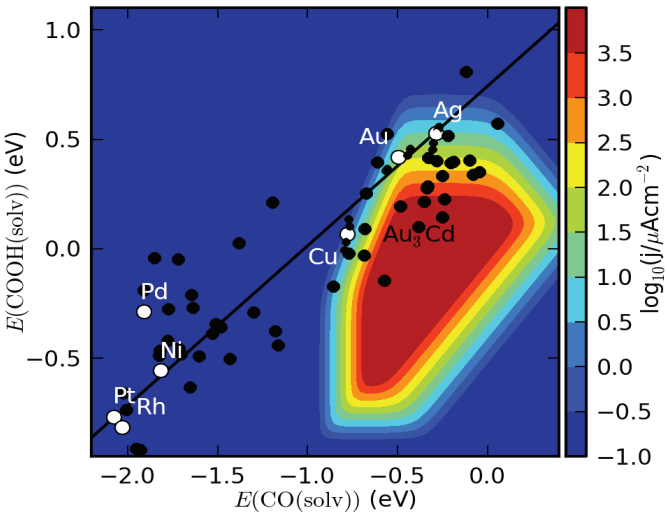

Figure 7.1: 2D kinetic volcano plot – Scaling of binding energies for COOH* relative to CO* on pure transition metals (white dots) and bimetallic alloys of type X_3Y (black dots). Colored region represents logarithmic values of current densities calculated using data from[15]. Figure made by Heine A. Hansen.

From previous theoretical considerations for CO_2 reduction to methanol on pure gold surface, we have pointed towards the step in the reaction mechanism that might be responsible for slow kinetics of further CO reduction. As discussed in Chapter 6, that potential limiting step corresponds to the hydrogenation of the adsorbed *CO to *CHO intermediate (reaction step 7.4).

$$*CO + e^- + H^+_{(aq)} \rightarrow *CHO \qquad \textbf{(7.4)}$$

$$CO_{(g)} + e^- + H^+_{(aq)} \rightarrow *CHO \qquad \textbf{(7.5)}$$

However, for surface with weak CO binding, it may be more relevant the chemical step of adsorption of CO from the gas phase, followed by its further reduction to *CHO (reaction step 7.5).

In any case, the stabilisation of *CHO relative to *CO would result in a lower limiting potential and thus, conversion of CO_2 to useful fuels with less energy input. The binding energy of the *CHO intermediate is mainly determined by its interaction with the surface through the carbon atom. However, as suggested by Peterson et al, it may also to a certain extent be affected by its interaction via oxygen atom, in an alloy containing an oxophillic element.[55] This interaction may influence the final geometry of *CHO intermediate at the surface and so affect its binding and stabilisation with respect to adsorbed *CO.

On Figure 7.2, a two-dimensional activity map is represented showing a linear dependence between the*CO* and *CHO binding on various pure transition metals marked as yellow dots. The color scale represents the variation of the limiting potential. Unfortunately, the majority of transition metals have limiting potentials more negative than -0.6 V vs. RHE for this step. Calculated values for the limiting potentials of alloys are marked as small crosses. In the region below the diagonal, the limiting potential ranges from -0.6 V to as low values as 0 V vs. RHE. Au_3Cd, marked as black triangle, falls into the green region with limiting potential of ca. -0.45 V vs. RHE.

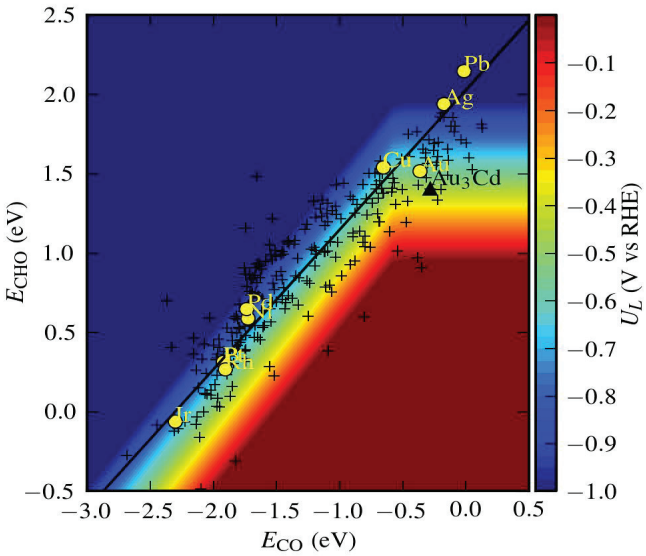

Figure 7.2: 2D-activity map - Scaling of binding energies of CO* and CHO* intermediates on pure transition metals (yellow dots) and bimetallic alloys of type X_3Y (small crosses), among which the black triangle corresponds to Au_3Cd. Colored regions represent values of predicted limiting potentials for adsorbed CO hydrogenation. Figure made by Heine A. Hansen.

7.1.2. Stability of alloys

The alloys predicted to be very active by theoretical calculations should additionally be stable under reaction conditions - at the working potential and at the pH value of the working electrolyte. Figure 7.3 shows plot of limiting potential against the free energy of formation for various alloys, taking into account their alloying energies, as well as their stability in solution at pH 7 and at 0 V vs. RHE. From this plot one can easily deduce that the most stable candidates should have most negative free energies of formation, while the most active should have least negative value of limiting potential U_L (upper left quadrant in Figure 7.3). Cadmium alloyed gold (Au_3Cd) stands out amongst the candadiates for its relatively positive limiting potential and appreciable stability.

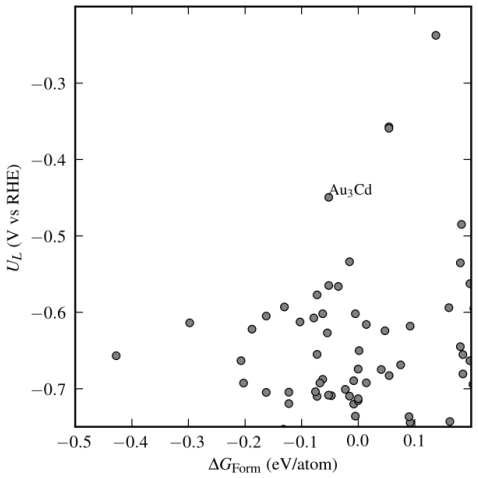

Figure 7.3: Stability plot – Predicted limiting potential for alloys against their stability represented as the free energy of formation (taking into account alloying energy and stability in electrolyte at pH 7 and 0 V vs. RHE). Au_3Cd has shown the least negative limiting potential (-0.46 V) with appreciable stability (ΔG_{Form} = -0.06 eV/atom). Figure made by Heine A. Hansen.

7.1.3. Selectivity of Au_3Cd - CH_4 vs. CH_3OH

On Figure 7.4, a whole free energy diagram for CH_4 and CH_3OH pathways is considered at -0.46 V vs. RHE, which is the limiting potential for initial CO_2 activation on Au_3Cd. At this potential, all following steps of CO_2 reduction on Au_3Cd are downhill in free energy, while Au and Cu still possess uphill steps – Au for CO_2 activation and Cu for *CO hydrogenation. However, the adsorbed *CO is slightly destabilised on Au_3Cd relative to pure Au. Since *CO is weaker bound on Au_3Cd than Au,

this suggests that it should desorb faster. Considering this and favorable energetics of CO_2 activation, one could anticipate that Au_3Cd is a more active catalyst for CO evolution than Au.

Furthermore, already at potential of -0.46 V vs. RHE, the *CHO intermediate is more stable on Au_3Cd relative to both pure Au and pure Cu. This means that as long as the rate of desorption of *CO is not much greater than the rate of its reduction, then, it should be downhill in free energy to reduce it further to *CHO at this low overpotential. Based on the free energy diagram alone, one cannot predict whether *CO will get reduced further, or simply desorb as gas phase CO. This would be dependent on the exact kinetic barriers and prefactors for *CO desorption versus *CO electro-reduction, which cannot be calculated accurately using current theoretical models. The CH_2O* intermediate formed after the fourth proton electron transfer has a similar thermodynamic stability on all three surfaces.

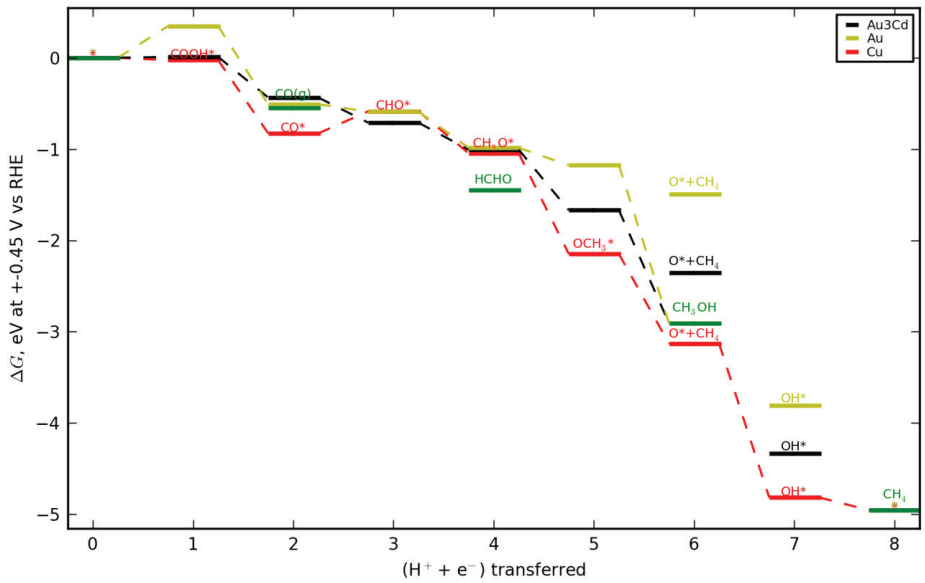

Figure 7.4: Free energy diagram at -0.46 V vs. RHE for Cu (red line), Au (yellow line) and Au_3Cd (black line). All the species marked with a * are in adsorbed state, as opposed to CO(g), HCHO, CH_3OH and CH_4, whose levels are independent of potential and hence marken as green. The binding energies are calculated assuming 1 bar CO_2 pressure and 0.001 bar CO pressure at 298.15 K. Figure made by Heine A. Hansen.

If the CH_2O* intermediate, instead of desorbing as formaldehyde, proceeds to react further, allowing the fifth and sixth proton electron transfer, the free energy diagram suggests preferable formation of methanol (CH_3OH) on Au_3Cd and Au, compared to Cu, which produces methane (CH_4).

According to the theoretical calculations, the affinity of the catalyst to atomic oxygen may play a crucial role in determining the selectivity between methane and methanol. As already mentioned,

copper binds oxygen rather strong and its experimentally measured activity for methane is much higher than for methanol. Following these theoretical considerations, on Au_3Cd, the model suggests higher activity towards methanol than methane.

7.1.4 Variety of surface compositions of Au-Cd system

Several variations of surface composition of Au-Cd system are considered for calculating the free energy diagram shown on Figure 7.5:

a) **Au_3Cd** – corresponds to a bulk alloy, $Au_3Cd(211)$, (black line)
b) **$AuCd_3$ on Au** – corresponds to a Cd rich surface alloy, $AuCd_3(211)$ on Au(211), (green line)
c) **Au_3Cd on Au** – corresponds to a Au rich surface alloy, $Au_3Cd(211)$ on Au(211), (blue line)
d) **CdAu step on Au** – corresponds to Cd atoms along the Au(211) step, (purple line)
e) **Au(fcc)** – corresponds to Au(211), (yellow line)
f) **Au on Au_3Cd** – corresponds to Au(211) on $Au_3Cd(211)$. (cyan line)

Au_3Cd represents the bulk alloy combining both the ligand and strain effects. Surfaces marked under *b)* and *c)* would correspond to Cd-rich and Au-rich surface alloys, respectively, with a bulk composed of pure Au. The **CdAu step on Au** models Au surface with Cd confined only to the (211) step sites. **Au(fcc)** models the active site on a rough gold surface. **Au on Au_3Cd** provides information about a bulk alloy with an overlayer of Au, which would model the structure obtained by leaching of Cd or the segregation of Au to the surface.

The plot in Figure 7.5 indicates that the presence of Cd stabilises the *COOH intermediate by up to 0.25 eV, relative to pure Au. It also shows that the other compositions with Cd at the step exhibit similar, albeit somewhat less pronounced stabilisation of *COOH. According to the calculations, the overpotential for CO evolution should increase in the following order: **Au_3Cd** << **CdAu step on Au** < **Au_3Cd on Au** < **$AuCd_3$ on Au** << **Au(fcc)** < **Au on Au_3Cd**.

It is downhill in free energy to form CO in the gas phase, relative to adsorbed *CO on all surfaces; this would imply that *CO may desorb rather than reduce further. The free energy change for this step increases (i.e. becomes more exorgenic) in the following order: **Au_3Cd on Au** < **$AuCd_3$ on Au** < **Au_3Cd ≈ CdAu step on Au** << **Au on Au_3Cd** < **Au(fcc)**. Notably, for the latter two surfaces, i.e. pure Au and the Au overlayer, although CO desorption is only slightly downhill in free energy, i.e. it is close to thermoneutral.

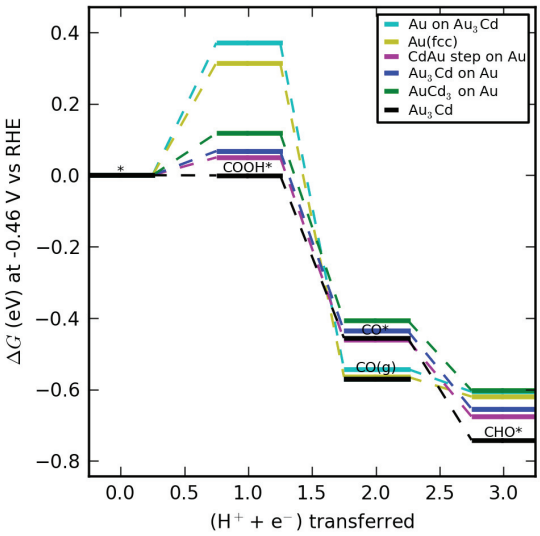

Figure 7.5: Free energy diagram of first three steps of CO_2 electro-reduction on various surface compositions of Au-Cd alloy system at -0.46 V vs. RHE. Figure made by Heine A. Hansen.

Assuming that there is an additional kinetic barrier for CO desorption and that it remains on the suface, the overpotential for *CO reduction to *CHO should increase in the following order: **$AuCd_3$ on Au** < **Au_3Cd** < **CdAu step on Au** ≈ **Au_3Cd on Au** << **Au(fcc)** ≈ **Au on Au_3Cd**. If CO is reduced from the gas phase, the overpotential for its reduction to *CHO should increase in the following order **Au_3Cd** << **CdAu step on Au** < **Au_3Cd on Au** ≈ **Au(fcc)** < **$AuCd_3$ on Au** << ≈ **Au on Au_3Cd**. << **$AuCd_3$ on Au**.

In summary, on the basis of the calculations above, Au_3Cd should shows the lowest overpotential for CO evolution and CO reduction. All surfaces with Cd in the surface layer should show improved CO evolution, and will typically show improved CO reduction activity. Of all the surfaces, only the Au overlayer should show slightly lower activity for CO evolution than Au, and similar activity for CO reduction.

7.1.5 Formate production on Au_3Cd

The free energy diagrams shown on Figure 7.6 indicate lower free energy pathways for formate production relative to CO evolution in both neutral (a) and alkaline (b) environment. The selectivity towards formate, determined at the initial step of CO_2 activation is a consequence of thermodynamically more facile hydrogenation of carbon (to form *OCHO*) relative to oxygen (to form *COOH), on both Au and Au_3Cd. Nevertheless, on polycrystalline Au, experimental measurements show that CO evolution prevails over formate production[58], the reason being most likely a high barrier for the carbon hydrogenation step.

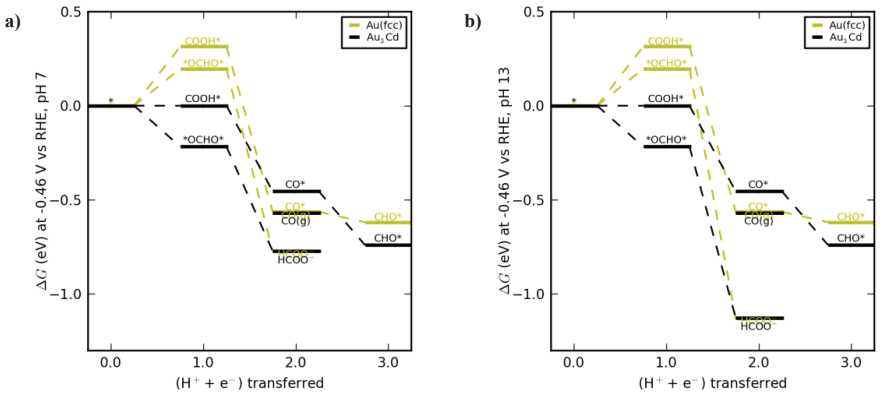

Figure 7.6: A free energy diagram for formate production in comparison to CO production on Au and Au_3Cd at -0.46 V vs. RHE: (a) pH 7 and (b) pH 13. Figure made by Heine A. Hansen.

7.1.6. Hydrogen Evolution Reaction on various Au-Cd surface compositions

Since the HER represents a competitive reaction to CO_2 reduction, the ideal CO_2 electro-reduction catalyst should be inactive for hydrogen production. On Figure 7.7, a free energy diagram for various Au-Cd surface compositions at 0 V vs. RHE is shown. The free energy diagram predicts that the HER would be more uphill in free energy on all Cd-containing surfaces, relative to Au(211), i.e. all Cd containing materials would exhibit a lower HER activity than Au(211). The overpotential increase in the following order **Au(fcc)** << **Au on Au_3Cd** < **Au_3Cd** << **Au_3Cd on Au** ≈ **CdAu step on Au** ≈ **Au_3Cd on Au** < **$AuCd_3$ on Au**.

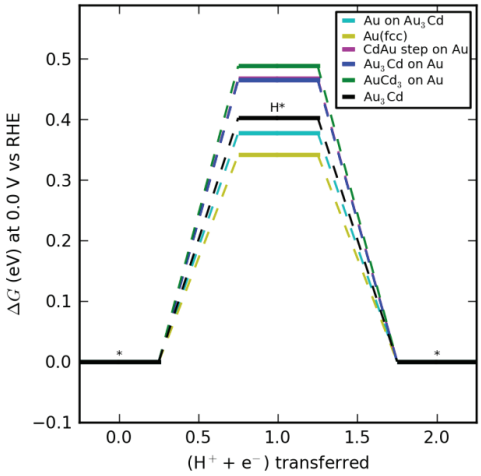

Figure 7.7: Free energy diagram for hydrogen evolution reaction on various Au-Cd alloy surface compositions at 0 V vs. RHE. Figure made by Heine A. Hansen.

7.1.7 Summary of theoretical modelling by DFT

Summarising, the DFT calculations propose a strategy which employs bimetallic alloys to break the scaling relations between the binding of the relevant intermediates, thus allowing downhill energy pathways for a challenging multi-electron transfer CO_2 reduction at lower overpotential. The screening of alloys identified Au_3Cd as the most promising catalyst predicting to be more active than Au towards CO evolution, while simultaneously exhibiting suppressed competitor hydrogen evolution reaction. The calculations also suggest that CO may reduce to methanol. The differences in activity of various Au-Cd structures and compositions should not affect the overall outcome of CO_2 reduction. The limiting potentials for various reaction steps on Au(211) and Au_3Cd(211) are shown in Table 7.1. Additionally, the table provides values of limiting potentials for the chemical step involving adsorption of CO from the gas phase, followed by the electrochemical step to form *CHO. Reducing CO at 1 bar relative to CO at 1 mbar (i.e. at 1 bar CO_2), shifts the limiting potentials by 180 mV less negative. The DFT calculations predict that Au_3Cd(211) surface, shown in Figure 7.8, exhibits the lowest theoretical overpotential for methanol production from 1 bar CO reduction, being 0.076 V – (–0.29 V) = 0.366 V.

Table 7.1: Summary of limiting potentials for various reaction steps of electrocatalytic CO_2 and CO reduction on Au(211) and Au_3Cd(211) at 1 bar CO_2 and 298.15K. Additionally, the limiting potentials for direct formation of *CHO from CO(g) are calculated considering 0.001 bar and 1 bar pressure of CO.

Surface	**Au(211)**		**Au_3Cd(211)**	
Reaction step	**U_L / V (RHE)** at 0.001 bar CO (CO_2 reduction)	**U_L / V (RHE)** at 1 bar CO (CO reduction)	**U_L / V (RHE)** at 0.001 bar CO (CO_2 reduction)	**U_L / V (RHE)** at 1 bar CO (CO reduction)
$CO_2 \rightarrow$ *COOH	-0.77	-0.77	-0.46	-0.46
*CO → *CHO	-0.40	-0.40	-0.17	-0.17
CO (g) →*CHO	-0.59	-0.41	-0.47	-0.29

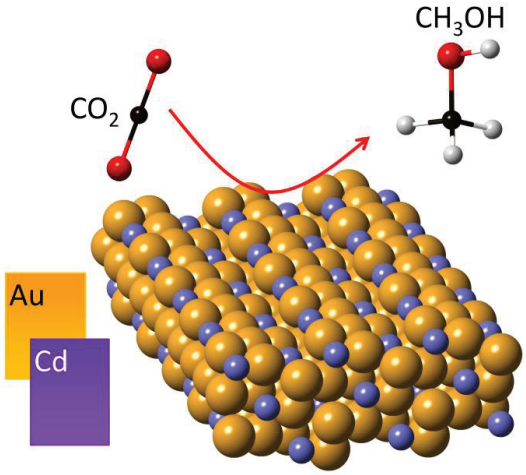

Figure 7.8: Model of $Au_3Cd(211)$ surface showing CO_2 reduction to CH_3OH. Figure made by Juan Maria Garcia Lastra.

7.2 CO_2 electro-reduction on Au_3Cd bulk alloy and Cd/Au surface alloy

On the basis of the theoretical screening study described above, we set up the experiments on a sheet of Au_3Cd bulk alloy consisting of CO_2 bulk electrolysis in various electrolytes and post-reaction surface and adsorbates characterisation. The electrolysis involved setting up numerous detection and quantification methods, many of which were new to our laboratory: including gas and liquid chromatography, NMR spectroscopy, static headspace analysis.

As an alternative to using the bulk polycrystalline alloy sheet of Au_3Cd, we also prepared and tested a Cd/Au surface alloy with Cd coverage in range of 0.1 – 0.3 ML. As described in Section 2.1.4, the Cd/Au(111) was previously investigated by Stickney and coworkers, who explored the relationship between the Cd coverage and surface structure by STM imaging.[34] The DFT calculations shown in Section 7.1 suggest that the CO_2 reduction activity of a Cd decorating the step edge of Au(211) or Cd/Au surface alloy on a bulk Au(211) surface should be almost as high as that of a bulk alloy.

7.2.1 Characterisation of Au_3Cd bulk alloy sheet

X-ray crystal diffraction

The initial X-ray diffraction measurements done on Au_3Cd sheet indicated several reference crystallographic phases, which are also listed on the Inorganic Crystal Structure Database[160]:

- Pt_3Pu, *cubic* (*Pm-3m*, a=b=c= 4.107 Å)
- Au_4Zr, *orthorhombic* (*Pnma*, a=5.006 Å, b=4.845 Å, c=14.294 Å)
- Au_3Cd, *tetragonal* (*P4/mmm*, a=b=4.107 Å, c=4.138 Å)[161]

The primitive cubic phase described above would have a similar structure to face centred cubic (FCC) Au, albeit with one in four Au replaced with Cd. Given that Au has a lattice parameter of 4.07 Å, Au_3Cd would exhibit tensile strain of ca. 1% relative to Au[162] as shown in equation 7.6:

$$\delta = \frac{4.11\ (\text{alloy}) - 4.07\ (\text{Au})}{4.07\ (\text{Au})} \approx 1\% \qquad \textbf{(7.6)}$$

Angle Resolved X-ray Photoelectron Spectroscopy

Figure 7.9 (a) represents a typical angle resolved X-ray photoelectron spectroscopy depth profile of the surface upon sputter cleaning. Both Cd *3d* and Au *4f* lines are observed at the surface, ratio being approximately the expected 3:1, i.e. surface concentration of Cd was in range of 20-27 %.

After sputter-cleaning, the sample is normally transferred from the UHV chamber into the electrochemical cell with inevitable, but short exposure to the air (lasting no longer than 2 min). In order to simulate the effect of air exposure on the sample, we recorded the depth profile after the exposure of the clean sample to the air for 10 min, shown on Figure 7.9 (b). Carbon and oxygen lines are observed at the very surface, arising from adventitious contamination. However, the most important observation is that the amount of Cd at the surface does not decrease significantly. Upon immersion to the cell, the impurities should be removed by performing cyclic voltammetry.

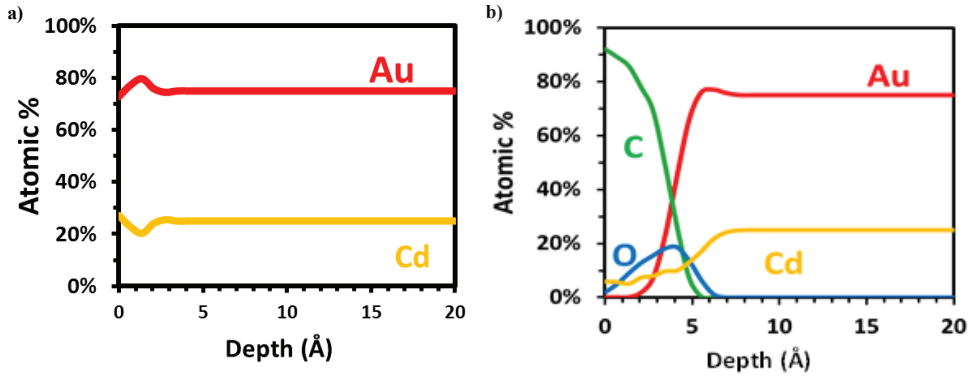

Figure 7.9: (a) Angle Resolved -XPS depth profile of Au_3Cd sheet following its sputter-cleaning in UHV chamber and (b) Angle Resolved – XPS depth profile after the air exposure for 10 min. The XPS measurements were performed by Paolo Malacrida (CINF).

Electrochemical Impedance Spectroscopy for Roughness Factor Estimation

For purpose of accessing the roughness factor of a sputter-cleaned Au_3Cd sheet, we compared the capacitances measured on a smooth polycrystalline gold disc electrode, prepared in previously described manner to ensure the roughness factor of 1 and the capacitance measured on the same disc electrode with depositing the amount of cadmium onto gold, corresponding to coverage of 0.25 ML.

Figure 7.10 shows a set of double layer capacitance measurements performed on the three electrodes using electrochemical impedance spectroscopy at various potentials in CO_2 saturated 0.5 M $KHCO_3$ with pH 7.7.

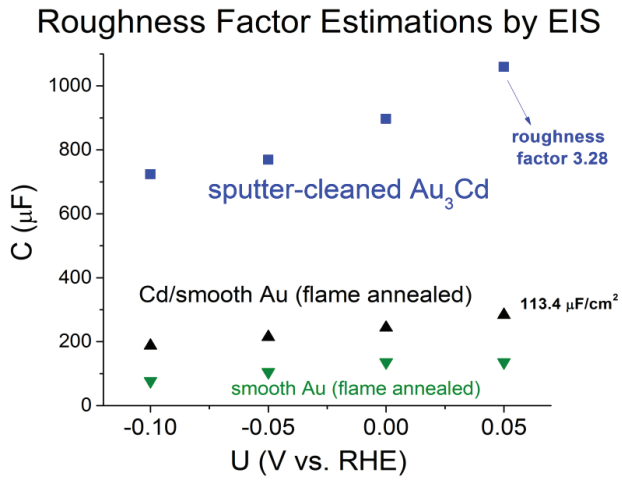

Figure 7.10: Demonstration of use of the electrochemical impedance spectroscopy (EIS) for estimations of the roughness factor, i.e. the real surface area of a bimetallic catalyst via measuring the double layer capacitance. Green triangles correspond to values of double layer capacitance of a smooth, flame-annealed polycrystalline gold surface; black triangles correspond to a flat Cd/Au surface alloy; blue squares correspond to the sample of unknown roughness (sputter-cleaned Au_3Cd sheet). The measurements are done in CO_2 saturated 0.5 M $KHCO_3$ in the potential region where neither cadmium dissolution nor hydrogen evolution should have a significant effect on the double layer capacitance.

The potential range was chosen with the respect to the dissolution potential of Cd and in the region where there is no hydrogen evolution activity, in order to avoid the effect of these processes on the capacitance measurements. At each electrode potential, an EIS spectrum was taken within ac frequency range from 50 Hz to 1MHz.

Using the double layer capacitance value obtained for 0.25 ML Cd/Au(pc) at 0.05 V vs. RHE – 113.4 $\mu F.cm^{-2}$, we estimated the roughness factor of a Au_3Cd sheet cleaned by sputtering to be ~3.3.

7.2.2 CO_2 electrolysis results on Au_3Cd

The CO_2 electrolysis measurements on Au_3Cd bulk alloy are performed in electrochemical cell in 6-8 mL of electrolyte (CO_2 saturated 0.5 M $KHCO_3$, pH 7.6) in a closed system. The electrolysis was running for 30 min, or 60 min in cases of very low current densities. The measurements on Au_3Cd sheet in this section were conducted in sets and not each independently. Once sputtered, the Au_3Cd sheet was introduced to the cell and held under potential control, so no Cd dissolution could occur. On the other hand, the potential was chosen according to the magnitude of the cathodic current, usually around -0.2 V vs. RHE. This ensured that no products were systematically omitted in our analysis. The electrolysis data was recorded by lowering the potential to the required value for a fixed amount of time. The data was recorded in two sets, whereby before each set the Au_3Cd sheet was sputter-cleaned. In first set, the electrolysis started at least negative potentials, taking each next measurement at more negative potential, in steps by 200 mV: -0.3 V, -0.5 V, -0.7 V and -0.9 V. Second set was recorded in opposite order, as follows: -0.8 V, -0.6 V and -0.4 V. In that manner, the effect of electrode pretreatment was minimised. The Ohmic drop correction was applied during the measurements automatically within the software, accounting for 85 % of the iR drop, whereby the rest 15 % were corrected for manually.

Upon the electrolysis at a certain potential, the product analysis from both gas and liquid samples were done, showing three major reaction products: hydrogen, CO and formate. The electrolysis charge balanced the quantified products with ± 5 % discrepancy in most of the cases. Occasionally, up to 15 % unbalanced charge was observed. In order to clarify whether this was a random leak of the gaseous products from the system or a possible undetected liquid product, we employed the headspace analysis using gas chromatography (see section 3.6). Notably, despite the sensitivity of this technique, we could not detect any of the small organic molecules reported in earlier studies[15,39] as CO_2 reduction products.

The Faradaic efficiency towards CO, formate and H_2 production during the CO_2 electrolysis measurements on Au_3Cd and Au is shown on the upper panels on Figure 7.11, from -0.3 V to -0.9 V RHE (the data for pure Au was also shown in Figure 6.5). On the lower panels on Figure 7.11, the respective partial current densities for these products are shown.

In contrast to the DFT predictions, the partial current densities, and hence Faradaic efficiency, towards CO evolution was actually higher for Au, than Au_3Cd. On the other hand, the partial current density towards H_2 evolution is remarkably similar between Au and Au_3Cd. Interestingly, the partial current densities towards formate production are roughly two- to threefold higher on Au_3Cd than Au in potential region from -0.4 V to -0.8 V.

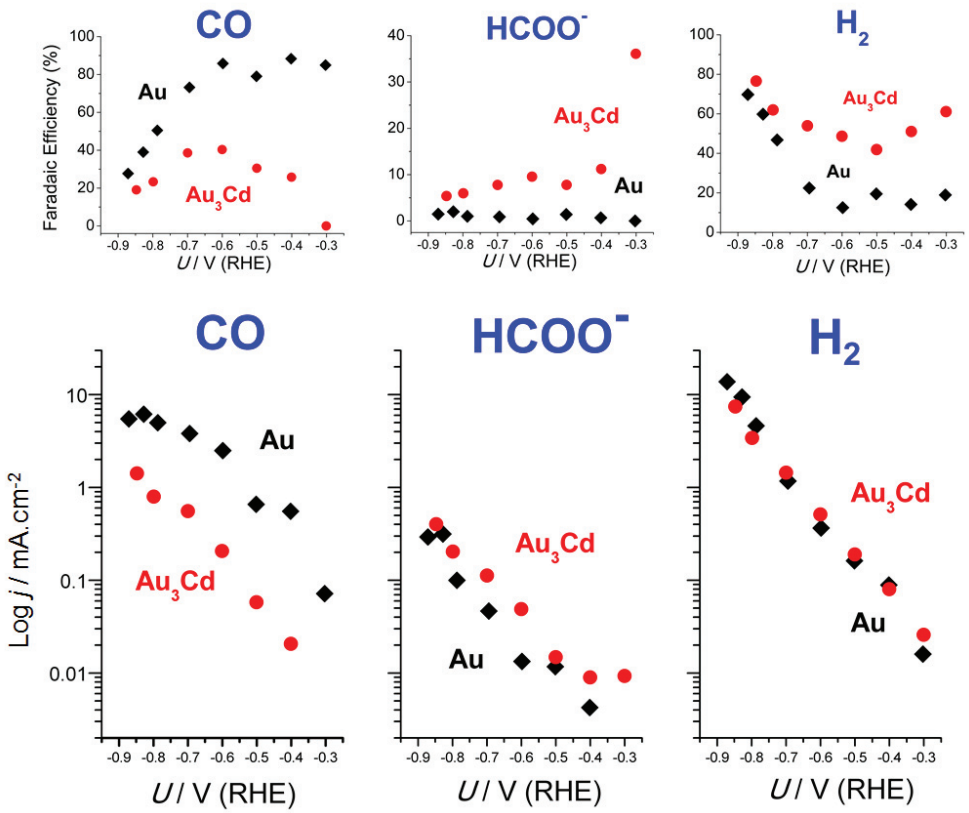

Figure 7.11: (*Upper panels*) Faradaic Efficiencies for CO_2 electro-reduction on a sheet of bulk alloy Au_3Cd relative to polycrystalline Au for the three major products: CO, $HCOO^-$ and H_2. (*Lower panels*) Partial current densities of bulk alloy Au_3Cd relative to polycrystalline Au for the three CO_2 reduction products: CO, $HCOO^-$ and H_2. Note current density is plotted on logarithmic scale. The current normalisation involved use of data obtained from the electrochemical impedance spectroscopy (as roughness factor for Au_3Cd sheet we used 3.3 and for polycrystalline Au sheet 1.5). The electrolysis was done in 1 bar CO_2-saturated 0.5 M $KHCO_3$ at pH 7.6. The data points were recorded in two sets, before each the Au_3Cd electrode was sputter-cleaned. The sets were as follow: -0.3 V, -0.5 V, -0.7 V and -0.9 V. Second set was done in following order: -0.8 V, -0.6 V and -0.4 V.

7.2.3 Post reaction characterisation of Au_3Cd sheet by AR-XPS

Figure 7.12 (a) shows a depth profile obtained on a Au_3Cd sheet after its brief exposure (30 seconds) to the electrolyte without potential control, and then drying in a stream of Ar. At the very surface there are traces of carbon (C) and oxygen (O) lines, presumably from organic contaminants that

would have accumulated during the transfer from the cell to the UHV chamber. The traces of potassium (K) are from the electrolyte.

The Cd in the bulk showed a Cd $3d_{5/2}$ XPS line at a binding energy of 404.6 eV, consistent with metallic Cd.[163] However, closer to the surface another Cd species exists, with a shift of 1.2 eV towards higher binding energies; this is consistent with CdO. Typically on Au_3Cd, the open circuit potential in CO_2 or Ar-saturated bicarbonate buffer came to +0.3 V vs. RHE. At such potentials, Cd is unstable against dissolution. However, the presence of Cd right up to the surface layer shows that the dissolution is not extensive (c.f. XPS depth profiles performed using the same instrument for acid-leached pure Pt overlayers on bulk Pt alloys).[164]

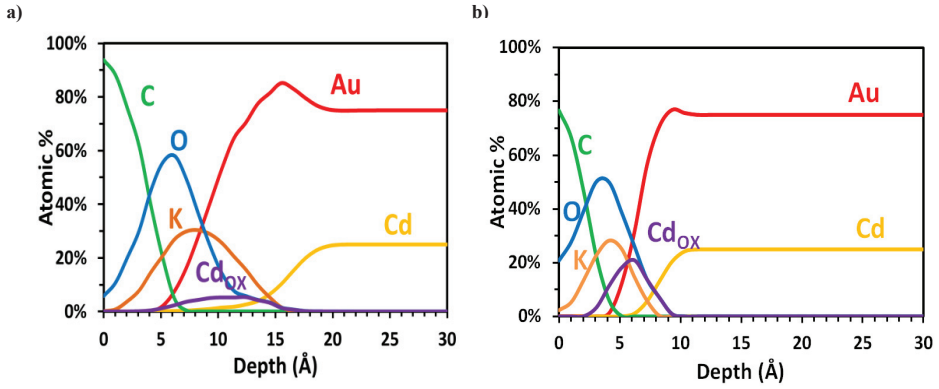

Figure 7.12: (a) Angle Resolved -XPS depth profile of Au_3Cd sheet after its exposure to the electrolyte (0.5 M $KHCO_3$, pH 7.5) at open circuit potential (ca. +0.3 V vs. RHE, 0.35 V of overpotential for Cd dissolution) for 30 seconds; (b) Angle Resolved – XPS depth profile on Au_3Cd sheet after the bulk CO_2 electrolysis at -0.5 V vs. RHE in 0.5 M $KHCO_3$, pH 7.5 (electrolyte removed rapidly from the cell and the sample dried in Ar flow). The XPS measurements were performed by Paolo Malacrida (CINF).

The plot in Figure 7.12 (b) shows a depth profile obtained on a Au_3Cd sample following a bulk CO_2 reduction electrolysis measurement at -0.5 V vs. RHE in 0.5 M $KHCO_3$. Although the figure is the output of a single measurement, similar profiles were obtained of the bulk Au_3Cd sample following a number of different electrolysis experiments, including electrolysis in CO-saturated 0.1 M KOH (see section 7.3); for each measurement the profile was remarkably similar to Figure 7.12 (b). To remove the sample, the electrolyte was flushed out under potential control, and the sheet was dried in a stream of Ar purge. The profile is qualitatively very similar to the sample exposed to open circuit, albeit with an apparently thinner surface layer of Au and CdO_x. The absence of K could be attributed to a lower amount of residual electrolyte at the surface following emersion from the electrolyte than for the sample shown in Figure 7.12(a). It should be noted that the depth profiles are generally more

qualitative than quantitative. A more quantitative measure of the composition can be made by comparing the Au:Cd and Au:CdO_x ratio of the photoelectrons emitted at 21 degrees to the sample normal; this showed that Au:Cd ratio was 6:1 at the surface, increasing as going deeper, i.e. to higher angles. It is likely that under reaction conditions, i.e. below – 0.3 V vs. RHE at pH 7.5, the Cd would be reduced to the metallic form, given that the standard potential for Cd reduction is -0.4885 V vs. NHE[34] (i.e. -0.05 V vs. RHE at pH 7.5). In the acidic and neutral pH region, surface Cd will be in equilibrium with Cd^{2+} ions, while at higher pH values, the stable phase at positive potentials is $Cd(OH)_2$. In summary, this profile provides a strong indication that there is a significant amount of Cd in the surface region of Au_3Cd during bulk electrolysis conditions. Even so, it cannot provide information about the exact composition of the surface layer.

7.2.4 CO_2 electrolysis results on Cd/Au surface alloy

There are several advantages for this approach over testing the bulk alloy, namely (a) Cd is deposited in the metallic form, and it can be tested for CO_2 reduction without loss of potential control or exposure to the air (b) the amount of Cd at the surface can be controlled (c), also, from a practical viewpoint, it is much less time consuming to prepare the Cd/Au surface alloy, enabling a higher throughput of samples.

On Figure 7.13, the partial current densities for CO, formate and H_2 are shown after CO_2 reduction on 0.1 ML Cd/Au surface alloy in 0.5 M $KHCO_3$, at pH 7.6. The surface activity of gold does not seem to be affected by addition of rather small submonolayer amounts of cadmium. The partial current densities for hydrogen and CO overlap with the values obtained on polycrystalline gold electrodes. The main difference results to be a slightly higher activity of 0.1 ML Cd/Au for the production of formate.

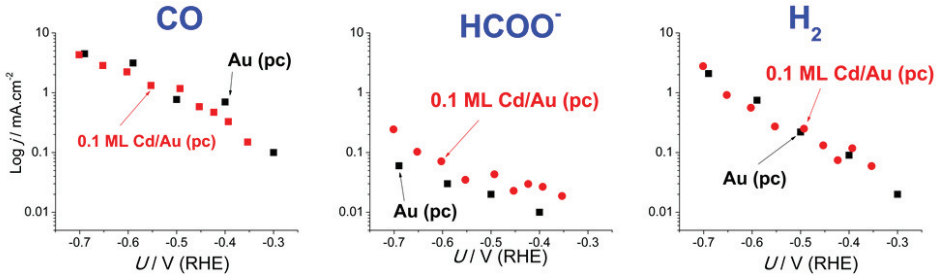

Figure 7.13: Partial current densities for CO_2 reduction in 0.5 M $KHCO_3$ at pH 7.6 on 0.1 ML Cd/Au surface alloy compared to polycrystalline Au. Each point represents an independent measurement lasting 30 min. The data is recorded in two sets – first (-0.35 V, -0.43 V, -0.5 V, -0.6 V and -0.7 V) and second set (-0.65 V, -0.55 V, -0.45 V and -0.4 V). Note the logarithmic scale of partial current densities.

In order to explore the possibility that an increased concentration of products may be formed over longer time periods, extended electrolysis experiments were performed on 0.15 ML Cd/Au surface alloy at a potential of -0.4 V. Only formate was detected; the formate concentration kept on increasing as shown in Figure 7.14 (a). The data also indicated that the efficiency for formate production did not change over time (Figure 7.14 b). No other products were detected at any of the reaction times, suggesting that no further formate reduction was occurring.

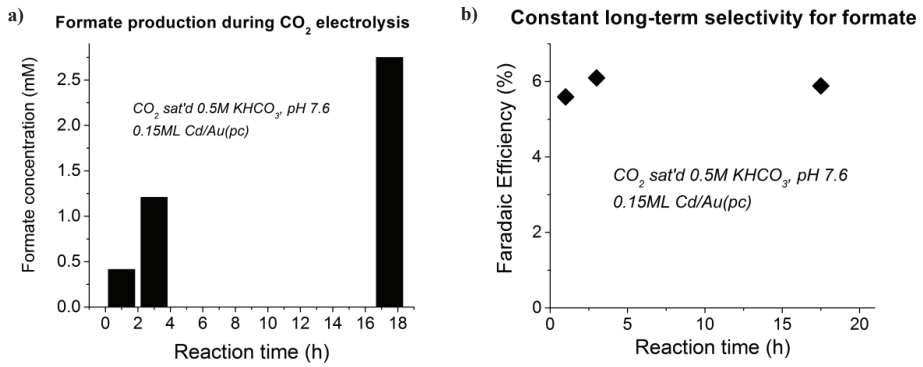

Figure 7.14: Long-term formate production during CO_2 electrolysis on 0.15 ML Cd/Au surface alloy at -0.4 V vs. RHE. (a) HPLC measured constant increase in formate concentration (cumulative values); (b) constant Faradaic efficiency of ca. 6 % over 18 hours of electrolysis.

7.2.5 Post reaction AR-XPS analysis on Cd/Au

Performing angle resolved XPS analysis on gold electrode containing 0.1 ML of cadmium after the CO_2 bulk electrolysis showed only presence of Au *4f* peak. The amount of cadmium present at the surface was undetectable, since no peak of Cd *3d* line was measured. On the other hand, the cyclic voltammetry in acidic media (0.1 M H_2SO_4) after electrolysis confirmed the presence of 0.098±0.006 ML of cadmium (oxidation CV not shown), essentially the same charge as the amount deposited. Presumably, such a small amount of Cd dissolved from the surface, as soon as potential control was lost.

7.2.6 Summary of CO_2 electrolysis measurements on polycrystalline alloyed gold surfaces

The reproducibility of the CO_2 bulk electrolysis measurements, performed on bulk Au_3Cd alloy and various Cd/Au surface alloys, is shown on two separate plots in Figure 7.15. Plot (a) shows the Faradaic efficiencies, in range of potentials from -0.3 V to -0.9 V, referring to Au_3Cd. Plot (b) represents the Cd/Au surface alloy data points, recorded in range from -0.4 V to -1.0 V. The error bars were assigned based on at least three different measurements. The error bars along the x-axis are consequence of slightly values for the ohmic resistance (see section 3.3.4). The larger error bars on the y-axis are due to several different factors: catalyst exact composition and structure, slightly different pH values of the electrolytes as well as random hydrogen leaks during electrolysis. The composition of the surface alloy was aimed to reach values of 0.1 - 0.2 ML Cd/Au. However, the inaccuracy during the deposition process may occur, being cause of slight variations in cadmium coverage. Despite the error, the data obtained on the bulk alloy does not differ to large extent from the data obtained on surface alloy. We observed slightly higher CO production efficiencies on surface alloys relative to the bulk alloy. However, this could be due to a low concentration of Cd at the active site for CO evolution, so that the catalytic activity behaves like a linear combination of Au and Cd.

Additionally, our results can be compared with Hori's measurements on Cd adatoms on Au, shown in Table 2.3, Chapter 2.[62] Hori reports $j_{CO}/(j_{CO}+j_{HCOO^-})$ ratio to be 0.82 at a fixed total current density of -5 $mA.cm^{-2}$, reaching ~-0.72 V vs. RHE. In this work, for 0.1 ML Cd/Au surface alloy, at -0.7 V and total current density of ~-10 $mA.cm^{-2}$, the $j_{CO}/(j_{CO}+j_{HCOO^-})$ ratio is ~0.95. However, for Au_3Cd bulk alloy, at -0.7 V and total current density of ~-2.8 $mA.cm^{-2}$, the $j_{CO}/(j_{CO}+j_{HCOO^-})$ ratio is ~0.87. This indicates that Hori produced more formate, which may be expected for smoother gold surfaces.

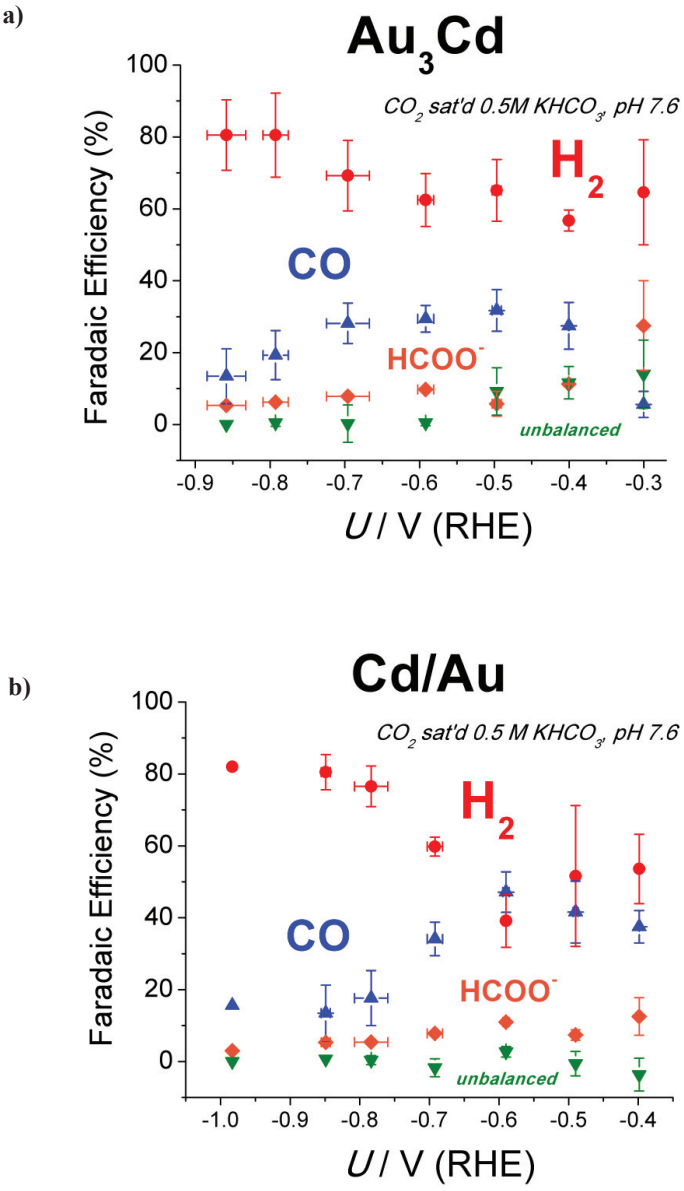

Figure 7.15: Reproducibility of CO_2 electrolysis results on – (a) bulk alloy Au_3Cd and (b) surface alloy Cd/Au with 0.1 - 0.2 monolayers of Cd. The plots show Faradaic Efficiencies for major products: H_2, CO and $HCOO^-$. To provide insight about the total charge balance, we present the unbalanced current efficiencies (green-colored triangles). The error bars are based on at least three separate measurements: on x-axis errors bars represent variations in ohmic drop. The error bars on the y-axis may be due to several different factors: catalyst exact composition and structure, slightly different pH values of the electrolytes as well as random hydrogen leaks during electrolysis.

The CO_2 reduction on Au alloyed with Cd, both bulk and surface alloy, leads to the three major products already observed on polycrystalline Au: H_2, CO and formate. The CO evolution activity increases in the following order: *Au_3Cd << Cd/Au surface alloy ≈ Au* (see Figure 7.16); this trend is the opposite to that which was predicted by the DFT calculations, which suggested the following trend: **Au(fcc) << Cd/Au step on Au < Au_3Cd** (see Figure 7.5). The hydrogen evolution activity is the same on all surfaces, i.e. *Au_3Cd ≈ Cd/Au surface alloy ≈ Au*, also in contrast to DFT predictions, which suggested the following trend **Au_3Cd < Cd/Au step on Au < Au(fcc)** (see Figure 7.7). The formate production activity is as follows: *Au* < *Au_3Cd ≈ Cd/Au surface alloy*.

Longer electrolysis experiments, for up to 18 hours, did not reveal the presence of any additional products, apart from formate. The increased rate of formate production on Cd-containing surfaces is not completely unexpected, given that Hori and coworkers reported formate production on pure Cd surfaces[15]. It also raises the question of whether formate could be acting as a site blocker, which could explain the lower than expected CO_2 reduction activity. This latter possibility will be investigated in more detail later in this chapter.

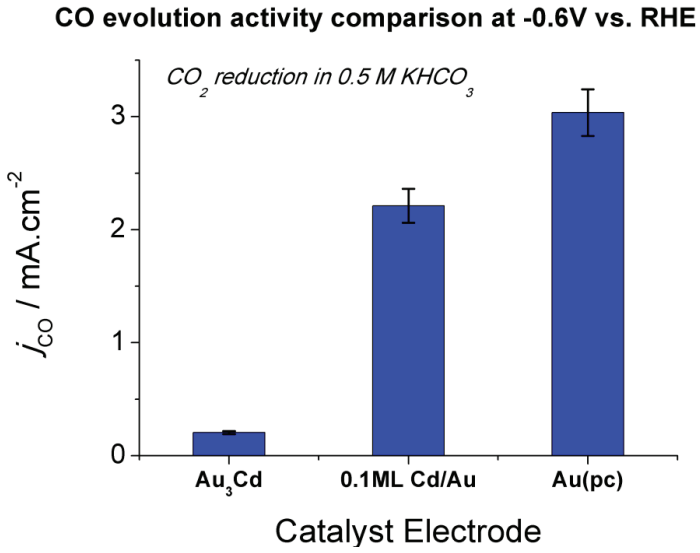

Figure 7.16: Comparison of partial current densities for CO evolution reaction at -0.6 V vs. RHE measured on Au_3Cd, 0.1 ML Cd/Au surface alloy and polycrystalline Au. CO_2 reduction was performed in 0.5 M $KHCO_3$.

7.3 CO electro-reduction on Au_3Cd bulk alloy and Cd/Au surface alloy

Given that no products apart from CO and formate were formed when using CO_2 as an initial reactant, the logical next step was to use CO as a starting reactant. This poses several advantages over the use of CO_2, namely (a) at any given potential, with respect to RHE, it would increase the driving force for the formation of several products, such as methanol, methane, acetaldehyde, ethylene and n-propanol (see Figure 2.7 (b) in Section 2.2); (b) the limiting potentials for gas phase CO reduction to *CHO are shifted to less negative values (see Table 7.1, Section 7.1); (c) it would avoid any additional barriers or ensemble effects for the reduction of CO_2 to CO (pertinent examples in relation to methanol oxidation on Pt[165]) (d) it could also avoid the formation of any site blocking species related that could be formed from CO_2 rather than CO, in particular formate, as discussed above.

7.3.1 CO electrolysis results on Au_3Cd

Figure 7.17 shows data points corresponding to partial current densities for hydrogen evolution measured during the electro-reduction of CO in various electrolytes on Au_3Cd bulk alloy sheet. Electrolysis was performed in acidic – 0.1 M $HClO_4$ (pH 1), neutral – phosphate buffer (pH 6.6), slightly alkaline media – CO saturated 0.5 M $KHCO_3$ (which adopts a stable bulk pH value of 8.7) and alkaline media – CO saturated 0.1 M KOH (pH 12.8). In perchloric acid and phosphate buffer, the surface showed 100±5 % selectivity towards hydrogen evolution. In the case of a bicarbonate buffer and KOH, traces of formate were measured in range of 1-7 % of Faradaic efficiency. Formate would probably be produced from the chemical decomposition of the CO_2, contained in the bicarbonate buffer.[146] On the other hand, Figure 7.17 shows the expected trends in dependence of hydrogen evolution activity on the electrolyte pH value.[82,166,167] The reason for higher activity for hydrogen evolution in KOH than in $KHCO_3$ at high current densities is most likely due to local pH changes, as previously described for Au in Section 6.3.2 (see Figure 6.7).

Additionally, in KOH, we present two sets of data points carried out using Au_3Cd: (1) *green open squares* – data points obtained using phosphate buffer solution in CE and REF compartments, where our major focus was quantification of the gaseous products (see Section 6.3.2); (2) *green filled squares* – data points referring to use of solely KOH and major focus on liquid product analysis. As previously discussed for Au (see Figures 6.8 and 6.9), presence of small amount of phosphate anions in KOH suppresses the hydrogen evolution activity.

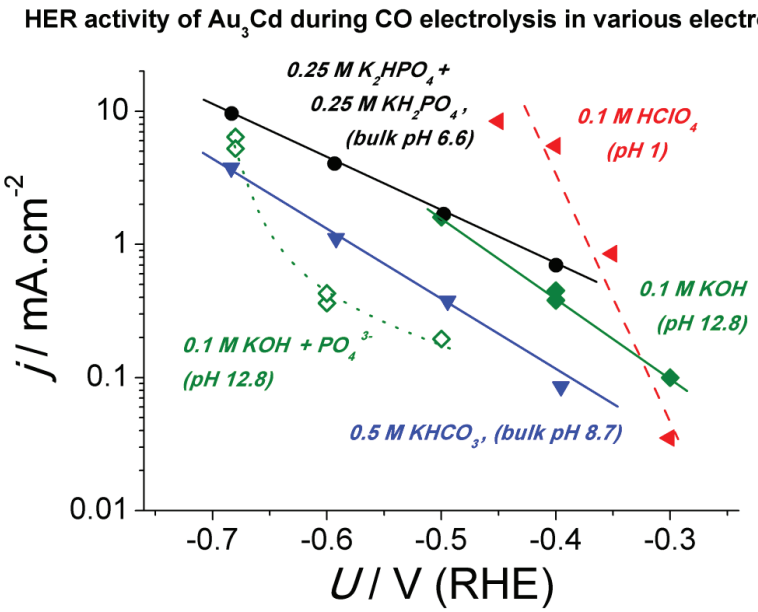

Figure 7.17: Partial current densities towards hydrogen evolution on Au_3Cd bulk alloy in various electrolytes during CO electrolysis: (1) CO-saturated 0.1 M $HClO_4$ at pH 1 (red triangles, red dashed line), (2) CO-saturated 0.25 M K_2HPO_4 + 0.25 M KH_2PO_4 at bulk pH 6.6 (black circles, black solid line), (3) CO-saturated 0.5 M $KHCO_3$ at bulk pH 8.7 (blue triangles, blue solid line) and (4) CO saturated 0.1 M KOH at pH 12.8 (green filled squares, green solid line) and (5) CO-saturated KOH with trace amounts of phosphate anions at pH 12.8 (green open squares, green dotted line). Note logarithmic current density scale. Current was normalised against the surface area established by electrochemical impedance spectroscopy measurements (roughness factor 3.3). The lines are plotted to guide the eyes.

In order to confirm the presence of any minor products that could account for the unbalanced charges obtained from the gas phase analysis, we focused in particular on liquid products analysis with high sensitivities: nuclear magnetic spectroscopy and static headspace analysis connected to the gas chromatograph (described in detail in Chapter 3). These electrolysis measurements were performed on Au_3Cd at low overpotentials (-0.5 V, -0.4 V and -0.3 V) for 60 min to enable more accurate product detection. Figure 7.18 shows the results of ^{1}H-NMR spectroscopy product analysis on aliquots after CO reduction on Au_3Cd at -0.5 V (a) and -0.4 V vs RHE (b). On the plots, the total current densities are shown, corresponding ca. 95 % of current efficiency towards H_2. Both NMR spectra in Figure 7.18 show a feature centered around 4-5 ppm corresponding to the water peak. Additional two peaks, in the region between 6.5 and 7.2 ppm correspond to hydrogen bound to a phenol molecule, a which is often used as an internal standard for the measurements (see more details in Experimental Methods – Chapter 3). Trace amounts of formate were detected at ~8.4 ppm in both spectra, corresponding to up to 5 % of current efficiency. Otherwise, the spectra do not reveal any of the possible interesting products such as alcohols, aldehydes or carboxylic acids.

a) Au_3Cd, -0.5V vs. RHE, -1.6 $mA.cm^{-2}$

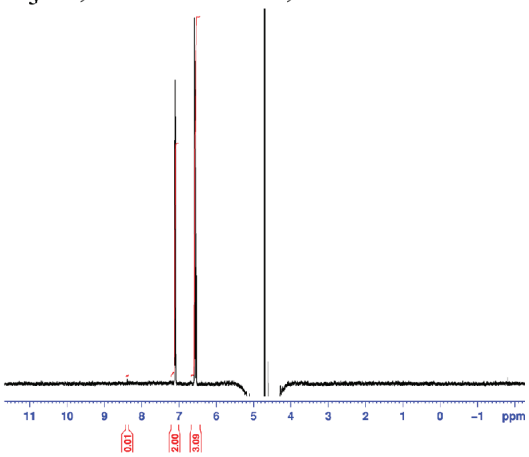

b) Au_3Cd, -0.4V vs. RHE, -0.45 $mA.cm^{-2}$

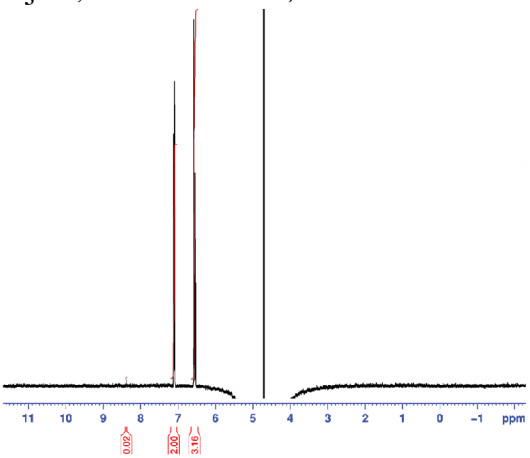

Figure 7.18: ^{1}H-NMR CO reduction product analysis done on aliquots taken from CO electrolysis in 0.1 M KOH at -0.4 V and -0.5 V on Au_3Cd bulk alloy sheet. Sharp feature around 4.7 ppm corresponds to water peak. The features at 6.6 ppm and 7.2 ppms correspond to the hydrogen atoms belonging to the internal standard (1 mM phenol solution). Formate is detected at 8.4 ppm. The values in red depict the peak area quantification relative to the internal standard.

Moreover, we employed static headspace analysis as other product detection techniques to obtain information about very small product concentrations. Figure 7.19 provides a typical chromatograph obtained upon analysis performed on aliquot samples taken after CO reduction on Au_3Cd bulk alloy sheet at -0.3 V and -0.4 V vs. RHE. Due to the high sensitivity of the method, even very small amounts of gases dissolved in the air, such as methane, are detected (at retention time of 2.4 min). No significant concentrations of either methanol or other interesting products are detected.

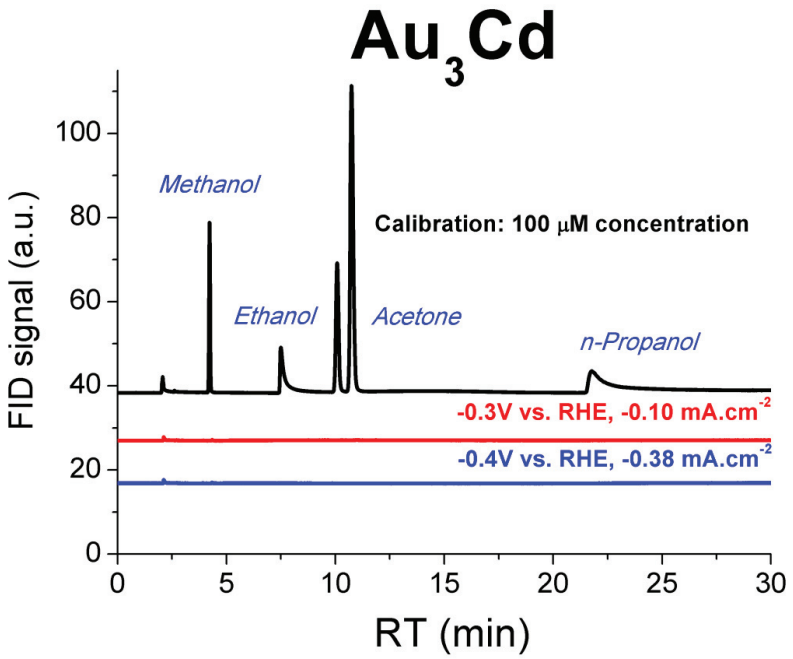

Figure 7.19: High sensitivity static headspace analysis -aliquots taken from CO electrolysis in 0.1 M KOH on Au_3Cd at -0.3 V and -0.4 V. The total current densities related to the 60 min long electrolysis measurements are shown on the plot. Calibration analysis containing 100 mM concentration of methanol, ethanol, acetone and n- propanol is contrasted to the data.

7.3.2 CO electrolysis results on Cd/Au surface alloy

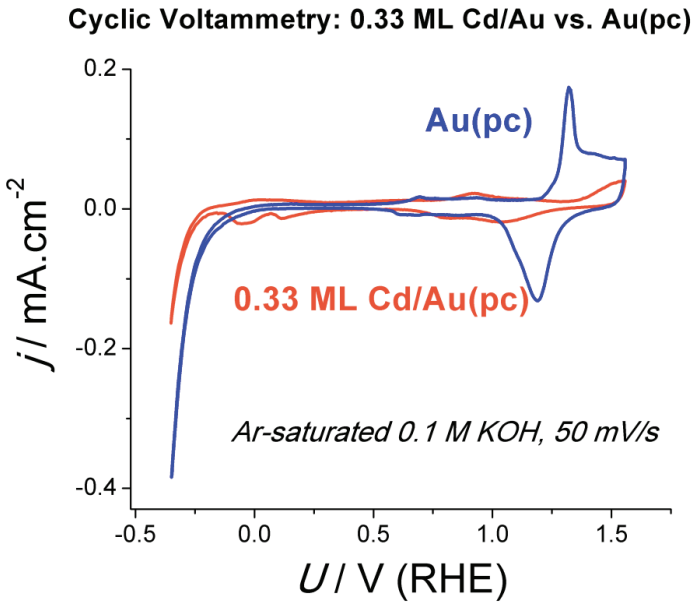

Figure 7.20: Comparison of independent cyclic voltammograms obtained on a surface alloy (0.33 ML Cd/Au) and on pure polycrystalline Au in Ar-saturated 0.1 M KOH, at 50 mV/s.

Figure 7.20 provides a comparison of cyclic voltammograms on 0.33 ML Cd/Au surface alloy and pure Au in alkaline media at 50 mV/s. The features obtained on surface alloy correspond to surface Cd oxidation to for surface $Cd(OH)_2$. Given that $Cd(OH)_2$ is insoluble at pH 13, the Cd would not dissolve into solution. To explore whether there was a change in the amount of Cd upon cycling in an alkaline environment, we performed Cd oxidation in acidic media and established the same cadmium oxidation charge as during deposition, confirming no Cd was lost in alkaline media. Alloyed gold surface exhibits a slight shift of the cathodic current to more negative potentials. However, one has to bear in mind that these are transient currents and they tend to decrease to a certain constant value during chronoamperometry.

The electrolysis results represented on Figure 7.21 show similar partial current densities for hydrogen on alloyed gold surfaces compared to pure Au in 0.1 M KOH at pH 12.8. The plot provides a comparison of hydrogen evolution partial current densities among the bulk alloy sheet (Au_3Cd), surface alloy (0.16 ML Cd/Au) and polycrystalline Au, on logarithmic scale. Within the potential range tested, there are almost no differences in activity for HER between the surface alloy and the polycrystalline gold. We observed however higher current densities for hydrogen evolution on the

bulk alloy sheet. Slightly differrent trends in the hydrogen evolution activity are observed during CO reduction in alkaline media compared to the CO_2 reduction in neutral media. Bulk alloy sheet in alkaline media appears to be more active for producing hydrogen. Overall measured trend in activity is as follows: *Au_3Cd > Cd/Au surface alloy ≈ Au*.

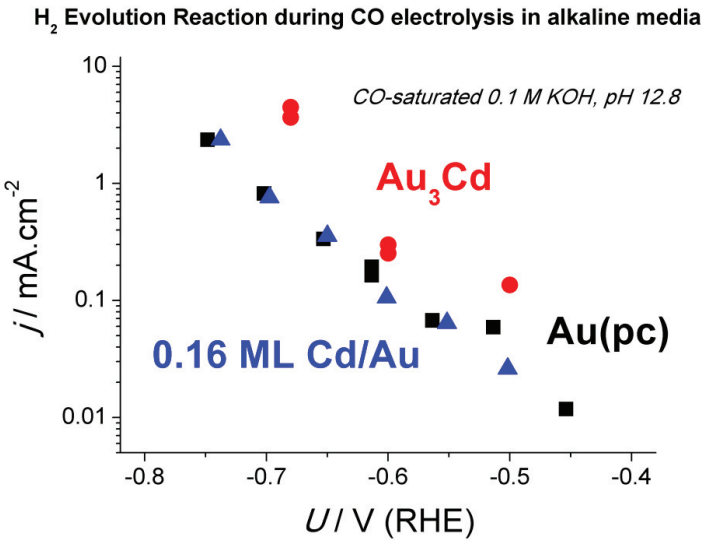

Figure 7.21: Comparison of hydrogen evolution activity on Au_3Cd bulk alloy, 0.16 ML Cd/Au surface alloy and polycrystalline Au in alkaline environment (0.1 M KOH, pH 12.8). Data points for Au_3Cd and Au(pc) are made as consecutive measurements with the fresh electrolyte each time. Surface alloy was prepared by deposition for each measurement to ensure similar structure of the surface.

Similarly, formate production is comparable for surface alloyed gold and pure gold, whereby there are some differenes in comparison to the bulk alloy. The formate production activity can be ranked as follows: *Au ≈ Cd/Au surface alloy < Au_3Cd* (see Figure 7.22). A comparison of formate production activities on Cd/Au surface alloy, during CO_2 and CO reduction, is represented in Figure 7.23. Expectedly, formate production is an order of magnitude higher in activity in neutral relative to the alkaline environment.

Similar to the measurements on Au, using HPLC, we were able to detect trace amounts of fomaldehyde, up to 0.5% of Faradaic efficiency to formaldehyde, but on the edge of the detection limit of the equipment.

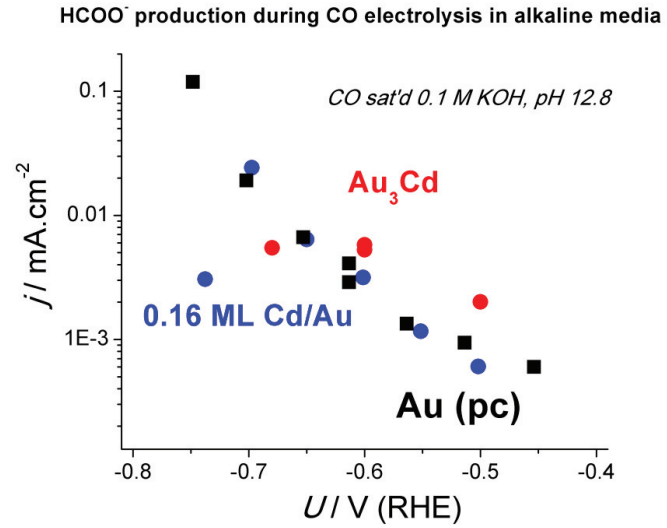

Figure 7.22: Comparison of formate production activity on Au_3Cd bulk alloy, 0.16 ML Cd/Au surface alloy and polycrystalline Au in alkaline environment (0.1 M KOH, pH 12.8). Data points for Au_3Cd and Au(pc) are made as consecutive measurements with the fresh electrolyte each time. The surface alloy was prepared by a separate deposition for each measurement, to ensure similar structure of the surface.

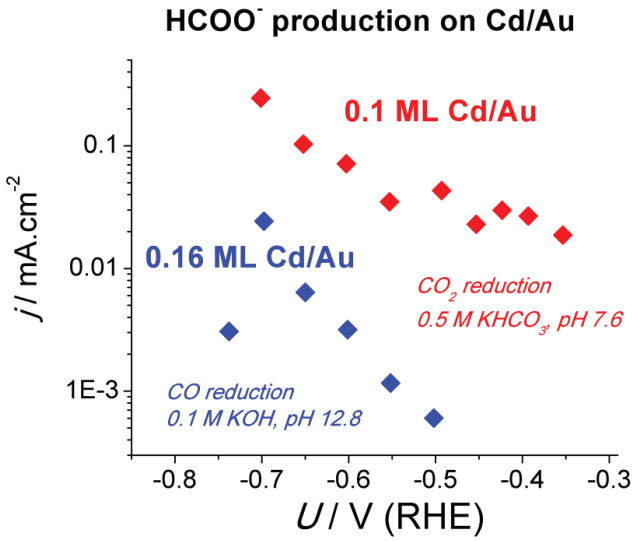

Figure 7.23: Comparison of formate production activities on Cd/Au surface alloy in CO_2-saturated 0.5 M $KHCO_3$ (pH 7.6) and in CO-saturated 0.1 M KOH (pH 12.8).

7.3.4 Post CO reduction AR-XPS analysis on Au_3Cd and Cd/Au

Similarly to previous post reaction characterisations of the electrodes, we used angle resolved XPS analysis for confirming the Cd presence at the surface on Au_3Cd and Cd/Au. In Figure 7.24, the depth profile obtained on the bulk alloy sheet after CO electrolyses in bicarbonate and phosphate buffer is shown (data from Figure 7.17). It exhibits a similar depth profile to the previously shown in Figure 7.12 (b). On the other hand, the surface alloy electrode showed presence of solely Au peaks, without any Cd detected.

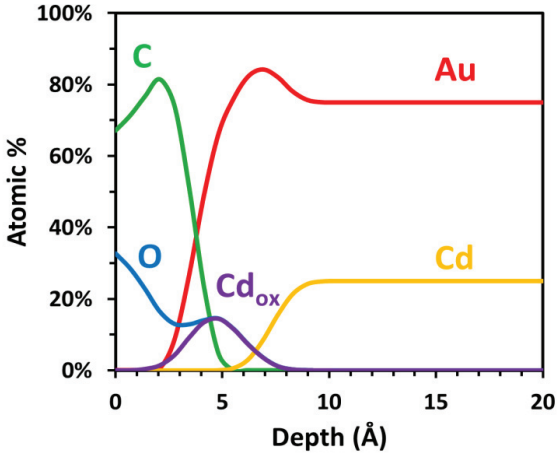

Figure 7.24: Angle Resolved – XPS depth profile on Au_3Cd sheet after the bulk CO electrolysis in 0.5 M $KHCO_3$ (pH 8.7) and 0.25 M K_2HPO_4 + 0.25 M KH_2PO_4 (pH 6.6), electrolyte removed rapidly from the cell and the sample dried in Ar flow.

7.3.5 CO reduction on high surface area catalysts

In order to increase the density of CdAu sites, we produced and tested some of the high surface area catalysts as substrate for Cd deposition: oxide derived Au – which has been successfully proven to be highly selective towards CO_2 electro-reduction[59] and nanoporous Au – tested for several other reactions.[59,89,90] We tried gold nanoparticles, oxide-derived gold and nanoporous gold leaves for CO reduction in alkaline media.

Figure 7.25 (a) shows a comparison of chromatograph obtained from the static headspace analysis for oxide derived gold (Au) in black (as reference) and Cd-alloyed oxide derived gold (Au) in blue, at -0.5 V and -0.6 V vs. RHE. The amount of cadmium deposited in each of these cases was arbitrary since it was challenging to accurately determine the surface area. However, a rough calculation based on estimated surface area and the deposition charge gives ~1/3 ML of Cd on oxide-derived Au.

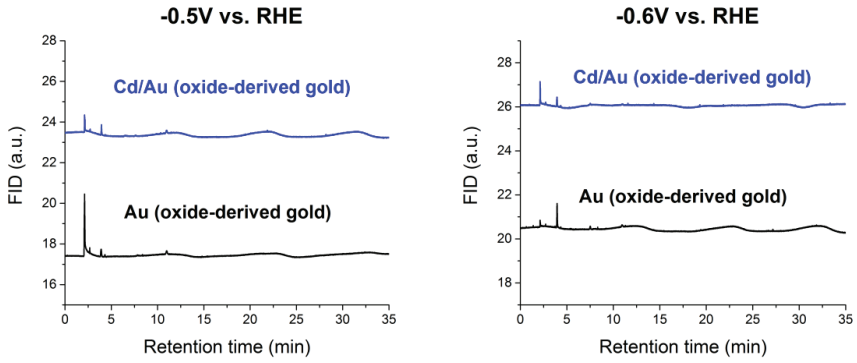

Figure 7.25: Static headspace analysis carried out on aliquots from CO electrolysis on oxide derived Au and surface alloy of Cd with oxide derived Au at (a) -0.5 V vs. RHE and (b) -0.6 V vs. RHE.

The chromatographs do not show any significant amounts of desired products. The peak at ca. 2.1 min retention time corresponds to the trace amounts of CH_4 present in the air, as discussed before in Chapter 3 and Chapter 6. On plot showing electrolysis at -0.6 V, a peak appearing in both Au and Cd/Au at retention time of 3.9 min corresponds to methanol. However, the concentrations on both Au and Cd/Au are the of range of several μM, transferred to Faradaic efficiency, it corresponds to less than 0.1 %. Nevertheless, the methanol concentration is slightly higher on Au than on Cd/Au.

Furthermore, we employed nanoporous gold leaves as support for Cd deposition, prepared as described in Section 6.3.2. Figure 6.11 (a) provides an idea of high roughness factor of nanoporous gold leaves (RF~100).

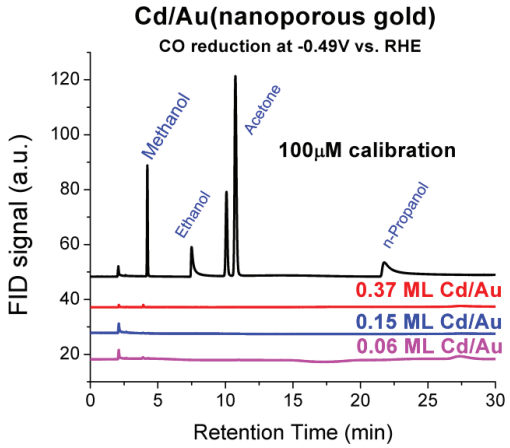

Figure 7.26: Results of the static headspace analysis carried out on aliquot samples from CO electrolysis at -0.49 V vs. RHE on nanoporous gold based surface alloys with different coverages of Cd. As reference, a calibration chromatograph is shown.

On the other hand, Figure 7.26 presented here, provides a comparison of a set of chromatographs obtained during the static headspace analysis of the aliquots obtained after CO reduction at -0.49 V vs. RHE on a Cd-alloyed nanoporous gold leaf. Various submonolayer amounts of Cd are deposited onto the nanoporous gold: 0.06 ML, 0.15 ML and 0.37 ML. However, the product analysis did not confirm any significant amounts of the volatile organic compounds. The addition of Cd to nanoporous Au did not increase the concentration of produced methanol.

7.3.5 Summary of CO electrolysis measurements on polycrystalline alloyed gold surfaces

The major product obtained during the CO electrolysis on bulk Au_3Cd sheet and Cd/Au surface alloy gold was hydrogen. The measured trends in hydrogen evolution activity were as follow: $Au_3Cd >$ *Cd/Au surface alloy* $\approx$ *Au*.

Trace amounts of formaldehyde are measured, however, being in range below 0.5% of Faradaic efficiency. The inevitable presence of CO_2 in alkalines electrolytes resulted in the production of formate with 1-7% current efficiency. Detailed product analysis of liquid phase products using tools with low detection limits, such as static headspace GC analysis and NMR analysis did not show any additional products of CO reduction. Cd was deposited on high surface area substrates such as gold nanoparticles, nanoporous gold leaves and oxide-derived gold electrodes. Despite the high surfacea areas, and the high sensitivity of the analysis tools, no significant concentrations of CO reduction could be detected on these nanostructured surfaces (less on Cd/Au than on Au), apart from trace amounts of methanol, far below 0.1% current efficiency.

7.4 Post reaction CV analysis on Cd/Au

7.4.1 Post reaction CVs after CO_2 bulk electrolysis

As in Section 6.4, we performed cyclic voltammetry in order to elucidate the possibility of *OCHO*(formate) or *CO adsorption.

In Figure 7.27, we provide a comparison of cyclic voltammograms, obtained on a surface alloy containing 0.27 ML of Cd on polycrystalline gold electrode. The stripping voltammogram, obtained after the CO_2 reduction reaction at -0.5 V vs. RHE, shows a broad anodic current feature starting at 0 V vs. RHE and finishing with a peak centered around +0.7 V vs. RHE (Figure 7.27, green solid line). To assign possible processes to these features, we performed independent stripping CVs, which could give a fingerprint of the oxidation currents of formate and CO, separately.

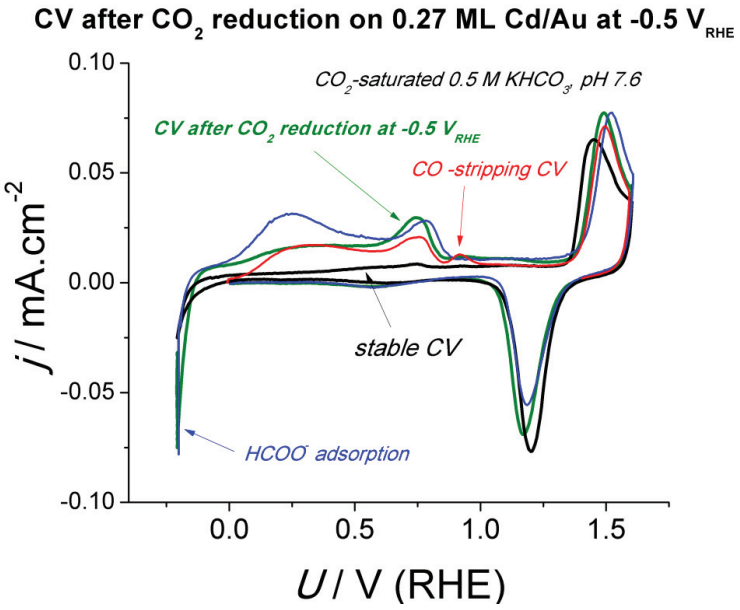

Figure 7.27: Comparison of independent cyclic voltammograms obtained on a surface alloy (0.27 ML Cd/Au) in CO_2-saturated 0.5 M $KHCO_3$ at 50 mV/s: (1) CV after CO_2 reduction reaction at -0.5 V vs. RHE and Ar-purge of electrolyte at -0.2 V (green solid line), (2) a CO-stripping CV following CO adsorption for 15 min at 0 V and 20-30 min Ar-purge (red solid line), (3) a formate stripping CV following $HCOO^-$ adsorption at -0.2 V for 30 min and exchange to formate-free electrolyte before ramping the potential to 1.6 V (blue solid line) and (4) stable CV obtained after several cycles following cadmium and intermediates co-oxidation (black solid line). The potentials are corrected for measured pH value of the 0.5 M $KHCO_3$ after Ar purge being ~ 9.

A typical CO-stripping CV was obtained after 15 min. of CO adsorption at 0 V followed by 20-30 min. of Ar-purge to remove any residual CO from the electrolyte (Figure 7.27, red solid line). The pH value of bicarbonate solution purged with Ar stabilised at ~ 9, where the stripping was carried out. Apart from the presence of the broad feature described previously, a small peak at potential around +0.9 V vs. RHE was recorded, most likely corresponding to the adsorbed CO oxidation. For obtaining a fingerprint of formate oxidation, we exposed the surface alloy (0.27 ML Cd/Au) to 50 mM $HCOO^-$ in CO_2-saturated 0.5 M $KHCO_3$ for 30 min. at -0.2 V (blue solid line) and exchanged to a fresh, formate free electrolyte.

In overall, the study suggests, that the broad feature ending with a peak centered at ~0.7 V may correspond to the oxidation of adsorbed formate. The CO stripping CV also resembles the formate stripping CV, suggesting that a considerable amount of formate is adsorbed at the surface alloy even at 0 V, ~ 0.2 V more positive than the redox potential for bulk formate formation from CO_2. Additionally, CO oxidises at somewhat higher potentials, presumably involving the peak at +0.9 V in Figure 7.27 (red solid line). However, this peak is not seen after the reaction(green solid line), suggesting a lower amount of CO is adsorbed at the surface alloy during the electrolysis at -0.5 V in neutral media than under the conditions of the stripping experiment. The separation of formate and CO oxidation features is consistent with the CVs performed on pure Au electrodes in alkaline media.[147] Moreover, the shift in oxidation potential of CO towards less positive values on Cd-alloyed gold is expected, because of a higher *OH coverage on Cd-containing surface relative to pure noble gold surface.[139,142]

7.4.2 Post reaction CVs after CO bulk electrolysis

In Figure 7.28, we present cyclic voltammetry, performed after a CO electrolysis measurement at -0.7 V vs. RHE on a surface alloy with composition 0.13 ML Cd/Au. Following the reaction at -0.7 V, the potential was kept at -0.15 V for 20-30 min, during which Ar was purged through the electrolyte to remove residual CO and other products in the bulk of the electrolyte. The first scan (red solid line) exhibits an anodic peak at +0.2 V vs. RHE that could correspond to phosphate anion adsorption (as previously introduced in Chapter 3). However, the absence of such anodic peak on bare Au surface (see Figure 6.8) indicates towards possible stabilisation of phosphate anions on Cd/Au surface. The peak at 1.0 V, as seen before, can be assigned to CO (or other carbon containing species) oxidation, as seen on Au in similar conditions in Figures 6.12 and 6.13.

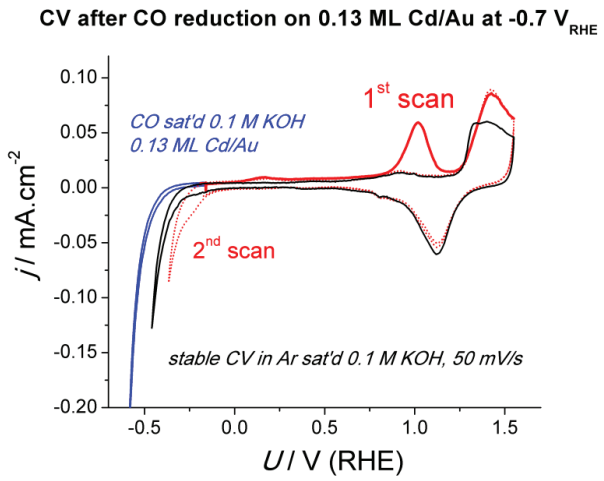

Figure 7.28: Cyclic Voltammetry on 0.13 ML Cd/Au after CO electrolysis at -0.7 V vs. RHE, in 0.1 M KOH, obtained in following procedure: (1) performing CO reduction at -0.7 V for 60 min (blue solid line), (2) purging for 20-30 min with Ar while holding at -0.15 V vs. RHE and (3) ramping the potential to 1.6 V vs. RHE (first scan is shown in red solid line, second scan is in red dotted line). Stable CV is shown in black solid line. The total stripping charge corresponds to 130 $\mu C.cm^{-2}$.

Interestingly, we observe here significant shifts in hydrogen evolution activity; initially, immediately after electrolysis conditions the hydrogen evolution potential at -0.075 $mA.cm^{-2}$ is most negative, ~-0.5 V (blue solid line), whereby after the stripping, it shifts positively, to ~-0.3 V (red dotted line). Judging by the shape of the cathodic feature after stripping (red dotted line), this effect could be related to phosphate desorption (a reversible peak to the feature at +0.2 V), as shown on Figure 6.8 for pure Au.

However, the increase in hydrogen evolution activity may be brought about by presence of $Cd(OH)_2$ at the surface, similarly observed by Markovic and co-workers on Pt single crystal surface covered with $Ni(OH)_2$.[82] A stable CV (black solid line) exhibits an intermediate hydrogen evolution activity (at -0.075 $mA.cm^{-2}$ reaching a potential of ~-0.4 V), possibly a combination of effect of both adsorbed phosphate or *OH.

7.5 DFT insight into adsorbate-surface interactions

7.5.1 *OCHO* and *OH adsorption induced site segregation and poisoning

As discussed earlier in Section 7.1.5, there exists a lower free energy pathway for production of formate than for CO evolution on both Au and Au_3Cd (see Figure 7.6). Figure 7.6 shows the free energy diagrams for CO_2 reduction to $HCOO^-$ as being downhill, both on Au(fcc) and Au_3Cd at -0.46 V vs. RHE. However, the experimentally observed Faradaic efficiencies for formate production on both catalysts are mostly in range of 0 - 10 %. Such low selectivities are likely caused by additional energy barriers for the formation of *OCHO*.
On the basis of our experimental observations that the Au-Cd alloy structures exhibit higher formate production activity, our collaborators, Heine Hansen and Jens Nørskov performed more detailed DFT calculations of different configurations of *OCHO* and HO* on the bulk Au_3Cd alloys, as shown on on Figure 7.29.

We note that the presence of co-adsorbing intermediates may stabilise each other, in particular CO*, HO* and H_2O*[117,139,142] This means that DFT based predictions of the absolute potential at which adsorbates such as HO*, or *OCHO*, will adsorb will have some degree of uncertainty. Nonetheless, relative changes in binding energies on different surfaces with the same orientation should be more accurately captured by DFT calculations.[127]

This new iteration of the DFT calculations includes the possibility of *OCHO* adsorption onto a site consisting of two contiguous Cd atoms. Such a configuration allows additional stabilisation of the *OCHO* intermediate relative to the mixed AuCd site. Theoretically, this could provide a driving force towards *OCHO*-induced rearrangements of the Cd-alloyed gold surface, causing Cd segregation and destruction of the AuCd active sites, or additionally, the poisoning of the active site.

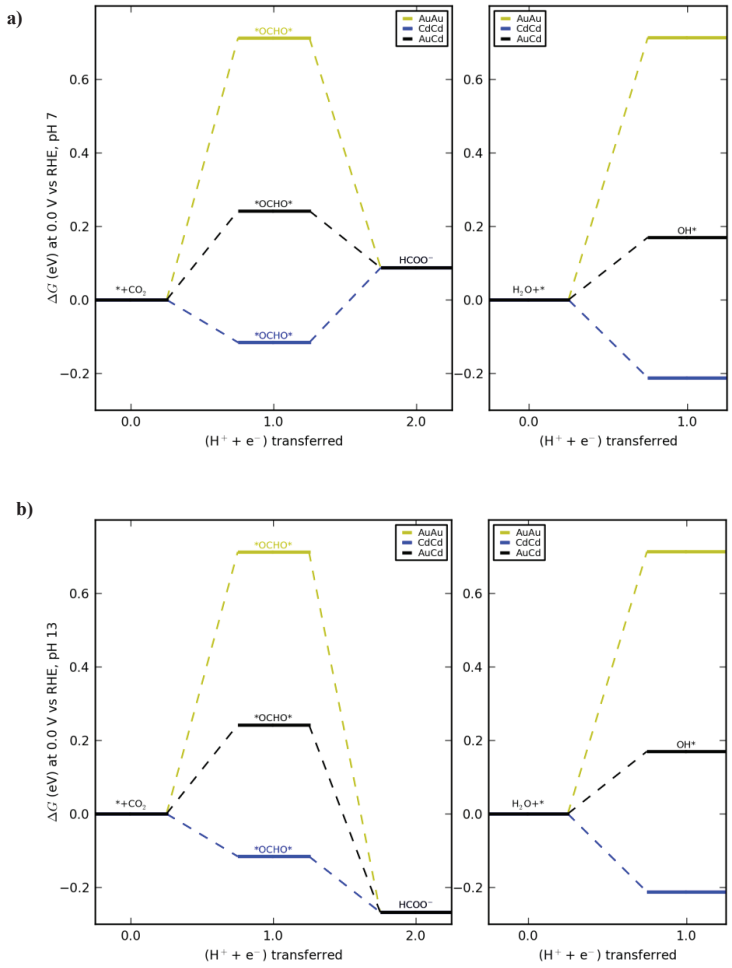

Figure 7.29: Comparison of the free energy diagrams for production of formate and for stability of adsorbed *OH on various sites – AuAu, AuCd and CdCd – at 0 V vs. RHE at pH 7 (a) and at pH 13 (b). AuAu, AuCd and CdCd refer to the step composition on a bulk Au_3Cd alloy – modelled as $Au_3Cd(211)$. Figure made by Heine A. Hansen.

The figure shows that, at least at 0 V vs. RHE, *OCHO* or HO* might rearrange AuCd sites to form CdCd sites. These intermediates, however, would be reduced further under operating conditions. The kinetics of these reactions will affect the extent of their coverage at the surface, which can be correlated to the extent of how much of the AuCd active sites are being reformed to CdCd sites. Should formate be adsorbed at Cd sites, then the surface would not be able to provide the predicted enhancement in CO evolution and CO reduction activity.

Figure 7.29 also shows that *OCHO* intermediate may be a better candidate for surface rearrangements and poisoning at neutral pH than in alkaline, since its removal from the surface is strongly exergonic in alkaline media. This agrees relatively well with the post-reaction CVs obtained in neutral media, suggesting formate coverage at the surfaces of both Au (Figure 6.12) and Cd/Au (Figure 7.27).

Similarly, Figure 7.29 explores the possibility of *OH poisoning at 0 V vs. RHE. Taking into consideration adsorption induced AuCd site segregation, there is a probability to have a stabilised adsorption of *OH, consequently causing poisoning on a Cd-alloyed gold surface until the potential, where *OH reduces off, i.e. below -0.2 V vs. RHE.

In CO-purged alkaline media, although HO* adsorption induced poisoning is a possibility, it is unlikely that formate adsorption could poison sites, both because CO_2 concentrations are low, and because at $HCOO^-$ production is strongly downhill in free energy across the potential scale where the measurements took place.

7.5.2 *H adsorption induced segregation of Au

An alternative explanation for why the surface is inactive could be H-adsorption induced surface rearrangements. In Figure 7.30, we show the DFT calculations considering *H and *OH adsorption on steps of Au(211) – shown as AuAu, Au-Cd step site on $Au_3Cd(211)$ – marked as AuCd and Cd(211) steps marked as CdCd. The theoretical model assumes that hydrogen desorption in the form of H_2 is negligible or very slow.

The lower the Gibbs free energy of the considered adsorbate-surface system, it is more thermodynamically stable. The stability of each site is measured relative to a step site of only Au atoms, and no Cd, occupied with adsorbed H, i.e. H/H-AuAu using the notation in the figure. Notably, the model suggests that this surface should be the most stable at potentials negative of -0.35 V. From -0.35 V to ~0.1 V, the step would be constituted of bare AuCd sites, and at potentials more positive than ~0.1 V, the most stable configuration would be HO* occupied Cd-Cd sites.

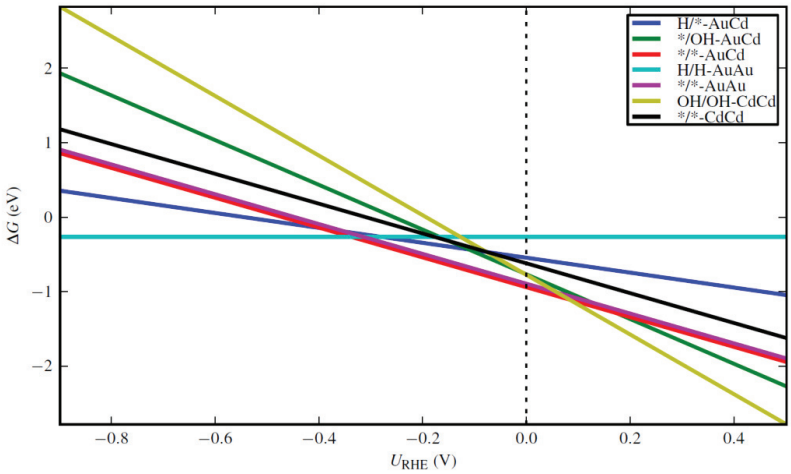

Figure 7.30: Comparison of the stability of *H and *OH on various sites – AuAu, AuCd and CdCd – as a function of potential (vs. RHE), relative to the stability of a H-occupied pure Au step site on H/H-AuAu. AuAu, AuCd and CdCd refer to the step composition on a bulk Au_3Cd alloy – modelled as $Au_3Cd(211)$. The model assumes that *H recombination in the form of H_2 is negligible or very slow. Figure made by Heine A. Hansen.

The above model has only taken into account H adsorption. However, given that experiments show that CO does adsorb onto pure Au, and it seems to be enhanced on step sites,[151] CO induced segregation onto the step site is very plausible on the alloyed surfaces investigated here.

7.6 Discussion

In this section we contrast the DFT based predictions about the catalytic properties of Cd-alloyed gold for CO_2 reduction to the experimentally measured activities. Involving more DFT considerations, we discuss several reasons related to the stability of alloyed gold surfaces, for which the reaction might have been inhibited, by either poisoning or reformation of the catalytically active sites.
In separate subsections, we overview the observed catalytic trends in CO_2 and CO reduction on Au_3Cd and Cd/Au obtained from electrolysis experiments, as well as their post reaction characterisation. Similarly to Cu displacement by CO on Cu overlayers on Pt, observed in Chapter 5, we analyse the surface interactions with various adsorbates and their possible effect on the catalyst surface composition, leading to loss of unique catalytic properties of alloy. We consider possible scenarios that might be occurring on bimetallic catalysts causing structural surface rearrangements or active site poisoning.

7.6.1 Summary of DFT calculations based predictions

Even though the binding of *CO intermediate on $Au_3Cd(211)$ is weaker with respect to Au(211), its overall free energy diagram becomes exergonic at less negative limiting potentials relative to Au(211) due to stabilisation of *COOH. Therefore, we would expect an increase in CO evolution activity. Additionally, the further reduction of *CO to CH_3OH would be possible, as it should also be for Au(211) at sufficient overpotential. Due to *CHO stabilisation on $Au_3Cd(211)$, the limiting potential for further *CO reduction to *CHO would be -0.17 V. Nonetheless, because of absolute weak binding of *CO, the chemical step of CO(g) adsorption becomes relevant when considering methanol production. Assuming the use of CO (at 1 bar) as a reactant gas instead of CO_2 (producing only ~0.001 bar of CO), DFT predicts a direct reduction of gas phase CO to *CHO at -0.29 V (see Table 7.1, Section 7.1).

The comparison of the electrolysis results from CO_2 reduction on the surface Cd/Au alloy and on the bulk Au_3Cd alloy to the polycrystalline gold reveals significant discrepancies from the DFT predicted trends. This suggests a possibility of active site poisoning or surface structure rearrangements.

On the basis of our experiments, additional theoretical calculations were performed which suggested that the Au-Cd active site may be blocked or modified by *OH and *OCHO*. Namely, DFT calculations suggest that during CO_2 reduction to formate, *OH and *OCHO* intermediates can be stabilised by adsorbing onto two contiguous Cd atoms. Hence, there could be a driving force for

converting two Au-Cd sites into a Au-Au site and a Cd-Cd site, when *OH or *OCHO* intermediates are present. DFT calculations suggest a potential dependent stability of the Au-Cd step sites (see Figure 7.30): at potentials more positive than ~ +0.1 V, *OH adsorption induced surface rearrangements and poisoning may occur. The removal of *OH from the Cd-Cd sites is not exergonic until -0.2 V. Similarly, at the potentials below ~ -0.37 V, *H or *CO adsorption may cause Au-Cd sites to reform, and poison the surface (see Figure 7.30). Consequently, the adsorption of CO molecules onto the catalytically relevant Au-Cd site without reforming it would only be possible in a rather narrow potential range, below -0.25 V and more positive than -0.37 V. According to the theoretical model presented in Figure 7.30, at potentials below -0.37 V, the driving force for Cd subsurface migration due to H-Au interaction becomes significant.

7.6.2 Summary of general processes on Cd-alloyed Au electrodes

It is not completely surprising that Cd-alloyed gold produces more formate relative to the pure Au, since metallic Cd on its own produces formate with high Faradaic efficiency.[15] Hence, the adsorbed formate (*OCHO*) may act as the site blocking species. *OH adsorption indeed may be relevant for Cd-alloyed Au; however, it occurs only at positive potentials. *OH would be removed from the surface at more negative potentials, under reaction conditions.

Effectively, prior to the electrolysis, all the electrodes were kept at potentials around -0.2 V, which would mean that both in neutral and alkaline media, Cd-alloyed gold surfaces could still have a certain coverage of *OH. Therefore, adsorbed *OH could be causing AuCd sites to reform. On the other hand, *OCHO* intermediate should easily be reduced off the surface in alkaline media at -0.25 V. Given the accuracy of DFT, adsorbed formate however may be a plausible explanation for AuCd sites rearrangements and poisoning in neutral media.

The use of high surface area catalyst could decrease the extent of adsorbate poisoning by decreasing the local concentration of poisoning solution species. Even so, the use of Cd deposited on oxide derived gold or nanoporous gold, exposed to minimal amounts of CO_2 in alkaline media did not provide a positive result. High sensitivity product analyses on aliquots from oxide-derived gold with and without Cd detect minor concentrations of methanol corresponding to <0.1% of Faradaic efficiency, produced at -0.6 V. Moreover, concentration of methanol produced by a bare gold surface is slightly higher than when Cd was deposited, suggesting that it is most likely unrelated to the presence of Cd. The lack of a positive identification of a more reduced product than CO suggests that there may be some additional processes occurring.

Reaction intermediates that bind stronger to Au than to Cd, such as *H and *CO, may be the reason for the Au enrichment at the surface of Cd-alloyed gold electrodes. Adsorbed H or C-based species could bring about segregation of Au to the surface. There are reports in the literature regarding the adsorption of *H[168] and *CO[140,141,147,149,153] on Au, in an electrochemical environment. On polycrystalline Au, potential decay measurements by Conway and coworkers suggest that the surface reaches a saturation coverage of 15 μC cm^{-2} in alkaline solution at -0.4 V;[168] presumably H would only adsorb at the step sites[169]; this would correspond to a coverage at step sites of 0.75 ML (assuming that the total density of surface atoms is equal to that of Au(111), and that step sites constitute 10% of that total surface, equation 6.3, section 6.1.1).

Likewise, on the basis of our own measurements, and measurements by others, the CO coverage also seems to be substantial in alkaline solution; it is also reported to be significant to a significant, albeit to a lesser extent in acid solution.[140,141,149] It seems reasonable to conjecture that the CO coverage should also be high under neutral conditions.

In addition, there are surface science studies confirming that Au atoms have a significant mobility in an electrochemical environment.[170] Notably, according to STM measurements by Shue et al[151], CO adsorption at Au causes roughening of the step sites. This shows that Au mobility is high enough, and that CO adsorption is strong enough on Au, to allow the presence of CO to bring about the movement of Au atoms at step sites.

The surface overall composition, and hence catalytic activity, should be correlated to the equilibrium coverages of all these species: *OH and *OCHO* at positive, and *H and *CO at negative potentials.

7.6.3 Cd/Au

CO_2 electrolysis experiments on 0.1 ML Cd/Au show that the addition of a small amount of Cd to polycrystalline gold has no significant effect to its catalytic behavior, as it resembles that of pure Au (Figure 7.13 and 7.16-b). Taking into account the reports about high activity and selectivity of oxide derived gold for CO evolution[59], our own measurements on smooth gold surfaces described in Section 6.2, and density functional theory calculations[60], we expect that CO evolution activity on Au(pc) comes from the undercoordinated sites. Such surface alloy possesses catalytic properties corresponding to the linear combination of Au and Cd. In order to understand if these results are due to surface reconstruction or to the presence of adsorbed species we characterised the surface after reaction.

Throughout the thesis, the post-reaction CVs indicate the presence of formate at the surface only after CO_2 electrolysis in neutral media, where formate is produced with higher current densities, for both Au (Figure 6.12) and Cd/Au (Figure 7.27). However, the stripping CVs performed after CO

electrolysis measurements in alkaline media do not indicate the presence of formate (Figure 6.13 for Au and Figure 7.28 for Cd/Au). Moreover, in alkaline media, the formation of the formate anion would be strongly exergonic, as shown in Figure 7.6 (b) and Figure 7.29 (b). The theoretical models suggest that *OH should removed at potentials below -0.2 V at all pH values, and that *OCHO* should be removed at potentials below -0.25 V at pH 7(see Figure 7.29).

Additionally, the CV obtained after CO_2 reduction at -0.5 V vs. RHE on 0.27 ML Cd/Au in neutral media (see green line in Figure 7.27), does not show any feature that might correspond to an oxidation of the surface bound CO. This could be a consequence of slightly different pH. However, the typical CO-stripping CV in neutral media (red line in Figure 7.27) shows a small peak after the formate fingerprint, at +0.9 V, which most likely corresponds to CO oxidation. Thus, there is no evidence to suggest that the strongly bound CO that is formed on Au is also formed on Cd/Au.

On the other hand, in alkaline media, the post reaction stripping voltammograms between Au and the Cd/Au surface alloy are remarkably similar, as shown in Figure 7.31 (based on CV's previously plotted in Figure 6.13 and 7.28). Consequently, it may be plausible to deduce that after CO reduction on Cd/Au surface alloy at -0.7 V that Cd is largely absent from the surface.

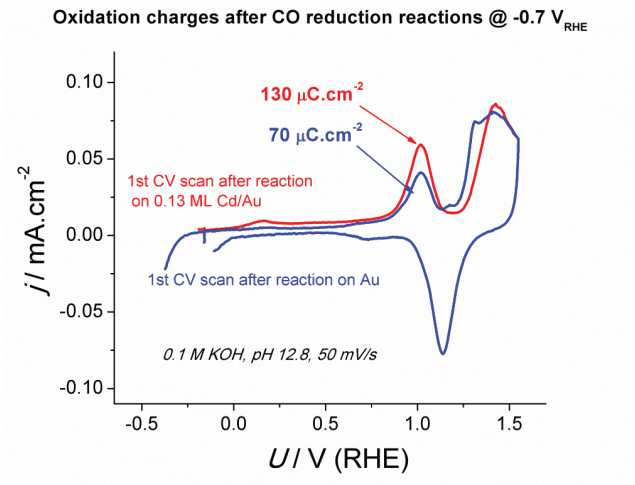

Figure 7.31: Comparison of post-reaction cyclic voltammetry shown previously for Au (on Figure 6.13) and for 0.13 ML Cd/Au surface alloy (on Figure 7.28) obtained both after CO electrolysis at -0.7 V vs. RHE, in 0.1 M KOH, in following procedure: (1) performing CO reduction at -0.7 V, (2) purging for 20-30 min with Ar while holding at -0.15 V vs. RHE and (3) ramping the potential to 1.6 V vs. RHE. The time of electrolysis for Au and 0.13 ML Cd/Au were 15 min. and 30 min., respectively. Co-plotting reveals no change in positions of the oxidation peaks at +1.0 V. The integrated stripping charges are 70 µC.cm^{-2} and 130 µC.cm^{-2} on Au and 0.13 ML Cd/Au, respectively.

Consistent with the electrochemical measurements, the post-reaction surface analysis of Cd/Au surface alloys by XPS did not show any Cd present at the surface, in either CO_2 reduction in neutral or CO reduction in alkaline media, which suggest that Cd either migrates subsurface and goes into the bulk, or is pushed aside (similar to Cu/Pt). Formation of such surfaces would in principle be possible under reaction conditions, whereby the presence of strong binding adsorbates such as *H or *CO could force Cd subsurface migration or even Cd island formation, as found to be the case for Cu/Pt[87,88,121]. In the case of the surface alloy, entropic considerations would make deeper movement of Cd into subsurface layers more favourable than in the bulk alloy. Nonetheless the exact form of the structure formed is unclear. The notion that the active sites are dominated by Au atoms on the surface alloy is consistent with its activity towards CO evolution and hydrogen evolution, which is similar to that of pure Au.

7.6.4 Au_3Cd

The CO evolution activity of the bulk alloy (Au_3Cd) is measured to be an order of magnitude lower than that of Au. The decrease in total current densities of CO_2 electrolysis measurements made on Au_3Cd relative to pure Au corresponds almost entirely to the amount by which the CO evolution activity on Au_3Cd decreased (shown in Figure 7.11). Interestingly, there is no significant difference in hydrogen evolution activity between the Cd-alloyed gold and the pure gold. This is surprising, given both the DFT prediction for HER of the alloyed surfaces(see Figure 7.7), and the experimental observation that Cd is at least four orders of magnitude less active for hydrogen evolution than Au.[28]

Furthermore, the CO electrolyses done on Au_3Cd at -0.5 V, -0.4 V and -0.3 V (see Figures 7.19 and 7.20) did not show any methanol, even when performing the product analysis using highly sensitive equipment.

In the presence of phosphate anions, on Au_3Cd, we observed the inhibition of HER (see Figure 7.17 open vs. filled green squares). Nonetheless, there is no identification of CO reduction products from Au_3Cd, established both in presence and absence of phosphate anions (Figures 7.19 and 7.20). This implies that the phosphate anion adsorption may not be the cause of changes in catalytic activity of Cd-alloyed gold surfaces.

The depth profiles of Au_3Cd sheet after CO_2 reduction in neutral media at -0.5 V and after CO electrolyses in bicarbonate and phosphate buffer, both obtained using the angle resolved-XPS (as shown on Figure 7.12-b and Figure 7.23) showed presence of oxidised Cd at the surface. This observation fits well with the assumption that there would be less driving force for Cd to migrate subsurface inside a bulk alloy electrode.

Previously, in Chapter 6, we introduced the hypothesis of having a stronger and a weaker bound *CO on Au, depending on the CO coverage at the surface. As proposed for Au in Section 6.5, point (4), there may be a stronger bound *CO on polycrystalline Au than initially estimated by DFT calculations. A similar offset in the *CO binding energies may exist for Au_3Cd , which should have an effect on the kinetics of *CO desorption. This may require further investigations.

In summary, the reactivity of Au_3Cd is most consistent with the structure modelled by DFT as a step composed of pure Au, lying on the alloy bulk. The free energy diagram of this surface for CO_2 reduction is described by Figure 7.5; it would show a higher overpotential for CO evolution, relative to Au(211), due to the weaker binding of *COOH. Moreover, the DFT calculations shown on Figure 7.7 suggest that its activity towards hydrogen evolution would be slightly lower than that of Au, but nonetheless more active than the other surfaces with Cd at the step site. Such a structure could be formed by processes similar to those documented in Chapter 5 for Cu/Pt, either by (a) the formation of Cd islands due to HO* and *OCHO* induced segregation, leaving behind pure Au atoms at the step, or (b) due to the strong interaction of Au with *H or *CO, resulting in the formation of Cd islands or subsurface Cd.

7.7 Conclusions

The fundamental understanding of catalysis of CO_2 electro-reduction on pure transition metals –the origin of large overpotentials and existence of the scaling relations between the key intermediates – indicated various strategies in search for new catalysts. In this chapter, we set to explore one of the proposed strategies, involving the breaking of the scaling relations via alloying.

Density functional theory calculations were employed for the screening of transition metal based bimetallic alloys, in order to identify the optimal stable catalyst possessing low overpotential for selective formation of products of interest, primarily hydrocarbons or alcohols. The theoretical model proposes Au_3Cd and a variety of gold cadmium surface alloy structures as the system being the most likely successful in breaking the scaling relations between the intermediates involved in CO evolution reaction. Additionally, the limiting potential related to the protonation of the adsorbed CO is found to be more favourable on $Au_3Cd(211)$ than on Cu(211). The predictions imply a higher CO evolution activity on Au_3Cd relative to Au at low overpotentials. The DFT model includes possibility of further reduction of CO on Au_3Cd with CH_3OH as a final product, contrasting Cu which mainly produces hydrocarbons. The competing reaction, hydrogen evolution, is predicted to be suppressed in Cd-alloyed gold surfaces. Even though it seems to be more thermodynamically favored to produce formate on Au_3Cd than on Au, high pre-exponential factors (barriers) are expected to play a determining role, as in case of Cu, Au or Ag.

Numerous experimental measurements, including both reduction of CO_2 and CO, were performed on a bulk alloy sheet of Au_3Cd, as well as on surface alloys with submonolayer amounts of underpotentially deposited Cd.

High sensitivity quantification analysis employed both for the gas and liquid phase products of CO_2 electrolysis in neutral media led to following main observations:

a) CO evolution activity is suppressed on Au-Cd relative to pure polycrystalline Au.
b) Hydrogen evolution activity remains similar to that of Au on all varieties of AuCd structures.
c) Formate production is enhanced relative to Au, but remains a minor product.
d) No methanol or other desired products were detected using a set of analytic tools – HPLC, static headspace analysis and ^{1}H-NMR spectroscopy.

Electrolysis in alkaline electrolyte saturated with 1 bar CO showed following results:

a) Trace amounts of formaldehyde were produced on Au_3Cd, corresponding to less than 0.5 % Faradaic efficiency.
b) No methanol or other desired products were detected using a set of analytic tools – HPLC, static headspace analysis and ^{1}H-NMR spectroscopy.
c) Trace amounts of CO_2 inevitably present in KOH are reduced to formate.

d) Hydrogen evolution activity was found to be higher on Au_3Cd and same on surface alloy compared to Au.
e) Trace amounts of phosphate anions, present in 0.1 M KOH, suppress hydrogen evolution reaction, contrary to the results initially obtained during CO_2 reduction in phosphate buffer as working electrolyte.

The attempts of CO reduction on surface Cd/Au alloys using high surface area catalyst supports such as gold nanoparticles, nanoporous gold structure and high roughness oxide-derived gold electrodes failed to give a result that would match the theoretical predictions.

In summary, the experiments show that alloying Au with Cd results in a decrease in CO evolution activity and a slight increase in formate production activity. These results suggest that there are additional processes involving various reaction intermediates, adsorbed *OCHO*, *H, *CO or *OH, which may cause changes in surface composition and morphology, and they need to be taken into account by the theoretical model.

In Summary, *OCHO* and *OH adsorbates may reform the surface, causing major segregation, probably through forming Cd islands surrounded by Au. The contact between Au support and Cd islands could still exist as a step edge, however, it would be poisoned by*OH and *OCHO*, until they are removed at more negative potentials: HO* at ~-0.2 V * and *OCHO* at ~-0.25 V, as shown in Figure 7.29. Even within the boundaries of the uncertainties of DFT, the formate or HO* poisoning hypothesis does not explain why at negative potentials one cannot achieve higher CO evolution or CO reduction activity relative to pure Au.

Alternatively, we considered that the adsorption of reactants as *H and *CO may bring about Cd subsurface migration at the step site, depleting the surface of Cd and forming an overlayer of Au at the step. Alternatively Cd could be pushed aside to form islands, as found to be the case for Cu/Pt in Chapter 5. Catalytic results indeed correlate better with the surface modelling an overlayer of pure gold on Au_3Cd, showing no formation of methanol on either of alloyed gold electrodes.

All the considered processes indicate towards a very narrow range of potential, from ~-0.25 V to ~-0.37 V, where Au-Cd could actually be both stable and active. The possibility of underestimated absolute binding of CO, could effect its surface coverage and desorption kinetics in a complex manner.

CHAPTER 8

8. General Conclusions

The work presented in this thesis represents efforts to extend our understanding of the fundamental catalysis of CO_2 electro-reduction. This may eventually lead to the development of active, selective, stable and abundant catalyst materials for sustainable energy storage and conversion technologies of the future.

Our current understanding of aqueous CO_2 electro-reduction is based on the experimental findings from several research groups and theoretical models that successfully explain general trends in the catalytic activity of transition metal surfaces. In particular, the DFT calculations propose an explanation for why copper is a unique electrocatalyst reducing CO_2 to hydrocarbons and elucidate the importance of the undercoordinated sites.[50,60,120] More specific details about the activity and selectivity of copper are a function of numerous factors – major still being the catalyst nature and morphology, but also the relevant reaction conditions as choice of electrolyte, its pH, partial pressure of CO_2, etc.

In Chapter 4, we explored the possibilities to control the activity and the selectivity towards CO_2 reduction by varying the surface morphology of copper. We propose an inexpensive and highly effective method for copper activation, by in-situ roughening of the surface. By modifying the surface morphology, we could influence the selectivity towards methane and ethylene production. We propose that this is primarily due to changes in the catalyst electronic structure. We use theoretical models to explain the surface morphology effect on CO_2 reduction assuming different facets dominating on our electrodes. In addition, we proposed that surface structure modification may indirectly imply other important factors, such as electrolyte buffer capacity – which to great extent determines the local pH at high current densities and thus, affects the overall reaction outcome. However, to explain the differences in selectivity for methane and ethylene additional mechanistic studies are required.

Following our work on polycrystalline copper, in Chapter 5 we looked for other methods to tune the reactivity of copper. We achieved this by depositing pseudomorphic overlayers on Pt single crystals. The higher reactivity of strained copper could affect the intermediates binding energies and thus result in a model catalyst with modified activity or selectivity. However, the interaction of the CO intermediates with the substrate platinum atoms caused the copper surface atoms to displace; this exposed platinum atoms to the surface and enforced hydrogen evolution over CO_2 reduction.

Electrochemical scanning tunneling microscopy provided evidence for the formation of islands of copper on platinum, thus changing the overall catalytic activity of the surface.[87] Consequently, from this study, we anticipate that employing a substrate with more moderate binding towards the intermediates (especially CO), as for instance gold or silver, could result in improved CO_2 reduction catalysis.

According to the theoretical models of Nørskov and coworkers, the scaling between the reaction intermediates, *COOH, *CO and *COH sets a minimum theoretical overpotential in order to drive CO_2 reduction. Inspired by the strategies proposed from these theoretical considerations, we investigate the route of alloying to break these scaling relations and reduce the large overpotentials. From our study on Cu overlayers on Pt, we learnt about the effects of strong adsorbate interactions with the relatively reactive surfaces. Hence, we focused on understanding the electrocatalysis of CO_2 reduction on polycrystalline Au in Chapter 6. As previously reported, pure Au is reasonably active for CO evolution. Although theoretical models suggested that CO could be reduced further, we could not detect any methanol using the high sensitivity liquid product analysis methods we established in our laboratory. We attempted to increase the yield towards more reduced products on Au by carrying out CO electrolysis in alkaline media; even under these conditions no products were formed on polycrystalline Au. However, on high surface area gold, such as oxide derived gold, trace amounts of formaldehyde and methanol were detected at potentials more negative than -0.4 V. Additionally, based on literature and our own post-reaction stripping experiments, we propose the existence of weakly and strongly bound *CO under CO_2 reduction conditions. In Chapter 7, we investigate the possibility of breaking the scaling relations between *COOH and *CO and *CHO to reduce the large overpotentials and possibly enhance the CO evolution or methanol formation on Au-Cd bimetallic systems. Unfortunately, a lower than expected CO evolution and CO reduction activity suggests that a surface phase is formed on Cd/Au and Au_3Cd, which is significantly different from the intended Au_3Cd step site. One possibility is that adsorbed species at the active sites, could have driven some kind of segregation or surface restructuring, analogous to the kind we reported in Chapter 5 for Cu/Pt. These adsorbates could include *OH, *OCHO*, *H and *CO. The bulk electrolysis experiments are more consistent with calculations on Au overlayer on $Au_3Cd(211)$, suggesting a possibility of Cd subsurface segregation or Cd island formation under reaction conditions. We use a combination of theoretical calculations and experimental electrochemistry methods to obtain an insight into the interactions of Au-Cd sites with the adsorbates. Most likely, the adsorbed *H and *CO may be responsible for rearrangements on the surface of bulk and surface alloyed gold resulting in the formation of less active Au overlayers. A combination of further *in situ* microscopic and spectroscopic studies may play a crucial role for verifying these hypotheses. Nevertheless, the conclusions of this work will hopefully serve as inspiration for new strategies for future studies.

We can safely conclude that the reactivity of the bimetallic systems depends highly on the exact configuration of atoms at the active site. In general, density functional theory predictions are most

successful when they model a system, which closely represents the structure formed under reaction conditions. [29,64,74,88,127,171-176]

CHAPTER 9

9. Future Directions

Further structural modifications of catalytic surfaces could potentially improve the activity and selectivity for producing hydrocarbons or alcohols from CO_2 or CO reduction, especially of copper. The overpotentials could be reduced by employing copper surfaces under compressive strain, as achieved by Strasser and coworkers by using dealloyed platinum-copper nanoparticles for oxygen reduction reaction.[66]

The kinetics of CO_2 reduction on Au requires further investigation, ideally on single crystals. Our work suggests that there is a high coverage of CO under reaction conditions, but it remains unclear why CO is not reduced further on Au. *In situ* spectroscopic studies may be necessary. A direct observation of the adsorbed species and their during the reaction at various potential would elucidate the above discussed processes. For such studies an ATR SEIRAS[148,150,177] or surface enhanced Raman spectroscopy (SERS) could be used.[178,179] From point of view of theoretical modelling and DFT calculations, it might be helpful to explore the existence of additional barriers for further reduction of CO.

For the Cd/Au system, electrochemical scanning tunneling microscopy might provide direct insight into mobility of surface atoms, under reaction conditions, as found to be the case for the Cu/Pt system.

For eliminating the effect of active sites segregation and poisoning, future investigations may direct to selective avoiding or inhibition of CO_2 reduction to formate, for instance by using surfactants or geometric effects, while simultaneously ensuring the active sites are still present at the surface.[83,174] Employing for instance surface nanostructuring (specific ion adsorption) or intermetallic alloys[180] with ensemble effects may be a promising strategy for inhibiting the restructuring and blocking of active sites.[14,81,83,174,176,180]

On the other hand, undesired species such as formate, which could poision or restructure surface, could be removed by employing a catalyst to reduce these species. For instance, theoretical considerations suggest that RuO_2 is able to reduce formate to methanol.[180]

In nature, it seems that there are already catalysts that can break scaling relations. For instance, cubane structures based on Ni-Fe-S are forming the active sites within the carbon monoxide dehydrogenase enzymes (CODH) in bacteria, capable of reducing CO_2 to CO reversibly.[181] Inspired

by these, novel biomimetic catalyst based on metal sulfides could exhibit high CO evolution activities at low overpotentials.

Bibliography

(1) Kianfar, M. Journal of American Sciences, 2013, 9.
(2) Lewis, N. S.; Nocera, D. G. Proc. Natl. Acad. Sci. U. S. A. 2006, 103, 15729.
(3) Ghoniem, A. F. Prog. Energy Combust. Sci. 2011, 37, 15.
(4) BP Statistical Review of World Energy January 2013, 2013.
(5) Chu, S.; Majumdar, A. Nature 2012, 488, 294.
(6) Kondratenko, E. V.; Mul, G.; Baltrusaitis, J.; Larrazábal, G. O.; Pérez-Ramírez, J. Energy & Environmental Science 2013, 6, 3112.
(7) Tomabechi, K. Energies 2010, 3, 686.
(8) Chorkendorff, I.; J.W., N. Concepts of Modern Catalysis and Kinetic; WIley-VCH, 2003.
(9) Graves, C.; Ebbesen, S. D.; Mogensen, M.; Lackner, K. S. Renew. Sust. Energ. Rev. 2011, 15, 1.
(10) Chemistry, R. S. o. Solar Fuels and Artificial Photosynthesis, Royal Society of Chemistry, 2012.
(11) Roy, S. C.; Varghese, O. K.; Paulose, M.; Grimes, C. A. ACS Nano 2010, 4, 1259.
(12) Whipple, D. T.; Kenis, P. J. A. J. Phys. Chem. Lett. 2010, 1, 3451.
(13) CRC Handbook of Chemistry and Physics; 90 ed.; Lide, D. R., Ed., 2009.
(14) Escribano, M. E.; Universidad Autónoma de Madrid, D. d. Q. F. A., Ed. 2011.
(15) Hori, Y. In Modern Aspects of Electrochemistry; Vayenas, C., White, R., Gamboa-Aldeco, M., Eds.; Springer New York: 2008; Vol. 42, p 89.
(16) Cook, R. L.; Macduff, R. C.; Sammells, A. F. Journal of the Electrochemical Society 1988, 135, 1470.
(17) Hoshi, N.; Hori, Y. Electrochimica Acta 2000, 45, 4263.
(18) Centi, G.; Perathoner, S.; Win, G.; Gangeri, M. Green Chemistry 2007, 9, 671.
(19) Delacourt, C.; Ridgway, P. L.; Kerr, J. B.; Newman, J. Journal of The Electrochemical Society 2008, 155, B42.
(20) Tang, W.; Peterson, A. A.; Varela, A. S.; Jovanov, Z. P.; Bech, L.; Durand, W. J.; Dahl, S.; Norskov, J. K.; Chorkendorff, I. Physical Chemistry Chemical Physics 2012, 14, 76.
(21) Vesborg, P. C. K.; Jaramillo, T. F. Rsc Advances 2012, 2, 7933.
(22) Sabatier, P. Berichte Der Deutschen Chemischen Gesellschaft 1911, 44, 1984.
(23) Calle-Vallejo, F.; Koper, M. T.; Bandarenka, A. S. Chemical Society reviews 2013, 42, 5210.
(24) Bligaard, T.; Nørskov, J. K.; Dahl, S.; Matthiesen, J.; Christensen, C. H.; Sehested, J. Journal of Catalysis 2004, 224, 206.
(25) Ferrin, P.; Nilekar, A. U.; Greeley, J.; Mavrikakis, M.; Rossmeisl, J. Surface Science 2008, 602, 3424.
(26) Falsig, H.; Hvolbæk, B.; Kristensen, I. S.; Jiang, T.; Bligaard, T.; Christensen, C. H.; Nørskov, J. K. Angewandte Chemie 2008, 120, 4913.
(27) Nørskov, J. K.; Bligaard, T.; Logadottir, A.; Kitchin, J. R.; Chen, J. G.; Pandelov, S.; Stimming, U. Journal of The Electrochemical Society 2005, 152, J23.
(28) Trasatti, S. Journal of Electroanalytical Chemistry and Interfacial Electrochemistry 1972, 39, 163.
(29) Hinnemann, B.; Moses, P. G.; Bonde, J.; Jorgensen, K. P.; Nielsen, J. H.; Horch, S.; Chorkendorff, I.; Norskov, J. K. Journal of the American Chemical Society 2005, 127, 5308.
(30) Bligaard, T.; Nørskov, J. K. Electrochimica Acta 2007, 52, 5512.
(31) Hammer, B.; Nørskov, J. K. Surface Science 1995, 343, 211.
(32) Mavrikakis, M.; Hammer, B.; Nørskov, J. K. Physical Review Letters 1998, 81, 2819.
(33) Herrero, E.; Buller, L. J.; Abruña, H. D. Chemical Reviews 2001, 101, 1897.
(34) Lay, M. D.; Varazo, K.; Srisook, N.; Stickney, J. L. Journal of Electroanalytical Chemistry 2003, 554-555, 221.

(35) Horanyi, G., Inzelt G. Journal of Electroanalytical Chemistry 2000, 491, 111.
(36) Horanyi, G. Journal of Solid State Electrochemistry 2000, 4, 177.
(37) Pourbaix, M. Atlas of Electrochemical Equilibria in Aqueous Solutions; National Association of Corrosion Engineers, 1974.
(38) Hori, Y.; Murata, A.; Takahashi, R. Journal of the Chemical Society, Faraday Transactions 1: Physical Chemistry in Condensed Phases 1989, 85, 2309.
(39) Kuhl, K. P.; Cave, E. R.; Abram, D. N.; Jaramillo, T. F. Energy & Environmental Science 2012, 5, 7050.
(40) Hori, Y.; Kikuchi, K.; Suzuki, S. Chemistry Letters 1985, 14, 1695.
(41) Hori, Y.; Takahashi, I.; Koga, O.; Hoshi, N. The Journal of Physical Chemistry B 2001, 106, 15.
(42) Hori, Y.; Murata, A.; Takahashi, R.; Suzuki, S. Journal of the American Chemical Society 1987, 109, 5022.
(43) Schouten, K. J. P.; Kwon, Y.; van der Ham, C. J. M.; Qin, Z.; Koper, M. T. M. Chemical Science 2011, 2, 1902.
(44) Terunuma, Y.; Saitoh, A.; Momose, Y. Journal of Electroanalytical Chemistry 1997, 434, 69.
(45) Schouten, K. J. P.; Qin, Z.; Gallent, E. P.; Koper, M. T. M. Journal of the American Chemical Society 2012, 134, 9864.
(46) Gonçalves, M. R.; Gomes, A.; Condeço, J.; Fernandes, R.; Pardal, T.; Sequeira, C. A. C.; Branco, J. B. Energy Conversion and Management 2010, 51, 30.
(47) Wasmus, S.; Cattaneo, E.; Vielstich, W. Electrochimica Acta 1990, 35, 771.
(48) Li, C. W.; Kanan, M. W. Journal of the American Chemical Society 2012, 134, 7231.
(49) Cook, R. L.; Macduff, R. C.; Sammells, A. F. Journal of the Electrochemical Society 1988, 135, 1320.
(50) Peterson, A. A.; Abild-Pedersen, F.; Studt, F.; Rossmeisl, J.; Nørskov, J. K. Energy & Environmental Science 2010, 3, 1311.
(51) Ogura, K.; Yano, H.; Shirai, F. Journal of The Electrochemical Society 2003, 150, D163.
(52) Hori, Y.; Takahashi, I.; Koga, O.; Hoshi, N. Journal of Molecular Catalysis A: Chemical 2003, 199, 39.
(53) Stephens, I. E. L.; Bondarenko, A. S.; Gronbjerg, U.; Rossmeisl, J.; Chorkendorff, I. Energy & Environmental Science 2012, 5, 6744.
(54) Nørskov, J. K.; Rossmeisl, J.; Logadottir, A.; Lindqvist, L.; Kitchin, J. R.; Bligaard, T.; Jónsson, H. The Journal of Physical Chemistry B 2004, 108, 17886.
(55) Peterson, A. A.; Nørskov, J. K. The Journal of Physical Chemistry Letters 2012, 3, 251.
(56) Hori, Y.; Takahashi, R.; Yoshinami, Y.; Murata, A. The Journal of Physical Chemistry B 1997, 101, 7075.
(57) Montoya, J. H.; Peterson, A. A.; Nørskov, J. K. ChemCatChem 2013, 5, 737.
(58) Hori, Y.; Murata, A.; Kikuchi, K.; Suzuki, S. Journal of the Chemical Society, Chemical Communications 1987, 728.
(59) Chen, Y.; Li, C. W.; Kanan, M. W. Journal of the American Chemical Society 2012, 134, 19969.
(60) Shi, C.; Hansen, H. A.; Lausche, A. C.; Norskov, J. K. Physical chemistry chemical physics : PCCP 2014, 16, 4720.
(61) Diaz-Morales, O.; Calle-Vallejo, F.; de Munck, C.; Koper, M. T. M. Chemical Science 2013, 4, 2334.
(62) Hori, Y., Wakebe H., Tsukamoto T., Koga O. Electrochimica Acta 1993, 39, 1833.
(63) Hoster, H. E.; Alves, O. B.; Koper, M. T. M. ChemPhysChem 2010, 11, 1518.
(64) Greeley, J.; Nørskov, J. K.; Kibler, L. A.; El-Aziz, A. M.; Kolb, D. M. ChemPhysChem 2006, 7, 1032.
(65) Esposito, D. V.; Hunt, S. T.; Stottlemyer, A. L.; Dobson, K. D.; McCandless, B. E.; Birkmire, R. W.; Chen, J. G. Angewandte Chemie International Edition 2010, 49, 9859.
(66) Strasser, P.; Koh, S.; Anniyev, T.; Greeley, J.; More, K.; Chengfei, Y.; Zengcai, L.; Kaya, S.;

Nordlund, D.; Ogasawara, H.; Toney, M. F.; Nilsson, A. Nature chemistry 2010, 2, 454.
(67) Heggen, M.; Oezaslan, M.; Houben, L.; Strasser, P. The Journal of Physical Chemistry C 2012, 116, 19073.
(68) Wang, J. X.; Inada, H.; Wu, L.; Zhu, Y.; Choi, Y.; Liu, P.; Zhou, W.-P.; Adzic, R. R. Journal of the American Chemical Society 2009, 131, 17298.
(69) Sasaki, K.; Kuttiyiel, K. A.; Barrio, L.; Su, D.; Frenkel, A. I.; Marinkovic, N.; Mahajan, D.; Adzic, R. R. The Journal of Physical Chemistry C 2011, 115, 9894.
(70) Kleiman-Shwarsctein, A.; Laursen, A. B.; Cavalca, F.; Tang, W.; Dahl, S.; Chorkendorff, I. Chemical Communications 2012, 48, 967.
(71) Price, S. W. T.; Speed, J. D.; Kannan, P.; Russell, A. E. Journal of the American Chemical Society 2011, 133, 19448.
(72) Huang, M.; Henry, J. B.; Fortgang, P.; Henig, J.; Plumere, N.; Bandarenka, A. S. RSC Advances 2012, 2, 10994.
(73) Schlaup, C.; Horch, S. Surface Science 2013, 608, 44.
(74) Friebel, D.; Viswanathan, V.; Miller, D. J.; Anniyev, T.; Ogasawara, H.; Larsen, A. H.; O'Grady, C. P.; Nørskov, J. K.; Nilsson, A. Journal of the American Chemical Society 2012, 134, 9664.
(75) Abrams, B. L.; Vesborg, P. C. K.; Bonde, J. L.; Jaramillo, T. F.; Chorkendorff, I. Journal of The Electrochemical Society 2009, 156, B273.
(76) Mayrhofer, K. J. J.; Juhart, V.; Hartl, K.; Hanzlik, M.; Arenz, M. Angewandte Chemie International Edition 2009, 48, 3529.
(77) Kobayashi, H.; Yamauchi, M.; Kitagawa, H.; Kubota, Y.; Kato, K.; Takata, M. Journal of the American Chemical Society 2010, 132, 5576.
(78) Noda, H.; Ikeda, S.; Yamamoto, A.; Einaga, H.; Ito, K. Bull. Chem. Soc. Jpn. 1995, 68, 1889.
(79) Gupta, N.; Gattrell, M.; MacDougall, B. Journal of Applied Electrochemistry 2006, 36, 161.
(80) Strmcnik, D.; van der Vliet, D. F.; Chang, K. C.; Komanicky, V.; Kodama, K.; You, H.; Stamenkovic, V. R.; Marković, N. M. The Journal of Physical Chemistry Letters 2011, 2, 2733.
(81) Escudero-Escribano, M.; Michoff, M. E. Z.; Leiva, E. P. M.; Markovic, N. M.; Gutierrez, C.; Cuesta, A. Chemphyschem 2011, 12, 2230.
(82) Subbaraman, R.; Tripkovic, D.; Strmcnik, D.; Chang, K. C.; Uchimura, M.; Paulikas, A. P.; Stamenkovic, V.; Markovic, N. M. Science 2011, 334, 1256.
(83) Strmcnik, D.; Escudero-Escribano, M.; Kodama, K.; Stamenkovic, V. R.; Cuesta, A.; Markovic, N. M. Nature chemistry 2010, 2, 880.
(84) Blizanac, B. B.; Lucas, C. A.; Gallagher, M. E.; Arenz, M.; Ross, P. N.; Markovic, N. M. J. Phys. Chem. B 2004, 108, 625.
(85) Hansen, H. A.; Varley, J. B.; Peterson, A. A.; Nørskov, J. K. The Journal of Physical Chemistry Letters 2013, 4, 388.
(86) Bondarenko, A. S.; Stephens, I. E. L.; Chorkendorff, I. Electrochemistry Communications 2012, 23, 33.
(87) Varela, A. S.; Schlaup, C.; Jovanov, Z. P.; Malacrida, P.; Horch, S.; Stephens, I. E. L.; Chorkendorff, I. The Journal of Physical Chemistry C 2013, 117, 20500.
(88) Bandarenka, A. S.; Varela, A. S.; Karamad, M.; Calle-Vallejo, F.; Bech, L.; Perez-Alonso, F. J.; Rossmeisl, J.; Stephens, I. E. L.; Chorkendorff, I. Angew. Chem.-Int. Edit. 2012, 51, 11845.
(89) Wittstock, A.; Zielasek, V.; Biener, J.; Friend, C. M.; Baumer, M. Science 2010, 327, 319.
(90) Fujita, T.; Guan, P.; McKenna, K.; Lang, X.; Hirata, A.; Zhang, L.; Tokunaga, T.; Arai, S.; Yamamoto, Y.; Tanaka, N.; Ishikawa, Y.; Asao, N.; Yamamoto, Y.; Erlebacher, J.; Chen, M. Nature materials 2012, 11, 775.
(91) www.intechopen.com, p Potentialwave form CV

(92) Paulus, U. A.; Schmidt, T. J.; Gasteiger, H. A.; Behm, R. J. Journal of Electroanalytical Chemistry 2001, 495, 134.
(93) E., G. Electrode Kinetics for Chemists, Chemical Engineers and Materials Scientists; VCH Publishers Inc.: New York, 1993.
(94) Berkes, B. B.; Maljusch, A.; Schuhmann, W.; Bondarenko, A. S. Journal of Physical Chemistry C 2011, 115, 9122.
(95) Instruments, B.-l. 2012.
(96) van der Vliet, D.; Strmcnik, D. S.; Wang, C.; Stamenkovic, V. R.; Markovic, N. M.; Koper, M. T. M. Journal of Electroanalytical Chemistry 2010, 647, 29.
(97) Chorkendorff, I. 2010.
(98) Somorjai, G. A. Chemistry in Two Dimensions, Surfaces; Cornell University, Press: Ithaca, 1981.
(99) http://www.thermo.com/eThermo/CMA/PDFs/Product/productPDF_56731.PDF
(100) Hong, J. D.; Zhang, W.; Ren, J.; Xu, R. Anal. Methods 2013, 5, 1086.
(101) http://nett21.gec.jp/CTT_DATA/WMON/CHAP_4/html/Wmon-083.html, p Gas Chromatography.
(102) http://www.picstopin.com/640/chemguide-chromatography-image-search-results/http:||www*tau*ac*il|~instanal|Links*files|image010*jpg/, p HPLC.
(103) Agilent 1200 Series Refractive Index Detector, S. M.
(104) Kaminski, J.; Atwal, A. S.; Mahadevan, S. J. Liq. Chromatogr. 1993, 16, 521.
(105) Morooka, S.; Wakai, C.; Matubayasi, N.; Nakahara, M. J. Phys. Chem. A 2005, 109, 6610.
(106) Atkins R. C., C. F. A. Organic Chemistry, A brief course; 2 ed.; The McGrow Hill Companies, 1996.
(107) http://www.restek.com/pdfs/59895B.pdf; Restek, Ed.
(108) http://www.americanlaboratory.com/913-Technical-Articles/1091-A-Generic-Method-for-the-Analysis-of-Residual-Solvents-in-Pharmaceuticals-Using-Static-Headspace-GC-FID-MS/.
(109) Maurice, V.; Strehblow, H. H.; Marcus, P. Surface Science 2000, 458, 185.
(110) Huemann, S.; Minh Hai, N. T.; Broekmann, P.; Wandelt, K.; Zajonz, H.; Dosch, H.; Renner, F. The Journal of Physical Chemistry B 2006, 110, 24955.
(111) Schlaup, C.; Horch, S. Surface Science 2013, 608, 44.
(112) Magnussen, O. M. Chemical Reviews 2002, 102, 679.
(113) http://www.sciencemadness.org/talk/viewthread.php?tid=7156.
(114) Michely, T.; Comsa, G. Surface Science 1991, 256, 217.
(115) McCarthy, D. N.; Strebel, C. E.; Johansson, T. P.; den Dunnen, A.; Nierhoff, A.; Nielsen, J. H.; Chorkendorff, I. Journal of Physical Chemistry C 2012, 116, 15353.
(116) Finšgar, M.; Peljhan, S.; Kokalj, A.; Kovač, J.; Milošev, I. Journal of The Electrochemical Society 2010, 157, C295.
(117) Casalongue, H. S.; Kaya, S.; Viswanathan, V.; Miller, D. J.; Friebel, D.; Hansen, H. A.; Norskov, J. K.; Nilsson, A.; Ogasawara, H. Nat. Commun. 2013, 4, 6.
(118) Wakisaka, M.; Suzuki, H.; Mitsui, S.; Uchida, H.; Watanabe, M. Langmuir 2009, 25, 1897.
(119) Le, M.; Ren, M.; Zhang, Z.; Sprunger, P. T.; Kurtz, R. L.; Flake, J. C. Journal of The Electrochemical Society 2011, 158, E45.
(120) Durand, W. J.; Peterson, A. A.; Studt, F.; Abild-Pedersen, F.; Nørskov, J. K. Surface Science 2011, 605, 1354.
(121) Varela, A. S.; Center for Individual Nanoparticle Functionality, T. U. o. D., Ed. Technical University of Denmark, Kongens Lyngby, 2013.
(122) Berná, A.; Climent, V.; Feliu, J. M. Electrochemistry Communications 2007, 9, 2789.
(123) Hitotsuyanagi, A.; Nakamura, M.; Hoshi, N. Electrochimica Acta 2012, 82, 512.
(124) Markovic, N.; Ross, P. N. Langmuir 1993, 9, 580.
(125) Greeley, J. Electrochimica Acta 2010, 55, 5545.
(126) Strasser, P.; Koh, S.; Greeley, J. Physical Chemistry Chemical Physics 2008, 10, 3670.

(127) Stephens, I. E. L.; Bondarenko, A. S.; Perez-Alonso, F. J.; Calle-Vallejo, F.; Bech, L.; Johansson, T. P.; Jepsen, A. K.; Frydendal, R.; Knudsen, B. P.; Rossmeisl, J.; Chorkendorff, I. Journal of the American Chemical Society 2011, 133, 5485.
(128) Liu, Z.; Jackson, G. S.; Eichhorn, B. W. Angewandte Chemie International Edition 2010, 49, 3173.
(129) Green, C. L.; Kucernak, A. The Journal of Physical Chemistry B 2002, 106, 1036.
(130) Trasatti, S.; Petrii, O. A. Journal of Electroanalytical Chemistry 1992, 327, 353.
(131) Velez, P.; Cuesta, A.; Leiva, E. P. M.; Macagno, V. A. Electrochemistry Communications 2012, 25, 54.
(132) Vitos, L.; Ruban, A. V.; Skriver, H. L.; Kollar, J. Philos. Mag. B-Phys. Condens. Matter Stat. Mech. Electron. Opt. Magn. Prop. 1998, 78, 487.
(133) El-Aziz, A. M.; Hoyer, R.; Kibler, L. A. Chemphyschem 2010, 11, 2906.
(134) Cuesta, A.; Kibler, L. A.; Kolb, D. M. Journal of Electroanalytical Chemistry 1999, 466, 165.
(135) Kibler, L. A.; Cuesta, A.; Kleinert, M.; Kolb, D. M. Journal of Electroanalytical Chemistry 2000, 484, 73.
(136) Weber, M.; Nart, F. C. Electrochimica Acta 1996, 41, 653.
(137) Cuesta, A.; Kleinert, M.; Kolb, D. M. Physical Chemistry Chemical Physics 2000, 2, 5684.
(138) Danilovic, N.; Subbaraman, R.; Strmcnik, D.; Chang, K. C.; Paulikas, A. P.; Stamenkovic, V. R.; Markovic, N. M. Angew. Chem.-Int. Edit. 2012, 51, 12495.
(139) Rodriguez, P.; Koverga, A. A.; Koper, M. T. Angewandte Chemie 2010, 49, 1241.
(140) Rodriguez, P.; Feliu, J. M.; Koper, M. T. M. Electrochemistry Communications 2009, 11, 1105.
(141) Rodriguez, P., Garcia-Araez N., Koverga A., Frank S., Koper M T M Langmuir 2010, 26, 12425.
(142) Rodriguez, P.; Kwon, Y.; Koper, M. T. Nature chemistry 2012, 4, 177.
(143) Auinger, M.; Katsounaros, I.; Meier, J. C.; Klemm, S. O.; Biedermann, P. U.; Topalov, A. A.; Rohwerder, M.; Mayrhofer, K. J. J. Physical Chemistry Chemical Physics 2011, 13, 16384.
(144) Blizanac, B. B.; Ross, P. N.; Markovic, N. M. Electrochimica Acta 2007, 52, 2264.
(145) Schmidt, T. J.; Gasteiger, H. A.; Stab, G. D.; Urban, P. M.; Kolb, D. M.; Behm, R. J. Journal of the Electrochemical Society 1998, 145, 2354.
(146) Kortlever, R.; Tan, K. H.; Kwon, Y.; Koper, M. T. M. Journal of Solid State Electrochemistry 2013, 17, 1843.
(147) Kita H., N. H., Hayashi K. J. Electroanal. Chem. 1985, 190, 141.
(148) Pronkin, S.; Hara, M.; Wandlowski, T. Russian Journal of Electrochemistry 2006, 42, 1177.
(149) Lai, S. C. S.; Lebedeva, N. P.; Housmans, T. H. M.; Koper, M. T. M. Top Catal 2007, 46, 320.
(150) Cuesta, A.; Cabello, G.; Hartl, F. W.; Escudero-Escribano, M.; Vaz-Dominguez, C.; Kibler, L. A.; Osawa, M.; Gutierrez, C. Catalysis Today 2013, 202, 79.
(151) Shue C., O. Y. L., Yau S., Itaya K. Langmuir 2005, 21, 1942.
(152) Grabow, L. C.; Hvolbaek, B.; Norskov, J. K. Top Catal 2010, 53, 298.
(153) Cuesta, A.; Lopez, N.; Gutierrez, C. Electrochimica Acta 2003, 48, 2949.
(154) Watanabe, M.; Motoo, S. Journal of Electroanalytical Chemistry 1975, 60, 259.
(155) Watanabe, M.; Motoo, S. Journal of Electroanalytical Chemistry 1975, 60, 267.
(156) Watanabe, M.; Motoo, S. Journal of Electroanalytical Chemistry 1975, 60, 275.
(157) Koper, M. T. M.; Shubina, T. E.; van Santen, R. A. Journal of Physical Chemistry B 2002, 106, 686.
(158) Schmidt, T. J.; Noeske, M.; Gasteiger, H. A.; Behm, R. J.; Britz, P.; Bonnemann, H. Journal of the Electrochemical Society 1998, 145, 925.
(159) Schmidt, T. J.; Noeske, M.; Gasteiger, H. A.; Behm, R. J.; Britz, P.; Bonnemann, H. Journal of the Electrochemical Society 1998, 145, 3697.
(160) Base, I. C. S. D. In http://icsd.fiz-karlsruhe.de/icsd/; FIZ Karlsruhe: Karlsruhe.
(161) Hirabayashi M., O. S. ACTA METAlLURGICA 1961, 9.
(162) Warlimont, H. Z. Metallk. 1959, 50, 708.

(163) Sen, P.; Hegde, M. S.; Rao, C. N. R. Appl. Surf. Sci. 1982, 10, 63.
(164) Malacrida, P.; Escudero-Escribano, M.; Verdaguer-Casadevall, A.; Stephens, I. E. L.; Chorkendorff, I. Journal of Materials Chemistry A 2014, 2, 4234.
(165) Neurock, M.; Janik, M.; Wieckowski, A. Faraday Discuss. 2008, 140, 363.
(166) Sheng, W.; Gasteiger, H. A.; Shao-Horn, Y. Journal of The Electrochemical Society 2010, 157, B1529.
(167) Schmidt, T. J.; Ross, P. N.; Markovic, N. M. Journal of Electroanalytical Chemistry 2002, 524, 252.
(168) Conway B. E., B. L. Electrochimica Acta 1986, 31, 1013.
(169) Skulason E., T. V., Bjorketun M.E., Gudmundsdottir S., Karlberg G., Rossmeisl J., Bligaard T., Jonsson H., Norskov J.K. Journal of Physical Chemistry C 2010, 114, 18182.
(170) M., G. Progress in Surface Science 2001, 68, 1.
(171) Kibler, L. A.; El-Aziz, A. M.; Hoyer, R.; Kolb, D. M. Angew. Chem.-Int. Edit. 2005, 44, 2080.
(172) Jaramillo, T. F.; Jorgensen, K. P.; Bonde, J.; Nielsen, J. H.; Horch, S.; Chorkendorff, I. Science 2007, 317, 100.
(173) Rossmeisl, J.; Karlberg, G. S.; Jaramillo, T.; Norskov, J. K. Faraday Discuss. 2008, 140, 337.
(174) Siahrostami, S.; Verdaguer-Casadevall, A.; Karamad, M.; Deiana, D.; Malacrida, P.; Wickman, B.; Escudero-Escribano, M.; Paoli, E. A.; Frydendal, R.; Hansen, T. W.; Chorkendorff, I.; Stephens, I. E. L.; Rossmeisl, J. Nature materials 2013, 12, 1137.
(175) Johansson, T. P.; Ulrikkeholm, E. T.; Hernandez-Fernandez, P.; Malacrida, P.; Hansen, H. A.; Bandarenka, A. S.; Nørskov, J. K.; Rossmeisl, J.; Stephens, I. E. L.; Chorkendorff, I. Top Catal 2013, 57, 245.
(176) Verdaguer-Casadevall, A.; Deiana, D.; Karamad, M.; Siahrostami, S.; Malacrida, P.; Hansen, T. W.; Rossmeisl, J.; Chorkendorff, I.; Stephens, I. E. L. Nano Letters 2014, 14, 1603.
(177) Cuesta, A.; Cabello, G.; Osawa, M.; Gutierrez, C. ACS Catal. 2012, 2, 728.
(178) Kudelski, A.; Kedzierzawski, P.; Bukowska, J.; Janik-Czachor, M. Russian Journal of Electrochemistry 2000, 36, 1186.
(179) Schmitt, K. G.; Gewirth, A. A. Abstr. Pap. Am. Chem. Soc. 2013, 246, 1.
(180) Karamad, M.; Center for Atomic-scale Materials Design, D. o. P., Technical University of Denmark, Ed. Technical University of Denmark, Kongens Lyngby, 2013.
(181) Varley, J. B.; Hansen, H. A.; Ammitzboll, N. L.; Grabow, L. C.; Peterson, A. A.; Rossmeisl, J.; Norskov, J. K. ACS Catal. 2013, 3, 2640.
(182) TAKENO, N.; Technology, N. I. o. A. I. S. a., Ed. 2005.

Appendix A

List of acronyms used throughout the thesis

AR-XPS – Angle Resolved X-ray Photoelectron Spectroscopy
ATR-SEIRAS – Attenuated Transmission Reflectance Surface Enhanced Infra Red Absorption Spectroscopy
CE – Counter Electrode
CPE – Constant Phase Element
CV – Cyclic Voltammogram
DAD – Diode Array Detector
DEMS – Differential Electrochemical Mass Spectrometer
DFT – Density Functional Theory
EC-STM – Electrochemical Scanning Tunneling Microscope
EIS – Electrochemical Impedance Spectroscopy
FID – Flame Ionisation Detector
FTIR – Fourier Transform Infra Red spectroscopy
GC – Gas Chromatography
HPLC – High Performance Liquid Chromatography
NHE – Normal Hydrogen Electrode
NMR – Nuclear Magnetic Resonance
OECD – Organisation for Economic Co-operation and Development
RE – Reference Electrode
RHE – Reversible Hydrogen Electrode
SEM – Scanning Electron Microscope
SERS – Surface Enhanced Raman Spectroscopy
STM – Scanning Tunneling Microscope
TCD – Thermal Conductivity Detector
TPD – Temperature Programmed Desorption
UHV – Ultrahigh Vacuum
UPD – Underpotential Deposition
WE – Working Electrode
XPS – X-ray Photoemission Spectroscopy
XRD – X-Ray Diffraction

Appendix B

Pourbaix diagrams

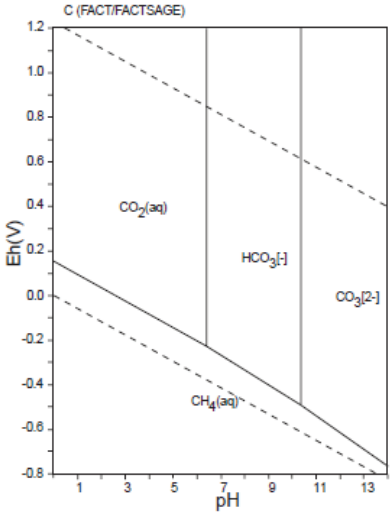

Figure A.B1: Pourbaix diagram of CO_2. Reprinted from[182]

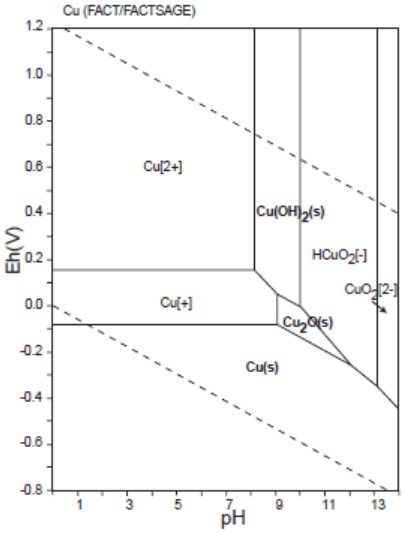

Figure A.B2: Pourbaix diagram of Cu. Reprinted from[182]

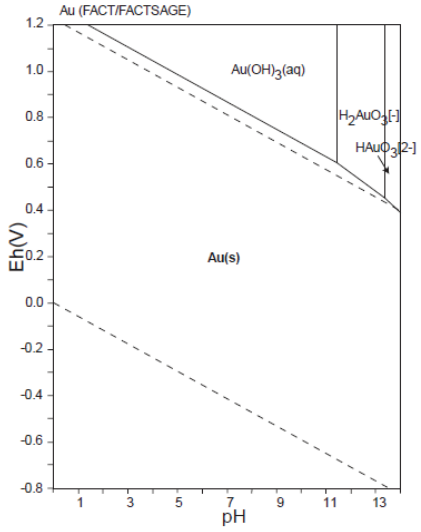

Figure A.B3: Pourbaix diagram of Au. Reprinted from[182]

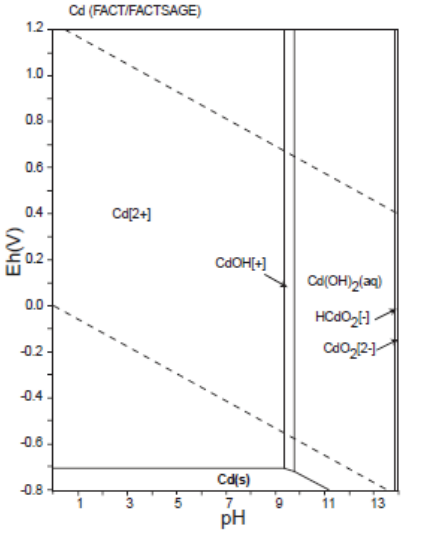

Figure A.B4: Pourbaix diagram of Cd. Reprinted from[182]

Appendix C

Included papers

1. W. Tang, A. A. Peterson, A. S. Varela, **Z. P. Jovanov**, L. Bech, W. J. Durand, S. Dahl, J. K. Nørskov and I. Chorkendorff , "*The importance of surface morphology in controlling the selectivity of polycrystalline copper for CO_2 electroreduction*", **Phys. Chem. Chem. Phys**., 2012, 14, 76-81.

2. A. S. Varela, C. Schlaup, **Z. P. Jovanov**, P. Malacrida, S. Horch, I.E.L. Stephens, I. Chorkendorff, "*CO_2 electro-reduction on well-defined bimetallic surfaces: Cu overlayers on Pt(111) and Pt (211)*", **J. of Phys. Chem. C**, 2013, 117, 20500-20508.

3. **Z. P. Jovanov**, H. Hansen, A. S. Varela, P. Malacrida, A.A. Peterson, I.E.L. Stephens, J. K. Nørskov, I. Chorkendorff, "*Investigation of CO_2 and CO reduction on Au and Au-Cd alloys",* in preparation, 2014.

PCCP

Cite this: *Phys. Chem. Chem. Phys.*, 2012, **14**, 76–81

www.rsc.org/pccp

COMMUNICATION

The importance of surface morphology in controlling the selectivity of polycrystalline copper for CO_2 electroreduction†

Wei Tang,[a] Andrew A. Peterson,[b] Ana Sofia Varela,[a] Zarko P. Jovanov,[a] Lone Bech,[a] William J. Durand,[b] Søren Dahl,[a] Jens K. Nørskov[b] and Ib Chorkendorff*[a]

Received 23rd August 2011, Accepted 20th October 2011
DOI: 10.1039/c1cp22700a

This communication examines the effect of the surface morphology of polycrystalline copper on electroreduction of CO_2. We find that a copper nanoparticle covered electrode shows better selectivity towards hydrocarbons compared with the two other studied surfaces, an electropolished copper electrode and an argon sputtered copper electrode. Density functional theory calculations provide insight into the surface morphology effect.

The electrochemical conversion of CO_2 into hydrocarbons is of growing interest, since it could offer a way to continue the convenient use of carbon based fuels in a CO_2 neutral manner. The challenge is to convert CO_2 under ambient conditions, such that the reaction can run at affordable cost and be adopted on a wide scale in decentralized units positioned where surplus electrical energy is available. The electrical energy would be provided by sustainable energy options (such as wind, solar and hydro) where the electricity production displays strong temporal variations and therefore must be averaged on different time scales. Electrochemical fixation of CO_2 is potentially a pathway for long term chemical storage of sustainable energy,[1] providing the products which could transport fuel.

In the past few decades, many metals were investigated as catalysts for the electroreduction of CO_2 with a view to improving the yield of desirable molecules and control the product selectivity.[2] Among the possible products, hydrocarbons such as methane and ethylene are the most desired, due to their high energy densities and widespread use in the current infrastructure. Among the studied metals, copper is the only metal that produces hydrocarbons with high Faradaic efficiency, instead of producing less valuable products such as formic acid or CO.[3,4] To produce useful hydrocarbons, such as CH_4 ($CO_2 + 2H_2O \rightarrow CH_4 + 2O_2$), a total potential of about 2.5 V is required, including the thermodynamic reaction potential of 1.1 V, an overpotential of $\sim$1 V[4] on the copper electrode for the hydrogenation reaction and an overpotential of $\sim$0.4 V[5,6] for the oxygen evolution reaction. This results in a total energy efficiency of $\sim$40%. With its unique electrocatalytic properties and high abundance, polycrystalline copper is a promising candidate for the electrochemical conversion of CO_2 at an industrial scale. Therefore, it is essential to understand how to prepare a polycrystalline copper electrode in order to optimize its catalytic activity. In the past, it has been reported that the Faradaic efficiencies for this reaction are strongly affected by pretreatment of the copper electrode.[7,8] However, the underlying reasons for the influence of the pretreatment are still not clearly established. In this work, different pretreatments were used to prepare copper electrodes for CO_2 reduction. Three copper electrodes (Samples A, B and C) were investigated:

Sample A: a copper electrode (25 mm × 12.5 mm, thickness 1 mm, 99.999%, Goodfellow) and a connecting copper wire (diameter 0.5 mm, 99.999%, Goodfellow) were cleaned by electropolishing. The electropolishing was performed by applying a potential of +2 V between the copper electrode and a platinum cathode in phosphoric acid (1 mol L^{-1}) for 20 min and rinsing the copper electrode with deionized water (18 MΩ). As electropolishing occurs at anodic potential, a certain amount of electrode material is stripped from the surface along with surface impurities.[9,10] During the stripping, the protruding parts in the surface profile are preferentially dissolved and thereby results in smooth, ordered terraces,[9–11] as shown by scanning tunneling microscopy (STM).[9,12,13] The surface morphology resulting from electropolishing is heavily influenced by electrolyte ion adsorption.[12,13] Strong binding of adsorbates enhances surface diffusion of metal atoms.[12] The terraces are stabilized by the formation of ordered adsorbate layers.[13] Consequently, the terraces are harder to dissolve than steps. Electropolishing in phosphoric acid is a routine procedure for the preparation of planar copper single crystal surfaces. The sample shows a smooth surface in scanning electron microscopy (SEM) as shown in Fig. 1a. Hence, based on our SEM images and earlier STM studies,[9,14] the electropolished surface will probably be dominated by low indexed terraces such as (100) and (111), but will also contain a significant number of low coordinated surface sites such as steps.

Sample B: a copper electrode as in Sample A covered with nanoparticles. The copper nanoparticles were formed in two steps. In the first step, the potential at the electropolished copper electrode was scanned between −0.6 and +1.15 V *vs.* RHE (see Fig. 2a) at 20 mV s^{-1} in N_2 saturated $KClO_4$ (0.1 M, Aldrich, 99.99%).

[a] *Center for Individual Nanoparticle Functionality, Department of Physics, Building 312, Technical University of Denmark, DK-2800 Lyngby, Denmark. E-mail: ibchork@fysik.dtu.dk*
[b] *SUNCAT Center for Interface Science and Catalysis, Department of Chemical Engineering, Stanford University, Stanford, CA, USA*
† Electronic supplementary information (ESI) available. See DOI: 10.1039/c1cp22700a

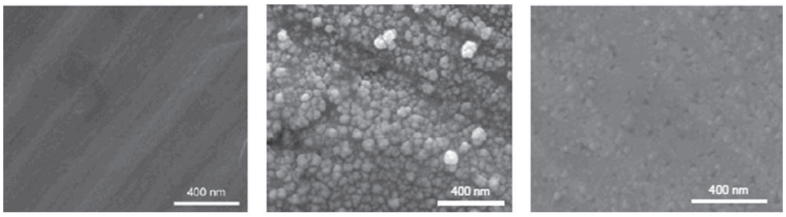

Fig. 1 Scanning Electron Microscopy for three surfaces: (a) Sample A (electropolished surface), (b) Sample B (copper nanoparticle covered surface) and (c) Sample C (sputtered surface).

The pH value of the electrolyte during the cyclic voltammetry was influenced by hydrogen evolution during the most scan potentials and it increased from an initially neutral value of ~7 up to the finally measured value of 10.5 after 20 cycles. After cyclic voltammetry, the electrolyte turned slightly yellow-brownish due to eventually dissolved species, as well as to formation of suspended brownish particles. According to the Pourbaix diagram for copper,[15] the species present in alkaline solution are not expected to be the Cu^{2+} ions, but rather CuO_xH_y species. In the second step, along with reduction of the copper containing species formed at the first step, the copper was redeposited on the electrode surface. The redeposition was performed in CO_2 saturated $KClO_4$ (pH = 6.0, 0.1 M) with a constant bias of −1.3 V *vs.* RHE for 20 minutes. The redeposition of copper is observed to be dependent on the pH value of the electrolyte, as reported previously.[16] Purging with CO_2 was used to adjust the pH of the electrolyte to a value of ~6. After redeposition of copper, the electrode surface turned dark as shown in Fig. S1 (ESI†). SEM was used to characterize the dark electrode. As seen in Fig. 1b a few layers of copper nanoparticles with size of 50–100 nm cover the copper surface. Estimated from the SEM image, the surface area of Sample B is greater than the geometric surface area of the electrode by a factor of 2–3.

Sample C: a copper electrode as in Sample A sputtered with argon ions. The sputtering was conducted in an XPS system (Theta Probe, Thermo Scientific) with 3 keV Ar^+ ions and 4 μA emission current for 10 min. At each cycle of Ar^+ sputtering, an area of 10 mm × 10 mm was bombarded with Ar^+ ions, removing approximately 30 monolayers (~10 nm) from the surface. Six different areas on both sides were sputtered to treat the whole electrode (25 mm × 12.5 mm). On a microscopic scale, Sample C shows a roughened surface topography, due to pit formation after Ar^+ bombardment and island growth by metal atoms redeposition, as observed before in the STM studies[17] (Fig. 1c).

There is some controversy in the literature as to whether the active phase for CO_2 electroreduction is metallic Cu[2–4,18–22] or Cu_2O.[8,23] Consequently, the three samples were characterized using X-ray Photoelectron Spectroscopy (XPS). The XPS spectrum of the sputtered copper surface (Sample C), as prepared, represents that of a clean metallic surface. The other two samples contain some surface oxygen due to the transfer under ambient conditions. However, there is no chemical shift observed due to copper (II) oxide. All three surfaces exhibit the following signals for copper: Cu 2p3/2 at 932.4 eV and Cu 2p1/2 at 952.2 eV, that correspond to metallic copper or copper (I), see Fig. S2a (ESI†).

To differentiate between metallic Cu and Cu_2O, the Cu Auger spectrum was measured.[24] Fig. S2b (ESI†) shows the copper Auger lines for the three surfaces, as prepared. The sputtered sample naturally only shows the fingerprint of metallic copper since no oxygen was present here at all. The electropolished sample also appears to be metallic, *i.e.*, the small amount of oxygen adsorbed during the transfer is not significantly influencing the Auger signal. This could be explained by the preparation procedure, which involves applying a positive potential in a phosphoric acid solution (pH 1.5) where, according to the copper Pourbaix diagram, the stable species should be Cu^{2+} and no oxide species are expected.[15] The nanoparticle covered surface (Sample B) shows an Auger peak that corresponds to Cu_2O. This sample was prepared in 0.1 M $KClO_4$ solution within the pH range where Cu_2O can be formed. It was unclear whether the nanoparticles were oxidized when they formed, during the redeposition step, or simply by the exposure to the electrolyte. With the aim of clarifying this issue, we studied the Auger signals on the sputtered sample in following cases: under UHV conditions, air exposed (30 min) and after being dipped into the electrolyte. Based upon Fig. S2c (ESI†), exposure to the air leads to a slightly oxidized surface, while dipping the sample into the electrolyte forms a fully oxidized surface, as observed on the nanoparticle covered sample. Therefore, the XPS measurements are insufficient to identify the active phase of copper for electrocatalytic CO_2 reduction. Only *in situ* measurements would be able to identify the real surface state during the electrocatalytic process.

Even though we do not have any measurements of the oxidation state of copper during the catalytic reaction, we take the view that it is highly unlikely that the active phase is a form of copper oxide, rather than metallic Cu. There is a significant driving force for the reduction of copper oxide under reaction conditions, *i.e.* ~−1.5 V overpotential relative to the Nernst potential of the reduction of Cu_2O to metallic Cu at pH ~6 and −1.1 V *vs.* RHE.[15] Notably, *in situ* STM studies have shown that at the most ~−1 V overpotential is required to completely reduce Cu oxide to form ordered Cu(111) terraces in 0.1 M NaOH.[25] Moreover, Le *et al.*[26] found that their Cu oxide catalyst reduced to metallic Cu at an overpotential of −1.3 V, relative to the Cu/Cu_2O reversible potential in CO_2 saturated 0.5 M $KHCO_3$.

As electrochemical characterization of the surfaces, cyclic voltammetries in N_2 saturated and CO_2 saturated atmospheres were performed on the three samples. A non-buffered solution

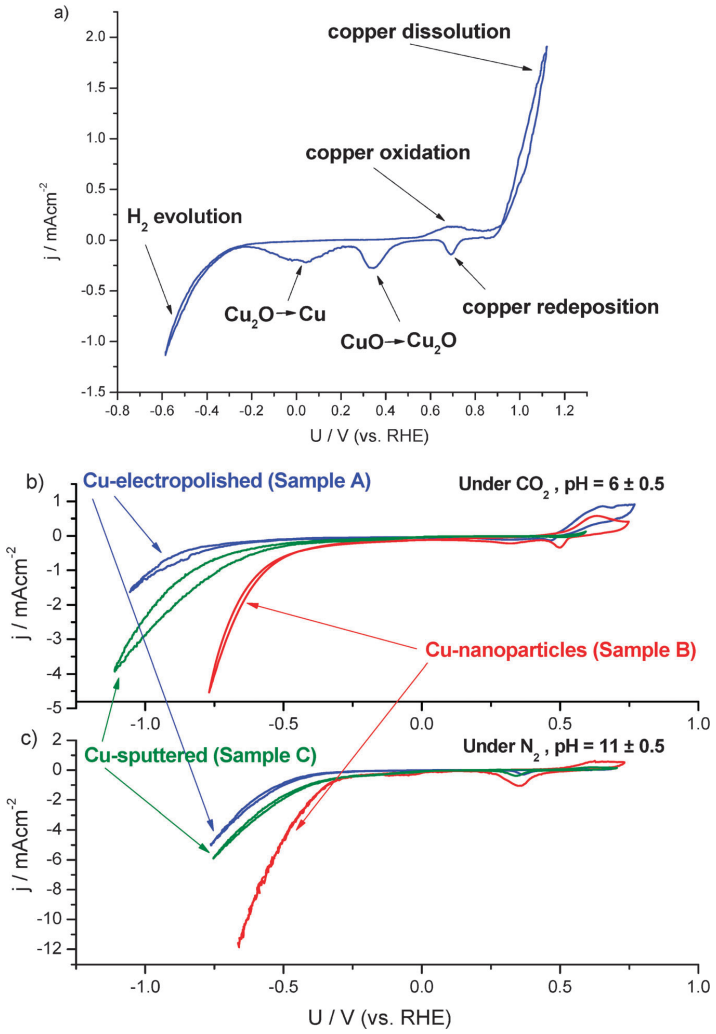

Fig. 2 Cyclic voltammogram of the formation of copper nanoparticles in 0.1 M $KClO_4$ purged with N_2 at pH 10.5 (a); cyclic voltammogram of the electropolished copper surface, copper nanoparticle covered surface and sputtered copper surface in 0.1 M $KClO_4$ purged with CO_2 (b) and N_2 (c). The current density is normalized by the geometric area of the electrode surface. The overpotentials are corrected for ohmic resistance between the working and reference electrode.

$KClO_4$ (0.1 M) was used as electrolyte, with the pH value monitored throughout all the steps of the electrochemical process. The as-made electrolyte has pH of 7 ± 0.5. Pre-electrolysis was performed in order to remove possible traces of impurities, which shifts the pH to values of *ca.* 8. Cycling to very negative potentials also increases pH. CVs in N_2 were recorded at alkaline pH 11 ± 0.5. However, CO_2 bubbling lowers the pH down to 6 ± 0.5. In Fig. 2(b and c), the cyclic voltammograms (CV) in saturated 0.1 M $KClO_4$ under CO_2 and N_2, respectively, are shown against the reversible hydrogen electrode (RHE), with the potential scales corrected for pH and confirmed through the alignment of the Cu(I)-oxide formation peak. As expected according to the copper Pourbaix diagram,[15] these peaks appear at the same potential against RHE when CVs are performed in the same potential range. Plotting the CVs against RHE enabled the comparison of the onset potentials for the reduction process, such as the hydrogen evolution reaction (HER) in the N_2 saturated environment and the two simultaneous processes HER and CO_2 reduction in the CO_2 saturated environment. Firstly in the N_2 saturated environment, the formation of the cuprous oxide is observed at potentials of *ca.* 0.65 V *vs.* RHE, followed by its reduction during cathodic scan at ~0.3 V *vs.* RHE, which is consistent with the thermodynamical potential of Cu to Cu_2O at 0.47 V *vs.* RHE.[15] The electropolished

polycrystalline copper surface (Sample A) exhibits an exponential increase of cathodic current at −0.45 V, indicative of hydrogen evolution. The nanoparticle covered surface (Sample B) and the sputtered surface (Sample C) have the onset potential for hydrogen evolution earlier than Sample A. Moreover, at the most negative potentials, the cathodic current density is greater on roughened surfaces than on the electropolished surface. This could partially be attributed to the increased surface area of the nanoparticle covered surface. However, we can consider that the electropolished sample and the argon sputtered sample have the same surface area. Therefore, the difference in onset potential and current values, between these two electrodes, can only be attributed to surface morphology. On the other hand, the difference between the current values for the electropolished electrode and the nanoparticles covered electrode is greater than the expected from the difference in surface area. For instance, at −0.6 V the current is 4.5 times higher on the nanoparticle covered surface than on the smooth one. The surface area increase contributes only with the previously estimated factor of 2–3.

In addition, higher surface area does not explain the improved onset potential of the roughened surface, which is more indicative of a better electrocatalytic activity for hydrogen evolution on the surface dominated by low coordinated surface atoms.

Cyclic voltammetry in CO_2 (pH 6.0 ± 0.5) shows similar trends as in nitrogen where the higher current densities were observed on roughened surfaces (Samples B and C). For instance, at −0.75 V *vs.* RHE, the current density of the nanoparticle covered surface (Sample B) is 10 times higher compared to the electropolished surface (Sample A), which again is a proof that the surface morphology contributes more to the current densities than just the effect of surface area increase.

The onset potentials, when the current density exceeds 1 mA cm^{-2}, appear at −1.0 V for the electropolished surface, at −0.8 V for the sputtered surface and around −0.6 V for the nanoparticle covered surface, which are more negative than that observed in N_2. The more negative onset potentials indicate the presence of adsorbed species during CO_2 reduction. According to Hori[2], the CO_2 reduction reaction proceeds with the formation of adsorbed CO as an intermediate product. The Faradaic current is being contributed from two competing reactions:

$$*CO_2 + 2H^+ + 2e^- \rightarrow *CO + H_2O$$

(The "*" indicates that it adsorbs to the surface)

$$2*H^+ + 2e^- \rightarrow H_2$$

To confirm a better catalytic performance of Sample B the reaction products were determined, after applying a constant potential of −1.1 V *vs.* RHE on a CO_2 saturated electrolyte for 15 minutes. Results from the electrocatalytic reactions on the three samples are shown in Fig. 3. Faradaic efficiencies of the major gas-phase products are expressed by monitoring the product distribution using gas chromatography and relating those to the charge consumed during the reaction. After 15 minutes of reaction, the concentration of the liquid product was below the detection limit. To identify the liquid products the reaction was run for 24 hours using the electropolished sample. According to the HPLC analysis the only product

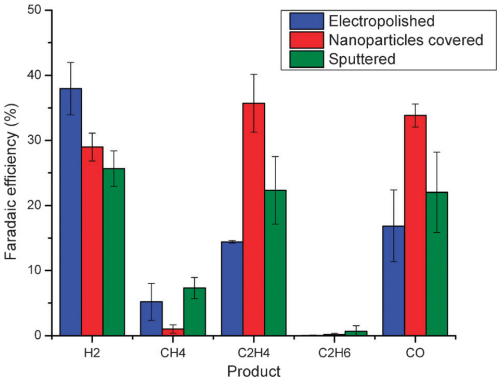

Fig. 3 Faradaic efficiency for the products of electroreduction of CO_2 on three surfaces in CO_2-saturated 0.1 M $KClO_4$ upon −1.1 V *vs.* RHE, including Sample A (electropolished surface), Sample B (copper nanoparticle-covered surface) and Sample C (sputtered surface).

present in the liquid phase is formic acid (faradaic efficiency of ~7.5%). During the 24 hour reaction the copper electrode turned black, therefore it was characterized by SEM (see Fig. S3, ESI†). The SEM images showed a nanoparticles covered surface which indicates that during the reaction some copper is dissolved and redeposited on the electrode, generating a roughened surface. Since the surface structure is modified during the reaction the faradaic efficiency obtained during the 24 hour experiment cannot be attributed only to a smooth surface. In Fig. 3 it is clear that a higher total efficiency towards CO_2 reduction gas products (methane, ethylene and CO) is obtained using the roughened surface (Sample B), while the smooth surface (Sample A) has a lower faradaic efficiency towards the products related to CO_2 reduction. On the other hand, the selectivity towards hydrogen is higher on the smooth surface (Sample A) than on the roughened surfaces (Samples B and C). These two facts imply the importance of the roughening of the copper surface for the better selectivity towards CO_2 reduction. The formation ratio between CH_4 and C_2H_4 is also noteworthy. Sample A produces C_2H_4 with the faradaic efficiency of 14% and CH_4 with 5%. Sample B preferentially converts CO_2 to C_2H_4 with the faradaic efficiency of 36%, but only 1% to CH_4. Sample C has a slightly lower faradaic efficiency of 26% towards C_2H_4, but only 8% towards CH_4. These results indicate that production of C_2 is favored on a roughened surface.

Better catalytic performance of the roughened surface is obtained due to two different effects: achieved higher current densities and improved faradaic selectivity to hydrocarbons. Increase in current densities is easily explained taking into account the higher surface area of the roughened sample, providing more active sites for both CO_2 conversion and hydrogen evolution. Improvement in the selectivity towards hydrocarbons suggests that the morphology of the surface plays a significant role in the process. As established earlier, the smooth surface consists mostly of low index crystal facets, such as Cu(100) and Cu(111). However, the roughened surfaces contain significantly more low-coordination sites, such as steps, edges and defects that seem to be more active towards CO_2 reduction.

Our observations on different surfaces are in agreement with Hori's investigations[2] of CO_2 electroreduction on single crystal Cu surfaces in 0.1 M $KHCO_3$ aqueous solution. These investigations include terrace facets, Cu(111) and Cu(100), that can be compared with the smooth surface of Sample A in our case. Stepped surfaces like Cu(311), Cu(511) and Cu (711) can be related to roughened surfaces on Samples B and C.[19–20,22] Hori *et al.* observed that the stepped copper surfaces exhibit different selectivities and that the reactions occur at lower potentials for a specific current density compared to the terrace facets. They also concluded that the selectivity ratio between CH_4 and C_2H_4 depends strongly on the crystal orientation.[19–20,22] They reported that Cu(111) produced CH_4 with a faradaic efficiency of 50.5% and C_2H_4 with an efficiency of 8.8%. On the other hand, the stepped surface, Cu(711), was more selective towards C_2H_4, with a Faradaic efficiency of 3.8% towards CH_4 and 51.6% towards C_2H_4. Given that CO_2 reduction is strongly influenced by the electrolyte, working potentials, and pH,[4] it is difficult to make a direct, quantitative comparison of Hori *et al.*'s results to our own. Nevertheless, our observations, whereby the selectivity towards C_2H_4 or CH_4 depends on the surface morphology, seem to be consistent with those of Hori *et al.* A recent paper by Koper and co-workers[27] sheds light on the correlation between the formation of CO and ethylene. They propose two different pathways: one for methane and another one for ethylene formation. Our results indicate that on different surfaces CO and ethylene formation follow the same trends. Higher CO production seems to favor the formation of ethylene, as previously suggested.[21,27] It is also worth mentioning that the highest selectivity for ethylene on nanoparticle covered surface seems to be a reason for suppressed methane production. However, based on our results, we are not able to make strong conclusions on intermediates required neither for methane nor for ethylene formation.

In order to understand the apparent effect of surface pretreatment on the catalytic performance of Cu towards CO_2 electroreduction, density functional theory (DFT) calculations were performed on the fcc(111), fcc(100) and fcc(211) facets of Cu. As discussed earlier, the roughened surfaces would contain a larger number of defects such as steps, the effect of which can be modeled by the (211) facet. On the other hand, the electropolished surface should be dominated by the terrace facets, such as (111) and (100).

Free energetics of the hydrogen evolution reaction was calculated with DFT and is shown in Fig. S4 (ESI†); the stepped sites (211) are predicted to have higher activity than the terrace (111) and (100) sites since the free energy of the adsorbed hydrogen intermediate (H*) is closer in free energy to the initial and final states of the reaction. This may translate into a higher activity for hydrogen evolution on these stepped sites. However, this may have less of an effect on the onset potential than the free energy diagram would suggest: the steps on the Cu surface are inaccessible to adsorbed H at low bias (less negative potentials), since they can be blocked by hydroxyl (OH) groups. This is shown in Fig. S5 (ESI†), in which DFT calculations show that OH adsorption from water proceeds spontaneously at 0 V *vs.* RHE on the (211) and (100) copper surfaces causing the surface blocking.

Density functional theory calculations were also employed to have a better understanding on the improved hydrocarbon selectivity of the roughened surfaces. The conversion of electronic energies to free energies, the effect of solvation, and the effect of electric fields were handled in a manner identical to that in a previous study that examined CO_2 reduction at copper electrodes.[21,28] In the previous study, the elementary proton–electron transfer steps have been proposed for the process of reducing CO_2 to hydrocarbons. The potential requirements in CO_2 reduction to methane on Cu fcc(211) surfaces have been proposed, where the protonation of adsorbed CO to produce adsorbed CHO is identified as the limiting step.[21] While many factors control the reactivity of the different facets of copper during the CO_2 electrochemical reduction and a complete understanding will require a more detailed model, we based on this previous study to determine the effect of surface roughness on the energetics of this transformation. Therefore we calculated the free energies of the transformation of CO* to both CHO* and COH* (where an asterisk, *, indicates an adsorbed species) on three different copper crystal facets, which were taken to be indicative of the range of smooth and roughened surfaces encountered in polycrystalline copper.

These three facets are the (111) surface, which is a smooth facet containing the highest surface density of metal atoms and 3-fold binding sites, the (100) surface, which is a smooth facet containing a lower surface density of metal atoms and 4-fold binding sites, and the (211) surface, which contains a step. Fig. 4 compares the energetics of CO* protonation on the (111), (100), and (211) surfaces at 0 V *vs.* RHE. It can be seen that on all surfaces, the route to CHO* is favored over the

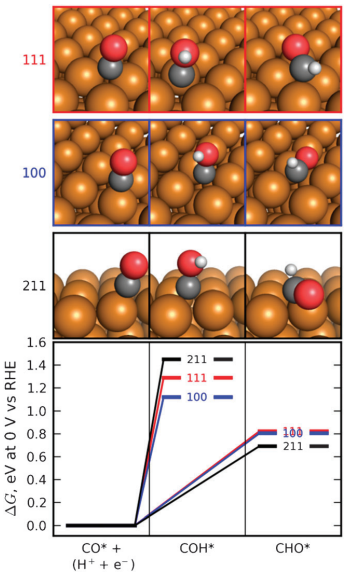

Fig. 4 Calculated free energies, at 0 V *vs.* reversible hydrogen electrode (RHE), of the protonation of adsorbed CO to form adsorbed COH or CHO on the (111), (100), and (211) facets of the face-centered cubic copper crystal. The protonation proceeds most favorably on the (211) facet to the CHO adsorbate. See also Durand *et al.*[28]

route to COH*, and the (211) surface stabilizes this transformation relative to the (111) and (100) surfaces. This may partially explain the higher current and higher selectivity to hydrocarbons experimentally observed on the roughened surfaces. It has been suggested that the ethylene is formed from a non-electrochemical surface reaction between adsorbed species, for example the coupling of CHO* to *OCHCHO*.[21] The high selectivity of C_2H_4 and low selectivity of CH_4 on Sample B are possibly due to high coverage of CHO* or other adsorbed species along step edges. Therefore the formation rate of C_2H_4 is influenced by the surface crystal orientation.

Among the three copper surfaces with different pretreatments and thus morphologies, the roughened copper surfaces (the copper nanoparticle covered surface and the sputtered surface) show higher selectivities towards hydrocarbons. In particular, our *in situ* activation method to prepare the copper nanoparticle surface is simple and effective. The morphology effect is explained by the greater abundance of undercoordinated sites on the roughened surfaces. DFT calculations indicate that these sites are more likely to be the active sites for CO_2 reduction. On the basis of our results, we propose that the activity of Cu could be enhanced further by preparing smaller nanoparticles of Cu, as these would have a greater density of undercoordinated sites.

Acknowledgements

This work was supported by the ''Catalysis for Sustainable Energy'' (CASE) research initiative, which is funded by the Danish Ministry of Science, Technology and Innovation. Center for Individual Nanoparticle Functionality is funded by The Danish National Research Foundation. The Center for Atomic-scale Materials Design is funded by the Lundbeck Foundation. This material is based in part upon work supported by the Air Force Office of Scientific Research through the MURI program under AFOSR Award No. FA9550-10-1-0572. The HPLC analysis of the liquid face was carried out at Haldor Topsøe by Christian Mårup Osmusdsen. The authors sincerely thank Dr Ifan Stephens and Dr Francisco Pérez Alonso for discussion and suggestion.

References

1 F. Schuth, *Eur. Phys. J. Spec. Top.*, 2009, **176**, 155–166.
2 Y. Hori, in *Modern Aspects of Electrochemistry*, ed. C. G. Vayenas, Springer, 2008, pp. 89–189.
3 M. Gattrell, N. Gupta and A. Co, *J. Electroanal. Chem.*, 2006, **594**, 1–19.
4 Y. Hori, A. Murata and R. Takahashi, *J. Chem. Soc., Faraday Trans. 1*, 1989, **85**, 2309–2326.
5 Y. Gorlin and T. F. Jaramillo, *J. Am. Chem. Soc.*, 2010, **132**, 13612–13614.
6 S. Trasatti, *Electrochim. Acta*, 1984, **29**, 1503–1512.
7 M. R. Goncalves, A. Gomes, J. Condeco, R. Fernandes, T. Pardal, C. A. C. Sequeira and J. B. Branco, *Energy Convers. Manage.*, 2010, **51**, 30–32.
8 Y. Terunuma, A. Saitoh and Y. Momose, *J. Electroanal. Chem.*, 1997, **434**, 69–75.
9 S. Huemann, N. T. M. Hai, P. Broekmann, K. Wandelt, H. Zajonz, H. Dosch and F. Renner, *J. Phys. Chem. B*, 2006, **110**, 24955–24963.
10 J. K. Zhang, G. N. Okeke and C. H. B. Mee, *J. Phys. E: Sci. Instrum.*, 1986, **19**, 314–314.
11 T. N. Andryushchenko, A. E. Miller and P. B. Fischer, *Electrochem. Solid-State Lett.*, 2006, **9**, C181–C184.
12 S. Horch, H. T. Lorensen, S. Helveg, E. Laegsgaard, I. Stensgaard, K. W. Jacobsen, J. K. Norskov and F. Besenbacher, *Nature*, 1999, **398**, 134–136.
13 O. M. Magnussen, *Chem. Rev.*, 2002, **102**, 679–725.
14 H. I. Rasool, E. B. Song, M. J. Allen, J. K. Wassei, R. B. Kaner, K. L. Wang, B. H. Weiller and J. K. Gimzewski, *Nano Lett.*, 2011, **11**, 251–256.
15 E. Protopopoff and P. Marcus, *Electrochim. Acta*, 2005, **51**, 408–417.
16 N. T. M. Hai, K. Wandelt and P. Broekmann, *J. Phys. Chem. C*, 2008, **112**, 10176–10186.
17 T. Michely and G. Comsa, *Surf. Sci.*, 1991, **256**, 217–226.
18 Y. Hori, H. Konishi, T. Futamura, A. Murata, O. Koga, H. Sakurai and K. Oguma, *Electrochim. Acta*, 2005, **50**, 5354–5369.
19 Y. Hori, I. Takahashi, O. Koga and N. Hoshi, *J. Phys. Chem. B*, 2002, **106**, 15–17.
20 Y. Hori, I. Takahashi, O. Koga and N. Hoshi, *J. Mol. Catal. A: Chem.*, 2003, **199**, 39–47.
21 A. A. Peterson, F. Abild-Pedersen, F. Studt, J. Rossmeisl and J. K. Norskov, *Energy Environ. Sci.*, 2010, **3**, 1311–1315.
22 I. Takahashi, O. Koga, N. Hoshi and Y. Hori, *J. Electroanal. Chem.*, 2002, **533**, 135–143.
23 P. Dubé and G. M. Brisard, *J. Electroanal. Chem.*, 2005, **582**, 230–240.
24 F. Matjaz, P. Sebastijan, K. Anton, C. J. Kova and M. Ingrid, *J. Electrochem. Soc.*, 2010, **157**, C295–C301.
25 V. Maurice, H.-H. Strehblow and P. Marcus, *Surf. Sci.*, 2000, **458**, 185–194.
26 M. Le, M. Ren, Z. Zhang, P. T. Sprunger, R. L. Kurtz and J. C. Flake, *J. Electrochem. Soc.*, 2011, **158**(5), E45–E49.
27 K. J. P. Schouten, Y. Kwon, C. J. M. van der Ham, Z. Qin and M. T. M. Koper, *Chem. Sci.*, 2011, **2**, 1902–1909.
28 W. J. Durand, A. A. Peterson, F. Studt, F. Abild-Pedersen and J. K. Nørskov, *Surf. Sci.*, 2011, **605**(15–16), 1354–1359.

THE JOURNAL OF PHYSICAL CHEMISTRY C

Article

pubs.acs.org/JPCC

CO_2 Electroreduction on Well-Defined Bimetallic Surfaces: Cu Overlayers on Pt(111) and Pt(211)

Ana Sofia Varela, Christian Schlaup, Zarko P. Jovanov, Paolo Malacrida, Sebastian Horch, Ifan E. L. Stephens,* and Ib Chorkendorff*

Center for Individual Nanoparticle Functionality, Technical University of Denmark, Fysikvej 312, DK-2800 Kongens Lyngby, Denmark

Supporting Information

ABSTRACT: We have studied the electrochemical reduction of CO_2 on Cu overlayers on Pt(111) and Pt(211) surfaces. These systems were chosen to investigate the effect of strain on the catalytic activity of Cu surfaces and to obtain information about the role of steps in this process. The selectivity toward hydrocarbons on the copper overlayers is much lower than on polycrystalline copper due to a higher selectivity for hydrogen evolution. With the aim of understanding the lower activity toward CO_2 electroreduction of the Cu overlayers, we also studied the surfaces under reaction condition using electrochemical scanning tunneling microscopy (EC-STM). In the presence of CO, the Cu overlayer changes from a flat to a granular structure exposing part of the Pt surface. The exposed Pt surface accounts for the high selectivity of these structures toward hydrogen evolution. These results illustrate the dynamic nature of the surface under reaction conditions and that *in situ* measurements are crucial to understand catalytic activity.

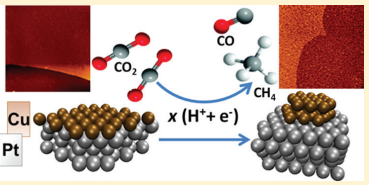

INTRODUCTION

In recent years, there has been an increasing amount of interest into the electrochemical reduction of CO_2.[1−9] This process could potentially be used to produce carbon neutral fuels using the otherwise wasted excesses of electricity generated from renewable sources. In addition, some of the possible reduction products may be used as feedstock for the chemical industry.[10]

Despite over two decades of research, Cu is the only metal found to produce hydrocarbons in considerable amounts.[11] Nevertheless, formation of hydrocarbons occurs at more than 0.7 V overpotential, which implies significant energy losses (the reversible potentials for most of the products are close to 0.0 V RHE).[12] In addition, the reduction of CO_2 on copper results in a mixture of products such as CO, formic acid, methane, and ethylene.[12] Besides these products, H_2 is evolved in a competitive reaction. Because of the low efficiency and selectivity of copper, it is crucial to find catalysts that selectively and efficiently reduce CO_2, to make this process technologically viable.

The reactivity of pure Cu toward CO_2 reduction can, to a certain degree, be tuned by modifying its structure and morphology. Nanostructured Cu seems to be more active and selective toward CO_2 reduction to ethylene and methane than electropolished polycrystalline Cu.[1,6] This can be rationalized on the basis of density functional theory calculations by Nørskov and co-workers on Cu(111), Cu(100), and Cu(211).[13] According to those calculations, on each of these surfaces the limiting step is the hydrogenation of *CO (where *CO denotes adsorbed CO), the most stable intermediate. The overpotential for this step is lower on the most undercoordinated surface, the fcc (211) step site. Since steps and other undercoordinated sites would be more prevalent on nanoparticles, these calculations explain the observation that nanostructured Cu is more active for CO_2 reduction.

Nanostructured Cu is also more selective to ethylene formation than methane.[1,6] These results are consistent with single crystals studies that have shown that at low index facets such as Cu(111) methane is the predominant hydrocarbon while on step surfaces such as Cu (711) ethylene formation is favored. Interestingly, when comparing CO reduction on different single crystal Cu surfaces using online electrochemical mass spectroscopy (OLEMS), Koper and co-workers[14] observe that C_2H_4 formation occurs at the lowest overpotentials on Cu(100); stepped surfaces appear to be less active. Nevertheless, it is important to bear in mind the inherent challenges in working with Cu single crystals in an electrochemical environment and that the overall surface structure might differ considerably. First, whereas Pt and Au single crystals are usually prepared for electrochemical measurements by thermal annealing, Cu single crystals are typically electropolished in phosphoric acid. Although electropolishing produces some ordered terraces, they are typically narrower than those of thermally annealed Au or Pt. Moreover, recent electrochemical scanning tunnel microscopy (EC-STM) studies from our laboratory have shown that the Cu(111) facets are unstable in phosphate buffer at neutral pH.[15] Therefore, the surface structure is modified appreciably under CO_2 electroreduction

Received: July 12, 2013
Revised: September 3, 2013
Published: September 16, 2013

conditions and does not correspond to the initial single crystal orientation.

Regardless of the exact orientation of the Cu single crystals, it is clear that surfaces with higher amount of undercoordinated sites favor ethylene production over methane. However, the mechanism by which ethylene is produced is still under debate. Nørskov and co-workers argue that the potential determining step is the hydrogenation of *CO, the same as for methane, and that the C−C bond is formed from a nonelectrochemical surface reaction between adsorbed species, for example the coupling of *CHO to *OCHCHO*.[4,16] On the other hand, Koper and co-workers propose that the C−C coupling step occurs prior to the hydrogenation of *CO.[2,17]

An alternative option for tuning the reactivity of Cu would be to modify its structure by forming overlayers of the metal on a foreign metal substrate. Metal overlayers afford unique opportunities toward tuning the activity of surfaces and have been investigated widely in the field of catalysis.[18−24] Overlayer structures exhibit improved catalytic activity in comparison with pure metals in a variety of gas phase catalytic and electrocatalytic processes; these include the water shift reaction, methanol oxidation,[25,26] CO electro-oxidation,[20] oxygen reduction reaction,[24] formic acid electro-oxidation,[22] and the hydrogen evolution reaction.[21,23] Their reactivity is determined by interplay between *ligand* and *strain* effects.[22,27−29] Ligand effects are due to a change in the electronic structure caused by the presence of dissimilar atoms.[19,30,31] Conversely, strain effects occur when the interatomic distance in the surface changes; in accordance with the d-band model compression results in weaker interaction with adsorbates whereas tensile strain results in stronger interaction.[29,32]

Placing a pseudomorphic Cu overlayer on Pt(111), i.e., an overlayer that adopts the interatomic distance of the host substrate, modifies the binding to CO by ∼0.4 eV,[29] relative to Cu(111). On that basis, we would anticipate that Cu overlayers on Pt(111) should show significantly different activity and selectivity toward CO_2 reduction.[4,33] Consequently, in the present paper, we investigate Cu overlayers on Pt(111) single crystals. Moreover, in order to investigate the presence of undercoordinated sites, we also investigate Cu overlayers on a stepped surface, Pt(211). We test the performance of these surfaces for CO_2 reduction in 0.1 M $KHCO_3$ buffer, using cyclic voltammetry and bulk electrolysis, using gas chromatography to measure the gas phase products.

In addition, we have monitored the structure of our Cu overlayer using EC-STM. Such *in situ* experiments are essential to obtain a holistic view of the factors determining the stability and activity of a surface. This is particularly important when working with bimetallic systems, in which CO is known to induce structural changes, causing segregation of one of the components[34−38] or transforming an overlayer to a surface alloy.[39]

EXPERIMENTAL PROCEDURE

The electrochemical measurements were performed in a custom-made three-electrode cell, which has been described elsewhere.[40] This cell allows annealing the crystal without exposing it to air before the electrochemical measurements. We have used a Biologic Instruments SP-150 potentiostat to control the potential during the measurements. The counter electrode was a Pt wire, while the reference electrode (Hg/$HgSO_4$) was in contact with the electrolyte through a capillary, separated by a ceramic firth. For a better comparison all potentials are given against the reversible hydrogen electrode (RHE). The cell has been coupled to a gas chromatograph (GC) (Agilent 6890) for quantification of the gas products. The liquid products were analyzed by high performance liquid chromatography (HPLC).

Before experiments, all glassware was cleaned in "piranha" solution consisting of a mixture of 96% H_2SO_4 and 30% H_2O_2 (3:1) for 24 h, to remove any metal or organic impurities, followed by extensive rinsing with Milli-Q water.

Single Crystal Preparation. Pt(111) and Pt(211) single crystals (MaTecK, Jülich) of 10 mm of diameter were used as working electrodes. Before experiments they were annealed at 850 ± 20 °C in a H_2(5%) + Ar atmosphere for 3 min, followed by annealing in a CO(0.1%) + Ar atmosphere for 1 min at 850 ± 20 °C.

Cu Overlayer Preparation. The copper overlayers were prepared by underpotential deposition (UPD) from a solution containing 2 mM Cu^{2+} (CuO from Alfa Aeser, 99.9995%) and 0.1 M $HClO_4$ (Merck, Suprapur) in ultrapure water (Millipore, Milli-Q). To form a Cu overlayer, the potential was held at 0.32 V vs RHE for 2 min.

Electrocatalytic Studies. CO_2 electroreduction was performed in 0.1 M $KHCO_3$ (pH 6.8), prepared by bubbling CO_2 through a 0.1 M KOH solution (Merck, Suprapur) until a stable pH was reached. For the CO reduction experiments, the 0.1 M $KHCO_3$ solution was saturated with CO by bubbling it for 15 min, resulting in a pH of about 8.3. The bulk electrolysis was performed by applying a constant potential between −0.7 and −1.3 V. The actual working potential was corrected for Ohmic resistance. For each measurement a freshly prepared Cu overlayer has been used to ensure that adsorbates from previous experiments do not influence the result. The catalytic results obtained with the Cu overlayer are compared to those obtained on polycrystalline copper in the same setup. For this purpose we used a Cu foil (10 mm × 10 mm, thickness 1 mm, 99.999%, Goodfellow) cleaned by electropolishing in H_3PO_4, following the procedure described by Hori et al.[12] The roughness factor of the Cu foil was determined via lead under potential deposition (Pb UPD).[41] For this purpose we have assumed a stripping charge of 300 $\mu A/cm^2$, as found by Brisard et al. for Cu(111).[42] All current densities have been normalized according to the roughness factor determined using this method, which was equal to 1.1. For the single crystals we assumed a roughness factor of 1.

EC-STM Studies. The STM measurements were carried out in a custom-built EC-STM setup, using the same experimental procedures as described earlier.[15] In order to avoid contamination, a Pt wire serves the electrochemical cell of the EC-STM setup as a pseudoreference electrode. Its potential is defined by the Pt + H_2O ↔ PtO + $2H^+$ + $2e^-$ equilibrium. This is influenced by the pH of the electrolyte and any species in the electrolyte that may have a higher affinity to Pt than oxygen.

Consequently, it need to be calibrated for each electrolyte solution either by comparison to literature or a NHE reference electrode. To provide comparability to the electrocatalytic measurements, all potentials in the following will be given with respect to RHE.

A Pt(111) single crystal (MaTecK, Jülich) was prepared by flame annealing in a butane/air flame; after cooldown in an argon atmosphere (scientific grade, 99.9999%), it was protected by a droplet of ultrapure water and built into the electrochemical cell of the STM setup.

dx.doi.org/10.1021/jp406913f | J. Phys. Chem. C 2013, 117, 20500−20508

The electrolyte solutions were prepared using the same high purity chemicals as for the electrochemical measurements; however, for Cu deposition a 0.1 M $HClO_4$ + 1 mM CuO solution was used. Because of experimental limitations, i.e., the onset of the oxygen reduction reaction at the STM tip, the used 0.1 M $KHCO_3$ solution was deaerated after saturation with CO_2 for about 10 min with argon. This yields in a higher pH of the solution of 8.5; however, the pH of the CO saturated solution is not affected by this procedure. Possible impacts of the different pH will be discussed in the corresponding section.

X-ray Photoelectron Spectroscopy. Angle-resolved X-ray photoelectron spectroscopy (AR-XPS) measurements were taken *ex situ* on a Theta Probe instrument (Thermo Scientific). The ultrahigh vacuum (UHV) chamber had a base pressure of 5×10^{-10} mbar. The X-ray source is monochromatized Al Kα (1486.7 eV), giving a resolution better than 1.0 at 100 eV pass energy; a beam spot size of 400 μm was chosen. For the angle-resolved profiles, 16 different channels were analyzed in parallel between 20° and 80° from the surface normal, without tilting the sample. Angle-resolved data were processed using the simulation tool, ARProcess (Thermo Avantage software), which uses a maximum entropy method combined with a genetic algorithm to define the depth profiles; angles over 65° were omitted to minimize the effects of elastic scattering.

An overview spectrum was initially taken for identifying the surface composition and possible contaminations. Once the surface elements were identified, detailed angle resolved spectra were acquired for each of the main peaks. Quantification was carried out after removal of a Shirley type background and normalization of the peak areas by Scofield cross sections and the analyzer transmission function.

RESULTS

Electrochemical Characterization of Pt Single Crystals. The single crystals where characterized by cyclic voltammetry (CV) in 0.1 M $HClO_4$ and 0.1 M $KHCO_3$ between 0.05 and 1.0 V to confirm their correct orientation (Figure 1). The CVs in 0.1 M $HClO_4$ are consistent with those reported previously.[43,44] For Pt(111) the CV (Figure 1a) shows the characteristic "butterfly peak" for OH^- adsorption/desorption between 0.6 and 0.8 V, with a peak current density of 70 $\mu A/cm^2$. In contrast, the CV for Pt(211) (Figure 1b) shows two distinct peaks in the region between 0.05 and 0.4 V and two broad signals for OH^- adsorption/desorption. When the electrolyte is exchanged for 0.1 M $KHCO_3$ the OH^- signal on Pt(111) is suppressed, and instead a broad reversible feature is observed at ~0.65 V assigned by Vega et al. to the adsorption of HCO_3^-.[45,46] For Pt(211), the OH^- feature in $HClO_4$ is emplaced by a broad feature at ~0.65 V in 0.1 M $KHCO_3$.

Cu Overlayer Formation. Figure 2 shows in red the anodic scans after Cu deposition on the Pt single crystals. They exhibit an oxidation peak due to Cu stripping at roughly 0.75 V. For Pt(111), this appears as a very sharp feature consistent with a strong interaction between the copper atoms.[47] The obtained charge for the oxidation of copper corresponds to 420 ± 20 $\mu C/cm^2$. In contrast, the oxidation of the Cu overlayer on Pt(211) appears as a broad signal. Furthermore, the Cu oxidation starts at 0.4 V, which corresponds to near bulk oxidation which is expected for step sites.[48] Figure 2 also shows CVs for the Cu overlayers recorded after the electrolyte was exchanged to Cu-free 0.1 M $HClO_4$ (blue lines). They exhibit that the current in the "hydrogen underpotential deposition"

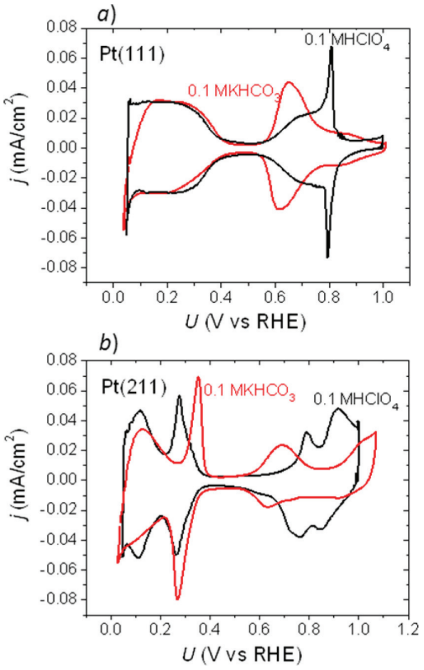

Figure 1. Cyclic voltammograms in Ar-saturated 0.1 M $HClO_4$ and 0.1 M $KHCO_3$ with dE/dt = 50 mV/s for (a) Pt(111) and (b) Pt(211).

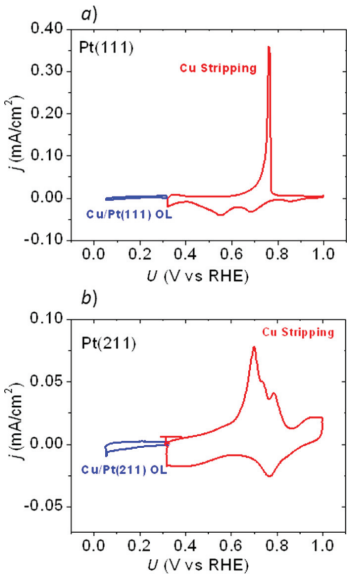

Figure 2. Cyclic voltammograms after Cu deposition in Cu containing 0.1 M $HClO_4$ (red) and in Cu free 0.1 M $HClO_4$ (blue) with dE/dt = 20 mV/s for (a) Pt(111) and (b) Pt(211).

dx.doi.org/10.1021/jp406913f | J. Phys. Chem. C 2013, 117, 20500−20508

regime, from 0.05 to 0.5 V has been suppressed, as previously reported.[20]

Electrocatalytic Activity. Cyclic voltammetry was used to provide an initial, qualitative assessment of the catalytic performance of the four studied surfaces, i.e., Pt(111), Pt(211), Cu/Pt(111), and Cu/Pt(211). They were characterized in a 0.1 M $HClO_4$ solution, saturated with three different atmospheres, i.e., Ar, CO_2, or CO (Figure 3). We note that

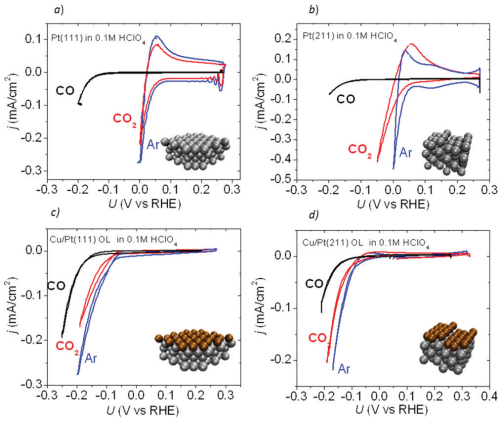

Figure 3. Cyclic voltammograms at 50 mV/s of Pt(111), Pt(211), Cu/Pt(111), and Cu/Pt(211) in 0.1 M $HClO_4$ saturated with Ar, CO_2, and CO. A schematic representation is shown next to the CVs.

CO_2 reduction experiments are not usually carried out in acidic solutions, as at low pH most catalysts show a poorer selectivity toward CO_2 reduction, relative to hydrogen evolution.[11] This is mainly due to the fact that the hydrogen evolution reaction is orders of magnitude more active in acidic than in neutral or alkaline electrolytes.[49] Nonetheless, the advantage of carrying out these measurements in perchloric acid is that the pH will not change significantly upon changing the purging gas, as it would in bicarbonate solutions in which bulk CO_2 electrolysis is usually carried out.

The CVs of the pure platinum surfaces in Ar-saturated solutions show only a reduction current due to the hydrogen evolution reaction (HER) (blue curves in Figure 3a,b). As expected, the onset potential, defined as the potential needed to draw a current of 0.1 mA/cm^2, is close to 0.0 V. In the presence of CO_2, however, the onset for the reduction current on Pt(211) is shifted to more negative potentials, whereas it remains the same for Pt(111) (red curves in Figure 3a,b). Presumably, this shift is caused by reduction of CO_2 to *CO[50] that blocks some of the active sites for the HER. The formation of *CO on Pt(211) was corroborated by CO stripping (Figure S1), where we observed an oxidation signal that corresponds to roughly 1/2 monolayer of CO. According to Hori and co-workers, planar Pt facets such as (100) and (111) are inert toward CO_2, while stepped surfaces are able reduce to CO_2 to *CO. This explains why only on Pt(211) the onset potential for the HER is moved to lower potentials.[51]

It can also be seen that in the presence of CO the onset potential for the reduction current on the pure Pt surfaces is shifted to approximately −0.2 V (black curves in Figure 3a,b). As previously reported, adsorbed *CO inhibits the HER.[52]

In the case of the copper overlayers, there is no significant difference between the two facets under study. The onset potential for the HER in Ar saturated solution shifts approximately 0.1 V with respect to the Cu free surfaces (red lines in Figure 3c,d). This appears intuitive, as Cu is much less active for the HER than Pt.[53,54] In the presence of CO_2, there is a small shift toward more negative potentials, which might be again due to the formation of adsorbed CO (red curves in Figure 3c,d). In contrast, when the electrolyte is saturated with CO, there is a clear shift to higher overpotentials, consistent with the adsorption of CO and the blockage of the active sites (black curves in Figure 3c,d).[45]

Bulk Electrolysis Experiments. On the basis of the CVs described above, we cannot determine the selectivity toward CO_2 reduction and hydrogen evolution of the surfaces under study. For this purpose, we performed potentiostatic bulk electrolysis experiments in 0.1 M $KHCO_3$ and analyzed the gas phase products by gas chromatography (GC).

Potential Dependence. The potential dependence of the CO_2 electroreduction on the Cu overlayers was studied by holding the potential for 15 min. For comparison, we also conducted bulk electrolysis measurements on polycrystalline Cu and on Pt(211). Pt(111) was not tested as the CVs under CO_2 showed that Pt(111) was not active toward CO_2 reduction (Figure 3a,b), in agreement with published results.[51]

It is important to note that these experiments were conducted at much more negative potentials than the onset of the reduction current. Similar to polycrystalline copper, the Cu/Pt surfaces start producing hydrocarbons at high overpotentials (roughly 0.7 V). However, one should be careful to interpret the catalytic results at these high overpotentials, where the total current densities are high, since under these conditions the catalytic results are strongly affected by local pH effects and mass transport limitations.[55]

The activity and selectivity measured for the polycrystalline Cu closely resemble those reported in the literature, producing the following gas products: hydrogen, methane, ethylene, and CO.[3,12] On the contrary, on Pt(211) hydrogen was the main product accompanied only with traces of methane (Faradaic efficiencies below 0.2%). For CO_2 reduction on the Cu/Pt(111) and Cu/Pt (211) overlayers, H_2 and methane were detected as the main products, together with only traces of ethylene (Faradaic efficiencies below 0.6%). CO could not be detected; however, volumetric CO concentrations lower than 0.15% are below the detection limit or our GC. Therefore, it is not possible to determine Faradaic efficiencies for CO production lower than ∼20% in our high-volume electrochemical cell.

Figure 4 shows the potential dependence of H_2 and CH_4 production in terms of Faradaic efficiencies and current densities. In general, the partial current densities toward hydrogen increase with overpotential. As expected, Pt(211) is the most active surface toward HER, while polycrystalline copper is the least active.[53] The Cu overlayers show an intermediate activity toward hydrogen production.

In order to determine the selectivity of each surface toward each product, the Faradaic efficiencies were calculated. A Faradaic efficiency of close to 100% for H_2 production on Pt(211) indicates that this surface is highly selective toward hydrogen production. In contrast, polycrystalline Cu has the lowest selectivity toward H_2 and exhibits a clear dependence on the potential, reaching a minimum value at −1.0 V. The

dx.doi.org/10.1021/jp406913f | J. Phys. Chem. C 2013, 117, 20500−20508

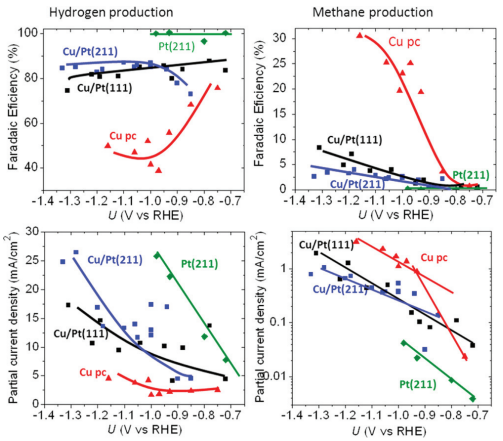

Figure 4. Faradaic efficiencies and partial current densities toward H_2 and CH_4 as a function of potential after 15 min of bulk electrolysis in CO_2 saturated 0.1 M $KHCO_3$ on Pt(211), Cu/Pt(211), Cu/Pt(111), and polycrystalline Cu. The partial current density toward methane is represented in a linear scale while the partial current density toward methane is in logarithmic scale (lines to guide the eyes).

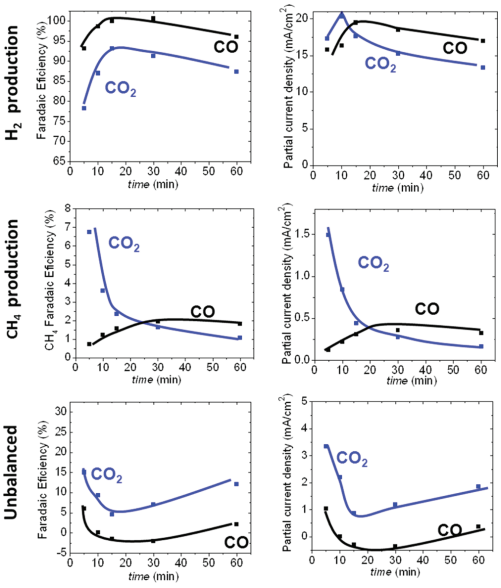

Figure 5. Faradaic efficiencies (left side) and partial current densities (right side) toward H_2 and CH_4 and unbalanced products on Cu/Pt(111) from the reduction of CO_2 and CO as a function of time. U = −1.0 V. Working electrolyte: 0.1 M $KHCO_3$.

selectivity of the Cu overlayers toward H_2 is in between that of pure Cu and Pt and does not show a clear trend with potential.

For methane production we found that both polycrystalline copper and the Cu overlayers start to form methane at around −0.7 V. In general, their Faradaic efficiencies and partial current densities increase when going to more negative potentials. However, whereas at lower overpotentials, the partial current densities for polycrystalline Cu and the Cu overlayers are comparable, at higher overpotentials the partial current densities for polycrystalline Cu are about 2−3 times higher. For example, at −1.0 V the partial current density toward methane on polycrystalline copper is ∼1.2 mA/cm^2, whereas on the Cu overlayers is ∼0.5 mA/cm^2. This lower selectivity toward hydrocarbons is consistent with a recent study by Reske et al. on Cu overlayers on polycrystalline Pt.[56]

Interestingly, there is no significant activity difference between Cu/Pt(111) and Cu/Pt(211). Even though the higher total current density for Cu/Pt(211) may suggest a higher activity, the partial current density for methane production remains the same as for Cu/Pt(111), suggesting that the Cu/Pt(211) overlayer is only more active toward the HER and not to the CO_2 reduction.

Time Dependence. We also studied the time dependence of the CO and CO_2 reduction on the Cu/Pt(111) surface by applying a constant potential of −1.0 V in either CO_2 or CO saturated 0.1 M $KHCO_3$ for 1 h. The gas products were quantified after 5, 10, 15, 30, and 60 min of reaction while the liquid phase was only analyzed after 1 h of reaction by HPLC. In case of the electroreduction of CO_2, formate was the only product detected in the liquid phase, with a corresponding Faradaic efficiency of only 1.4%. For CO electroreduction, no products could be detected in the liquid phase.

Figure 5 shows the Faradaic efficiencies and partial current densities toward methane and hydrogen production and, in addition, the contributions of undetectable products (unbalanced). In the case of CO_2, the unbalanced charge can be attributed to the production of CO, with a concentration below the detection limit of our GC, and formate, which remains in the liquid phase. For the reduction of CO, the unbalanced charge contribution is much lower (less than 5%), and as neither CO nor formate are feasible products, it is mainly an artifact of the measurements.

Previous results for bulk Cu surfaces have shown that for the reduction of CO and CO_2 the same hydrocarbon distribution is obtained.[14,57] On the Cu overlayers, however, the product distribution from CO and CO_2 can be considerably different, depending on the reaction time. The catalytic activity of the Cu/Pt(111) toward the reduction of CO does not change significantly during the 1 h reaction. The Faradaic efficiency of methane is 2% or lower during the whole reaction time, suggesting that methane production is not favored in the presence of CO. In contrast, the production of methane from CO_2 decreases drastically during the first 15 min, reaching an efficiency of ∼2% after half an hour of reaction. This result indicates that during the reduction of CO_2 the surface is being modified, changing its catalytic activity. In addition, the final of methane production rate from CO_2 is comparable to that from the reduction of CO, suggesting a similar surface structure for both cases.

XPS Results. The Cu/Pt(111) surface was characterized after 1 h of bulk electrolysis using X-ray photoelectron spectroscopy (XPS). Figure 6 shows the composition of the sample as a function of depth obtained from angle-resolved (AR)-XPS. The surface contains C, O, and K from the electrolyte and Cu and Pt. These results confirm that copper remains at the surface and that it has not been dissolved into the electrolyte or alloyed into the bulk of Pt. In addition, the survey spectrum shown in Figure S2 indicates that there is no

dx.doi.org/10.1021/jp406913f | J. Phys. Chem. C 2013, 117, 20500−20508

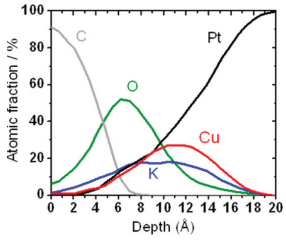

Figure 6. Depth profile for Cu/Pt(111) after 1 h of bulk CO_2 electrolysis obtained by AR-XPS using the Pt 4f, Cu 2p, K 2p, C 1s, and O 1s peaks.

significant amount of other metal that may influence the catalytic activity of the surface. The structure of the overlayer, however, cannot be determined from the XPS analysis.

EC-STM. In order to understand our observations regarding the reduction of CO and CO_2 on the Cu overlayer on Pt(111), we carried out EC-STM measurements.

We took particular care to model the conditions of the electrocatalytic measurements as close as possible. For the preparation of the Cu overlayer, we used the same experimental procedures, i.e., Cu underpotential deposition from a 0.1 M $HClO_4$ + 1 mM CuO solution, followed by an electrolyte exchange for a Cu-free 0.1 M $HClO_4$ electrolyte at a constant potential of 0.35 V. Under these conditions it is ensured that no Cu dissolves during the electrolyte exchange and the deposited Cu overlayer remains in a pseudomorphic structure.[58]

For the second electrolyte exchange for a 0.1 M $KHCO_3$ solution, it has to be considered that the potential of the used Pt pseudoreference electrode depends on the pH. An increase in pH corresponds to an increase of the reference potential and thus a more positive electrode potential. Therefore, in order to prevent any oxidation of the Cu layer, the electrolyte exchange had to be carried out at a rather low initial potential of about −0.05 V. During the electrolyte exchange, the sample potential shifted by ∼0.38 V, which corresponds to an electrode potential after the electrolyte exchange of ∼0.33 V.

STM images recorded after the electrolyte exchange show that the Cu overlayer retains an atomically flat morphology, as shown in Figure 7a. Hence, the established procedure for the second electrolyte exchange does not affect the morphology of the Cu overlayer. For comparison with the above electrochemical measurements, it has to be considered that the pH of the 0.1 M $KHCO_3$ electrolyte used for the STM measurements is slightly higher (refer to Experimental Procedure section).

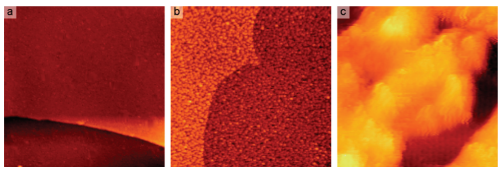

Figure 7. (a) Atomically flat morphology of the Cu overlayer in a CO-free electrolyte $(499\ nm)^2$, $U = 0.02$ V, $U_B = 292$ mV, $I_T = 1$ nA. (b) Granular morphology of the Cu overlayer after exposure to a CO-saturated electrolyte $(499\ nm)^2$, $U = 0.01$ V, $U_B = 356$ mV, $I_T = 10$ nA. (c) Disordered Cu overlayer with (2 × 2)-CO structure inside the vacancies $(13.6\ nm)^2$, $U = 0.01$ V, $U_B = 356$ mV, $I_T = 10$ nA.

However, a direct influence of the pH on the morphology of the Cu overlayer appears unlikely: STM obtained in an acidic 0.1 M $HClO_4$ electrolyte has also shown an atomically flat morphology,[58] and an aberration for an intermediate pH of 6.8 seems implausible. In addition, in the Pourbaix diagram of copper, no pH-induced phase change is found for such negative potentials.[59] The retainment of the closed film-like morphology of the Cu overlayer is in agreement with the results for its electrocatalytic activity: The inhibition of the HER with respect to the Cu-free systems suggests that no significant parts of the Pt(111) surface are exposed to the electrolyte.

In order to study the effects of CO on the Cu overlayer, a third electrolyte exchange for a CO saturated 0.1 M $KHCO_3$ solution was carried out. The high affinity of platinum to CO affects the potential of the pseudoreference electrode used in the EC-STM setup, causing a potential drop during the electrolyte exchange from about 0.33 to 0.18 V.

The morphology of the Cu overlayer changes fundamentally upon exposure to CO. Instead of being atomically flat, it appears now granular with many defects (Figure 7b). Because of these defects, part of the Pt(111) surface becomes directly exposed to the electrolyte. The driving force for this morphology change is presumably the formation of very strong Pt−CO bonds. On the other hand, Cu binds more weakly to CO, even when it is in the form of a pseudomorphic overlayer on Pt.[26]

Considering tip-convolution effects, a total exposure of 0.2 ML of the Pt(111) surface to the electrolyte can be estimated. On high-resolution STM images (Figure 7c) a structure with a hexagonal symmetry can be found within the defects of the Cu overlayer. Its symmetry and lattice constant of 0.55 ± 0.04 nm are in good agreement with a commensurable (2 × 2) structure, which is known in the literature for adsorbed CO on Pt(111).[60] This proves that in fact the Pt(111) surface becomes directly exposed to the electrolyte and gets thus covered with CO. In contrast, no ordered structure can be found for the islands of the Cu overlayer (Figure 7c). Most likely, the initially pseudomorphic Cu overlayer becomes laterally compressed until it adopts an amorphous structure with nearest-neighbor distance close to bulk Cu.

DISCUSSION

It is well established that during the reduction of CO_2 to hydrocarbons *CO is formed as an intermediate.[14,57] Hence, after a certain reaction time one would expect that *CO would induce the same morphological changes on the Cu overlayer as in the presence of pure CO. For this reason, the structural changes of the Cu/Pt(111) in the presence of CO must be taken in to consideration for the analysis of the catalytic activity of the Cu overlayers on Pt.

As demonstrated by EC-STM, the presence of CO forces the Cu atoms on the Cu/Pt(111) surface to move closer together and to expose part of the Pt surface. This is in agreement with the AR-XPS profile, which shows that the surface contains both Pt and Cu. Previously, we have shown that CO induces surface reconstruction of Cu/Pt(111) at temperature above 400 °C. In the present paper, we have demonstrated that the high binding energy between Pt−CO also induces a restructuring of the overlayer in an electrochemical environment at room temperature.[39]

We anticipate that the high binding energy between Pt and CO induces a similar reconstruction on Cu/Pt(211), causing the exposure of Pt atoms.[29] Therefore, instead of considering

the surfaces as perfect pseudomorphic overlayers, under reaction conditions, they should be considered as Pt surfaces partially covered by polycrystalline copper. The exact structure of the Cu islands is challenging to elucidate. Nonetheless, earlier surface studies of similar structures suggest that the substrate will impose some strain onto the overlayer, even if it the overlayer is defective or collapsed.[32,61] On that basis, we anticipate that the Cu overlayer will be under some degree of tensile strain, with an interatomic distance between that of pure Cu and pure Pt.

This dynamic behavior explains both the rather poor performance of the Cu overlayers for CO and CO_2 reduction and the decay of activity for CO_2 reduction. As platinum is known to be highly active for the HER, this reaction will dominate the observed overall activity as soon as a reasonable amount of Pt is exposed to the electrolyte. The Cu islands will reduce CO_2 and water producing a mixture of hydrogen, CO, formate, and methane. The current densities on copper, however, are expected to be lower than on Pt, and therefore the Faradaic efficiency toward these products is much lower than for hydrogen.

The surface restructuring in the presence of CO also allows us to explain the decay of methane production from CO_2 on Cu/Pt (111). At the beginning of the reaction the surface is a pseudomorphic Cu overlayer on Pt(111) on which CO_2 is reduced to *CO and then to methane. However, as *CO is being formed, Pt starts to be exposed, favoring the hydrogen evolution reaction over the reduction of CO_2.

Our results also explain the recent observations by Reske et al.[56] We expect that the Cu segregation observed on Pt single crystals also occurs on polycrystalline Pt. This would account for the lower selectivity toward hydrocarbons, in comparison with polycrystalline copper. Furthermore, on thicker Cu layers the exposure of the Pt atoms should be inhibited, explaining their observation that Pt with 5 and 15 nm of Cu showed higher selectivity toward hydrocarbons.

This is a clear example of the importance of *in situ* characterization techniques. Knowledge of the catalyst surface structure under reaction conditions can be crucial for the understanding of the catalyst reactivity. This is especially relevant when working with bimetallic catalysts. As demonstrated here, adsorbate−metal interactions can induce surface restructuring and influence the surface catalytic activity.

It is worth noticing that almost no ethylene is produced on these Cu/Pt surfaces, while the efficiency toward ethylene on polycrystalline copper can reach 30%. On the basis of our STM images, we judge that the Cu islands on the Pt surface contain large enough ensembles of contiguous sites covered by C-containing intermediates for the C−C bond to be formed. Therefore, in our experiments the suppression of ethylene production can be attributed to a change in the copper reactivity in comparison to polycrystalline copper. As described earlier, we anticipate that the Cu may be under some degree of tensile strain, relative to pure Cu. According to the d-band model, this would result in a more reactive surface, which would bind intermediates such as *CO more strongly.[29] Nørskov and co-workers have suggested that the potential limiting step for the CH_4 and C_2H_4 formation is the protonation of *CO to *CHO.[4] However, the magnitude of this step should be largely insensitive to the *CO binding energy, as the *CHO binding energy scales with that of *CO. On the other hand, they propose that ethylene production may be limited by a chemical step, not involving charge transfer. We speculate that the barrier for C−C coupling may be higher on the strained Cu islands than on pure Cu. This would favor the production of CH_4 over C_2H_4.[16] An alternative explanation could be that the sites required for ethylene production are absent on the Cu/Pt surfaces. According to recent works by Koper and co-workers, these sites are located on the (100) facets of Cu.[14,17]

CONCLUSION

The catalytic activity of Cu/Pt(111) and Cu/Pt(211) surfaces toward CO_2 electroreduction is intermediate between that of pure Pt and Cu. These surfaces exhibit higher total current densities than pure copper, but the main reaction product is hydrogen instead of hydrocarbons. The high activity toward the HER on the Cu/Pt surfaces is attributed to the presence of CO. During the reduction of CO_2, *CO is formed as an intermediate that destabilizes the Cu overlayer. Our EC-STM measurements show that the structure of the Cu/Pt (111) changes from a smooth pseudomorphic to a granular structure in the presence of *CO, exposing a part of the Pt surface.

The structural changes induced by *CO are crucial in understanding the catalytic activity of the Cu/Pt surfaces. The exposure of the Pt surface accounts for the high activity of these structures toward the HER and their poor selectivity toward the reduction of CO_2. These results illustrate that the catalyst surface morphology is sensitive to reaction conditions. This confirms the importance of *in situ* characterization techniques in elucidating the reactivity of bimetallic catalysts.

Furthermore, our results suggest that systems containing Pt would not be stable during the electrochemical reduction of CO_2. The strong interaction between Pt and CO would likely cause Pt segregation, favoring the HER over CO_2 reduction. For this reason, we propose the use of bimetallic systems made of materials with lower affinity toward CO as catalysts for the electrochemical reduction of CO_2. On such materials, *CO would not induce surface restructuring, ensuring stability under reaction conditions.

ASSOCIATED CONTENT

Supporting Information

Details about product quantification; CV for *CO on Pt(211); XPS survey spectrum for Cu/Pt(111) after bulk electrolysis. This material is available free of charge via the Internet at http://pubs.acs.org.

AUTHOR INFORMATION

Corresponding Authors

*E-mail ibchork@fysik.dtu.dk (I.C.).
*E-mail ifan.stephens@fysik.dtu.dk (I.E.L.S.).

Notes

The authors declare no competing financial interest.

ACKNOWLEDGMENTS

This work was supported by the "Catalysis for Sustainable Energy" (CASE) research initiative, funded by the Danish Ministry of Science, Technology and Innovation. This work was (partly) supported by The Danish National Research Foundation's Center for Individual Nanoparticle Functionality (DNRF54). The authors acknowledge the contribution of Mohammedreza Karamad, who made the figures of the structure included in Figure 3 and in the graphical abstract.

REFERENCES

(1) Li, C. W.; Kanan, M. W. CO_2 Reduction at Low Overpotential on Cu Electrodes Resulting from the Reduction of Thick Cu_2O Films. *J. Am. Chem. Soc.* **2012**, *134*, 7231−7234.

(2) Schouten, K. J. P.; Kwon, Y.; van der Ham, C. J. M.; Qin, Z.; Koper, M. T. M. A New Mechanism for the Selectivity to C1 and C2 Species in the Electrochemical Reduction of Carbon Dioxide on Copper Electrodes. *Chem. Sci.* **2011**, *2*, 1902−1909.

(3) Kuhl, K. P.; Cave, E. R.; Abram, D. N.; Jaramillo, T. F. New Insights into the Electrochemical Reduction of Carbon Dioxide on Metallic Copper Surfaces. *Energy Environ. Sci.* **2012**, *5*, 7050−7059.

(4) Peterson, A. A.; Abild-Pedersen, F.; Studt, F.; Rossmeisl, J.; Norskov, J. K. How Copper Catalyzes the Electroreduction of Carbon Dioxide into Hydrocarbon Fuels. *Energy Environ. Sci.* **2010**, *3*, 1311−1315.

(5) Nie, X.; Esopi, M. R.; Janik, M. J.; Asthagiri, A. Selectivity of CO_2 Reduction on Copper Electrodes: The Role of the Kinetics of Elementary Steps. *Angew. Chem., Int. Ed.* **2013**, *52*, 2459−2462.

(6) Tang, W.; Peterson, A. A.; Varela, A. S.; Jovanov, Z. P.; Bech, L.; Durand, W. J.; Dahl, S.; Norskov, J. K.; Chorkendorff, I. The Importance of Surface Morphology in Controlling the Selectivity of Polycrystalline Copper for CO_2 Electroreduction. *Phys. Chem. Chem. Phys.* **2012**, *14*, 76−81.

(7) Gonçalves, M. R.; Gomes, A.; Condeço, J.; Fernandes, T. R. C.; Pardal, T.; Sequeira, C. A. C.; Branco, J. B. Electrochemical Conversion of CO_2 to C_2 Hydrocarbons Using Different ex Situ Copper Electrodeposits. *Electrochim. Acta* **2013**, *102*, 388−392.

(8) Whipple, D. T.; Kenis, P. J. A. Prospects of CO_2 Utilization via Direct Heterogeneous Electrochemical Reduction. *J. Phys. Chem. Lett.* **2010**, *1*, 3451−3458.

(9) Peterson, A. A.; Nørskov, J. K. Activity Descriptors for CO_2 Electroreduction to Methane on Transition-Metal Catalysts. *J. Phys. Chem. Lett.* **2012**, *3*, 251−258.

(10) Jhong, H.-R. M.; Ma, S.; Kenis, P. J. A. Electrochemical Conversion of CO_2 to Useful Chemicals: Current Status, Remaining Challenges, and Future Opportunities. *Curr. Opin. Chem. Eng.* **2013**, *2*, 191−199.

(11) Hori, Y. Electrochemical CO_2 Reduction on Metal Electrodes. In *Modern Aspects of Electrochemistry*; Vayenas, C. G., White, R. E., Gamboa-Aldeco, M. E., Eds.; Springer: New York, 2008; Vol. *42*, pp 89−189.

(12) Hori, Y.; Murata, A.; Takahashi, R. Formation of Hydrocarbons in the Electrochemical Reduction of Carbon Dioxide at a Copper Electrode in Aqueous Solution. *J. Chem. Soc., Faraday Trans. 1* **1989**, *85*, 2309−2326.

(13) Durand, W. J.; Peterson, A. A.; Studt, F.; Abild-Pedersen, F.; Nørskov, J. K. Structure Effects on the Energetics of the Electrochemical Reduction of CO_2 by Copper Surfaces. *Surf. Sci.* **2011**, *605*, 1354−1359.

(14) Schouten, K. J. P.; Qin, Z.; Gallent, E. P.; Koper, M. T. M. Two Pathways for the Formation of Ethylene in CO Reduction on Single-Crystal Copper Electrodes. *J. Am. Chem. Soc.* **2012**, *134*, 9864−9867.

(15) Schlaup, C.; Horch, S. In-situ STM Study of Phosphate Adsorption on Cu(111), Au(111) and Cu/Au(111) Electrodes. *Surf. Sci.* **2013**, *608*, 44−54.

(16) Montoya, J. H.; Peterson, A. A.; Nørskov, J. K. Insights into C═C Coupling in CO_2 Electroreduction on Copper Electrodes. *ChemCatChem* **2013**, *5*, 737−742.

(17) Calle-Vallejo, F.; Koper, M. T. M. Theoretical Considerations on the Electroreduction of CO to C_2 Species on Cu(100) Electrodes. *Angew. Chem., Int. Ed.* **2013**, *52*, 7282−7285.

(18) van der Vliet, D. F.; Wang, C.; Li, D.; Paulikas, A. P.; Greeley, J.; Rankin, R. B.; Strmcnik, D.; Tripkovic, D.; Markovic, N. M.; Stamenkovic, V. R. Unique Electrochemical Adsorption Properties of Pt-Skin Surfaces. *Angew. Chem., Int. Ed.* **2012**, *124*, 3193−3196.

(19) Stephens, I. E. L.; Bondarenko, A. S.; Perez-Alonso, F. J.; Calle-Vallejo, F.; Bech, L.; Johansson, T. P.; Jepsen, A. K.; Frydendal, R.; Knudsen, B. P.; Rossmeisl, J.; Chorkendorff, I. Tuning the Activity of Pt(111) for Oxygen Electroreduction by Subsurface Alloying. *J. Am. Chem. Soc.* **2011**, *133*, 5485−5491.

(20) Bandarenka, A. S.; Varela, A. S.; Karamad, M.; Calle-Vallejo, F.; Bech, L.; Perez-Alonso, F. J.; Rossmeisl, J.; Stephens, I. E. L.; Chorkendorff, I. Design of an Active Site towards Optimal Electrocatalysis Overlayers, Surface Alloys and Near-Surface Alloys of Cu/Pt(111). *Angew. Chem., Int. Ed.* **2012**, *51*, 11845−11848.

(21) Esposito, D. V.; Hunt, S. T.; Stottlemyer, A. L.; Dobson, K. D.; McCandless, B. E.; Birkmire, R. W.; Chen, J. G. Low-Cost Hydrogen-Evolution Catalysts Based on Monolayer Platinum on Tungsten Monocarbide Substrates. *Angew. Chem., Int. Ed.* **2010**, *49*, 9859−9862.

(22) Kibler, L. A.; El-Aziz, A. M.; Hoyer, R.; Kolb, D. M. Tuning Reaction Rates by Lateral Strain in a Palladium Monolayer. *Angew. Chem., Int. Ed.* **2005**, *44*, 2080−2084.

(23) Greeley, J.; Nørskov, J. K.; Kibler, L. A.; El-Aziz, A. M.; Kolb, D. M. Hydrogen Evolution Over Bimetallic Systems: Understanding the Trends. *ChemPhysChem* **2006**, *7*, 1032−1035.

(24) Toyoda, E.; Jinnouchi, R.; Ohsuna, T.; Hatanaka, T.; Aizawa, T.; Otani, S.; Kido, Y.; Morimoto, Y. Catalytic Activity of Pt/TaB2(0001) for the Oxygen Reduction Reaction. *Angew. Chem., Int. Ed.* **2013**, *52*, 4137−4140.

(25) Schumacher, N.; Boisen, A.; Dahl, S.; Gokhale, A. A.; Kandoi, S.; Grabow, L. C.; Dumesic, J. A.; Mavrikakis, M.; Chorkendorff, I. Trends in Low-Temperature Water−Gas Shift Reactivity on Transition Metals. *J. Catal.* **2005**, *229*, 265−275.

(26) Schumacher, N.; Andersson, K.; Grabow, L. C.; Mavrikakis, M.; Nerlov, J.; Chorkendorff, I. Interaction of Carbon Dioxide with Cu Overlayers on Pt(111). *Surf. Sci.* **2008**, *602*, 702−711.

(27) Stamenkovic, V. R.; Mun, B. S.; Arenz, M.; Mayrhofer, K. J. J.; Lucas, C. A.; Wang, G.; Ross, P. N.; Markovic, N. M. Trends in Electrocatalysis on Extended and Nanoscale Pt-bimetallic Alloy Surfaces. *Nat. Mater.* **2007**, *6*, 241−247.

(28) Bligaard, T.; Nørskov, J. K. Ligand Effects in Heterogeneous Catalysis and Electrochemistry. *Electrochim. Acta* **2007**, *52*, 5512−5516.

(29) Mavrikakis, M.; Hammer, B.; Nørskov, J. K. Effect of Strain on the Reactivity of Metal Surfaces. *Phys. Rev. Lett.* **1998**, *81*, 2819−2822.

(30) Kitchin, J. R.; Norskov, J. K.; Barteau, M. A.; Chen, J. G. Modification of the Surface Electronic and Chemical Properties of Pt(111) by Subsurface 3d Transition Metals. *J. Chem. Phys.* **2004**, *120*, 10240−10246.

(31) Calle-Vallejo, F.; Martínez, J. I.; García-Lastra, J. M.; Rossmeisl, J.; Koper, M. T. M. Physical and Chemical Nature of the Scaling Relations Between Adsorption Energies of Atoms on Metal Surfaces. *Phys. Rev. Lett.* **2012**, *108*, 116103.

(32) Strasser, P.; Koh, S.; Anniyev, T.; Greeley, J.; More, K.; Chengfei, Y.; Zengcai, L.; Kaya, S.; Nordlund, D.; Ogasawara, H.; Toney, M. F.; Nilsson, A. Lattice-Strain Control of the Activity in Dealloyed Core-Shell Fuel Cell Catalysts. *Nat. Chem.* **2010**, *2*, 454−460.

(33) Schumacher, N.; Andersson, K. J.; Nerlov, J.; Chorkendorff, I. Formate Stability and Carbonate Hydrogenation on Strained Cu Overlayers on Pt(111). *Surf. Sci.* **2008**, *602*, 2783−2788.

(34) Friebel, D.; Miller, D. J.; Nordlund, D.; Ogasawara, H.; Nilsson, A. Degradation of Bimetallic Model Electrocatalysts: An In Situ X-Ray Absorption Spectroscopy Study. *Angew. Chem., Int. Ed.* **2011**, *50*, 10190−10192.

(35) Mayrhofer, K. J. J.; Juhart, V.; Hartl, K.; Hanzlik, M.; Arenz, M. Adsorbate-Induced Surface Segregation for Core−Shell Nanocatalysts. *Angew. Chem., Int. Ed.* **2009**, *48*, 3529−3531.

(36) Kobayashi, H.; Yamauchi, M.; Kitagawa, H.; Kubota, Y.; Kato, K.; Takata, M. Atomic-Level Pd−Pt Alloying and Largely Enhanced Hydrogen-Storage Capacity in Bimetallic Nanoparticles Reconstructed from Core/Shell Structure by a Process of Hydrogen Absorption/Desorption. *J. Am. Chem. Soc.* **2010**, *132*, 5576−5577.

(37) Abrams, B. L.; Vesborg, P. C. K.; Bonde, J. L.; Jaramillo, T. F.; Chorkendorff, I. Dynamics of Surface Exchange Reactions Between Au and Pt for HER and HOR. *J. Electrochem. Soc.* **2009**, *156*, B273−B282.

(38) Yang, R. Z.; Strasser, P.; Toney, M. F. Dealloying of Cu_3Pt (111) Studied by Surface X-ray Scattering. *J. Phys. Chem. C* **2011**, *115*, 9074−9080.
(39) Andersson, K. J.; Calle-Vallejo, F.; Rossmeisl, J.; Chorkendorff, I. Adsorption-Driven Surface Segregation of the Less Reactive Alloy Component. *J. Am. Chem. Soc.* **2009**, *131*, 2404−2407.
(40) Bondarenko, A. S.; Stephens, I. E. L.; Chorkendorff, I. A Cell for the Controllable Thermal Treatment and Electrochemical Characterisation of Single Crystal Alloy Electrodes. *Electrochem. Commun.* **2012**, *23*, 33−36.
(41) Bjorketun, M. E.; Bondarenko, A. S.; Abrams, B. L.; Chorkendorff, I.; Rossmeisl, J. Screening of Electrocatalytic Materials for Hydrogen Evolution. *Phys. Chem. Chem. Phys.* **2010**, *12*, 10536−10541.
(42) Brisard, G. M.; Zenati, E.; Gasteiger, H. A.; Markovic, N.; Ross, P. N. Underpotential Deposition of Lead on Copper(111): A Study Using a Single-Crystal Rotating Ring Disk Electrode and ex Situ Low-Energy Electron Diffraction and Scanning Tunneling Microscopy. *Langmuir* **1995**, *11*, 2221−2230.
(43) Berná, A.; Climent, V.; Feliu, J. M. New Understanding of the Nature of OH Adsorption on Pt(111) Electrodes. *Electrochem. Commun.* **2007**, *9*, 2789−2794.
(44) Hitotsuyanagi, A.; Nakamura, M.; Hoshi, N. Structural Effects on the Activity for the Oxygen Reduction Reaction on n(111)−(100) Series of Pt: Correlation with the Oxide Film Formation. *Electrochim. Acta* **2012**, *82*, 512−516.
(45) Vega, J. A.; Mustain, W. E. Effect of CO_2, HCO_3^- and CO_3^{-2} on Oxygen Reduction in Anion Exchange Membrane Fuel Cells. *Electrochim. Acta* **2010**, *55*, 1638−1644.
(46) Morallón, E.; Vázquez, J. L.; Pérez, J. M.; Aldaz, A. Electrochemical Behaviour of Pt(100), Pt(111) and Pt Polycrystalline Surfaces in Hydrogencarbonate Solution. *J. Electroanal. Chem.* **1995**, *380*, 47−53.
(47) Greeley, J. Structural Effects on Trends in the Deposition and Dissolution of Metal-supported Metal Adstructures. *Electrochim. Acta* **2010**, *55*, 5545−5550.
(48) Strasser, P.; Koh, S.; Greeley, J. Voltammetric surface Dealloying of Pt Bimetallic Nanoparticles: an Experimental and DFT Computational Analysis. *Phys. Chem. Chem. Phys.* **2008**, *10*, 3670−3683.
(49) Sheng, W.; Gasteiger, H. A.; Shao-Horn, Y. Hydrogen Oxidation and Evolution Reaction Kinetics on Platinum: Acid vs Alkaline Electrolytes. *J. Electrochem. Soc.* **2010**, *157*, B1529−B1536.
(50) Smolinka, T.; Heinen, M.; Chen, Y. X.; Jusys, Z.; Lehnert, W.; Behm, R. J. CO_2 Reduction on Pt Electrocatalysts and its Impact on H_2 Oxidation in CO_2 Containing Fuel Cell Feed Gas − A Combined In Situ Infrared Spectroscopy, Mass Spectrometry and Fuel Cell Performance Study. *Electrochim. Acta* **2005**, *50*, 5189−5199.
(51) Hoshi, N.; Hori, Y. Electrochemical Reduction of Carbon Dioxide at a Series of Platinum Single Crystal Electrodes. *Electrochim. Acta* **2000**, *45*, 4263−4270.
(52) López-Cudero, A.; Cuesta, A.; Gutiérrez, C. Potential Dependence of the Saturation CO Coverage of Pt Electrodes: The Origin of the Pre-peak in CO-stripping Voltammograms. Part 1: Pt(111). *J. Electroanal. Chem.* **2005**, *579*, 1−12.
(53) Skúlason, E.; Tripkovic, V.; Björketun, M. E.; Gudmundsdóttir, S. d.; Karlberg, G.; Rossmeisl, J.; Bligaard, T.; Jónsson, H.; Nørskov, J. K. Modeling the Electrochemical Hydrogen Oxidation and Evolution Reactions on the Basis of Density Functional Theory Calculations. *J. Phys. Chem. C* **2010**, *114*, 22374−22374.
(54) Trasatti, S. Work Function, Electronegativity, and Electrochemical Behaviour of Metals: III. Electrolytic Hydrogen Evolution in Acid Solutions. *J. Electroanal. Chem. Interfacial Electrochem.* **1972**, *39*, 163−184.
(55) Kortlever, R.; Tan, K. H.; Kwon, Y.; Koper, M. T. M. Electrochemical Carbon Dioxide and Bicarbonate Reduction on Copper in Weakly Alkaline Media. *J. Solid State Electrochem.* **2013**, *17*, 1843−1849.
(56) Reske, R.; Duca, M.; Oezaslan, M.; Schouten, K. J. P.; Koper, M. T. M.; Strasser, P. Controlling Catalytic Selectivities During CO_2 Electroreduction on Thin Cu Metal Overlayers. *J. Phys. Chem. Lett.* **2013**, *4*, 2410−2413.
(57) Hori, Y.; Takahashi, R.; Yoshinami, Y.; Murata, A. Electrochemical Reduction of CO at a Copper Electrode. *J. Phys Chem B* **1997**, *101*, 7075−7081.
(58) Schlaup, C.; Horch, S. *Phys. Chem. Chem. Phys.* **2013**, submitted.
(59) Pourbaix, M. *Atlas of Electrochemical Equilibria in Aqueous Solutions*; National Association of Corrosion Engineers: Houston, TX, 1974.
(60) Inukai, J.; Tryk, D. A.; Abe, T.; Wakisaka, M.; Uchida, H.; Watanabe, M. Direct STM Elucidation of the Effects of Atomic-Level Structure on Pt(111) Electrodes for Dissolved CO Oxidation. *J. Am. Chem. Soc.* **2013**, *135*, 1476−1490.
(61) Friebel, D.; Viswanathan, V.; Miller, D. J.; Anniyev, T.; Ogasawara, H.; Larsen, A. H.; O'Grady, C. P.; Nørskov, J. K.; Nilsson, A. Balance of Nanostructure and Bimetallic Interactions in Pt Model Fuel Cell Catalysts: In Situ XAS and DFT Study. *J. Am. Chem. Soc.* **2012**, *134*, 9664−9671.

Investigation of CO_2 and CO reduction on Au and Au-Cd alloys

------Manuscript in preparation-------

Zarko P. Jovanov[1], Heine A. Hansen[2], Ana Sofia Varela[1], Paolo Malacrida[1], Andrew A. Peterson[2,3], Ifan E. L. Stephens[1], Jens K. Nørskov[2] and Ib Chorkendorff[1]

1. *Center for Individual Nanoparticle Functionality, Technical University of Denmark, Fysikvej 312, 2800, Kongens Lyngby,Denmark.*
2. *SUNCAT Center for Interface Science and Catalysis, Department of Chemical Engineering, Stanford University, Stanford, CA, USA.*
3. *School of Engineering, Brown University, Providence, Rhode Island 02912, USA.*

Abstract

Guided by the theoretical models, we followed a strategy of alloying to break the existing scaling relations between the key CO_2 reduction intermediates. DFT calculations suggested Au_3Cd to possess respectable stability and lower overpotential for CO evolution or CH_3OH production than Au. However, numerous CO_2 electrolysis measurements on gold-cadmium bulk and surface alloy exhibited lower activities for CO evolution relative to Au. Despite the promising predictions about low overpotentials based on DFT calculations, the CO electrolyses in alkaline media on cadmium alloyed gold surfaces revealed rather low activities for further reduction of CO. We propose possibilities of adsorbate induced rearrangements of the surface, involving possible segregation of elements and thus loss of active sites. The most likely candidates are *CO and *H under reaction conditions and possibly *OH and *OCHO* at more positive potentials. The reactivity of the bimetallic systems depends highly on the exact configuration of atoms at the active site.

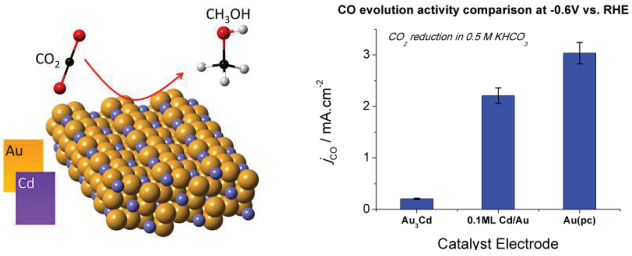

1. Introduction and motivation

In order to perform effective reduction of CO_2, Peterson et al propose the use of an electrocatalyst with stronger binding energy towards *CHO relative to the binding energy for *CO. For the materials on the righ side of the volcano in Figure 1.1, a possible approach could be increasing the partial pressure of gas phase CO. Otherwise, there should be found other strategies for decouling the binding energies of *CO and *CHO. Peterson *et al*[1] suggest various decoupling strategies involving alloying, ligand stabilisation, tethering, addition of promoters. All strategies rely on employing an approach to tackle the different geometries of adsorbed *CO intermediate and the adsorbed *CHO intermediate. CO in adsorbed state has a linear geometry, whereby carbon tends to bind the catalyst surface. On the other hand, adsorbed *CHO possesses a planar geometry.

2. Experimental methods

Electrolysis cell. Electrolysis was performed in H-cell with cathode and anode compartments separated by a Nafion membrane conducting protons. The measurements were performed for 30 min potentiostatically in CO_2 saturated 0.5 M $KHCO_3$ at pH 7.5 and CO-saturated 0.1M KOH at pH 12.8. The Ohmic drop was corrected for 85% automatically and 15% manually. The Ohmic drop across the cell and surface areas of electrodes were estimated using electrochemical impedance spectroscopy(more details shown in Supporting Information).

Bulk alloy Au_3Cd. As received Au_3Cd sheet was polished using 0.25 mm grain size diamond paste on a *MD Nap* cloth (further details in the list of materials and suppliers at the end of this section). After polishing the sample was unltrasonicated in acetone, ethanol and ultrahigh purity water multiple times. The procedure involved bombardment of the Au_3Cd sheet with 1 keV Ar^+ ions and 1 μA emission current until no carbon or oxygen contamination were observed, which usually lasted for 20 min.

Surface alloy Cd/Au. A polycrystalline gold sheet, prepared as described above, was cycled in Ar-saturated 0.1 M H_2SO_4 to improve its cleanliness and obtain an estimation of the surface area. Although the electrolysis measurements are carried at pH 7 for CO_2 reduction in bicarbonate and pH 13 for CO reduction in KOH, Cd can only be deposited at pH below 7 (Cd is insoluble at pH above 7).[2] In order to maintain potential control, the electrolyte in the reference and counter compartments could be not be exchanged. Within these two latter compartments, a 0.25 M phosphate buffer was used (0.25 M K_2HPO_4 + 0.25 M KH_2PO_4). An Ar-saturated solution of 0.1 mM $CdSO_4$ dissolved in 0.1 M H_2SO_4 was introduced into the working electrode compartment and potential was cycled between +0.74 V and 0 V or -0.05 V vs. NHE. The deposition potential, hold time and scan rate were chosen emipirically in order to achieve a specific coverage of Cd. A low Cd concentration in solution means that a longer hold time may be needed to achieve the same deposition charge, which is correlated to coverage based on the surface charge estimations obtained for Cu upd on Au.. For achieving very lower Cd coverages, a fast scan rate was used.

Angle resolved XPS. The XPS equipment (*Sigma Probe, Thermo Scientific*) uses monochromated Al Kα line as X-ray source and a six channel detector for the detection of emitted electrons.

Product analyses:

Gas phase product analysis.We used gas chromatograph of type Agilent 6890. We used two different columns, one of type HP/Molesieve for separation of H_2, O_2, N_2 and CO and another of type SUPEL-PLOT/Q for the separation of all the hydrocarbon species such as CH_4, C_2H_6, C_2H_4, C_3H_8 and C_3H_6. ***Liquid phase product analysis.*** HPLC used for data in this thesis is of type Agilent 1200 Series equipped with an autosampler, degasser, quaternary pump, as well as both refractive index and diode array detectors. We used column purchased from BIORAD, Aminex HPX-87H. Samples were analysed both at room temperature and slightly elevated temperatures (30ºC) using 0.005 M H_2SO_4 as eluent at flow rate of 0.6 mL/min. Injection volume was 30 μL.Static Headspace Gas Cromatography:We used the Agilent Headspace Sampler 7694E in connection to our GC of type Agilent 7890A. Nuclear Magnetic Resonance Spectroscopy (NMR)^{1}H-NMR, 600MHz, Queen Mary University of London, London, UK.

3. Electrocatalytic Results

Breaking scaling relations via alloying. The screening of bimetallic alloys performed by Nørskov's group included a large number of transition metals forming alloy compositions in ratio of 3:1 (of type X_3Y). Among several alloys that potentially have higher activity for CO evolution (red region on the volcano) one of the most promising is Au_3Cd, because it has high stability under reaction conditions.

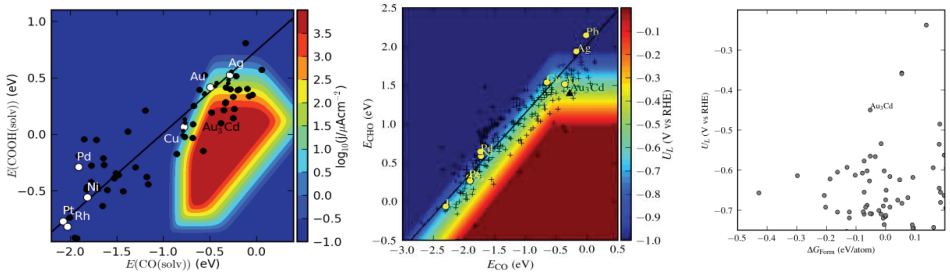

Figure 1.1: (a) 2D kinetic volcano plot – Scaling of binding energies for COOH* relative to CO* on pure transition metals (white dots) and bimetallic alloys of type X_3Y (black dots). Colored region represents logarithmic values of current densities calculated using data from[3]. **(b)** 2D-activity map - Scaling of binding energies of CO* and CHO* intermediates on pure transition metals (yellow dots) and bimetallic alloys of type X_3Y (small crosses), among which the black triangle corresponds to Au_3Cd. Colored regions represent values of predicted limiting potentials for adsorbed CO hydrogenation. **(c)** Stability plot – Predicted limiting potential for alloys against their stability represented as the free energy of formation (taking into account alloying energy and stability in electrolyte at pH 7 and 0 V vs. RHE). Au_3Cd has shown the least negative limiting potential (-0.46 V) with appreciable stability (ΔG_{Form} -0.06 eV/atom).

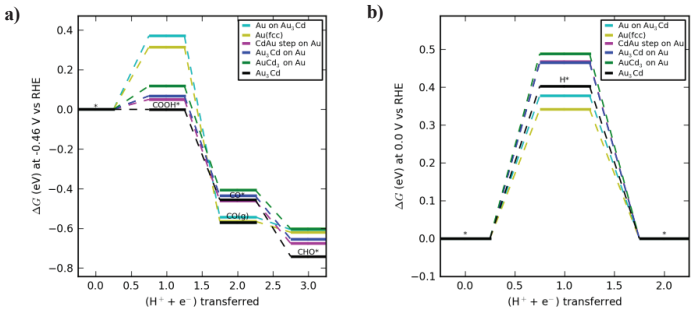

Figure 1.2: Free energy diagram of first three steps of CO_2 electro-reduction on various surface compositions of Au-Cd alloy system at -0.46 V vs. RHE.

From previous theoretical considerations for CO_2 reduction to methanol on pure gold surface, we have pointed towards the step in the reaction mechanism that might be responsible slow kinetics of further CO reduction. In any case, the stabilisation of *CHO relative to *CO would result in a lower limiting potential and thus conversion of CO_2 to useful fuels with less energy input. The binding energy of the *CHO intermediate is mainly determined by its interaction with the surface through the carbon atom. However, as suggested by Peterson *et al*, it may also to a certain extent be affected by its interaction via oxygen atom in an alloy containing an oxophillic element.[1] This interaction may influence the final geometry of *CHO intermediate at the surface and so affect its binding and stabilisation with respect to adsorbed *CO.

The alloys predicted to be very active by theoretical calculations should additionally be stable under electrochemical conditions, such as stability under reaction conditions - at the working potential and at the pH value of the working electrolyte. Figure 1.2 shows plot of limiting potential against the free energy of formation for various alloys, taking into

account their alloying energies as well as their stability in solution at pH 7 and at 0 V vs. RHE. From this plot one can easily deduce that the most stable candidates should have most negative free energies of formation, while the most active should have least negative value of limiting potential U_L. Cadmium alloyed gold (Au_3Cd) stands out amongst the candadiates for its relatively positive limiting potential and appreciable stability.

Table 1.1: Summary of limiting potentials for various reaction steps of electrocatalytic CO_2 and CO reduction on Au(211) and Au_3Cd(211) at 1 bar CO_2 and 298.15K. Additionally, the limiting potentials for direct formation of *CHO from CO(g) are calculated considering 0.001 bar and 1 bar pressure of CO.

Surface	**Au(211)**		**Au_3Cd(211)**	
Reaction step	**U_L / V (RHE)** at 0.001bar CO (CO_2 reduction)	**U_L / V (RHE)** at 1 bar CO (CO reduction)	**U_L / V (RHE)** at 0.001bar CO (CO_2 reduction)	**U_L / V (RHE)** at 1 bar CO (CO reduction)
$CO_2 \rightarrow *COOH$	-0.77	-0.77	-0.46	-0.46
$*CO \rightarrow *CHO$	-0.40	-0.40	-0.17	-0.17
$CO\,(g) \rightarrow *CHO$	-0.59	-0.41	-0.47	-0.29

CO_2 electro-reduction on Au_3Cd bulk alloy and Cd/Au surface alloy.

In contrast to the DFT predictions, the partial current densities, and hence Faradaic efficiency, towards CO evolution was actually higher for Au, than Au_3Cd. On the other hand, the partial current density towards H_2 evolution is remarkably similar between Au and Au_3Cd. Interestingly, the partial current densities towards formate production are roughly two- to threefold higher on Au_3Cd than Au in potential region from -0.4 V to -0.8 V.There are several advantages for this approach over testing the bulk alloy, namely (a) Cd is deposited in the metallic form, and it can be tested for CO_2 reduction without loss of potential control or exposure to the air (b) the amount of Cd at the surface can be controlled (c), also, from a practical viewpoint, it is much less time consuming to prepare the Cd/Au surface alloy, enabling a higher throughput of samples. On Figure 1.4, the partial current densities for CO, formate and H_2 are shown after CO_2 reduction on 0.1 ML Cd/Au surface alloy in 0.5 M $KHCO_3$, at pH 7.6. The surface activity of gold does not seem to be affected by addition of rather small submonolayer amounts of cadmium. The partial current densities for hydrogen and CO overlap with the values obtained on polycrystalline gold electrodes. The main difference results to be a slightly higher activity of 0.1 ML Cd/Au for the production of formate.

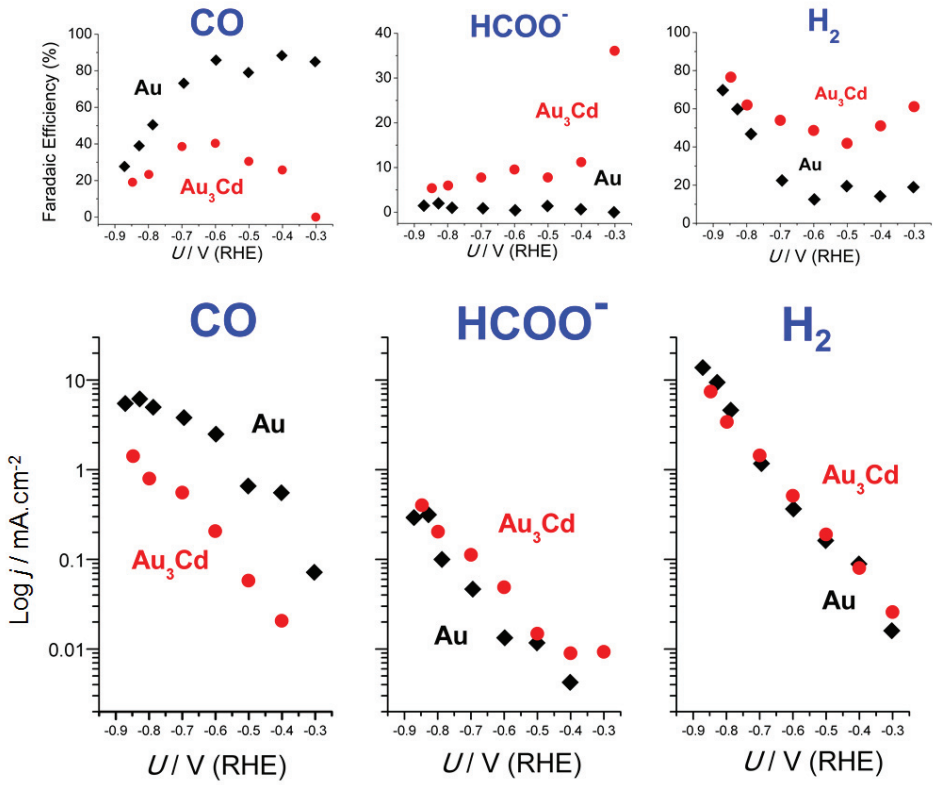

Figure 1.3: (*Upper panels*) Faradaic Efficiencies for CO_2 electro-reduction on a sheet of bulk alloy Au_3Cd relative to polycrystalline Au for the three major products: CO, $HCOO^-$ and H_2. (*Lower panels*) Partial current densities of bulk alloy Au_3Cd relative to polycrystalline Au for the three CO_2 reduction products: CO, $HCOO^-$ and H_2. Note current density is plotted on logarithmic scale. The current normalisation involved use of data obtained from the electrochemical impedance spectroscopy (as roughness factor for Au_3Cd sheet we used 3.3 and for polycrystalline Au sheet 1.5). The electrolysis was done in 1 bar CO_2-saturated 0.5 M $KHCO_3$ at pH 7.6. The data points were recorded in two sets, before each the Au_3Cd electrode was sputter-cleaned. The sets were as follow: -0.3 V, -0.5 V, -0.7 V and -0.9 V. Second set was done in following order: -0.8 V, -0.6 V and -0.4 V.

.

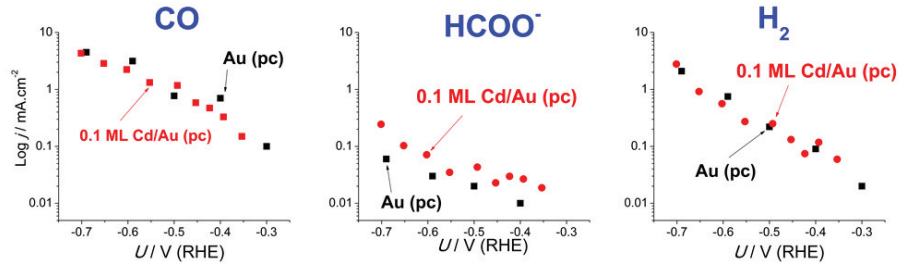

Figure 1.4: Partial current densities for CO_2 reduction in 0.5 M $KHCO_3$ at pH 7.6 on 0.1 ML Cd/Au surface alloy compared to polycrystalline Au. Each point represents an independent measurement lasting 30 min. The data is recorded in two sets – first (-0.35 V, -0.43 V, -0.5 V, -0.6 V and -0.7 V) and second set (-0.65 V, -0.55 V, -0.45 V and -0.4 V). Note the logarithmic scale of partial current densities.

The CO_2 reduction on Au alloyed with Cd, both bulk and surface alloy, leads to the three major products already observed on polycrystalline Au: H_2, CO and formate. The CO evolution activity increases in the following order: Au_3Cd << Cd/Au surface alloy ≈ Au (see Figure 1.5); this trend is the opposite to that which was predicted by the DFT calculations, which suggested the following trend: Au(211) << Cd/Au(211) surface alloy < Au_3Cd(211) (see Figure 1.2). The hydrogen evolution activity is the same on all surfaces, i.e. Au_3Cd ≈ Cd/Au surface alloy ≈ Au, also in contrast to DFT predictions, which suggested the following trend Au_3Cd < Cd/Au surface alloy < Au (see Figure 1.2). The formate production activity is as follows: Au < Au_3Cd ≈ Cd/Au.

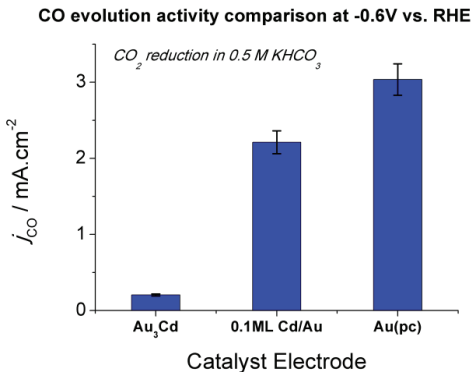

Figure 1.5: Comparison of CO ecolution activities for various gold cadmium surfaces relateive to Au at -0.6 V in CO_2 saturated 0.5 M $KHCO_3$..

CO electro-reduction on Au_3Cd bulk alloy and Cd/Au surface alloy. In order to confirm the presence of any minor products that could account for the unbalanced charges obtained from the gas phase analysis, we focused in particular on liquid products analysis with high sensitivities: nuclear magnetic spectroscopy and static headspace analysis connected to the gas chromatograph. The electrolysis measurements were performed on Au_3Cd at low overpotentials (-0.5 V, -0.4 V and -0.3 V) for 60 min to enable more accurate product detection. On the plots, the total current densities are shown, corresponding ca. 95 % of current efficiency towards H_2..

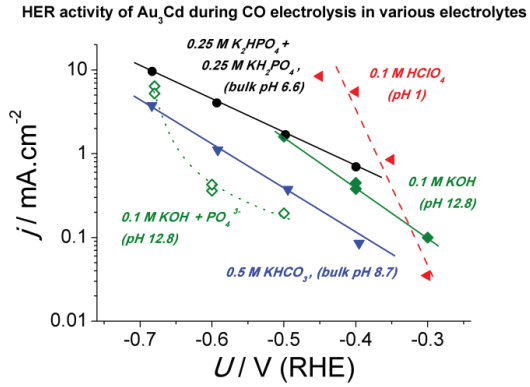

Figure 1.5: Partial current densities towards hydrogen evolution on Au_3Cd bulk alloy in various electrolytes during CO electrolysis: (1) CO-saturated 0.1 M $HClO_4$ at pH 1 (red triangles, red dashed line), (2) CO-saturated 0.25 M K_2HPO_4 + 0.25 M KH_2PO_4 at bulk pH 6.6 (black circles, black solid line), (3) CO-saturated 0.5 M $KHCO_3$ at bulk pH 8.7 (blue triangles, blue solid line) and (4) CO saturated 0.1 M KOH at pH 12.8 (green filled squares, green solid line) and (5) CO-saturated KOH with trace amounts of phosphate anions at pH 12.8 (green open squares, green dotted line). Note logarithmic current density scale. Current was normalised against the surface area established by electrochemical impedance spectroscopy measurements (roughness factor 3.3). The lines are plotted to guide the eyes.

Moreover, we employed static headspace analysis as other product detection techniques to obtain information about very small product concentrations. Figure 7.19 provides a typical chromatograph obtained upon analysis performed on aliquot samples taken after CO reduction on Au_3Cd bulk alloy sheet at -0.3 V and -0.4 V vs. RHE. Due to the high sensitivity of the method, even very small amounts of gases dissolved in the air, such as methane, are detected (at retention time of 2.4 min). No significant concentrations of either methanol or other interesting products are detected. The major product obtained during the CO electrolysis on bulk Au_3Cd sheet and Cd/Au surface alloy gold was hydrogen. The measured trends in hydrogen evolution activity were as follow: Au_3Cd > Cd/Au surface alloy ≈ Au.

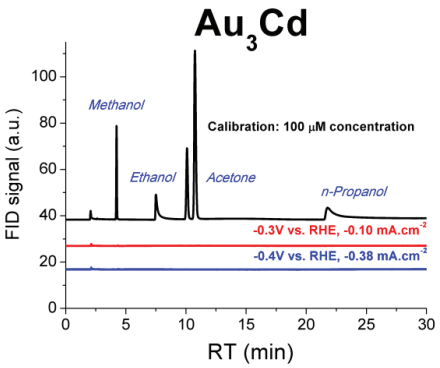

Figure 1.6: High sensitivity static headspace analysis -aliquots taken from CO electrolysis in 0.1 M KOH on Au_3Cd at -0.3 V and -0.4 V. The total current densities related to the 60 min long electrolysis measurements are shown on the plot. Calibration analysis containing 100 mM concentration of methanol, ethanol, acetone and n- propanol is contrasted to the data.

4. Discussion

Even though the binding of *CO intermediate on $Au_3Cd(211)$ is weaker with respect to Au(211), its overall free energy diagram becomes exergonic at less negative limiting potentials relative to Au(211) due to stabilisation of *COOH. Therefore, we would expect an increase in CO evolution activity. Additionally, the further reduction of *CO to CH_3OH would be possible, as it should also be for Au(211) at sufficient overpotential. Due to *CHO stabilisation on $Au_3Cd(211)$, the limiting potential for further *CO reduction to *CHO would be -0.17 V. Nonetheless, because of absolute weak binding of *CO, the chemical step of CO(g) adsorption becomes relevant when considering methanol production. Assuming the use of CO (at 1 bar) as a reactant gas instead of CO_2 (producing only ~0.001 bar of CO), DFT predicts a direct reduction of gas phase CO to *CHO at -0.29 V (see Table 1.1).

The comparison of the electrolysis results from CO_2 reduction on the surface Cd/Au alloy and on the bulk Au_3Cd alloy to the polycrystalline gold reveals significant discrepancies from the DFT predicted trends. This suggests a possibility of active site poisoning or surface structure rearrangements.

On the basis of our experiments, additional theoretical calculations were performed which suggested that the Au-Cd active site may be blocked or modified by *OH and *OCHO*. Namely, DFT calculations suggest that during CO_2 reduction to formate, *OH and *OCHO* intermediates can be stabilised by adsorbing onto two contiguous Cd atoms. Hence, there could be a driving force for converting two Au-Cd sites into a Au-Au site and a Cd-Cd site, when *OH or *OCHO* intermediates are present. DFT calculations suggest a potential dependent stability of the Au-Cd step sites: at potentials more positive than ~ +0.1 V, *OH adsorption induced surface rearrangements and poisoning may occur. The removal of *OH from the Cd-Cd sites is not exergonic until -0.2 V. Similarly, at the potentials below ~ -0.37 V, *H or *CO adsorption may cause Au-Cd sites to reform, and poison the surface. Consequently, the adsorption of CO molecules onto the catalytically relevant Au-Cd site

without reforming it would only be possible in a rather narrow potential range, below -0.25 V and more positive than -0.37 V. According to the theoretical model, at potentials below -0.37 V, the driving force for Cd subsurface migration due to H-Au interaction becomes significant.

It is not completely surprising that Cd-alloyed gold produces more formate relative to the pure Au, since metallic Cd on its own produces formate with high Faradaic efficiency.[3] Hence, the adsorbed formate (*OCHO*) may act as the site blocking species. *OH adsorption indeed may be relevant for Cd-alloyed Au; however, it occurs only at positive potentials. *OH would be removed from the surface at more negative potentials, under reaction conditions.

Effectively, prior to the electrolysis, all the electrodes were kept at potentials around -0.2 V, which would mean that both in neutral and alkaline media, Cd-alloyed gold surfaces could still have a certain coverage of *OH. Therefore, adsorbed *OH could be causing AuCd sites to reform. On the other hand, *OCHO* intermediate should easily be reduced off the surface in alkaline media at -0.25 V. Given the accuracy of DFT, adsorbed formate however may be a plausible explanation for AuCd sites rearrangements and poisoning in neutral media.

Reaction intermediates that bind stronger to Au than to Cd, such as *H and *CO, may be the reason for the Au enrichment at the surface of Cd-alloyed gold electrodes. Adsorbed H or C-based species could bring about segregation of Au to the surface. There are reports in the literature regarding the adsorption of *H[4] and *CO[5-9] on Au, in an electrochemical environment. On polycrystalline Au, potential decay measurements by Conway and coworkers suggest that the surface reaches a saturation coverage of 15 μC cm^{-2} in alkaline solution at -0.4 V;[4] presumably H would only adsorb at the step sites[10]; this would correspond to a coverage at step sites of 0.75 ML (assuming that the total density of surface atoms is equal to that of Au(111), and that step sites constitute 10% of that total surface).
Likewise, on the basis of our own measurements, and measurements by others, the CO coverage also seems to be substantial in alkaline solution; it is also reported to be significant to a significant, albeit to a lesser extent in acid solution.[6-8] It seems reasonable to conjecture that the CO coverage should also be high under neutral conditions.
In addition, there are surface science studies confirming that Au atoms have a significant mobility in an electrochemical environment.[11] Notably, according to STM measurements by Shue et al[12], CO adsorption at Au causes roughening of the step sites. This shows that Au mobility is high enough, and that CO adsorption is strong enough on Au, to allow the presence of CO to bring about the movement of Au atoms at step sites.
The surface overall composition, and hence catalytic activity, should be correlated to the equilibrium coverages of all these species: *OH and *OCHO* at positive, and *H and *CO at negative potentials.[4,13-16]

Cd/Au. CO_2 electrolysis experiments on 0.1 ML Cd/Au show that the addition of a small amount of Cd to polycrystalline gold has no significant effect to its catalytic behavior, as it resembles that of pure Au (Figure 1.4). In order to understand if these results are due to surface reconstruction or to the presence of adsorbed species we characterised the surface after reaction.

Au_3Cd. The CO evolution activity of the bulk alloy (Au_3Cd) is measured to be an order of magnitude lower than that of Au. The decrease in total current densities of CO_2 electrolysis measurements made on Au_3Cd relative to pure Au corresponds almost entirely to the amount by which the CO evolution activity on Au_3Cd decreased (shown in Figure 1.3). Interestingly, there is no significant difference in hydrogen evolution activity between the Cd-alloyed gold and the pure gold. This is surprising, given both the DFT prediction for HER of the alloyed surfaces(see Figure 1.2), and the experimental observation that Cd is at least four orders of magnitude less active for hydrogen evolution than Au.[17] Furthermore, the CO electrolyses done on Au_3Cd at -0.4 V and -0.3 V (see Figure 1.6) did not show any methanol, even when performing the product analysis using highly sensitive equipment.

5.Conclusions

The fundamental understanding of catalysis of CO_2 electro-reduction on pure transition metals –the origin of large overpotentials and existence of the scaling relations between the key intermediates – indicated various strategies in search for new catalysts. In this section, we set to explore one of the proposed strategies, involving the breaking of the scaling relations via alloying.

Density functional theory calculations were employed for the screening of transition metal based bimetallic alloys, in order to identify the optimal stable catalyst possessing low overpotential for selective formation of products of interest, primarily hydrocarbons or alcohols. The theoretical model proposes Au_3Cd and a variety of gold cadmium surface alloy structures as the system being the most likely successful in breaking the scaling relations between the intermediates involved in CO evolution reaction. Additionally, the limiting potential related to the protonation of the adsorbed CO is found to be more favourable on $Au_3Cd(211)$ than on Cu(211). The predictions imply a higher CO evolution activity on Au_3Cd relative to Au at low overpotentials. The DFT model includes possibility of further reduction of CO on Au_3Cd with CH_3OH as a final product, contrasting Cu which mainly produces hydrocarbons. The competing reaction, hydrogen evolution, is predicted to be suppressed in Cd-alloyed gold surfaces. Even though it seems to be more thermodynamically favored to produce formate on Au_3Cd than on Au, high pre-exponential factors (barriers) are expected to play a determining role, as in case of Cu, Au or Ag.

Numerous experimental measurements, including both reduction of CO_2 and CO, were performed on a bulk alloy sheet of Au_3Cd, as well as on surface alloys with submonolayer amounts of underpotentially deposited Cd.

High sensitivity quantification analysis employed both for the gas and liquid phase products of CO_2 electrolysis in neutral media led to following main observations:

a) CO evolution activity is suppressed on Au-Cd relative to pure polycrystalline Au.
b) Hydrogen evolution activity remains similar to that of Au on all varieties of AuCd structures.
c) Formate production is enhanced relative to Au, but remains a minor product.
d) No methanol or other desired products were detected using a set of analytic tools – HPLC, static headspace analysis and ^{1}H-NMR spectroscopy.

Electrolysis in alkaline electrolyte saturated with 1 bar CO showed following results:

a) Trace amounts of formaldehyde were produced on Au_3Cd, corresponding to less than 0.5 % Faradaic efficiency.
b) No methanol or other desired products were detected using a set of analytic tools – HPLC, static headspace analysis and ^{1}H-NMR spectroscopy.
c) Trace amounts of CO_2 inevitably present in KOH are reduced to formate.
d) Hydrogen evolution activity was found to be higher on Au_3Cd and same on surface alloy compared to Au.
e) Trace amounts of phosphate anions, present in 0.1 M KOH, suppress hydrogen evolution reaction, contrary to the results initially obtained during CO_2 reduction in phosphate buffer as working electrolyte.

The attempts of CO reduction on surface Cd/Au alloys using high surface area catalyst supports such as gold nanoparticles, nanoporous gold structure and high roughness oxide-derived gold electrodes failed to give a result that would match the theoretical predictions.

In summary, the experiments show that alloying Au with Cd results in a decrease in CO evolution activity and a slight increase in formate production activity. These results suggest that there are additional processes involving various reaction intermediates, adsorbed *OCHO*, *H, *CO or *OH, which may cause changes in surface composition and morphology, and they need to be taken into account by the theoretical model.

In summary, *OCHO* and *OH adsorbates may reform the surface, causing major segregation, probably through forming Cd islands surrounded by Au. The contact between Au support and Cd islands could still exist as a step edge, however, it

would be poisoned by*OH and *OCHO*, until they are removed at more negative potentials: HO* at ~-0.2 V * and *OCHO* at ~-0.25 V.. Even within the boundaries of the uncertainties of DFT, the formate or HO* poisoning hypothesis does not explain why at negative potentials one cannot achieve higher CO evolution or CO reduction activity relative to pure Au.

Alternatively, we considered that the adsorption of reactants as *H and *CO may bring about Cd subsurface migration at the step site, depleting the surface of Cd and forming an overlayer of Au at the step. Alternatively Cd could be pushed aside to form islands, as found to be the case for Cu/Pt in Section 5. Catalytic results indeed correlate better with the surface modelling an overlayer of pure gold on Au_3Cd, showing no formation of methanol on either of alloyed gold electrodes.

All the considered processes indicate towards a very narrow range of potential, from ~-0.25 V to ~-0.37 V, where Au-Cd could actually be both stable and active. The possibility of underestimated absolute binding of CO, could effect its surface coverage and desorption kinetics in a complex manner.

References

(1) Peterson, A. A.; Nørskov, J. K. The Journal of Physical Chemistry Letters 2012, 3, 251.
(2) Pourbaix, M. Atlas of Electrochemical Equilibria in Aqueous Solutions; National Association of Corrosion Engineers, 1974.
(3) Hori, Y. In Modern Aspects of Electrochemistry; Vayenas, C., White, R., Gamboa-Aldeco, M., Eds.; Springer New York: 2008; Vol. 42, p 89.
(4) Conway B. E., B. L. Electrochimica Acta 1986, 31, 1013.
(5) Cuesta, A.; Lopez, N.; Gutierrez, C. Electrochimica Acta 2003, 48, 2949.
(6) Rodriguez, P., Garcia-Araez N., Koverga A., Frank S., Koper M T M Langmuir 2010, 26, 12425.
(7) Lai, S. C. S.; Lebedeva, N. P.; Housmans, T. H. M.; Koper, M. T. M. Top Catal 2007, 46, 320.
(8) Rodriguez, P.; Feliu, J. M.; Koper, M. T. M. Electrochemistry Communications 2009, 11, 1105.
(9) Kita H., N. H., Hayashi K. J. Electroanal. Chem. 1985, 190, 141.
(10) Skulason E., T. V., Bjorketun M.E., Gudmundsdottir S., Karlberg G., Rossmeisl J., Bligaard T., Jonsson H., Norskov J.K. Journal of Physical Chemistry C 2010, 114, 18182.
(11) M., G. Progress in Surface Science 2001, 68, 1.
(12) Shue C., O. Y. L., Yau S., Itaya K. Langmuir 2005, 21, 1942.
(13) Binnig, G.; Rohrer, H.; Gerber, C.; Weibel, E. Physical Review Letters 1982, 49, 57.
(14) Kleinert, M.; Cuesta, A.; Kibler, L. A.; Kolb, D. M. Surface Science 1999, 430, L521.
(15) Schmidt, T. J.; Markovic, N. M.; Stamenkovic, V.; Ross, P. N.; Attard, G. A.; Watson, D. J. Langmuir 2002, 18, 6969.
(16) Schmidt, T. J.; Ross, P. N.; Markovic, N. M. Journal of Electroanalytical Chemistry 2002, 524, 252.
(17) Trasatti, S. Journal of Electroanalytical Chemistry and Interfacial Electrochemistry 1972, 39, 163.